

Evaluation of Photography of a Plastic Scintillator for Quality Assurance in Radiation Therapy



Mansour Almurayshid

Department of Medical Physics and Biomedical Engineering
University College London

A thesis submitted for the degree of
Doctor of Philosophy

November 2016

Declaration

I, Mansour Almurayshid, confirm that the work presented in this thesis is my own. Where information has been derived from other sources, I confirm that this has been indicated in the thesis.

Signature

.....

Acknowledgments

First of all, I want to thank Almighty Allah for his guidance and mercy for making this thesis possible. This thesis would not have been accomplished without the generous help of my supervisors. I am heartily thankful to my supervisor, **Professor Adam Gibson** whose guidance, encouragement, attention and support from the initial to the final level allowed me to develop an understanding of the subject. I owe my deepest gratitude to **Professor Jem Hebden** and **Professor Gary Royle** who have made available their support, and guidance.

I am gratefully thankful to **Dr Yusuf Helo** for his time and help in Monte Carlo simulation and **Dr Essam Banoqitah** for assistance with data processing. It is my pleasure to thank **Dr Daniel O'Flynn** for letting me using his x-ray machine. I am grateful to **Dr Lindsay Macdonald** for providing a light system for image vignetting correction.

I would also like to show my gratitude to **Dr Andrzej Kacperek** and the **staff** at the proton facility in the Clatterbridge Cancer Centre for their helpful assistance and beam delivery. I would like to gratefully thank **Dr Anna Subiel** at the NPL for her help and assistance during photon and electron beam delivery and measurements

It is an honour for me to thank my **parents, wife, brother** and **sisters** for their usual support and encouragement in all my life – especially for the last few years.

I would like thank the King Abdulaziz City for Science and Technology (KACST) in Saudi Arabia for their support and funding. Lastly, I would like to thank all the radiation physics group at UCL and would like to show my appreciation to all of those who supported and helped me in any respect during the completion of the research.

Abstract

Quality assurance is a vital part of modern radiation therapy. This thesis deals with the development of a detector system for the quality assurance (QA) of modern external beam radiation therapy. The system consists of a plastic scintillator, a commercial camera and a computer.

Different available organic scintillators were initially evaluated to select the most suitable scintillator for our design. Subsequently, many optical artefacts in our prototype design were evaluated and possible correction methods were presented to reduce the impact of the optical artefacts. The basic characteristics of the system (e.g. the reproducibility and response to changes of dose) were assessed in a series of low energy x-rays and high energy proton irradiations. Photographs of the scintillation light distributions were acquired using the detector system for low and high energy photons, electrons and protons and compared with the depth-dose curves measured with an ionisation chamber. During proton irradiation, there was a reduction in the light intensity in the Bragg peak region because the protons' high linear energy transfer (LET) leads to quenching where less light is produced than expected. We developed an approach which used Birks equation to correct for the quenching using the Monte Carlo code, Geant4. LET was modelled in Geant4 and was combined with the measured scintillation light to calculate Birks' constant. We then used the derived value of Birks constant to correct the measured scintillation light distribution for quenching using Geant4.

The results show that the light output increased linearly with the x-rays and proton dose with a correlation coefficient greater than 0.99. The system is stable and provides reproducible results to within 1% in all type of radiation. Good agreements were obtained between the scintillation and the ionisation chamber depth dose curves for both photon and electron beams if depth-scaling factor was considered for the depth dose for electrons. However, energy dependence was seen with low energy x-rays due to the mechanism of interaction at these energies depending on the material's mean atomic number. For protons, no energy and dose rate dependencies were observed for the dose rates and energies used in this work. The results show that Geant4 simulation offered an effective way to correct for quenching for any desired energy. The quenched simulated scintillation results are in good agreement with the measured scintillation results and with the variation in the position of the Bragg peak is less than 0.7%.

The results show that the system has the advantage of providing 2D visualisation of individual radiation fields and responded linearly to dose for low energy x-ray beam (50-100 kV) but suffers from energy dependency. The detector system provides acceptable depth dose curves for high energy photons and electron beams but could be enhanced if the optical artefact is corrected for. In addition, we developed an effective way to correct for quenching during proton irradiation. The technique provides a convenient method for rapid, convenient, routine quality assurance for clinical proton beams.

CONTENTS

| | |
|--|------------------|
| <u>ACKNOWLEDGMENTS</u> | <u>3</u> |
| <u>ABSTRACT.....</u> | <u>4</u> |
| <u>LIST OF FIGURES</u> | <u>10</u> |
| <u>LIST OF TABLES</u> | <u>16</u> |
| <u>1. INTRODUCTION AND LITERATURE REVIEW</u> | <u>17</u> |
| 1.1 INTRODUCTION | 18 |
| 1.2 RADIATION THERAPY..... | 19 |
| 1.2.1 RADIOTHERAPY | 19 |
| 1.2.2 PROTON THERAPY..... | 20 |
| 1.2.3 THE BIOLOGICAL EFFECT OF DIFFERENT IONISING RADIATION | 22 |
| 1.3 RADIATION INTERACTION WITH MATTER..... | 24 |
| 1.3.1 PHOTONS | 25 |
| 1.3.2 ELECTRONS | 28 |
| 1.3.3 PROTONS | 30 |
| 1.4 QUALITY ASSURANCE AND DOSIMETRY IN RADIATION THERAPY..... | 31 |
| 1.4.1 DOSIMETER REQUIREMENTS IN RADIATION THERAPY | 32 |
| 1.4.2 CURRENT PRACTICE IN THE DOSIMETRY OF RADIATION THERAPY | 33 |
| 1.4.3 THE DEPTH-DOSE DISTRIBUTION AND OFF-AXIS DOSE PROFILE | 35 |
| 1.4.4 CURRENT APPROACHES FOR RADIATION DOSIMETRY | 37 |
| 1.5 THE THEORY OF SCINTILLATION..... | 43 |
| 1.5.1 SCINTILLATION MATERIAL..... | 43 |
| 1.5.2 MECHANISM OF THE ORGANIC SCINTILLATOR | 44 |
| 1.5.3 IONISATION QUENCHING EFFECTS IN THE SCINTILLATION PROCESSES | 46 |
| 1.6 THE DEVELOPMENT OF THE DETECTOR SYSTEM IN RADIATION THERAPY | 49 |
| 1.6.1 EXPERIMENTS EMPLOYING PLASTIC SCINTILLATING FIBRES | 49 |
| 1.6.2 EXPERIMENTS EMPLOYING PLASTIC SCINTILLATORS | 50 |
| 1.6.3 EXPERIMENTS EMPLOYING LIQUID SCINTILLATORS | 52 |
| 1.6.4 SCINTILLATORS IN PROTON THERAPY | 53 |
| 1.7 THESIS OBJECTIVE..... | 55 |
| 1.8 MAJOR RESULTS AND NOVELTY | 56 |

| | |
|---|-------------------|
| <u>2. OPTIMAL DESIGN OF A PHOTOGRAPHIC SCINTILLATION DETECTOR SYSTEM.....</u> | <u>59</u> |
| 2.1 INTRODUCTION | 60 |
| 2.2 CAMERA SELECTION AND CHARACTERISATION..... | 62 |
| 2.2.1 CAMERA LINEARITY | 64 |
| 2.3 SELECTION OF THE SCINTILLATOR FOR THE DETECTOR SYSTEM | 65 |
| 2.3.1 INTRODUCTION..... | 65 |
| 2.3.2 SELECTION OF THE PLASTIC AND LIQUID SCINTILLATORS | 66 |
| 2.3.3 LIQUID SCINTILLATOR VERSUS PLASTIC SCINTILLATOR | 71 |
| 2.3.4 RESULTS..... | 72 |
| 2.3.5 DISCUSSION..... | 76 |
| 2.4 EVALUATION OF THE OPTICAL ARTEFACTS IN THE CAMERA-SCINTILLATOR DETECTOR SYSTEM | 77 |
| 2.4.1 INTRODUCTION..... | 77 |
| 2.4.2 DESIGN PRINCIPLE | 78 |
| 2.4.3 ARTEFACT CHARACTERISATIONS AND CORRECTION METHODS | 79 |
| 2.4.4 RESULTS..... | 92 |
| 2.4.5 OPTICAL ARTEFACTS DISCUSSION..... | 102 |
| 2.5 PROTOCOL OF USE OF THE DETECTOR SYSTEM | 103 |
| 2.5.1 PHOTODETECTOR SETUP AND MEASUREMENTS..... | 103 |
| 2.5.2 IMAGE ANALYSIS | 105 |
| 2.6 CONCLUSION..... | 107 |
| <u>3. SCINTILLATION DETECTOR SYSTEM FOR LOW ENERGY RADIOTHERAPY.....</u> | <u>109</u> |
| 3.1 INTRODUCTION | 110 |
| 3.2 MATERIALS AND METHODS | 113 |
| 3.2.1 THE DETECTOR SYSTEM SETUP | 113 |
| 3.2.2 BACKGROUND NOISE | 116 |
| 3.2.3 SYSTEM CHARACTERISATION | 118 |
| 3.2.3.1 SHORT-TERM REPRODUCIBILITY AND REPEATABILITY | 118 |
| 3.2.3.2 LINEARITY..... | 119 |
| 3.2.3.3 COMPARISON OF MEASUREMENTS WITH IONISATION CHAMBER..... | 119 |
| 3.2.4 MONTE CARLO SIMULATIONS..... | 120 |
| 3.3 RESULTS..... | 122 |
| 3.3.1 SHORT-TERM REPRODUCIBILITY AND REPEATABILITY | 122 |
| 3.3.2 LINEARITY..... | 123 |
| 3.3.3 PDD MEASUREMENTS | 124 |

| | |
|---|-------------------|
| 3.3.4 MONTE CARLO VALIDATION | 125 |
| 3.4 DISCUSSION | 128 |
| 3.5 CONCLUSION | 130 |
| | |
| <u>4. SCINTILLATION DETECTOR SYSTEM FOR HIGH ENERGY RADIOTHERAPY</u> | <u>132</u> |
| | |
| 4.1 INTRODUCTION | 133 |
| 4.2 MATERIALS AND METHODS..... | 135 |
| 4.2.1 THE DETECTOR SYSTEM SETUP | 135 |
| 4.2.2 TESTING THE WATER EQUIVALENCY OF BC-408 SCINTILLATOR FOR PHOTONS AND ELECTRONS | 138 |
| 4.2.3 MEASUREMENT OF SHORT-TERM REPRODUCIBILITY AND REPEATABILITY | 141 |
| 4.2.4 THE CENTRAL PDD CURVES FOR PHOTONS AND ELECTRONS | 142 |
| 4.2.5 OFF-AXIS DOSE PROFILE | 146 |
| 4.3 RESULTS..... | 147 |
| 4.3.1 BACKGROUND SIGNAL CONTRIBUTION | 147 |
| 4.3.2 SHORT-TERM REPRODUCIBILITY AND REPEATABILITY | 149 |
| 4.3.3 THE CENTRAL PDD CURVES FOR PHOTONS AND ELECTRONS | 149 |
| 4.3.4 OFF-AXIS DOSE PROFILE | 154 |
| 4.4 DISCUSSION | 159 |
| 4.4.1 MEASUREMENTS OBSERVATION | 159 |
| 4.4.2 SOURCE OF ERRORS | 161 |
| 4.5 CONCLUSION | 164 |
| | |
| <u>5. SCINTILLATION DETECTOR SYSTEM FOR PROTON THERAPY.....</u> | <u>166</u> |
| | |
| 5.1 INTRODUCTION | 167 |
| 5.2 MATERIALS AND METHODS | 168 |
| 5.2.1 PROTON THERAPY CYCLOTRON | 168 |
| 5.2.2 DETECTOR SYSTEM SET UP | 169 |
| 5.2.3 DARK IMAGE MEASUREMENTS..... | 170 |
| 5.2.4 DETECTOR SYSTEM CHARACTERISATION | 170 |
| 5.2.5 VALIDATION..... | 172 |
| 5.3 RESULTS..... | 173 |
| 5.3.1 BACKGROUND IMAGES | 173 |
| 5.3.2 BRAGG PEAK MEASUREMENTS..... | 175 |
| 5.3.3 SHORT-TERM REPRODUCIBILITY | 175 |
| 5.3.4 DOSE LINEARITY | 176 |
| 5.3.5 SCINTILLATION LIGHT WITH DIFFERENT DOSE RATE | 178 |

| | | |
|----------------------------|---|-------------------|
| 5.3.6 | SCINTILLATION LIGHT WITH DIFFERENT ENERGY | 178 |
| 5.3.7 | MEASUREMENT VALIDATION..... | 179 |
| 5.4 | DISCUSSION | 180 |
| 5.5 | CONCLUSION..... | 182 |
| <u>6.</u> | <u>ANALYSIS AND CORRECTION OF QUENCHING IN A PROTON BEAM</u> | <u>184</u> |
| 6.1 | INTRODUCTION | 185 |
| 6.2 | QUENCHING CORRECTION..... | 187 |
| 6.2.1 | METHODS | 187 |
| 6.2.2 | RESULTS..... | 193 |
| 6.2.2.1 | DETERMINATION OF BIRKS CONSTANT | 193 |
| 6.2.2.2 | QUENCHING CORRECTION..... | 194 |
| 6.3 | SYSTEM VALIDATION | 196 |
| 6.3.1 | METHOD..... | 197 |
| 6.3.2 | RESULTS..... | 197 |
| 6.4 | DISCUSSION | 201 |
| 6.5 | CONCLUSION..... | 202 |
| <u>7.</u> | <u>OVERALL CONCLUSIONS.....</u> | <u>204</u> |
| 7.1 | ACCOMPLISHED WORK | 205 |
| 7.2 | POTENTIAL QA APPLICATIONS OF THE SCINTILLATOR DETECTOR SYSTEM..... | 208 |
| 7.3 | FUTURE DIRECTION | 209 |
| <u>APPENDICES</u> | <u>.....</u> | <u>214</u> |
| APPENDIX A: | CAMERA CONTROL PRO SOFTWARE..... | 214 |
| APPENDIX B: | RADIATION IMPACT ON THE CAMERA | 216 |
| APPENDIX C: | CORRECTION FOR THE MAGNIFICATION AND REFRACTION ARTEFACTS IN THE 60 MeV PROTON BEAM..... | 217 |
| APPENDIX D: | DEFINITION OF THE BC-408 SCINTILLATOR IN GEANT4..... | 218 |
| <u>BIBLIOGRAPHY</u> | <u>.....</u> | <u>220</u> |

List of Figures

| | |
|---|----|
| Figure 1: Schematic drawing of components in the head of the linac and the MLC collimator image of Varian linacs [8] | 20 |
| Figure 2: The depth-dose distribution for 60 MeV proton beam measured by ionisation chamber in water at the Clatterbridge proton therapy facility | 21 |
| Figure 3: The relationship between LET and RBE [20] | 24 |
| Figure 4: The impact of E and Z on the occurrence of the photoelectric effect, Compton effect and pair production [3]..... | 27 |
| Figure 5: The mechanisms of electron interactions a) ionisation b) excitation c) Bremsstrahlung photon production d) characteristic x-photon production..... | 29 |
| Figure 6: The measured or simulated depth dose distributions for photons, electrons and protons (and practical range (R_p) in protons) in water obtained in this thesis | 36 |
| Figure 9: Schematic description of the bond benzene molecule. The scintillation mechanism happens in the dashed lines indicating the delocalised π -electrons between the carbon atoms | 44 |
| Figure 10: Electron energy levels of an organic molecule possessing a π -electron | 45 |
| Figure 11: The scintillation light response of a liquid scintillator (expressed in equivalent electron energy deposition) to different energies of proton beam [3]..... | 48 |
| Figure 12: 3 mm long cylindrical scintillating fibres inserted vertically into a plastic water slab and perpendicular to the detection plane [33]..... | 50 |
| Figure 13: The scintillation sheet detector [79] | 51 |
| Figure 14: The IMRT dose verification system a) The phantom outer box with camera b) the inner mirror at 45° to the scintillator sheet [45]..... | 52 |
| Figure 15: The LSD system (the z-direction goes from the gantry towards the tank) [42] | 53 |
| Figure 16: Scintillation image by which the data for depth-dose and off-axis profile measurements can be extracted, obtained by a BC-408 scintillator for a 60 MeV proton beam used in this thesis at the Clatterbridge Cancer Centre. | 54 |
| Figure 17: Linearity of light intensity as a function of current measured by the camera. Error bars demonstrate the standard deviation and some of the error bars are smaller than the point size at certain points. | 64 |
| Figure 18: The setup of the detector system based on the liquid scintillator or plastic scintillator..... | 72 |

| | |
|---|----|
| Figure 19: The light profiles obtained by a) liquid scintillator in PMMA container; b) liquid scintillator in glass container; c) plastic scintillator | 73 |
| Figure 20: A horizontal radiation beam passes through the wall of the contained and then interact with the liquid scintillator. | 74 |
| Figure 21: Interface issue – the PMMA container wall was found to be scintillating when left empty..... | 76 |
| Figure 22: The detector system components..... | 79 |
| Figure 23: Demonstration of the vignetting correction for the entire camera image..... | 81 |
| Figure 24: The comparison of off-axis dose profile obtained by the detector system and the ionisation chamber for 15 MeV electron beam. A variation between the two profiles appears at the low dose region (black circles). | 82 |
| Figure 25: Schematic flow process of a Geant4 simulation..... | 83 |
| Figure 26: The geometry used in the simulation to predict the optical behaviour of the scintillator..... | 84 |
| Figure 27: Demonstration of the geometrical magnification for the experiment geometry used in this work. The camera would detect the integrated scintillation light along the line of sight by which the light near the camera contributes a higher intensity and covers a wider field of view than light generated from behind the midline..... | 87 |
| Figure 28: The refraction of light traveling from the scintillator into air bending away from the normal at the flat interface..... | 90 |
| Figure 29: Demonstration of the refraction experiment setup showing the camera and the PMMA container..... | 91 |
| Figure 30: The scintillation compared to the Cerenkov light for $10 \times 10 \text{ cm}^2/6 \text{ MeV}$ electron beam | 93 |
| Figure 31: The resulting image of the sum of images of all planes with 100 steps across the $10 \times 10 \text{ cm}^2$ field size after applying the geometry and the intensity changes assuming the distance left between the camera and the scintillator is 10 cm (top) and comparison of the profile of the central plane or axis and the profile of the sum of all plane (bottom). The results are normalised to the maximum values of each data sets..... | 95 |
| Figure 32: The resulting image of the sum of all planes with 100 steps across the $10 \times 10 \text{ cm}^2$ field size after applying the geometry and the intensity changes assuming the distance left between the camera and the scintillator is 92 cm (top) and comparison of the profile of the central plane or axis and the profile of the sum of all plane (bottom). | 96 |
| Figure 33: The resulting image of the sum of all planes with 30 steps across the $3 \times 3 \text{ cm}^2$ field size after applying the geometry and the intensity changes when the distance left between the camera and the scintillator is 92 cm (top) and comparison of the profile of the central plane or axis and the profile of the sum of all plane (bottom). | 97 |
| Figure 34: Magnification effects in off-axis profile of the ionisation chamber for a $10 \times 10 \text{ cm}^2$ field size when r is 92 cm. For illustrative purposes, three profiles are shown in the top figure (a)..... | 98 |

| | |
|--|-----|
| Figure 35: Magnification effects in off-axis profile of the ionisation chamber for a 3×3 cm^2 field size when r is 92 cm. | 99 |
| Figure 36: Demonstration of the impact of the absorption in the measured scintillation light in Geant4. The simulation used 10^7 electrons. | 100 |
| Figure 37: The resulting image of the two overlaid images of the ruler when the container was empty and filled was enlarged at the 1 cm point of the ruler. The distance between the phantom and the camera was 23 cm. | 101 |
| Figure 38: The distance to pixel calibration image. | 104 |
| Figure 39: Demonstration of two widths of the ROIs selected for a 60 MeV proton image to extract the scintillation light depth distributions. | 106 |
| Figure 40: The scintillation light depth distributions of the two widths of the ROI and the difference between the distributions. | 106 |
| Figure 41: Approximate sketch diagram showing the spectrum of kilovoltage x-rays (100kVp) acquired using the x-rays. | 110 |
| Figure 42: a) The effect of increasing the current b) The effect of increasing the applied voltage. | 111 |
| Figure 43: Schematic of the setup used in this experiment. | 114 |
| Figure 44: Main window of SpekCalc. | 115 |
| Figure 45: The impact of subtracting the background signal in the measured depth dose distribution. Error bars demonstrate the standard deviation of three repeated measurements. | 118 |
| Figure 46: The scintillation light as a function of x-ray tube current for different applied voltages. Error bars demonstrate the standard deviation of three repeated measurements. | 123 |
| Figure 47: Comparison of measured scintillation light distribution and PDD curves by ionisation chamber for 50 kVp beam. Error bars demonstrate the standard deviation of three repeated measurements. | 124 |
| Figure 48: The simulated PDD curves for water, PMMA and BC-408 scintillator at the same irradiation parameters (50kVp). | 125 |
| Figure 49: The simulated PDD curves for the BC-408 scintillator and liquid water for different applied voltages. | 127 |
| Figure 50: The percentage maximum difference between the depth-dose distributions deposited in water and scintillator for different applied voltages Error bars demonstrate the combined statistical deviation of the simulation results. | 128 |
| Figure 51: The Linac and the reference water tank used in this experiment. | 136 |
| Figure 52: The scintillator setup in the case of a) photons and b) electrons. | 137 |
| Figure 53: a) SDD adjustment b) pixel to distance calibration. | 137 |
| Figure 54: Comparison of simulated PDD curves obtained in water and BC-408 scintillator, for a 15 MV photon beam. Error bars demonstrate the statistical deviation of the simulation results and some of error bars appears smaller than the point size at certain points of the curve. | 139 |

Figure 55: Comparison of PDD curves obtained in water and BC-408 scintillator for 6, 12 and 15 MeV electron beams with $10 \times 10 \text{ cm}^2$ field size. Error bars demonstrate the statistical deviation of the simulation results. 140

Figure 56: Comparison of PDD curves obtained in water and corrected scintillation obtained in BC-408 scintillator for 6, 12 and 15 MeV electron beam with $10 \times 10 \text{ cm}^2$ field size. 141

Figure 57: Demonstration of two scintillation images for 15 MV photon beam for two field sizes..... 143

Figure 58: Regions of validity of the criteria, showing (1) the depth dose directly measured by the camera (solid blue line); and (2) the measured ionisation chamber depth dose (red dashes). 144

Figure 59: The characterisation of the PDD curve for an electron beam in ICRU (1984). The blue continuous line is measured from the camera-scintillator detector system and the dashed line is measured with an ionisation chamber in water. 145

Figure 60: Scintillation images for four energies of an electron beam. 146

Figure 61: Profiles comparison, showing (1) the depth dose directly measured by the camera (solid blue line); and (2) the measured ionisation chamber depth dose (red dashes)..... 147

Figure 62: Comparison of the raw image and analysed image for photon beam and effect of background signal in the analysed image compared to the raw image..... 148

Figure 63: Comparison of the raw image and analysed image for electron beam and effect of background signal in the analysed image compared to the raw image..... 149

Figure 64: Comparison between the PDD values, of a $10 \times 10 \text{ cm}^2$ field, obtained by: the scintillation detector system (continuous line) and the ionisation chamber as a function of the depth in water (dashed line) for the 6 MV and 15 MV photon beams. Error bars demonstrate the standard deviation of three repeated scintillation measurements of photon beams and some of error bars appears smaller than the point size at certain points on the curves. 151

Figure 65: Comparison of depth dose profile between ionisation chamber measurement and scintillation measurements, for a 6, 10, 12 and 15 MeV electron beams. Error bars demonstrate the standard deviation of three repeated scintillation measurements of electron beams and some of error bars appears smaller than the point size at certain points along the curves..... 153

Figure 66: Comparison of normalised cross profiles obtained by the scintillator detector and the ionisation chamber for $3 \times 3 \text{ cm}^2$ and $10 \times 10 \text{ cm}^2$ and 6 MV and 15 MV photon beam at 5 cm depth . Error bars demonstrate the standard deviation of three repeated scintillation measurements of photon beams and some error bars appear smaller than the point sizes at certain points on the curves..... 156

Figure 67: Comparison of normalised cross-beam profile at depth of maximum dose between ionisation chamber measurements and scintillation measurements, for a 6, 10, 12 and 15 MeV electron beams. The field size was $10 \times 10 \text{ cm}^2$. Error bars demonstrate

the standard deviation of three repeated scintillation measurements of electron beams and some error bars appear smaller than the point size at certain points along the curves. 158

Figure 68: Scintillation image obtained in the scintillator for 6 MV photon beams and the glow in the area surrounding the edges of the radiation showing light (or dose) not being detected by the ionisation chamber Scintillation light images. 162

Figure 69: 1D plot of the blurring function of the CCD chip [83]. 163

Figure 70: The experimental setup. The camera was positioned at 50 ± 0.5 cm perpendicular to the proton beam. 169

Figure 71: The SOBP modulator wheel 171

Figure 72: The PMMA sheets placed in the way of the proton beam to obtain different energies 172

Figure 73: Background signals in three different situations 174

Figure 74: Comparison between the raw and corrected image 174

Figure 75: Measurements of dose distributions produced by a 60 MeV proton beam. . 175

Figure 76: Scintillation light depth distributions of seven repeated measurements to deliver 4.5 Gy in top graph and the difference between the measurements to the mean in the bottom graph. 176

Figure 77: The impact of the radiation dose on the scintillation light on PBP and SOBP irradiations. Error bars demonstrate the standard deviation of three repeated scintillation measurements and some error bars appear smaller than the point size at certain points. 177

Figure 78: The scintillation light after delivering 5MU at different dose-rates 178

Figure 79: The impact of the beam energy on the scintillation light. The images represent each curve in the figure and protons came from the left. 179

Figure 80: Scintillation light profile measured with the camera-scintillation detector system along the depth of the beam and compared to ion chamber depth dose curve measurements. 180

Figure 81: LET values simulated by Geant4, depth dose profile simulated in Geant4, and the measured scintillation light distribution as a function of depth for a 60 MeV proton beam in a BC-408 scintillator 188

Figure 82: The depth- dose simulated in water and BC-408 scintillator. 190

Figure 83: Validation of the simulated scintillation light with ionisation chamber measurements. 191

Figure 84: simulation and measurements validation of the transverse profile of 2.5 cm^2 proton beam. 191

Figure 85: The summary of the quenching correction procedure 192

Figure 86: The measured scintillation light vs simulated LET for the 60 MeV proton beam. 194

Figure 87: Percentage depth dose curves at 38.94, 46.77, 53.86 and 60.00 MeV, showing (1) the simulated depth dose (blue crosses); (2) the depth dose directly measured by the

| | |
|--|-----|
| camera (solid black line); (3) the simulated quenched light output (blue bars); and (4) the measured light output after correction for quenching (red dashes)..... | 195 |
| Figure 88: The simulated ideal and quenched scintillation depth distribution using Geant4, the measured scintillation depth distribution, the ionisation chamber depth-dose and the corrected scintillation depth distribution of the SOBPs beams used at the Clatterbridge Cancer Centre..... | 196 |
| Figure 89: Linearity of the scintillation detector system as a function of dose for a 60 MeV proton beam. | 198 |
| Figure 90: The response of the scintillation detector system after delivering 4.5 Gy at different dose-rates for a 60 MeV proton beam. Vertical bars on the right hand graph give the measurements error of three repeated scintillation measurements..... | 199 |
| Figure 91: The response of the scintillation detector system with the proton energies used in this study..... | 200 |
| Figure 92: Comparison between the range measured by the scintillation detector system and the tabulated range by ICRU in plastic scintillator of different proton beams..... | 200 |
| Figure 93: Telecentric lens arrangement [184] | 210 |
| Figure 95: The dual-camera detector system design..... | 212 |
| Figure 96: Experimental setup of the proposed optical dosimetry system | 213 |
| Figure 97: Camera Control Pro2 software | 215 |
| Figure 98: Measured scintillation data after correction for magnification was applied, compared with simulated scintillation distribution and actual measurement. | 217 |

List of Tables

| | |
|--|-----|
| Table 1: The cross section of each mechanism varies with atomic number and photon energy [24] | 28 |
| Table 2: Review of the above dosimeters evaluated in external photon therapy | 42 |
| Table 3: Properties of different scintillators [75], [76], [114], [115] | 67 |
| Table 4: The range and stopping power of different materials | 75 |
| Table 5: Artefacts could be present in the scintillation detector system. Adopted from [117] | 80 |
| Table 6: The properties of the BC-408 plastic scintillators [76] | 85 |
| Table 7: The magnitude of Cerenkov photons relative to the scintillation photons in the scintillator | 92 |
| Table 8: The characteristics of the x-ray beams | 116 |
| Table 9: The fractional weight of component of the materials used in the simulation .. | 121 |
| Table 10: The reproducibility of results of six images for three set of applied voltage | 122 |
| Table 11: The requirements of the performance of a clinical QA system | 130 |
| Table 12: The difference values between the ionisation chamber and the scintillation detector system, obtained at 90% and at 70 mm | 152 |
| Table 13: The electron beam characteristics for the ionisation chamber and the scintillation detector system | 154 |
| Table 14: The difference values between the cross beam profiles obtained by ionisation chamber and profile obtained by the scintillation detector system, for different photon beam energies and field sizes | 157 |
| Table 15: The difference values between the cross beam profiles obtained by ionisation chamber and profiles obtained by the scintillation detector system, for different electron beam energies | 159 |
| Table 16: The requirements of the performance of a clinical QA system | 160 |
| Table 17: The requirements of the performance of a clinical QA system | 181 |

CHAPTER 1

1. INTRODUCTION AND LITERATURE REVIEW

1.1 Introduction

Cancer is a threatening and potentially lethal disease affecting one in three people in the UK. The procedures used in efforts to treat cancer are surgery, chemotherapy, and radiation therapy [1]. A cancer patient may be assigned to all three treatments or just one of them, depending on the stage and how much the disease has spread in the individual's body. With the recent development and progression of many diagnostic modalities, including screening and imaging, more patients are expected to be eligible for loco-regional treatment including surgery and /or radiation therapy. This is due to the fact that the cancer tumour is now more likely to be diagnosed in an early stage. This also has an impact in utilising a better physical conformation of the dose to the tumour, resulting in higher cure rates and improved avoidance of the healthy tissues, thus enhancing patients' the quality of life [2]. In order to achieve the best possible results, radiation therapy dosimetry is necessary to determine the correct radiation dose for different radiation delivery machines and radiation delivery techniques with various equipment and techniques. The recent development of proton therapy delivery machines has encouraged many countries such as the UK and Saudi Arabia to look for other dosimeter systems, as not all dosimetric requirements can be fulfilled by a single dosimeter system [3]. In addition, there is ongoing research in radiation detecting materials and techniques to improve existing methods in dosimetry. One particular area of radiation therapy dosimetry, which is the concern of this thesis, is scintillation dosimetry. The work presented in this thesis explains the development and the characterisation of plastic scintillator for dosimetry in radiation therapy.

1.2 Radiation therapy

The key purpose behind radiation treatment is to deposit sufficient radiation in the tumour to damage the cancer cells and minimise radiation to the surrounding tissues in order to avoid any serious complications resulting from treatment. Radiation can be delivered via several methods and can be external (i.e. radiotherapy or proton therapy), or internal (i.e. brachytherapy).

1.2.1 Radiotherapy

Radiotherapy has been used to treat cancer using many delivery techniques such as conventional radiation therapy using two-dimensional (2D) beams of electrons or photons. A linear accelerator (Linac) is widely used to deliver high energy beams in radiotherapy. A treatment plan is produced for each individual based on computed tomography (CT) images of the patient. Sometimes, if it is necessary to identify the position of the tumour more precisely, other diagnostic modalities could be used to provide additional 'functional' information, such as positron emission tomography (PET) and magnetic resonance imaging (MRI) [4], [5].

The gantry of the Linac as shown in Figure 1 has different collimators that allow modulation of the photon beam. Primary and secondary collimators shape the beam to create rectangular fields. Subsequently, the beam travels through the last collimator consisting of typically 120 individually controlled leaves, called the multi-leaf collimator (MLC), for full modulation of the shape of the treatment site during the

irradiation [6]. In addition, clinical research has led to the utilisation of more complicated radiation delivery techniques which have had a huge impact on reducing treatment time; examples of these techniques are intensity modulated radiation therapy (IMRT) and volumetric modulated arc therapy (VMAT) [7]. These techniques aim to deliver a dose distribution that conforms to the target volume, and minimise doses to surrounding normal tissues. Current developments of Linacs and the different techniques of treatment delivery enable improved dose conformity.

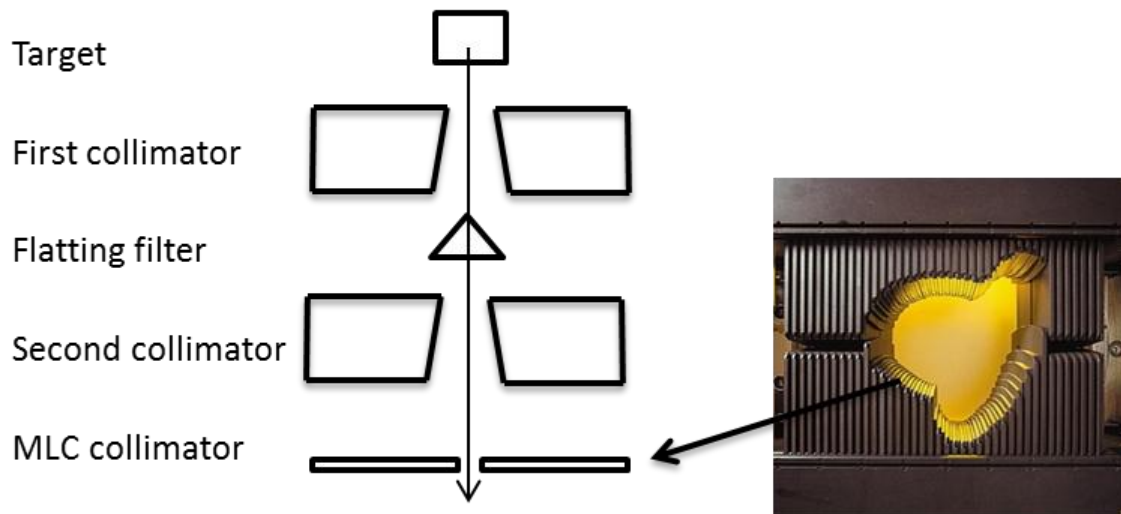


Figure 1: Schematic drawing of components in the head of the linac and the MLC collimator image of Varian linacs [8]

1.2.2 Proton therapy

Proton beam therapy has become widely studied in recent years due to its high precision dose localisation performance compared to conventional radiotherapy. This is achieved by the Bragg peak effect, in which protons deposit most of their energy at the end of their path due to the resulting energy loss of the protons is inversely

proportional to the squared velocity of the protons [9]. Figure 2 demonstrates how the protons lose their energy as they penetrate the medium [10]. In the protons' depth-dose curve, a sharp dose peak is known as the Bragg peak.

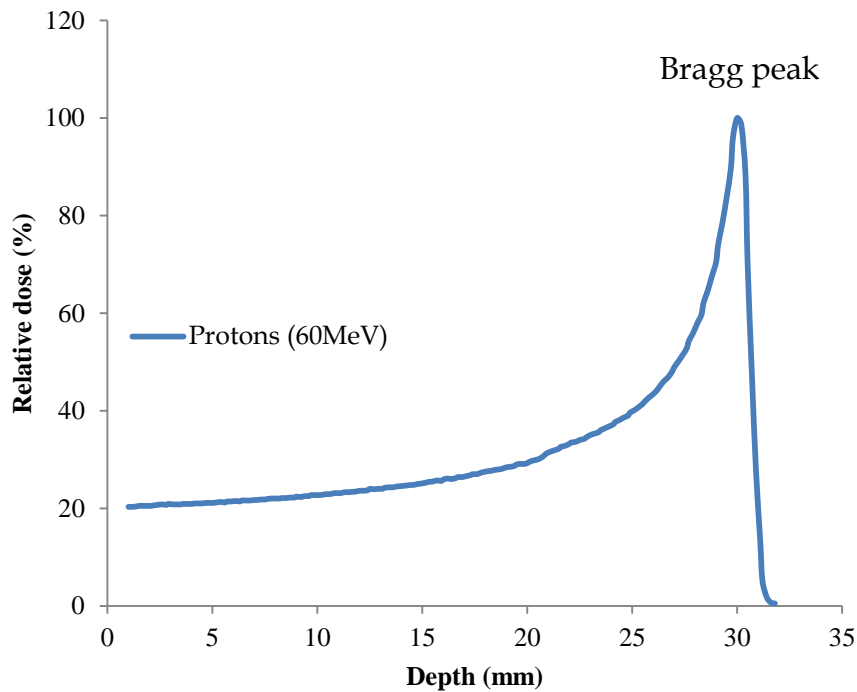


Figure 2: The depth-dose distribution for 60 MeV proton beam measured by ionisation chamber in water at the Clatterbridge proton therapy facility

In radiation therapy, protons can improve the conformity and uniformity of dose delivery, whereas photons deposit their energy within absorbed material without causing direct chemical or biological damage. Instead, photons transfer their energy to secondary electrons that can cause chemical and biological damage [11], [12]. Therefore, protons are defined as direct ionising radiation whereas photons are defined as indirect ionising radiation [13].

The available techniques to deliver the proton beams are either passive scattering beams or spot scanning beams [14]. In the passive scattering delivery technique, a scatterer is placed in the path of the initial pencil proton beam to broaden the beam (more commonly double scatterers are used) and collimators are required to provide uniform dose profiles (i.e. single Bragg peaks). Range modulator wheels or thicknesses are also employed in the beamline to form a spread out Bragg peak (SOBP) to appropriately cover a target volume. In spot scanning beams, magnets are used to deflect and steer the pristine pencil proton beam to scan the narrow beam across the patient. Two methods are commonly used in scanning protons which can be either single field uniform dose (SFUD) to deliver a uniform dose distribution to the target or intensity modulated proton therapy (IMPT) to deliver multiple fields of variable energy and intensity [15].

However, no internationally accepted standards are available for dosimetry of proton beams. Many dosimeters have been reported for the use of clinical proton dosimetry such as ionisation chambers and diodes [16], [17].

1.2.3 The biological effect of different ionising radiation

Different radiation types of the same energy can deposit different doses. The absorbed dose (D) in equation 1.1 is the most fundamental parameter in radiotherapy and gray (Gy) is the unit of absorbed dose ($1 \text{ Gy} = 6.24 \times 10^{12} \text{ MeV/kg} = 1 \text{ J/kg} = 100 \text{ rad}$).

$$D = \frac{dE \text{ (energy)}}{dm \text{ (mass)}} \quad \text{Eq 1.1}$$

In radiobiology and radiation protection, two quantities should be considered when defining the quality of an ionising radiation beam and the damage the radiation caused. These quantities are relative biological effectiveness (RBE) and linear energy transfer (LET). The definition of LET is the linear rate of energy absorption by the medium when a charged particle passes through the medium [18].

$$\text{LET} = \frac{\text{dE (the average energy deposited)}}{\text{dx (distance)}} \quad \left(\frac{\text{MeV}}{\text{cm}} \right) \quad \text{Eq 1.2}$$

Radiation of higher LET causes more biological damage. This means that higher LET results in a higher RBE. The RBE, describing the amount of dose from a test radiation source required to produces the same biological damage as a standard radiation source, is defined by the following ratio [19]:

$$\text{RBE} = \frac{D_x}{D_R} \quad \text{Eq 1.3}$$

where D_x is an absorbed dose from standard radiation x which is usually 250 kV x-ray and D_R is the dose from radiation type R that produces the same amount of biological damage. RBE differs depending on the type of radiation and type of tissue. Figure 3 shows the relationship between RBE and LET [20].

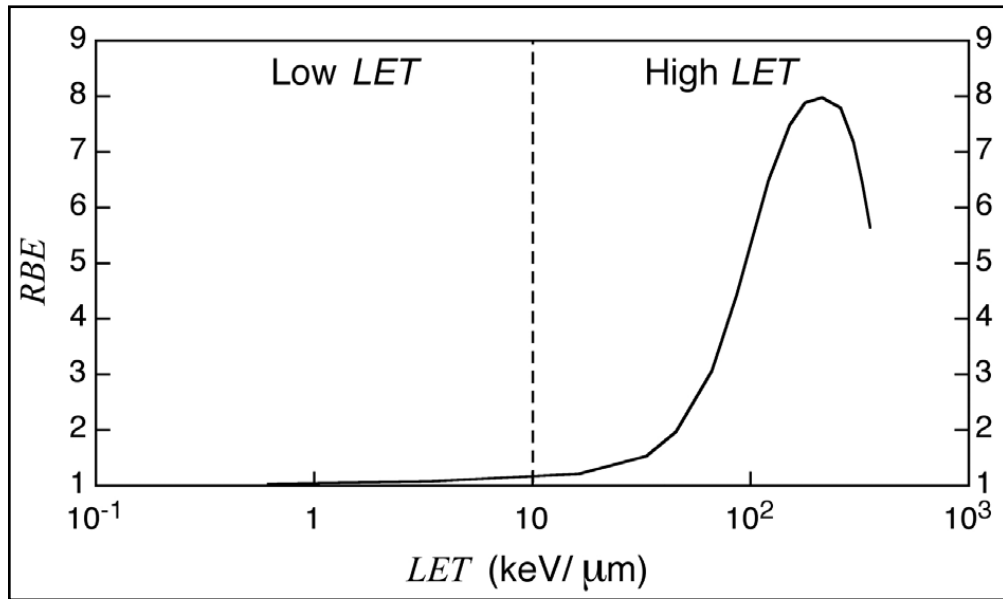


Figure 3: The relationship between LET and RBE [20]

1.3 Radiation interaction with matter

For the purposes of this thesis, it is worth mentioning some of the basic and predominant physical processes that occur when photons, electrons, and protons penetrate matter and their resulting impacts for radiation therapy. The interaction of photons, electrons, and protons is different within tissue. For example, the energy loss is higher in small increments for an electron beam as it traverses tissue compared to a photon beam in radiotherapy.

1.3.1 Photons

Attenuation of photons: an exponential law (Eq 1.4) called the Lambert-Beer law describes the attenuation of a photon beam intensity (I) passing through distance (x) of a material.

$$I(x) = I_0 \cdot e^{-\mu x} \quad \text{Eq 1.4}$$

with μ denominating a material-dependent attenuation coefficient and incident intensity (I_0). Three main interactions lead to this behaviour:

Photoelectric effect: The most dominant attenuation mechanism for incident photons with low energies occurring with inner shell electrons is the photoelectric effect. In this mechanism, the incident x-ray photon gives all its energy to one of the bound electrons which is then ejected from the atom as a photoelectron [21]. This allows measurement of the photon energy. The energy of the incident photon has to be greater or equal to the binding energy of the electron. The kinetic energy (E_{e^-}) of the electron is represented as follows:

$$E_{e^-} = h\nu - E_b \quad \text{Eq 1.5}$$

where ($h\nu$) represents the photon energy and E_b is the binding energy of the electron in its shell [22].

Compton scattering: When the incoming photon collides with an electron in the atom, an inelastic collision takes place in which the electron obtains energy and the scattered photon has energy less than that of the incoming photon. The energy of the incident photon must be large as compared to binding energy of the electron. The energy of the scattered photon $h\nu'$ in terms of the scattering angle θ is given by the following equation [22], [23]:

$$h\nu' = \frac{h\nu}{1 + \left(\frac{h\nu}{m_0 c^2}\right)(1 - \cos\theta)} \quad \text{Eq 1.6}$$

where $h\nu$ is the initial energy of x-rays and $m_0 c^2$ is the rest mass energy of the electron (0.511 MeV). The kinetic energy E_e of the electron after collision is given by:

$$E_e = h\nu - h\nu' \quad \text{Eq 1.7}$$

Pair production: The incident photon interacts with the Coulomb field of the nucleus of the absorbing material. This creates an electron-positron pair of the entire photon energy. This interaction requires high energy photons with energy greater than $2m_0 c^2 = 1.02 \text{ MeV}$ [23]. When the positron comes into rest, it combines with an electron to produce two 511 keV annihilation radiation photons.

The dominance of each interaction depends on energy (E) and the atomic number (Z) of the medium as shown in Figure 4. The dominant interaction mechanism at low energies in water is the photoelectric effect, resulting in either a partial or complete transfer of energy from a photon to an electron. Table 1 illustrates the probability of

occurrence of each mechanism (i.e. the cross section) according to E and Z [24]. In a photon beam, a specific material can be described as tissue or water equivalent if the average fractional amount of incident photon E transferred to kinetic energy of charged particles is equivalent to that of water or tissue. This is highly dependent on Z and E of the incident beam [25], [26].

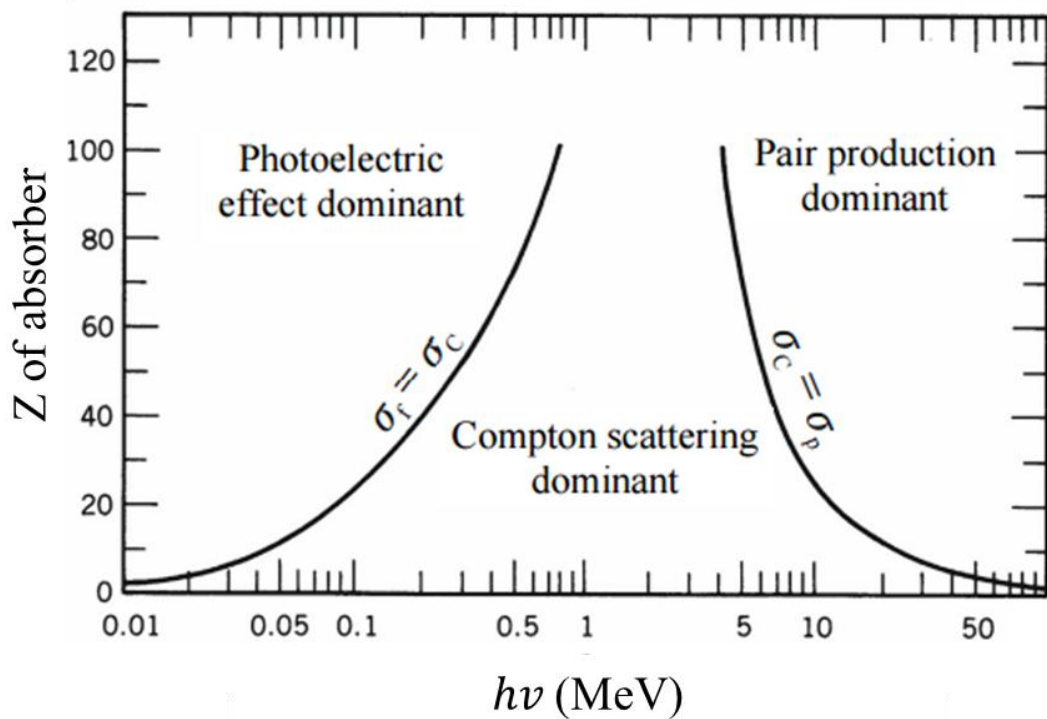


Figure 4: The impact of E and Z on the occurrence of the photoelectric effect, Compton effect and pair production [3].

Table 1: The cross section of each mechanism varies with atomic number and photon energy [24]

| <i>Mechanism</i> | <i>Cross section (σ) dependency</i> | | <i>Energy range in water</i> |
|------------------------|---|-------------------|------------------------------|
| | <i>Atomic number (Z)</i> | <i>Energy (E)</i> | |
| Photoelectric | $\propto Z^4$ | $\propto E^{-2}$ | 1-30 keV |
| Compton | independent | $\propto f(E)$ | 30 keV - 20 MeV |
| Pair production | $\propto Z^2$ | $\propto \ln(E)$ | above 20 MeV |

1.3.2 Electrons

Coulomb electric fields surrounding atoms in the tissue interact with incoming electrons by four prevailing mechanisms, depending on the energy of the incident electrons as depicted in Figure 5. As an electron interacts with orbital electrons, some of the initial incident energy of the electron is dissipated by depositing some of its energy in the medium which causes either ionisation or excitation depending primarily on the atomic number of the interaction medium. As a result, the atom may be ionised and eject the orbital electron (Figure 5a) or excite an electron to a higher energy level as seen in Figure 5b, causing the excess energy to be emitted as light or heat when the atom returns to its stable state [27]. Alternatively, the incident electron shown in Figure 5c is suddenly deflected from its trajectory by the nuclear Coulomb field. Subsequently, electromagnetic radiation is emitted, called Bremsstrahlung or braking x-ray radiation. Another mechanism for electromagnetic radiation emission shown in Figure 5d occurs when the bombarding electrons have sufficient energy to eject an electron from the

inner shells of the atoms. An electron from a higher energy states then fills the vacancy in the lower atomic energy levels emitting characteristic x-ray photons [27]. For electron dosimetry, a specific material would be water equivalent if it matched the stopping power of water [26]. The energy loss of an electron beam in collisional interactions such as ionisation and excitation is proportional to the electron density (Z/A). It is proportional to the energy and Z^2 in radiation losses interactions, as in Bremsstrahlung [27].

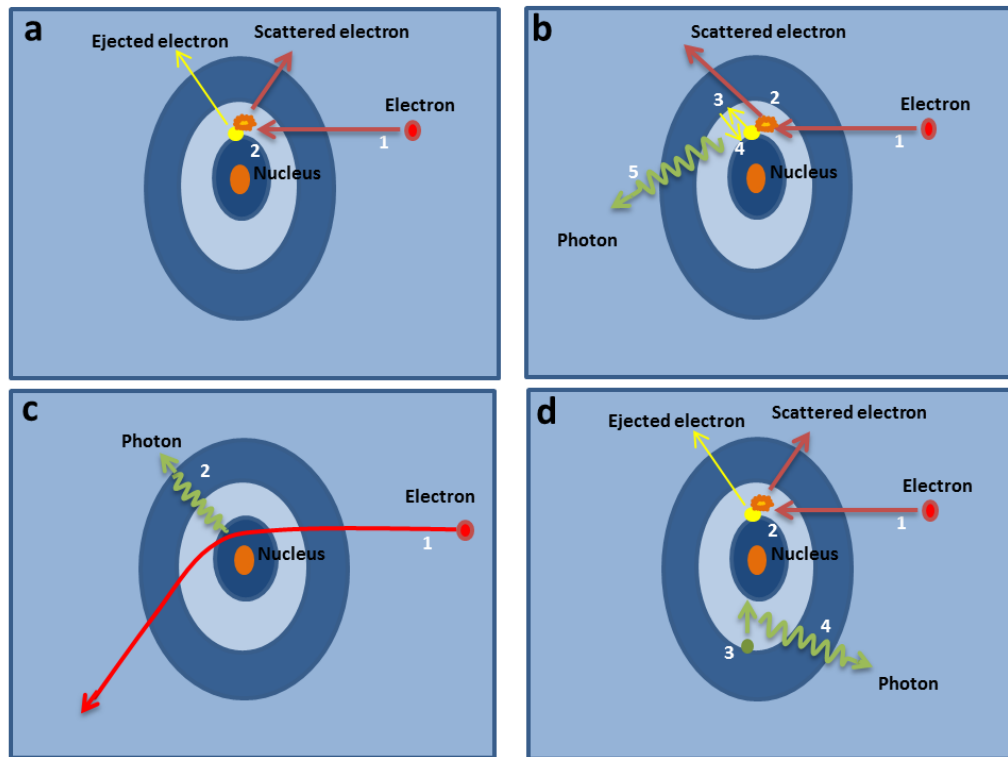


Figure 5: The mechanisms of electron interactions a) ionisation b) excitation c) Bremsstrahlung photon production d) characteristic x-photon production

1.3.3 Protons

Mechanisms for proton energy loss and scattering will be briefly explained to understand the protons' dose distribution when the protons travel through a medium. As a proton travels through matter, it loses its energy continuously because of Coulomb collisions (i.e. collisions between protons and electrons or protons and nuclei interacting through their own electric field) that cause ionisation or excitation of the matter, causing multiple Coulomb scattering. The protons deposit energy in inverse proportion to the square of their velocity. When they enter the tissue, their energy is relatively high, so they deposit little energy. As they gradually slow, they increasingly deposit more energy and continue to slow, so that most of the energy of the proton is deposited at the end of its range.

The stopping power or the mean energy loss by a charge particle per unit thickness ($-\frac{dE}{dx}$) can be determined by using the Bethe-Bloch equation [28], [29]:

$$-\frac{dE}{dx} = C \frac{Z}{A} \frac{1}{\beta^2} \left[\frac{1}{2} \ln\left(\frac{2m_o\beta^2\gamma^2 E_{\max}}{I^2}\right) - \beta^2 \right] \quad \text{Eq 1.8}$$

where $C=4\pi \times N_A$ (Avogadro number= $6.022 \times 10^{23} \text{ mol}^{-1}$) $\times r_e^2$ (electron radius= 2.8 fm) $\times m_e$ (electron mass= 511 keV) $\times c^2$ (speed of light)= $0.307 \text{ MeVg}^{-1} \text{ cm}^2$, m_o is the rest mass of the electron, β is relative particle velocity, (v/c), E_{\max} is maximum energy transferred in a single collision, I indicates the excitation energy (eV), γ is Lorentz factor ($(1-\beta^2)^{-1/2}$) and Z and A are the atomic number of the absorber and the atomic weight of the absorber respectively [30].

The range of protons can be identified by integrating $-\frac{dE}{dx}$ from 0 to E :

$$R = \int_0^E -\left(\frac{dE}{dx}\right)^{-1} dE \quad \text{Eq 1.9}$$

where E is the particle energy (MeV) and x is the path length (cm). However, not all protons that start with the same energy will have precisely the same range due to statistical fluctuations in the energy loss process [31], [32]. The mean range of the protons R in a medium can be defined as the depth in a medium after which one half of protons have stopped and R corresponds to the distance at which the dose decreased to 80% of the maximum, beyond the Bragg peak [14].

1.4 Quality assurance and dosimetry in radiation therapy

Quality assurance (QA) procedures aim to ensure that a treatment machine provides the desired level of accuracy by performing dose evaluation prior to treatment and comparing it to standard measurements. Optimisation is an essential element of advanced radiation therapy treatment techniques for achieving positive outcomes from quality treatment. In actual radiation therapy treatments, QA of the dose is necessary as many individual beams with variable intensities and energies are used to target the tumour. This is achieved by the latest generation of treatment machines which can offer significant reductions in treatment times, with many radiation beams delivered to the tumour site in each treatment course. As a result of these complex beam delivery techniques, a high precision QA is required to ensure that the planned treatment dose

distribution matches the delivered dose distribution to avoid any possible errors and uncertainties (e.g. machine output fluctuations) in the treatment process that could affect the patient's health. In other words, real-time dosimeters with high spatial resolution, sensitivity and accuracy are necessary in order to achieve good results from treatment [33].

Dosimetry is the practice of measuring radiation doses resulting from ionising radiation and modelling the particle interactions within the tissue [34]. As previously mentioned, the interaction of photons with matter is indirect as they contribute to produce charged particles (e.g. electrons) and the electrons then do the ionisation along their tracks. However, charged particles produce the ionisation directly as well as via secondary particles. The mechanism of radiation interaction with matter differs depending on the type of radiation. Hence, different detectors are recommended for use depending on the application and the type of radiation.

1.4.1 Dosimeter requirements in radiation therapy

Two main tasks in dosimetry for external radiation therapy must be examined fully in order to acquire accurate knowledge of:

- Beam characterisation to measure the absorbed dose to water at a point
- Determination of dose in the patient

These tasks need a dosimeter which can accurately measure and characterise the incident radiation beam [35]. Although different dosimetry detectors are available, several issues should be considered when selecting a particular detector type and its

uses such as the energy range and radiation type. For example, external radiation therapy can be generally summarised as:

- Kilovoltage therapy: x-rays range from 50 to 300 kV used in treating skin lesions up 2 cm depth such as Lentigo Maligna [36].
- Photon therapy: x-rays range from 4 MV to 25 MV (e.g. used for prostate cancer treatment [37])
- Electron therapy: electrons range from 6 MeV to 20 MeV (e.g. to treat pancreatic cancer intraoperatively [38]).
- Proton therapy: protons range from 30 MeV to 200 MeV (e.g. to treat ocular melanomas cancer [9]).

The specific requirements of a dosimeter should be assessed to study its feasibility. These include tissue equivalence at the energy range used, resolution, efficiency, count rate performance, response time, pressure and temperature independence, ease of use, and cost. An important feature of any detector is the linearity of dose response. In addition, the detector should be independent of the dose rate [39]. No single dosimeter can meet all these requirements. However, in practice, after selecting the most suitable dosimeter for a particular application, corrections can be applied to tackle the specific limitation of the dosimeter.

1.4.2 Current practice in the dosimetry of radiation therapy

Ideally, the absorbed dose would be measured directly by a radiation detector in radiation therapy. However, no single dosimeter fulfils the whole range of

requirements perfectly. Nowadays, most centres use different types of ionisation chambers for their reference dosimetry which are calibrated against an absolute dosimeter, which in turn is calibrated at a national standards laboratory. The aim of absolute dosimetry is to ensure consistency and reproducible results between different centres in a reference situation. The calibrated ionisation chamber can then measure the signals and convert them to the absorbed dose in the user's beam. In radiotherapy, relative dosimetry is accurately determined by the use of a calibrated ionisation chamber placed in a standardised water phantom. Then, the depth dose distributions are exported as inputs to the treatment plan system, and a computer algorithm can then estimate the depth dose distribution in each patient's treatment plan. The QA of the treatment plan of the actual dose (i.e. in vivo dosimetry) is performed to ensure that the treatment planning software calculates the predicted dose correctly. Therefore, QA is an essential procedure necessary to provide adequate confidence between the prescribed dose and the delivered dose as well as to avoid any systemic errors during defining the patient setup that may arise from any components of current radiation delivery machines, such as machine gantry or gantry stand or support [39].

In order to safely deliver a radiation dose to a patient, the performance characteristics of the specific machine delivering the radiation must be monitored. Many QA examinations (daily, weekly, monthly, annual) of the beam parameters should also be performed.

1.4.3 The depth-dose distribution and off-axis dose profile

Measuring percentage depth dose (PDD) and lateral or off-axis profiles at different energies and different field sizes is important to validate the machine output and to provide data for the treatment planning system. Thus, PDD distribution is important in radiotherapy because it helps to determine the absorbed dose in the patient at a specific depth. It is widely obtained using an ionisation chamber or diodes placed in a standard water tank at various depths in external radiotherapy QA. The PDD distributions are normalised to the depth where 100% of the maximum dose (d_{\max}) is deposited [20], [27]. The PDD can be calculated as follows:

$$\text{PDD}(d, A, \text{SSD}, E) = \frac{D_d}{D_{d_{\max}}} \times 100 \quad (\%) \quad \text{Eq 1.10}$$

where

- PDD (d, A, SSD, E) represents the percentage depth dose at depth (d) resulting from field size (A), source to surface distance (SSD) and radiation energy (E)
- D_d is the absorbed dose at depth (d)
- $D_{d_{\max}}$ is the dose at the depth of maximum dose (d_{\max})

PDD curves have a high dependency on field size and it is a very important dosimetry procedure to measure the off-axis profile of the dose. The larger the field size is, the greater the contribution from scattered photons will be, increasing the dose along the central axis.

In proton therapy, a parallel-plate ionisation chamber is used to measure the depth dose in a water phantom. The depth-dose profile contains two regions: the plateau region, where the dose increases a little with depth and the Bragg peak region, where

the dose increases promptly to the maximum. In proton therapy, the practical range (R_p) is defined as the range of the 10% distal dose point of the maximum dose [40].

Figure 6 shows the physical depth dose distributions for different types of radiation measured by either ionisation chamber measurements or the Monte Carlo calculations.

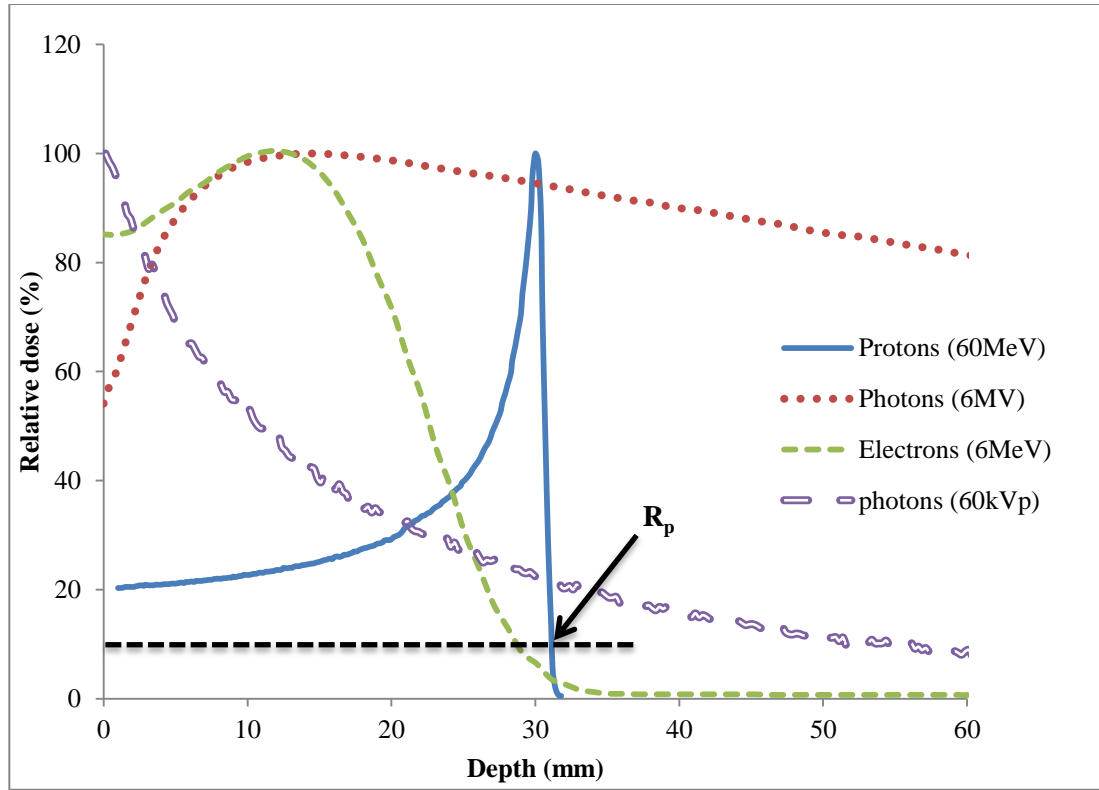


Figure 6: The measured or simulated depth dose distributions for photons, electrons and protons (and practical range (R_p) in protons) in water obtained in this thesis

Radiographic films are usually suggested to map the dose distribution to extract the flatness and the symmetry information of the proton beam at different depths along the central axis.

1.4.4 Current approaches for radiation dosimetry

As there are different treatment parameters to be checked, the choice of a detector system depends on the desired QA process. In radiation therapy, depth-dose curves and off-axis dose profiles are measured for QA and are used to provide data for the treatment plan; the treatment plan is produced based on the obtained measurement. Individual verification of dose calculations should then be checked with a detector system before delivering it to patients and then compared with a treatment planning system [10], [41]. The available detectors for QA of the dose for photons, electrons, and protons treatment will be discussed below.

1.4.4.1 Point dosimetry

The most commonly used dosimeters are ionisation chambers, diodes, and thermoluminescence dosimeters (TLD).

Ionisation chambers are the gold standard detectors when it comes to evaluating the accuracy of dose measurement in radiotherapy. Many types of ionisation chambers are used in a variety of fields such as standards labs, radiation therapy, and diagnostic radiology. They can be precise and accurate in standard conditions with correction for temperature and pressure. In addition, they are simple to calibrate, have no dead time, and do not suffer from radiation damage. However, due to the shape of IMRT fields, and because of their small active volume, ionisation chambers will introduce dose determination uncertainty because of partial volume effects [10], [41].

Diodes offer high sensitivity and immediate read-out. However, uncertainties arise from energy dependence and dose rate effect and they also depend on the angles of incidence of the beam [10], [41]. In radiotherapy, many individual beams with variable intensities, energies, and positions are used. Therefore, an ionisation chamber or a semiconductor as a point detector would be insufficient and the dose distribution would have insufficient representation [42].

TLDs are used in both radiation therapy and diagnostic radiology. The main use of the TLD is for individual protection against radiation to estimate the ionising radiation exposure over a period of time. The advantages of TLDs are maintaining cumulative records and their availability in many different sizes and shapes. However, TLDs suffer from relatively low precision in daily clinical usage, resulting in high uncertainty on dose determination and they are not real time dosimeters [10], [41].

1.4.4.2 Array detectors

The demands of a rapid dosimetric system, increased provision of information and fewer uncertainties have all had an impact on the development on dosimetric detector systems for QA of IMRT. Different two-dimensional (2D) dosimeter arrays composed of hundreds of detectors (e.g. diode and ion-chamber arrays) became commercially available to measure the variable dose distributions. Examples of the clinically used ion chambers detector arrays, as shown in Figure 7, are the 2D-ARRAY seven29 (PTW, Freiburg, Germany) and IC PROFILER™ (Sun Nuclear Corporation, Melbourne, USA) which offer fast read-out [43], [44].

The complexity of IMRT delivery requires an accurate detector, since potential errors can cause health problems. Although they have many advantages, these arrays are made of non-tissue equivalent materials. In addition, the available systems of diode and ionisation chamber arrays for IMRT verification suffer from poor spatial resolution due to the separation between the chambers in the array. As discussed above, all these systems have inherent drawbacks and their function would be enhanced if they were developed to be water-equivalent and angular independent devices [45].

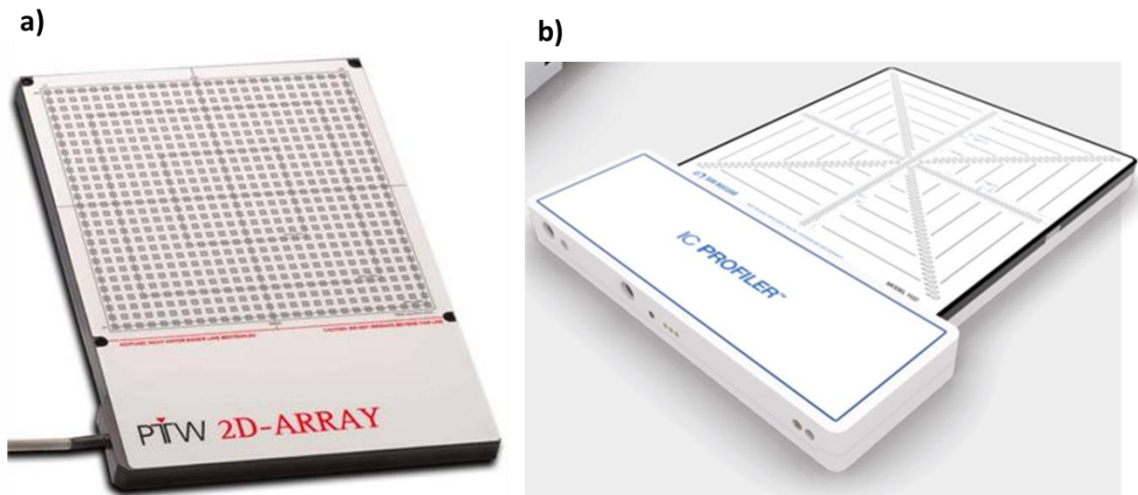


Figure 7: Oblique view images of a) The 2D Array Seven29 having 729 ionisation chambers (5 mm x 5 mm grey squares in the image) in 27 x 27 cm² b) The IC PROFILER™ array having 251 ionisation chambers in 32 x 32 cm²

1.4.4.3 Film and flat panel detectors

Radiographic and radiochromic films and electronic portal imaging devices (EPIDs) are available to measure the transmitted dose through the patient and can evaluate the dose across the whole field. Films have many applications as radiation detectors,

relative dosimeters and an archival medium as they are easy to use, quick, and cheap. In addition, they have high resolution and can record the dose distribution permanently. They are commonly used in dosimetry for radiotherapy, where the film is positioned in a phantom to estimate the 2D dose distribution [46]. However, film processing and the procedure of data analysis decide the accuracy of the final result. As a result, it can be said that film dosimetry is not a real-time dosimeter. In addition, the dose response is considerably nonlinear, particularly if the beam is protons [47].

Electronic portal imaging devices (EPIDs) are used mainly as image guided tool for pre-treatment verification of patient's position. EPIDs can be used for QA measurements such as multi-leaves collimators (MLCs) movement [48]. However, because IMRT treatment verification requires high precision, in order to avoid any possible error which could affect the patients' health, EPIDs cannot be used for IMRT treatment verification. The reasons are due to the light scatter in the detector, which means that corrections are required and the depth doses in EPIDs are not equivalent to the dose in water. Moreover, the response of such a system depends on the energy [49], [50].

1.4.4.4 Gel detector

Another detector is dosimetric gel which may be used in radiotherapy in order to have better spatial resolution and tissue equivalence, based on radiation induced chemical changes in molecules. The gel itself is prepared in a laboratory and placed into a desired phantom, which is then irradiated. The read out of dose distribution is performed using an imaging modality (e.g. MRI). However, the main disadvantage of

gels as dosimeters is the difficulty inherent in preparing the polymer gels in the hospital as the gels are made from toxic constituents. In addition, gels require lengthy processing to manipulate the dose information [10], [41], [51].

1.4.4.5 Scintillation detector

Scintillator detectors are used in many ionising radiation-based imaging modalities. Recently, there has been an increase in research on characterising and evaluating scintillators for use as dosimeters for QA applications [33], [52]–[55]. When a miniature plastic scintillating fibre coupled to an optical fibre and attached to a photomultiplier tube was exposed to a photon beam, it exhibited high sensitivity, a linear dose response, a fast response to ionising radiation, and a low angular dependence [56], [57]. In addition, scintillators were also found to have the best energy independence compared to other dosimeters used in radiotherapy, and were independent of pressure and temperature. However, the detector possessed some optical artefacts such as a Cerenkov signal generated in the optical fibre light guide. Cerenkov radiation occurs when a charged particle moves faster than light in a transparent medium [58], [59].

With the high demand of proton therapy worldwide, most of the detectors mentioned above are currently being re-evaluated for use in proton beam dosimetry. Extensive research is ongoing in the proton therapy field that may lead to more complex delivery techniques requiring accurate dosimeters. Table 2 compares the dosimetric properties of many detectors for high energy photon beam radiotherapy [20], [27], [57], [60], [61]. Scintillators are shown to have excellent dosimetric properties for high energy photon beams.

Table 2: Review of the above dosimeters evaluated in external photon therapy

| <i>Dosimeter</i> | <i>Ionisation chamber</i> | <i>Diode</i> | <i>TLD</i> | <i>EBT Film</i> | <i>Scintillator</i> |
|---|---------------------------|--------------|------------|-----------------|---------------------|
| Required voltage supply | × | ✓ | ✓ | ✓ | ✓ |
| Dose response | ✓ | ✓ | o | ✓ | ✓ |
| Real time or Instant readout | ✓ | ✓ | × | × | ✓ |
| Temperature independence | o | o | o | ✓ | O |
| Insensitive to optical noise | ✓ | ✓ | ✓ | ✓ | × |
| Energy independence | ✓ | × | o | o | ✓ |
| Dose rate independence | ✓ | × | o | o | ✓ |
| Usability | ✓ | ✓ | ✓ | × | ✓ |
| Level of dose accuracy (if 2% required) | ✓ | ✓ | o | o | ✓ |
| Detector density (ρ) and Atomic number (Z_{eff}) | High | High | High | Low | Low |
| Real-time | Yes | Yes | No | No | Yes |

✓: good o: adequate ×: poor

1.5 The theory of scintillation

1.5.1 Scintillation material

Scintillators are materials that can act as detectors by emitting luminescence in a particular wavelength range when irradiated. The history of scintillation began when Wilhelm Rontgen witnessed the luminescent behaviour of crystals in the vicinity of his cathode ray tube during his discovery of x-rays in 1895 [62]. Scintillation light was observed as a coincidence when the x-ray tube was switched on. Luminescence is a broad term outlining the emission of radiation– specifically radiation in visible or near-visible light spectrum [63].

Since then, scintillation detectors continued to be studied which led to the production of the first inorganic scintillators, made of ZnS. Continuous research of different inorganic scintillators has led to the creation of many inorganic scintillators [64]. Although they have high light yield, inorganic scintillators have slow decay times. Eventually, an organic scintillator (crystalline anthracene ($C_{14}H_{10}$)) was discovered in 1947. This organic scintillator has a faster response time and is measured in nanoseconds (ns) [65]. However, anthracene cannot be made in large crystals resulting in the need to develop more convenient types of organic scintillators, both plastics and liquids [66], [67].

Scintillators have been applied widely in radiation detection. For example, they are used in portal imaging systems to improve patient placement and pre-treatment localisation in radiotherapy by their sensitivity and rapid response time [68].

1.5.2 Mechanism of the organic scintillator

The scintillation mechanism of the organic scintillator selected for this study will be briefly explained. The base of an organic scintillator molecule is its carbon atoms that determine the electronic structure. The ground state configuration of the carbon is $1s^2 2s^2 2p^2$ but the binding ground state configuration would be $1s^2 2s^2 2p^3$ as it is considered that one of the 2s-electrons is excited into a 2p-state. In this configuration, carbon can accommodate four valence electron orbitals (i.e. one 2s and three 2p) of which a linear combination can contribute to every molecule orbital. To explain the luminescence procedure, consider benzene (C_6H_6), which is the base of a liquid scintillator, shown in Figure 8. Here, the carbons bonds would be formed in the s-orbital with the H atoms and in the p-orbitals with C atoms by which the molecular π -orbitals are formed [56].

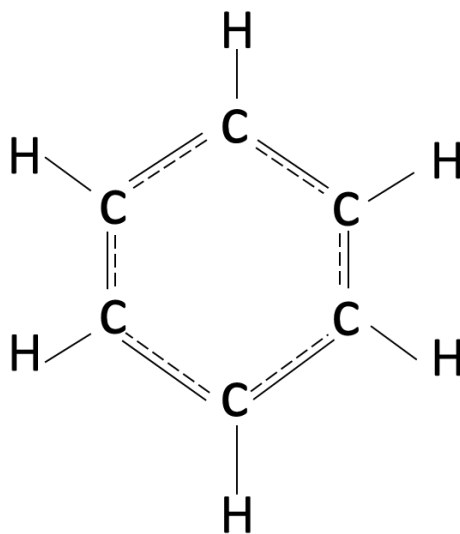


Figure 8: Schematic description of the bond benzene molecule. The scintillation mechanism happens in the dashed lines indicating the delocalised π -electrons between the carbon atoms

The excitation and de-excitation of these delocalised π -electrons is responsible for luminescence. The molecular structures of most organic scintillators have a covalent bond that is formed by two electrons called the π -electrons of the carbon-carbon bond. The energy level states of π -electrons are shown in Figure 9 [69].

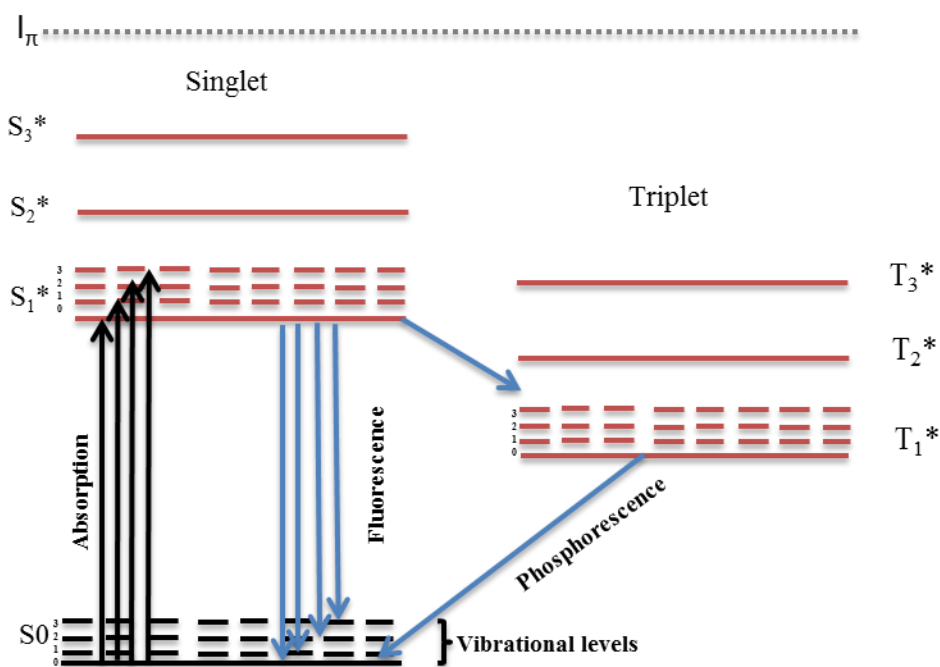


Figure 9: Electron energy levels of an organic molecule possessing a π -electron

Scintillation photons result from radiation exposure, by which secondary electrons are produced. The energy of the electrons would be lost by ionising and exciting the molecules along their paths. In case of excitation, the emission of visible light can be caused by many luminescence processes that depend on the spin orientation of the excited electron, which separates the electronic states into singlet (anti-parallel

orientation) and triplet (parallel orientation) states. Prompt fluorescence is the result of transitions in the energy level structure of a molecule. This emission of light occurs within ns and is the predominant process. Fluorescence occurs when the ground singlet (S_0) state is excited to an excited singlet (S^*) state, then the decay from the S^* state to the S_0 state results in the fluorescent emission of photons. At the singlet level, the total spin of the electron level ($\pm 1/2$) is equal to zero. In the process of fluorescence, the electron does not change its spin direction. Furthermore, most of the deposited energy is wasted as non-radiative processes (e.g. vibration).

Another type of luminescence caused by ionisation of a π -electron is phosphorescence, which is distinguished from fluorescence because of its longer wavelength and a decay time of more than 10 microseconds (μs) [3]. Luminescence happens when the triplet state becomes excited (T_1^*) (spin equal to 1). This is caused by the molecule recombining with an electron trapped in a triplet state; the decay from T_1^* to S_0 transition is then referred to as phosphorescence [3].

To maximise the timing precision, the desired luminance process is fluorescence where photons are produced within a short time window after the interaction of radiation. Therefore, scintillator developers aim to reduce the probability of other luminance processes [70].

1.5.3 Ionisation quenching effects in the scintillation processes

The scintillator response is linked directly to ionisation generated by charged particles. Photons are uncharged particles but produce secondary electrons which cause indirect scintillation. A small fraction of the kinetic energy is emitted as fluorescent

light. The remaining energy is transferred mostly into vibrations or heat. Therefore, the scintillation efficiency, which is the conversion of the particle energy into fluorescence, depends on the scintillator type and the type of charged particle causing the ionisation [3].

For an ideal dosimeter based on a scintillation material, the amount of fluorescent light should be proportional to the energy (E) deposited:

$$\frac{dL}{dx} = L_0 \cdot \frac{dE}{dx} \quad \text{Eq 1.11}$$

where L is the scintillation light, dE/dx is the energy loss and L_0 is the scintillation efficiency (i.e. number of photons per unit energy deposited). However, this is not the case if an organic scintillator is irradiated with charged particles with high LET like protons [71]. In this case, the light output is suppressed in a process known as quenching. This effect is well known and is described by Birks [72].

Quenching effect is a short-lived process due to molecular damage and occurs when particles with high LET such as protons produce a scintillation signal that is not directly proportional to the energy deposited by the interactions between the excited and ionised molecules produced along the particle track [72], [73]. As protons slow down due to the energy loss (dE/dx), more energy is transferred to the medium as the LET increases. However, a greater proportion of energy is lost to interactions which do not emit light (e.g. heat); hence, L is reduced in the single Bragg Peak and at the end of the SOBP. In equation 1.12, k_B is Birks constant (with units $mm MeV^{-1}$), which depends on the charged particle type and the scintillation material, and L_0 [3], [74].

$$\frac{dL}{dx} = L_0 \frac{\frac{dE}{dx}}{1 + kB \cdot \frac{dE}{dx}} \quad \text{Eq 1.12}$$

Lighter particles such as electrons have lower LET and therefore produce more light output in an organic scintillator than heavier particles (e.g. protons) of equal energy. Figure 10 illustrates the relation between the energy of the protons and luminescence [75], [76]. The non-linearity of the light output is most severe when protons have high LET at low energy..

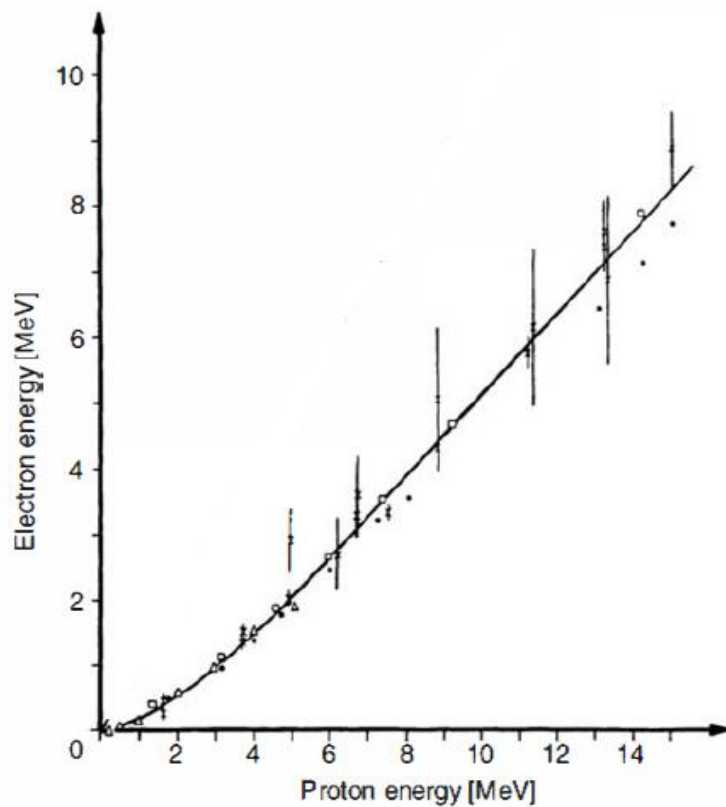


Figure 10: The scintillation light response of a liquid scintillator (expressed in equivalent electron energy deposition) to different energies of proton beam [3].

1.6 The development of the detector system in radiation therapy

Developments in scintillation material and high energy physics have led to significant improvements in radiation therapy and have led to a variety of applications in many areas of life science such as medical imaging. Different detector prototypes designed with different scintillation sizes, designs and materials (e.g. liquid) were used to examine the feasibility of a scintillator as a relative dosimeter in radiation therapy. Some of these experiments will be briefly described below.

1.6.1 Experiments employing plastic scintillating fibres

Early studies proposed using a point dosimeter containing a miniature scintillator of a short length coupled to an optical fibre and then attached to a photomultiplier tube (PMT) [77], [78]. However, this system did not appear to be useful in complex radiotherapy due to the fact that it was a point detector and was rather slow. Although the system did have advantages for small field dosimetry, it was not used in clinical settings. The reason for this was the relative ease of use of alternative point detectors such as ionisation chambers.

Scintillation dosimetry in radiotherapy has been extended to 2D by using a plastic scintillation detector (PSD) array to assess the dose distributions produced by photons [53]. Further modifications of the design were applied to simulate roughly the same number of ionisation chambers in an array using 781 PSDs placed in a plane of a water-equivalent phantom that is imaged by a camera as seen in Figure 11. It would be

feasible to have a system of PSDs for the dosimetry of photon beams [33]. The PSD system has excellent precision and accuracy, but a disadvantage in the system is its angular dependence and the accumulated signals in a megavoltage beam that suffer from excess noise (i.e. a Cerenkov signal generated in the optical fibre light guide). The production of Cerenkov radiation occurs when a charged particle moves faster than light through a transparent medium [58], [59].

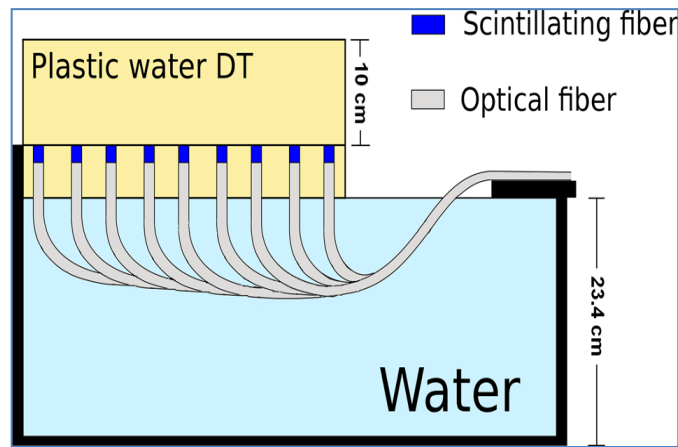


Figure 11: 3 mm long cylindrical scintillating fibres inserted vertically into a plastic water slab and perpendicular to the detection plane [33].

1.6.2 Experiments employing plastic scintillators

An attempt was made to employ a plastic scintillator by using a sheet of scintillator placed distally behind a slab of water equivalent material as seen in Figure 12, with the scintillation light measured using a charge-coupled device (CCD) camera [79]. The system was promising and accurate within 5% for a simple light distribution. However, further examination was required for complicated and complex light distribution (e.g. IMRT). The same setup was used in the IMRT plan verification and the results showed an acceptable agreement between the measured and the calculated dose distributions.

On the other hand, such a design was limited to a single 2D imaging plane that was perpendicular to the direction of the beam. Furthermore, another disadvantage of the system was that the sheet was only 5 mm thick and no depth dose distribution or any type of depth information could be measured directly. Due to the many radiation fields that are used in IMRT, the scintillation sheet could be missed during the irradiation because the scintillation sheet was initially designed for a fixed source and did not account for movement of the MLCs during the irradiation [79], [80].

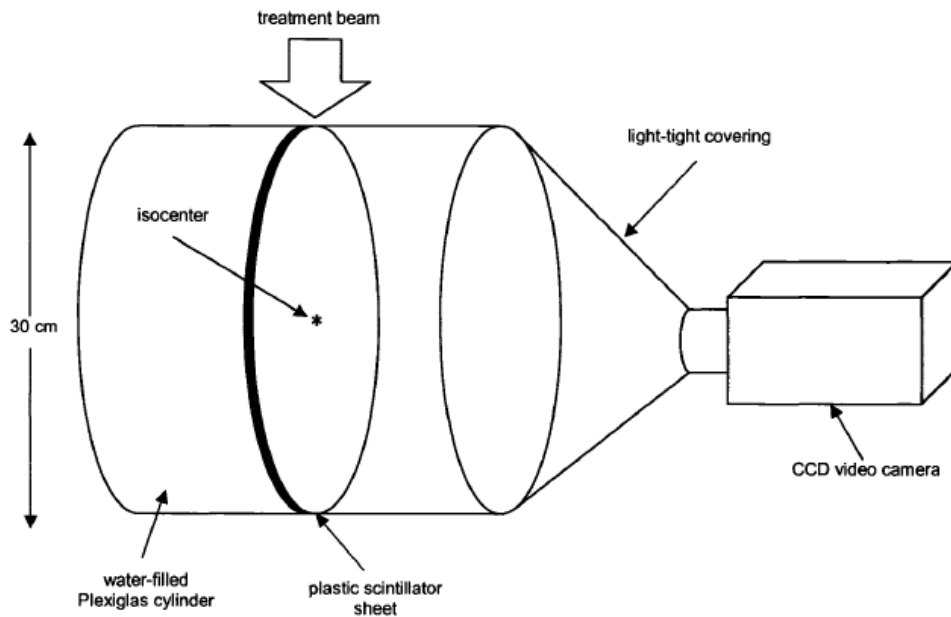


Figure 12: The scintillation sheet detector [79]

It is possible to improve the position of the plastic scintillator sheet, as can be seen in Figure 13. In the diagram, a mirror is used to reflect the scintillating photons into the camera. However, further development was required since the system was angular dependent and suffered from the production of Cerenkov light in the whole volume of irradiated water [45].

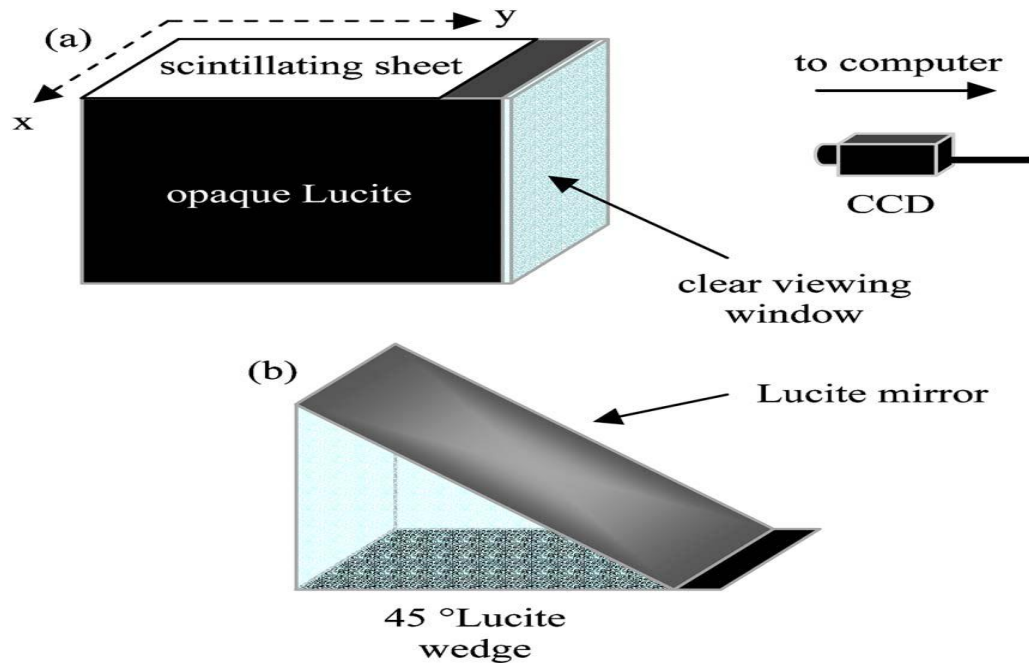


Figure 13: The IMRT dose verification system a) The phantom outer box with camera b) the inner mirror at 45° to the scintillator sheet [45].

1.6.3 Experiments employing liquid scintillators

To avoid the system's angular dependence, a large tank field of liquid scintillator as shown in Figure 14 was tested for 2D dosimetry [42], [81]. The three main components of the detector include a scintillation medium, a light tight enclosure or optical fibres for light guidance, and a camera. The camera is placed a certain distance away to reduce the stray radiation effects and, captures images by which the scintillation light depth distributions were extracted. A comparison between the measured (i.e. the scintillation detector) and the expected (i.e. the ionisation chamber) depth-dose distributions was carried out to show the accuracy of the scintillation detector [82]. This

system required corrections because the wall of the container reflected some of the light, which added noise to the image [83].

Overall, the response of a scintillator to megavoltage energy photons for dosimetric purposes was found to be in positive agreement with the reference measurements. In addition, the use of the system could potentially be quick and accurate.

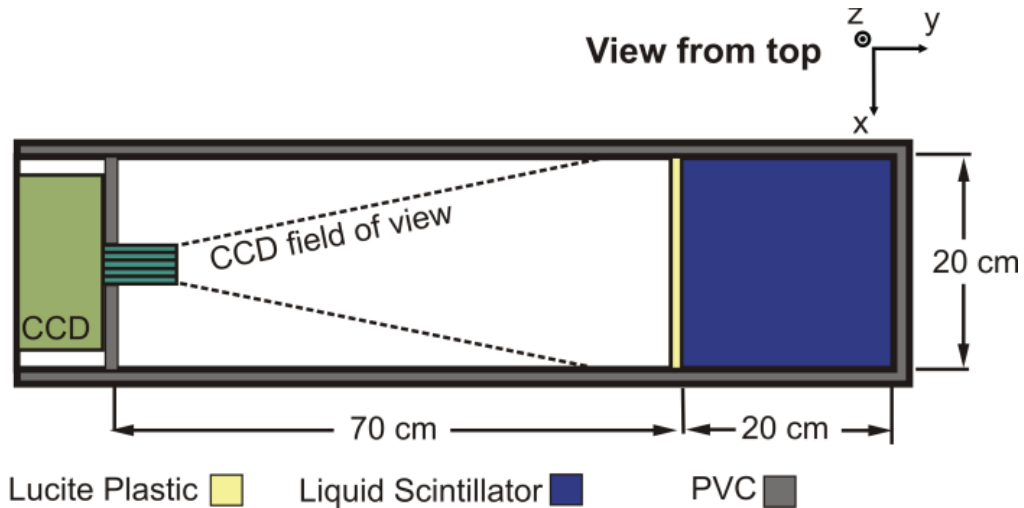


Figure 14: The LSD system (the z-direction goes from the gantry towards the tank) [42]

1.6.4 Scintillators in proton therapy

The increased availability of proton beam therapy facilities in recent years has encouraged the investigation of scintillation detector systems. For instance, a liquid scintillator detector (LSD) system containing a $20 \times 20 \times 20 \text{ cm}^3$ liquid scintillator and camera was used for scanning proton beams to obtain the scintillation light distributions. The result was then compared to ionisation chamber measurements [42]. The results showed a 40% reduction at the Bragg peak in the light depth distributions obtained by the LSD and the ionisation chamber due to the quenching effects in the

LSD and the optical properties of the imaging system. As a solution, a correction for the quenching effect can be achieved via Monte Carlo simulations [81]. Several studies have used Birks equation to estimate Birks constant in order to calculate the quenching of the measured scintillation data [84]–[86]. Another study investigated the proton range in IMPT. The LSD system showed itself to be a successful detector for beam range determination [42]. Therefore, this system can be used as both a range and dose verification detector. The use of the detector system based on a large scintillator could offer fast measurements, as shown in Figure 15. However, further investigation into proton beams should also be carried out. There are no successful camera-scintillator detector systems available commercially and such systems are still in the developmental stages.

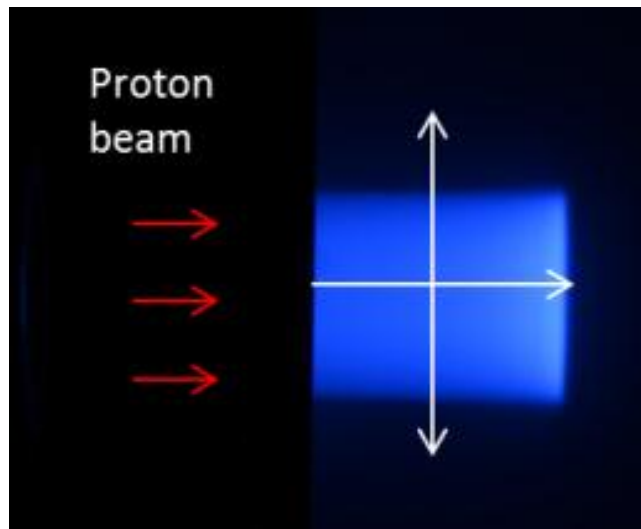


Figure 15: Scintillation image by which the data for depth-dose and off-axis profile measurements can be extracted, obtained by a BC-408 scintillator for a 60 MeV proton beam used in this thesis at the Clatterbridge Cancer Centre.

1.7 Thesis objective

In thesis, a tissue equivalent detector system based on a large scintillation material is proposed. Through the research and study of relevant literature, it was found that a large plastic scintillator which is larger than the beam dimensions has not previously been used in external radiation therapy. The primary objective of this work is to investigate the potential use of imaging scintillation light in x-ray, electron, and proton beams as a general QA tool using a commercial camera. We are looking to achieve the following aims by the end of the research:

- Evaluate the light output profiles obtained by a detector system consisting of a plastic scintillator, camera, and computer.
- Characterise the inherent artefacts in the detector system and provide a possible correction method to tackle each source of error.
- Study the system characterisations (e.g. dose linearity, stability, dose rate dependency) by correlating the delivered doses and dose rates to the measured image intensities in scintillation light photographs in both low and high energy beams.
- Validate the depth-dose curves of different radiation obtained by the scintillation detector system by comparing the measured scintillation light distribution to an expected depth dose curve.
- For protons, there is expected to be a decrease in the light signal in the Bragg peak region as a result of a quenching effect. Therefore, a correction for quenching will be obtained using a Monte Carlo simulation.

1.8 Major results and novelty

The overall aim of this project is to investigate the suitability of a camera-scintillator detector system for use in radiation therapy dosimetry. The possibility of using a standard commercial camera to image scintillation light generated from x-rays, electron, and proton beams was investigated for fast QA measurement. The experimental work in this thesis is separated into five chapters:

- At the beginning, we needed to decide which organic scintillator to purchase. In the chapter 2 of this thesis, the performance of two different scintillator types (liquid and plastic) was evaluated, by analysing their scintillation light output. It was found that liquid scintillator produced more artefacts than the plastic scintillator. The accuracy of the measurements of the scintillation light distribution is affected by several optical artefacts which were evaluated and potential correction methods were used to remove or mitigate these artefacts.
- A large plastic scintillator was selected to be evaluated in low energy radiotherapy (chapter 3), in high energy radiotherapy (chapter 4), and in proton therapy (chapter 5). To date and to our knowledge, large plastic scintillators have not been used anywhere in the literature for QA in radiation therapy.
- The use of specific phantom or detection material in low energy photon beams (i.e. x-rays) requires validation to ensure the interaction mechanism is as similar as possible to water. The detector system can offer fast and easy measurement of the PDD required for QA of therapeutic x-rays, but large liquid or plastic scintillators have not been used before. It is not clear whether the scintillator is a suitable material, and if not, what the magnitude of errors would be when

using the scintillator in low energy x-ray dosimetry. With respect to measurements in an x-ray beam, it was found that the measurement obtained by the detector system showed a linear response to dose and provided reproducible results. However, the results did not match the PDD obtained by the ionisation chamber. In addition, Geant4 simulations revealed that there was an overestimation of the scintillator PDD by 23% at very low energy (50 kVp), compared to water. This discrepancy was decreased by increasing the energy until it started to disappear, when a 150 kVp x-ray beam was used.

- Chapter 4 presents evaluations of the developed prototype scintillation detector for use in clinical high energy photon and electron therapy. It discussed the scintillation light depth distributions and the off-axis light profiles compared to ionisation chamber measurements in water. The results indicated that the detector system is suitable for use for photon and electron beams and that the uncertainties could be reduced by correcting the optical artefacts.
- The potential of using a large plastic scintillator in proton therapy for dosimetry was explored in chapter 5. A series of experiments was conducted using proton beams. The experiments were to investigate and validate the light distribution obtained by a camera. The experiment investigated the response of the detector system to various dosimetric parameters, including the dose, dose rate dependency, energy dependency, and field size dependency. Excellent responses of the detector system were seen in various dosimetric parameters but a reduction in the scintillation light signal at the Bragg peak was observed compared to ionisation chamber due to a quenching effect. The results were presented in a poster at the NPL workshop in London “Proton physics research

and implementation group (PPRIG), 2014” and at the 8th Saudi Student Conference in London (see below A).

A. Investigation into the Feasibility of a CCD-scintillator Detector System for Dosimetry in Proton Therapy

Mansour Almurayshid, Gary Royle, Jem Hebden, Adam Gibson

- After demonstrating the limited applicability of the detector system in proton therapy in the previous chapter, we attempted to correct for the quenching effect caused by high LET protons by using the Birks equation in chapter 6. The technique was shown to offer a convenient way to correct for quenching at any given energy. The results in chapter 5 and 6 were submitted for publication in Medical Physics (under review) (see below B) and for conference proceeding in PTCOG 2016 (see below C).

B. Evaluation of photography of a plastic scintillator for quality assurance in proton therapy

Mansour Almurayshid, Yusuf Helo, Andrzej Kacperek, Jennifer Griffiths, Jem Hebden and Adam Gibson

C. Feasibility of a plastic scintillator and commercial camera system for routine quality assurance in proton therapy

Mansour Almurayshid, Yusuf Helo, Andrzej Kacperek, Jennifer Griffiths, Jem Hebden and Adam Gibson

CHAPTER 2

2. OPTIMAL DESIGN OF A PHOTOGRAPHIC SCINTILLATION DETECTOR SYSTEM

2.1 Introduction

In quality assurance (QA) tests, and especially for dosimetry in radiotherapy, each measured point used in depth distributions is usually assessed using acceptance criteria of 3% or 3 mm to quantify whether the dose difference between the measured and the anticipated values exceeds the pass/fail criterion [87], [88]. The QA producer's challenge is to accurately meet the above agreement with current developments of different complex techniques of radiation treatment delivery and with increasing numbers of proton facilities worldwide. For example, dose verification for narrow beams used in scanned proton beam treatments would be a challenge. Ionisation chambers cannot measure complex 3D treatment fields. Although there is no widely accepted standard dosimeter for proton beams at present, the 2D arrays of many ionisation chambers can potentially be used for proton dose verification, however, these arrays are limited by the number of ionisation chambers, the number of measurement depths, and the ionisation chamber spacing [89], [90].

Organic scintillators have many desired features. Particularly due to their water equivalency tested in high energy photon beams, many organic scintillators used as detection materials are increasingly being examined for dosimetric use in radiation therapy, which is required by treatment planning systems and for routine dosimetric verification prior to treatment delivery [33], [91], [92]. An organic scintillator can be plastic, liquid, or crystal. A wide variety of scintillators of each type is commercially available at present. Organic scintillators can be produced by dissolving primary

scintillating compounds (*e.g.* polyphenyl hydrocarbons) in a solvent, such as polystyrene, and then polymerising the solvent, as in the case of plastic scintillators [3]. A common base of scintillating fibre is polystyrene or polyvinyltoluene for plastic scintillators. Mineral oil can be used as a base for liquid scintillators. Liquid scintillators are often employed in neutron detection application because of their ability to produce distinguishable signals between fast neutrons and gamma radiation [93]. Plastic scintillators have attractive features for some applications because they are robust and, durable, and there is no risk of leaks.

The two main components of the scintillator detector system are the scintillator where the deposited photon energy is converted into light, and the camera where the light is imaged and then subsequently analysed by computer. The scintillator can be either small (*e.g.* scintillation fibres to be arranged in 2D arrays) or large (*e.g.* liquid or plastic scintillators). Because the scintillation medium is the main component of the detector system, we have to select the optimal scintillator for our detector system. Our choice of scintillator was a critical step in our final design. In addition, evaluating artefacts in the detector system and optical artefacts caused by the light propagating from the scintillator to the camera is essential to accurately estimating the scintillation light profiles.

The aim of this chapter is to select a camera and optimal scintillator, examine many optical artefacts in our prototype design for radiation therapy dosimetry, and present possible correction methods to reduce the impact of optical artefacts.

2.2 Camera selection and characterisation

Investigations into the use of commercial cameras have been increasingly carried out in radiotherapy for the past ~20 years (*e.g.* in EPIDs for verification of patient positioning) [94], [95]. In addition, commercial cameras have been employed for photodetection in radiotherapy dosimetry, being used in dosimeters based on detecting scintillation and Cerenkov light [96]–[98]. This is because they have become relatively inexpensive, provide fast read outs, and can be used to monitor a large field. In addition, they are stable and sensitive enough to monitor small doses [59], [99]. The performances of commercial complementary metal-oxide-semiconductor (CMOS), charge-coupled device (CCD), and intensified charge-coupled device (ICCD) cameras were examined in a clinical radiotherapy setting [96]–[98], [100]. ICCD cameras proved to be viable specifically for real-time Cerenkov imaging of tissue due to the low intensity of the photon signals with ambient room lighting but they were very expensive (\$55k–\$60k) [101]. By comparison, the commercial CMOS and CCD cameras have relative low costs of \$600 and \$3k, respectively, and provide fast and stable results for QA applications within $\pm 1\%$. The CMOS camera provided higher frame rate per second (fps) and a better resolution image of 5184×3456 pixels compared to the CCD camera which had an array of 3326×2504 pixels [101]. A CMOS camera provided linear responses to the amount of energy incident on the sensor in the visible light range (400–700 nm) [102]. The scintillation light yield is high and in the visible range, which corresponds with the range to which commercial cameras are sensitive [75].

The camera in this work was selected because it was relatively cheap, convenient to use in a clinical environment, and provided raw file data with a high resolution to avoid compression of the images and hence ensure the reproducibility of the results. The spatial resolution is important to distinguish between intensities at closely spaced points as it increases as the pixels of the camera get smaller, hence increasing the array of pixels in the sensor. The D7100 was the most recent camera widely sold by Nikon in 2013. Nikon cameras have been used recently to image optical light in radiotherapy dosimetry, and they demonstrated high sensitivity to light and provided reproducible results to within 1% [103]-[106]. The intensity images of Cerenkov light emission and scintillation light acquired by the CMOS camera exhibited excellent linear dose agreement with the reference data for photon energies ranging from 6 to 18 MeV [98], [107].

The camera used in this study was a Nikon D7100 camera with a Nikon AF-S DX NIKKOR 35mm f/1.8G lens mounted on a tripod. The sensor matrix had one of the highest camera resolutions at the time of purchase with 6034×4024 pixels. It uses a CMOS sensor which has 6034×4024 pixels (2.4 cm \times 1.6 cm) with a 4 μ m pixel size and a 14-bit dynamic range. It was used in manual exposure control with a USB 2.0 connection to transfer the image data to the computer. Continuous shooting speeds of up to 6 frames per second are possible. The raw format obtained by the camera is .nef (Nikon Electronic Format). The main advantage of acquiring images as raw .nef image files is "that no in-camera processing for white balance, hue, tone and sharpening are applied to the NEF file; rather, those values are retained as instruction sets included in the file" [108].

2.2.1 Camera linearity

Because the sensitivity of the CMOS sensor is uniform over the spectrum of 380–760 nm [109], an easily available red light-emitting diode (LED) was used to study the linearity of the camera's sensor to the optical light. Because the relationship between the current and the light intensity of an LED is linear, currents ranging from 5 to 20 mA were applied to an LED. As the current through the LED increased, the intensity of the light emitted by the LED increased and was measured by the lens-free camera to test the linearity of the camera's sensor itself. Three images were obtained for each current. A region of 50×50 pixels was selected in the middle of the image and was then averaged and combined to obtain a cumulative light intensity to be plotted against the corresponding current. The light output was found in Figure 16 to be directly proportional to the current, with a correlation coefficient of 0.99.

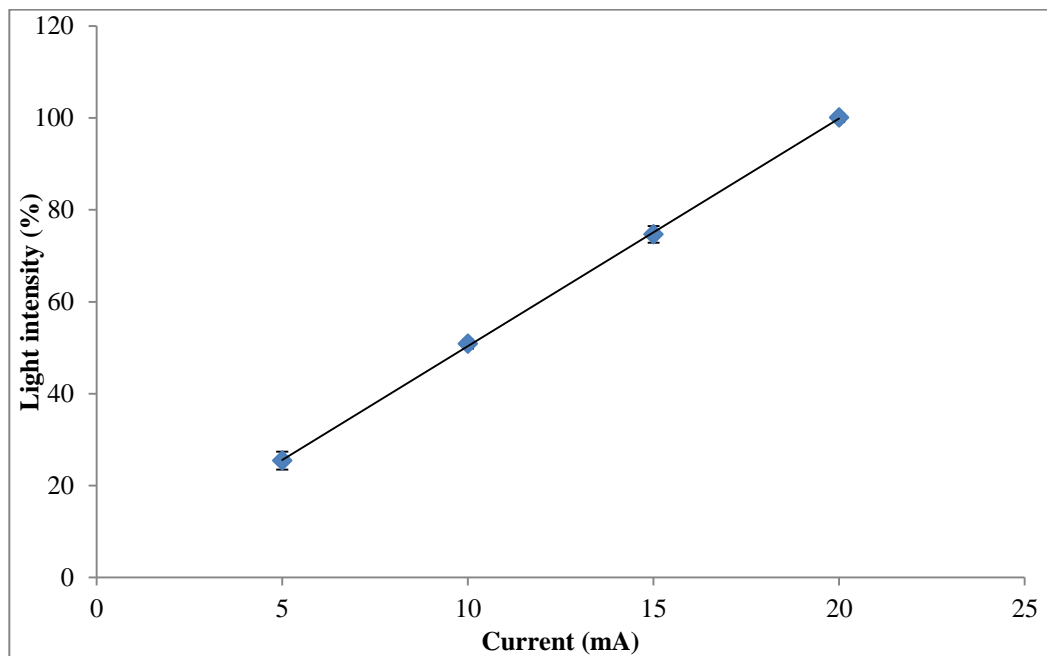


Figure 16: Linearity of light intensity as a function of current measured by the camera. Error bars demonstrate the standard deviation and some of the error bars are smaller than the point size at certain points.

2.3 Selection of the scintillator for the detector system

2.3.1 Introduction

For photon beams, arrays of different numbers of scintillating fibres have been used previously in the literature for 2D dosimetry applications such as depth-dose measurements [111], [142], [143]. The active scintillating part of the fibre is usually 1 cm long, which is coupled with a non-scintillating fibre as a light guide to the camera. A disadvantage of using a prototype based on scintillating fibres was that the production of Cerenkov light emission in the optical fibre creates a serious noise factor [58]. The Cerenkov light emission in the optical fibres is a major noise source, and the magnitude of error in signal caused by Cerenkov is energy- and angle dependent. The cutting efficiency of the scintillating fibres affects the light signal because it might be compressed during cutting procedure, and the mechanical difficulty of accurately coupling many scintillating fibres to optical fibres [110]. The scintillating signals from the fibres in array and the light collection efficiency is strongly dependent on the diameter and the length of the fibres [110]. The length of the fibres should have the exact length required to ensure a uniform signal across the fibres in the array. This proved to be difficult to attain [111]. The construction process for manually building a single scintillating detector (i.e. a plastic scintillating fibre coupled to an optical fibre) takes more than 30 minutes [91]. Furthermore, the spatial resolution of the detector would not be better than that of instant ionisation chambers, if arranged in the array. The relative ease of use of alternative arrays, such as ionisation chamber arrays

discourages further investigation. In addition, the optical fibres could scintillate when the incident beam is formed of protons [112].

Large 3D volume detectors based on liquid scintillators have also been used [80]. They have been shown to provide fast and accurate results, and have high resolution for photon quality assurance in 3D volume [81]. Therefore, we decided to choose a large scintillator material, which could be a plastic or a liquid scintillator. The aim of this section is to choose a specific plastic scintillator and liquid scintillator, to evaluate them experimentally and from the literature by analysing the light output, and then to select a suitable scintillator for our final prototype.

2.3.2 Selection of the plastic and liquid scintillators

Organic scintillators including plastic and liquids have promising advantages due to the simplicity and low cost of fabrication, and they have short decay times (few ns), compared to inorganic scintillators, which allow them to be attractive for fast timing measurements [113]. They are produced by different companies such as Saint-Gobain Crystal Corporation, (USA), Eljen Technology (USA), and Nuclear Enterprises Limited (UK). Different scintillators are produced for different applications by modifying the amount of organic compounds and adding materials to alter the probability of interaction (e.g. gadolinium (Gd) can be added for neutron detection) [75], [76]. Many different scintillators are available of for each type, and their properties are shown in Table 3.

Table 3: Properties of different scintillators [75], [76], [114], [115]

| Type | Scintillator material and commercial equivalents | | | Light output percent anthracene % | Emission peak (λ), nm | Decay constants | Light attenuation length cm | H : C atomic ratio | Refractive index | Density g cm ⁻³ | Principal applications | Research group |
|---------|--|--------------|---------|-----------------------------------|-----------------------|-----------------|-----------------------------|--------------------|------------------|----------------------------|---|-------------------|
| | EJen | Saint Gobain | NE | | | | | | | | | |
| Plastic | EJ-200 | BC-408 | Pilot F | 64 | 425 | 2.1 | 380 | 1.104 | 1.58 | 1.03 | Best overall general properties, large, for gamma rays+ fast neutron+ charged particles | [45] |
| | EJ-204 | BC-404 | NE-104 | 68 | 408 | 1.8 | 160 | 1.107 | 1.58 | 1.03 | Good general properties, for < 100 keV x-rays+ alphas + betas | |
| | EJ-208 | BC-412 | NE-110 | 60 | 434 | 3.3 | 400 | 1.104 | 1.58 | 1.03 | Good general properties, large, for fast neutrons + charged particles | |
| | EJ-212 | BC-400 | NE-102A | 65 | 423 | 2.4 | 250 | 1.103 | 1.58 | 1.03 | General purpose, thin films, for alpha+ beta+ >5 MeV gamma | [77], [86], [116] |
| | EJ-228 | BC-418 | Pilot U | 67 | 391 | 1.4 | 100 | 1.107 | 1.58 | 1.03 | Ultra-fast timing, high pulse pair resolution, for use in small sizes | |
| | EJ-240 | BC-444 | NE-115 | 41 | 435 | 230 | 180 | 1.109 | 1.58 | 1.03 | Long decay time, for heavy ion research, particle identification, low background counting | |
| | EJ-260 | BC-428 | NE-103 | 36 | 490 | 9.2 | 150 | 1.109 | 1.58 | 1.03 | Green emitting scintillator | |
| Liquid | EJ-301 | BC-501A | NE-213 | 78 | 425 | 3.2 | 250 | 1.212 | 1.50 | 0.87 | Fast neutron-gamma discrimination | |
| | EJ-305 | BC-505 | NE-224 | 80 | 425 | 2.5 | 150 | 1.331 | 1.50 | 0.87 | High light output, fast neutron and gamma rays | |
| | EJ-313 | BC-509 | NE-226 | 20 | 425 | 3.1 | 100 | 0.0035 | 1.37 | 1.61 | Hydrogen-free, neutron and gamma studies | |
| | EJ-321L | BC-517L | NE-235L | 39 | 425 | 2 | 500 | 2.01 | 1.47 | 0.86 | Mineral oil based, standard efficiency, large tanks, Fast neutron and gamma rays | |
| | EJ-325 | BC-519 | NE-235C | 60 | 425 | 4 | 100 | 1.73 | 1.49 | 0.87 | Mineral oil based, pulse shape discrimination, fast neutron and gamma discrimination, large tanks | |

| | | | | | | | | | | | | |
|--|--------|--------|--------|----|-----|-----|-----|------|------|------|--|------------------|
| | EJ-331 | BC-521 | NE-323 | 60 | 425 | 4 | 400 | 1.31 | 1.50 | 0.89 | Highest light output, neutron spectrometry (Gd loaded), neutrinos | |
| | EJ-335 | BC-525 | NE-313 | 64 | 425 | 3.8 | 500 | 1.57 | 1.50 | 0.88 | Mineral oil based, large tanks, neutron spectrometry, long- term chemical stability | |
| | EJ-339 | BC-523 | NE-321 | 65 | 425 | 3.7 | 400 | 1.67 | 1.41 | 0.98 | Neutron spectrometry, pulse shape discrimination, thermal neutrons | |
| | | BC-531 | | 59 | 425 | 3.5 | 350 | 1.63 | 1.47 | 0.87 | Mineral oil based, fast neutron, cosmic | [81]-[83], [117] |

The light output of a scintillator, which is a measure of its ability to effectively convert ionising radiation into visible light, is an essential feature to consider in any scintillator. Light output can be measured by the average number of photons per MeV of absorbed radiation or as relative to another scintillator such as anthracene (an organic crystal commonly used as the standard for scintillators) [118]. Anthracene light output is approximately 50% of a high light output efficiency inorganic scintillator of sodium iodide activated with thallium (NaI(Tl)) [119]. Other important features that need to be studied from Table 3 are the emission peak and the time profile of the scintillation light pulse to be generated, which should be fast allowing rejection of random events [120]. Each scintillator has a unique decay time. If a scintillator has a long decay time such as that in CsI(Tl) (inorganic scintillator), having roughly 1000 ns, it would suffer from the afterglow artefact impacting the background, which will change from pre-irradiation to post-irradiation for subsequent irradiations [119]. An important consideration when designing plastic and liquid scintillators is minimising the attenuation of scintillation photons. Therefore, light attenuation length is an important parameter to ensure the scintillation light generated is not re-absorbed by the scintillator itself. The scintillator should have little self-absorption [121]. Another requirement for the scintillator in our design was that it had to be available in a large volume so as to accommodate the desired radiation beam.

No commercially available scintillator can meet all requirements. Therefore, the enhancement of the performance of new scintillators is of continued interest in research [120]. One of the key parameters in selecting a suitable scintillator for this research was for it to have a good optical quality including a long attenuation length and thus, good

light collection. This had to be combined with the effect of a fast response and a high light output. A particular scintillator of each type was chosen to be examined in a proton beam test to determine the best choice for the fabrication of the final prototype of the detector system.

- The BC-525 liquid scintillator, made by Saint-Gobain Crystals Corporation, USA, was chosen based on its high light transmission path length, which is 500 cm, to minimise the self-absorption of the scintillation light generated in the scintillator. In addition, it has long-term chemical stability and a refractive index of 1.50 similar to that of poly-methyl methacrylate (PMMA) container which allows a good coupling efficiency of the scintillation light produced.
- The plastic scintillator used is BC-408 by Saint-Gobain Crystals Corporation, USA. Two scintillators can be fabricated in large volumes instead of sheets or rods, namely BC-408 and BC-412. The former scintillator was chosen because it has long attenuation length (380 cm) and fast decay (2.1 ns). In addition, because the camera was to be used as a photo-detector, it was important to have the maximum light output near or in the visible light wavelength range. The light emission peak was 425 nm. In addition, the light yield emission of BC-408 was 64% that of anthracene.

2.3.3 Liquid scintillator versus plastic scintillator

We had the chance to visit the Clatterbridge Cancer Centre (*i.e.* more details of the proton experiments will be explained in chapter 5). We decided to test the responses of large-volume scintillators being irradiated by a proton beam in order to obtain scintillation depth distributions.

- The BC-525 liquid scintillator was prepared in two containers: one container was made of glass (4 cm × 4 cm × 4 cm) and the other container was made of PMMA (5 cm × 5 cm × 5 cm), which accommodated the range of a 60 MeV proton beam of 3.09 g cm⁻² and the field size of 2.5 cm².
- The plastic scintillator that we used was BC-408, which is the best general purpose scintillator, measuring 20 cm × 20 cm × 10 cm.

These scintillators were positioned at the isocentre 7 cm from the nozzle of the proton source and aligned with the central axis of the proton beam, as shown in Figure 17. A 60 MeV proton beam was utilised and the camera was used, to acquire scintillation images during irradiation. The detector system was placed in complete darkness to avoid any contamination by unwanted background noise. For future work, a light-tight container or box could potentially be used with the whole detector system placed inside it to avoid the dark environment settings, allowing reproducible placement of the camera and the scintillator.

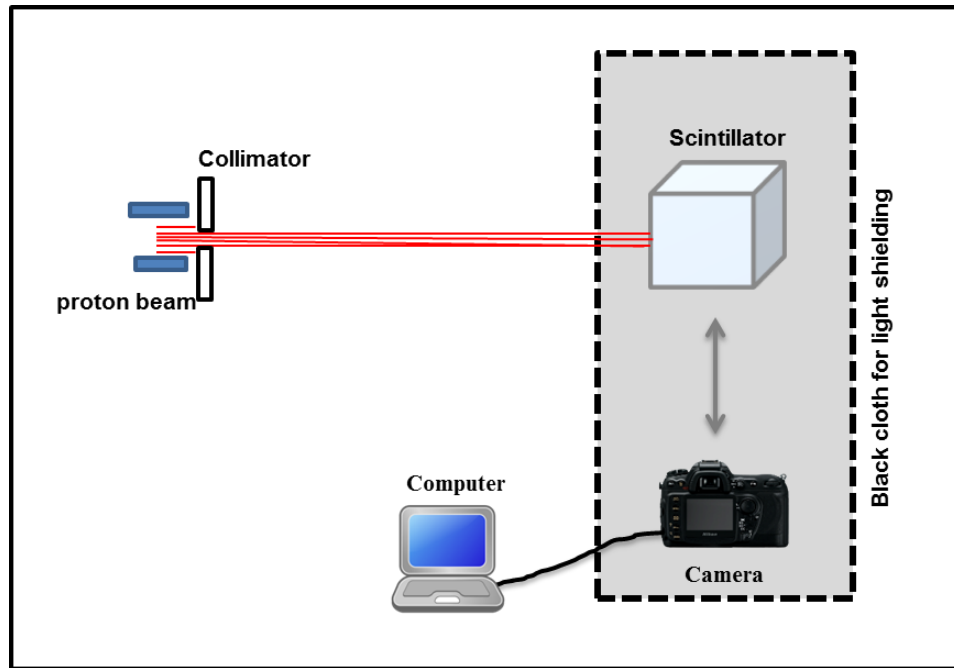


Figure 17: The setup of the detector system based on the liquid scintillator or plastic scintillator.

2.3.4 Results

The comparison of the scintillation light distributions obtained in liquid and plastic scintillators is illustrated in Figure 18. Protons came from the left. The zero point is the boundary of the liquid scintillator container. The scintillator itself is in the plastic scintillator.

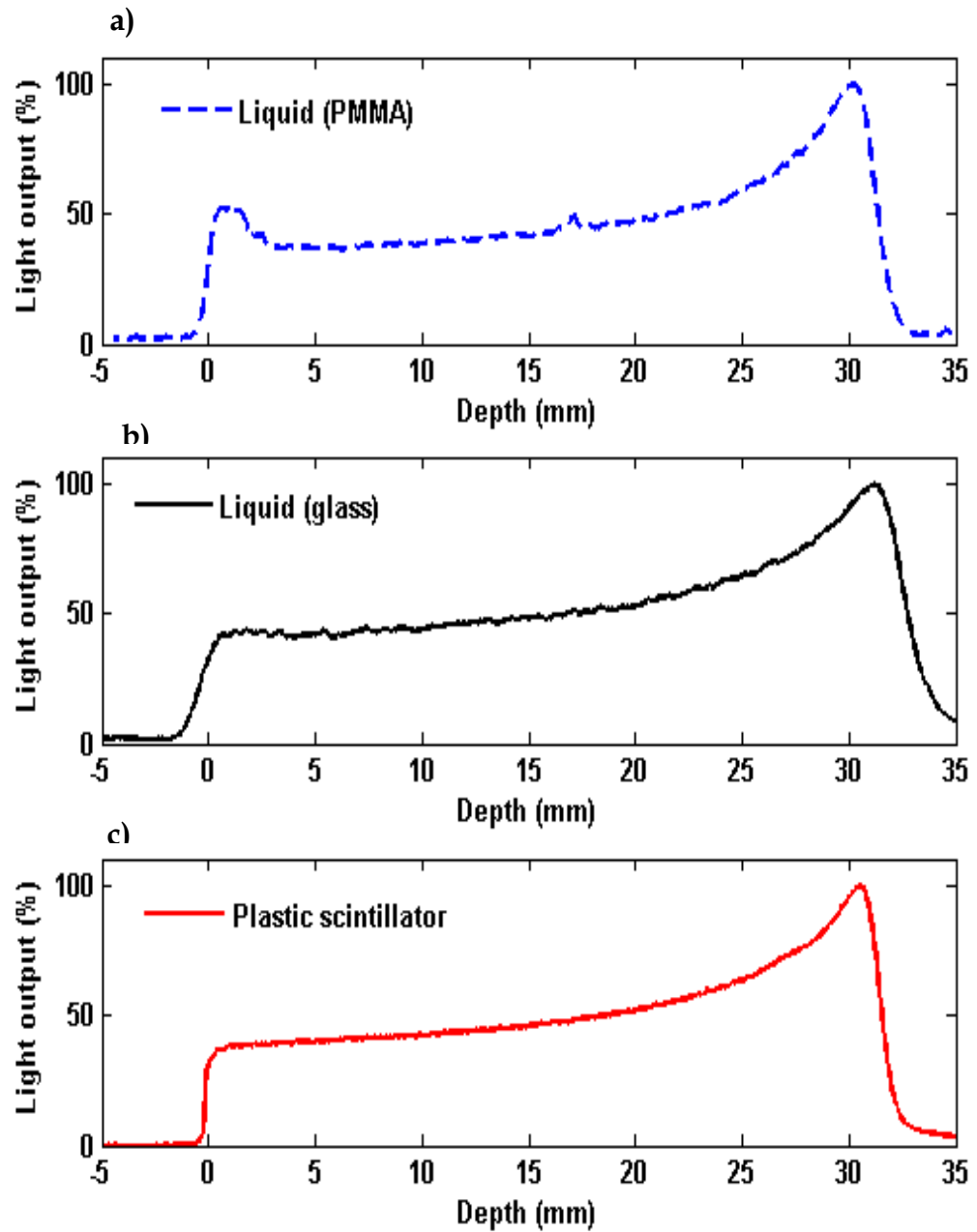


Figure 18: The light profiles obtained by a) liquid scintillator in PMMA container; b) liquid scintillator in glass container; c) plastic scintillator

Figure 18a, shows a hump caused by the scintillation of the wall of the PMMA container by a 60 MeV proton beam. As the measurements were taken in a machine that has a fixed horizontal gantry, as shown in Figure 19, it was necessary for the proton beam to penetrate the wall of the container holding the liquid scintillator, or the face of the solid plastic scintillator. This introduced additional uncertainty in the protons' range in the measured scintillation depth profile of the liquid scintillator due to the wall of the container. This has not been previously mentioned in the literature [82], [83], [117].

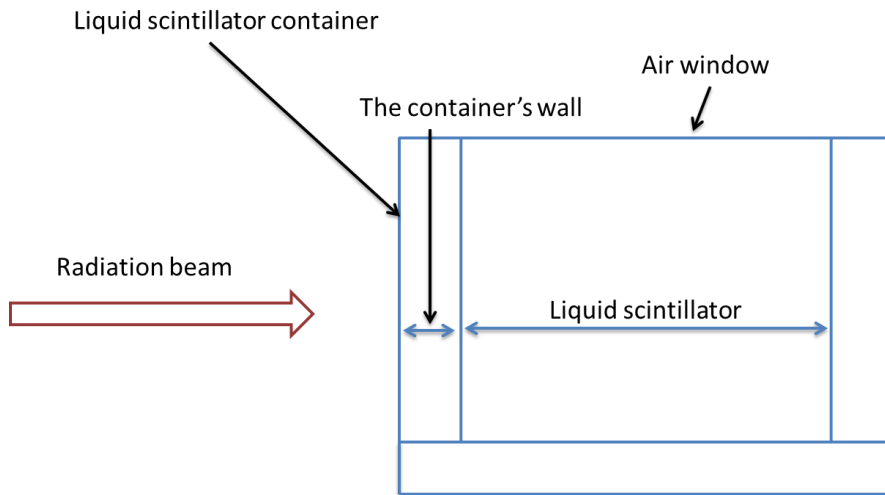


Figure 19: A horizontal radiation beam passes through the wall of the contained and then interact with the liquid scintillator.

According to ICRU 49, the dose deposition in any material can be found by the energy loss of a proton due to stopping power [122], [123]. Table 4 illustrates the range and stopping power of a 60 MeV proton beam in the container's materials used in this

study compared to water, a liquid scintillator, and a plastic scintillator [124]. The use of a glass container would result in a variation compared to water, since the stopping power and the range of protons were not similar. The stopping power is not only proportional to the density of the material ρ , but also to electron density, which takes into account the atomic number (Z) and the relative atomic mass (A) [125]. We also found that the liquid scintillator dissolved the wall of the PMMA container and the PMMA container scintillated, as shown in Figure 20. The scintillation depth distribution will be validated for all types of radiation used (see chapters 3, 4 and 5).

Table 4: The range and stopping power of different materials

| <i>Materials</i> | <i>Density (g cm⁻³)</i> | <i>Stopping power (MeV cm² g⁻¹)</i> | <i>Range (g cm⁻²)</i> |
|-----------------------------|------------------------------------|---|----------------------------------|
| Water | 1.00 | 10.78 | 3.09 |
| Plastic scintillator | 1.03 | 10.73 | 3.10 |
| Liquid scintillator | 0.87 | 10.80 | 3.08 |
| PMMA | 1.18 | 10.50 | 3.17 |
| Glass | 2.23 | 8.88 | 3.78 |



Figure 20: Interface issue – the PMMA container wall was found to be scintillating when left empty.

2.3.5 Discussion

The performances of two different types of scintillators were examined; it was found **experimentally** and in the **literature** that the disadvantages of using liquid scintillators are:

- Scintillation of the container in the 60 MeV proton beam.
- The need to deoxygenate of the scintillator prior to use, to obtain high output and maintain the light output [76].
- Toxicity (not suitable for hospital environment).
- Interface issues of the tank or of the container for the liquid scintillator in which the proton beam will lose some of its energy before the generating scintillation light.
- The emitted light of the liquid scintillator may be reflected or refracted at the walls of the acrylic tank causing unwanted light signals.
- The liquid scintillator dissolves the wall of the PMMA container.

A drawback of the plastic scintillator is that:

- It must be handled with care as it is vulnerable to scratches, which could affect the transmission of the scintillation light generated.

2.3.5.1 The optimum choice of scintillator for this research

It was found that liquid scintillators would have a container artefact, whereas plastic scintillators would introduce fewer artefacts than liquid one in our design. Therefore, we decided to choose a large plastic scintillator. Plastic scintillation materials are relatively cheap, do not require containers and can be made in different shapes. This type of scintillator is robust and durable [76]. The components of the BC-408 scintillator selected for this study are ~97 % PVT (polyvinyltoluene), ~3% PT (p-terphenyl) and 0.05% POPOP (p-bis (2-5-phenyloxazolyl) benzene) [126].

2.4 Evaluation of the optical artefacts in the camera-scintillator detector system

2.4.1 Introduction

This work aims to develop fast, high-resolution, immediate readout radiation detectors based on a plastic scintillator. This detector system design has the potential to reduce the time required for QA tests, allowing all radiation field data, including depth-dose distributions and off-axis dose profiles, to be measured by a single

measurement. However, the accuracy of the measurements of the scintillation light distribution is affected by several optical artefacts that were generated during light propagation from the scintillator to the camera, and in the CMOS camera while measuring the incident light [83]. The objective of this section is to evaluate the sources of the optical artefacts present in the scintillator-based detector system. Subsequently, potential correction methods to remove or mitigate these artefacts were developed to obtain meaningful dosimetric measurements.

2.4.2 Design principle

As mentioned, descriptions of the methods for characterising and correcting the optical artefacts of interest will be presented. However, the main components of the detection system used in this study should be described to consider the relevant optical artefacts. A schematic overview of the prototype scintillator detector system is shown in Figure 21 for reader convenience. The scintillator detector system contains a BC-408 plastic scintillator (20 cm × 20 cm × 10 cm) where the deposited proton energy is converted into light, and a Nikon D7100 camera, which captures images of the emitted light that are subsequently analysed by a computer to convert the light into appropriately scaled radiation dose values. The camera was mounted on a tripod and positioned perpendicular to the beam, and the data acquisition was performed using Nikon camera control software on a laptop computer outside the treatment room connected via a 25 m USB cable. Black cloths and black tape were used to exclude ambient light.

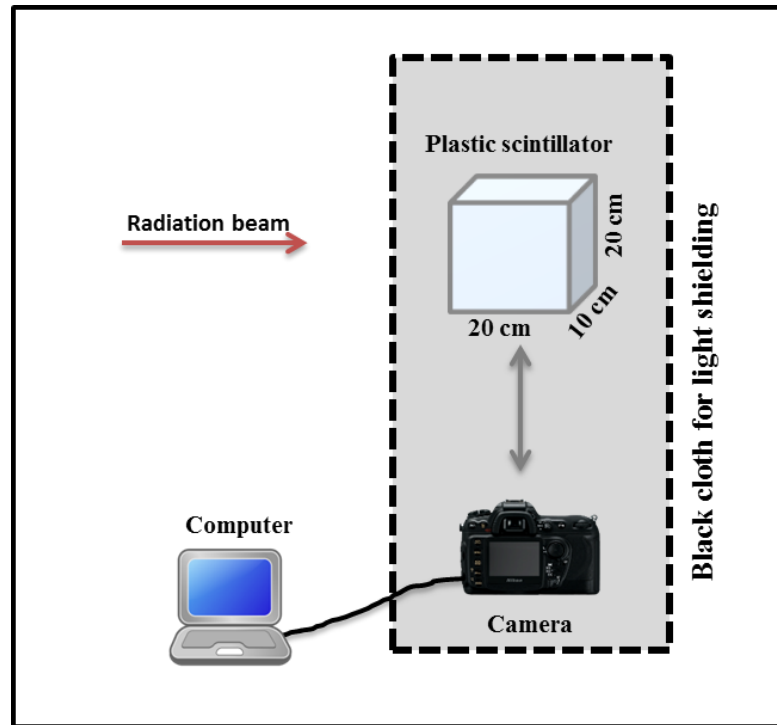


Figure 21: The detector system components

2.4.3 Artefact characterisations and correction methods

Table 5 shows various artefacts that are generated in the CMOS camera and while measuring the incident light during light propagation from the scintillator to the camera. In this section, we review potential sources of error, and describe experiments which were carried out to characterise each in turn. The results are presented in section 2.4.4. A correction method will be addressed below and applied to the image processing chain when this is required in section 2.5.

Table 5: Artefacts could be present in the scintillation detector system. Adopted from [117]

| <i>Artefact's source</i> | <i>Physical phenomenon</i> | <i>Impact associated with the artefact</i> |
|--|----------------------------------|---|
| Camera chip | Background noise | - Measurement uncertainty |
| | Stray radiation | - Hot pixels and streaks |
| optical system | Vignetting | - Decreased brightness at image periphery |
| Light propagation in the scintillator | Magnification | - Changes in effective pixel size and intensity depend on the beam field size |
| | Refraction | - Changes in effective pixel size |
| | Reflection and absorption | - Decreasing the light intensity over distance |
| | Cerenkov light production | - Assumed to produce unwanted signals in the low dose region [83] |

2.4.3.1 Background noise

This artefact contributes to the measurement uncertainty, so dark images were obtained to estimate the random noise of the camera chip by taking three repeated images. These images were averaged and used for background subtraction.

2.4.3.2 Stray radiation:

Stray radiation causes spikes and streaks in the scintillation light images and can be eliminated by using a median filter which helps to remove noise and extract actual data [127]. It was applied to each image in MATLAB, specifically to the 3×3 region surrounding each pixel.

2.4.3.3 Vignetting correction

Vignetting is an undesired artefact caused mechanically and optically that reduces the brightness at the edge of the image and is dependent on the aperture [104], [117]. The effect of vignetting at two apertures ($f/8$, $f/22$) used in this thesis was measured to obtain a complete vignetting profile of the sensor with the lens used, which would provide a vignetting map on any image plane which applies to all the measured images. A clear difference was observed between the intensity of the image generated in the centre and on the edge of the image frame, where features are only 88% as bright as those in the centre. The vignetting was calculated by placing the camera 17 cm away and acquiring a flat white image for a homogeneous light field supplied by a lightbox transilluminating a homogeneous scattering medium from which a correction can be determined. The correction factor was obtained for each pixel and is shown in Figure 22.

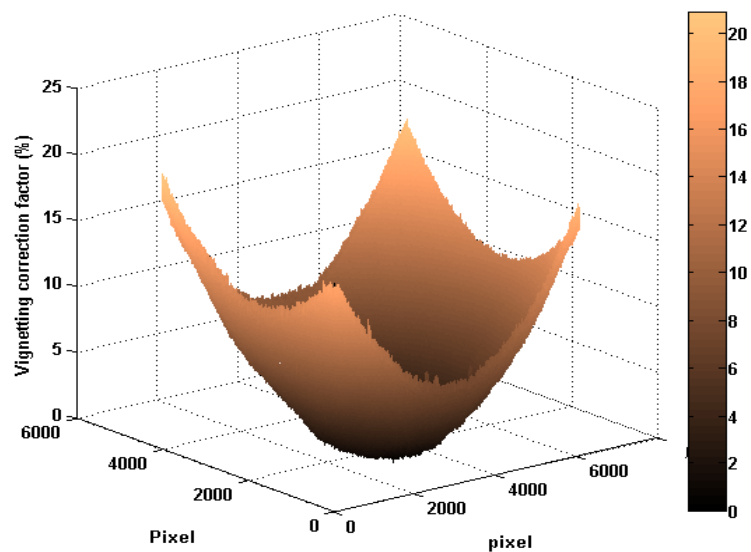


Figure 22: Demonstration of the vignetting correction for the entire camera image.

2.4.3.4 Evaluation of the background noise on the light output intensity generated in the scintillator using Monte Carlo simulation

In literature, Cerenkov light has been deemed a source of unwanted light noise generated in the whole scintillator, especially in the low-dose region, causing a low-intensity tail observed out of the main beam, as shown in Figure 23 [83]. The Cerenkov signals have been investigated using Geant4.

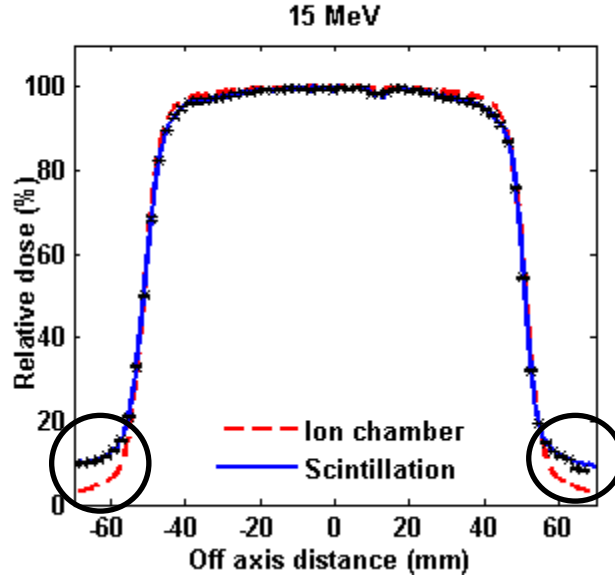


Figure 23: The comparison of off-axis dose profile obtained by the detector system and the ionisation chamber for 15 MeV electron beam. A variation between the two profiles appears at the low dose region (black circles).

Geant4 (GEometry ANd Tracking), which is a C++ Monte Carlo simulation package of the passage of radiation through matter, can precisely model many radiation dosimetry experiments. Many simulation packages are available but the only package that has the capability to handle both radiation and optical light transportation

simultaneously is Geant4 [128]. Geant4 requires details of the desired detector geometry, including materials selection and key properties of the materials such as the refractive index and attenuation length, the initial radiation source, the physics processes that the particles can undergo in the simulation, and the file format for storing the event data for further analysis, as illustrated in Figure 24 [20], [129].

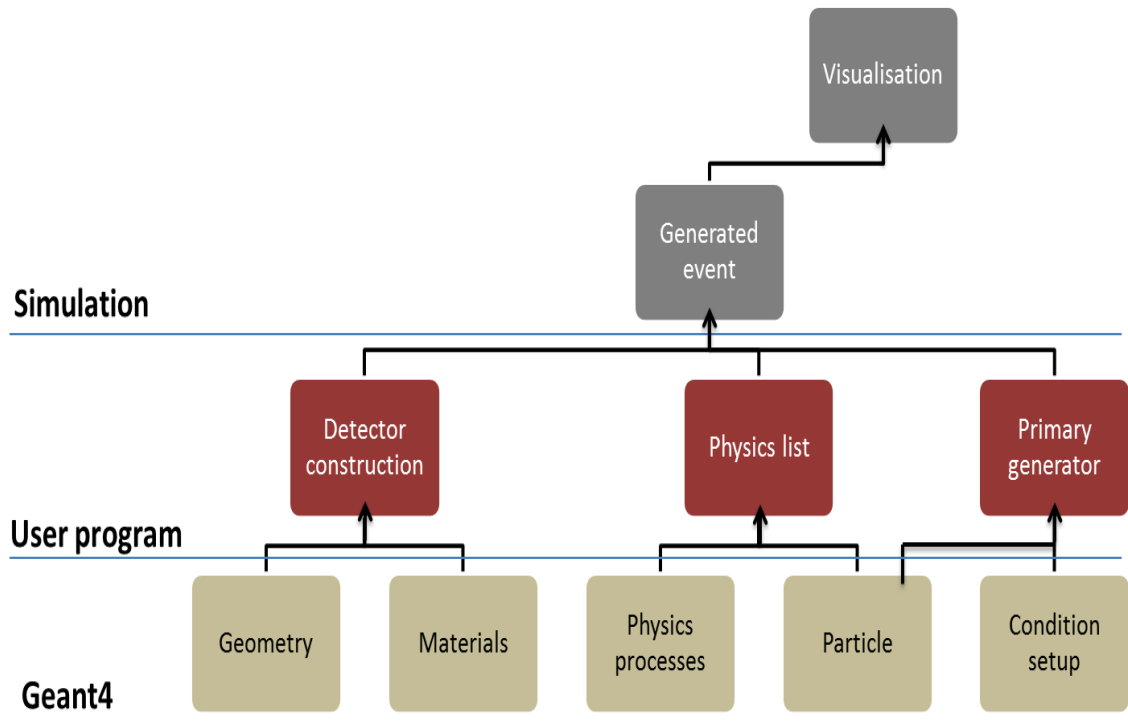


Figure 24: Schematic flow process of a Geant4 simulation.

Geant4 can generate optical processes such as Cerenkov and scintillation and handle optical photon-medium interactions (absorption, reflection and refraction) by implanting the user-defined optical properties of a medium into the detector construction, including the energies of the optical photons (eV), which could be constant or a function of the photon energy, the absorption length (cm), and the

refractive indices of the medium utilised in the user simulation. The effect of any or all of these optical properties on the observed optical remission can be studied.

Geant4 Monte Carlo simulations version 10.00 was used to construct a geometry which was a box volume filled with the BC-408 scintillator as shown in Figure 25. The BC-408 scintillator phantom with dimensions 20 cm × 20 cm × 10 cm was divided into voxels with dimensions of 0.25 mm × 0.25 mm × 0.125 mm. The principal characteristics of the chosen plastic scintillator are shown in Table 6. Geant4 standard physics package was employed for electromagnetic interactions covering the interactions of photons and electrons. For protons, the physics list class used contains primarily the QGSP_BIC_EMY, which is the reference physics list recommended for the simulation of hadron therapy applications [175].

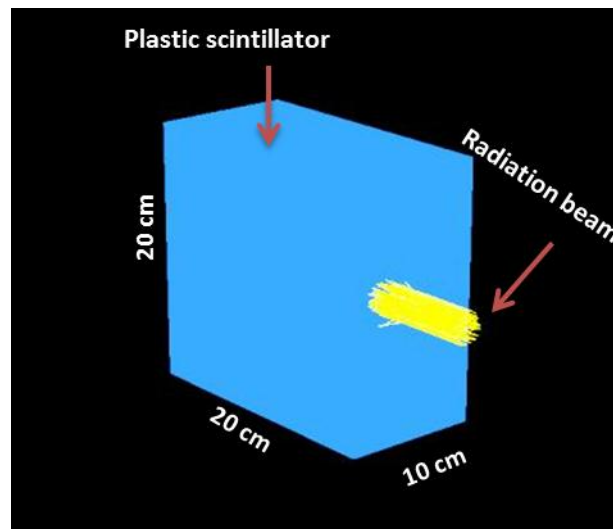


Figure 25: The geometry used in the simulation to predict the optical behaviour of the scintillator.

Table 6: The properties of the BC-408 plastic scintillators [76]

| <i>Parameter</i> | <i>BC-408 scintillator</i> |
|---|----------------------------|
| Core material | Polyvinyltoluene |
| Refractive index | 1.58 |
| Density, g cm⁻³ | 1.03 |
| Emission peak (λ), nm | 425 |
| Light output, % anthracene | 64 |
| No of photon /MeV | ~ 8000 |
| Light attenuation length, cm | 380 |

The aim of this section is to evaluate the Cerenkov light relative to the scintillation light profiles in each radiation used in this thesis and to investigate whether the low-intensity tail observed out of the main beam is caused by Cerenkov light emission mentioned in the literature [129]. In this thesis, three types of radiation beams, including 6 MV photon, 6 MeV electron, and 60 MeV proton beams were simulated entering a BC-408 plastic scintillator using Geant4. The off-axis scintillation and Cerenkov light profiles were calculated in the BC-408 scintillator phantom.

2.4.3.5 Evaluation of magnification for the geometries used

Image perspective or magnification artefact which could particularly be problematic when measuring steep dose gradients is the result of the 3D light field within the scintillator being projected onto a 2D image plane. This would impact: 1) the geometry or the apparent size of an object since a decrease in the object-camera distance will result in an increase in the object's apparent size; and 2) the detected light intensity projection, which follows the inverse square law in the camera [117]. The geometry and intensity of projections of the 3D light field in the image are strongly dependent on the field size of the photon beam and the distance between the camera and the beam. Figure 26 shows the parameters that contribute to the magnification, such as the distance between a given projection and the midline projection, x , the depth of the midline projection, y , and the distance between the midline projection and the camera, r . Therefore, light generated near the camera (*e.g.* +1.5 cm from the midline) contributes a higher intensity and covers a wider field of view than light generated from behind the midline. Photographs of the light output show the light emitted from a volume of light; the plane nearest to the camera will contribute the most, but we need to know the light distribution along the central axis. Therefore, to compare both the ionisation chamber measurements and the simulated scintillation depth distributions with the measured scintillation light depth distributions, it was necessary to consider the effects of geometry, especially those due to magnification.

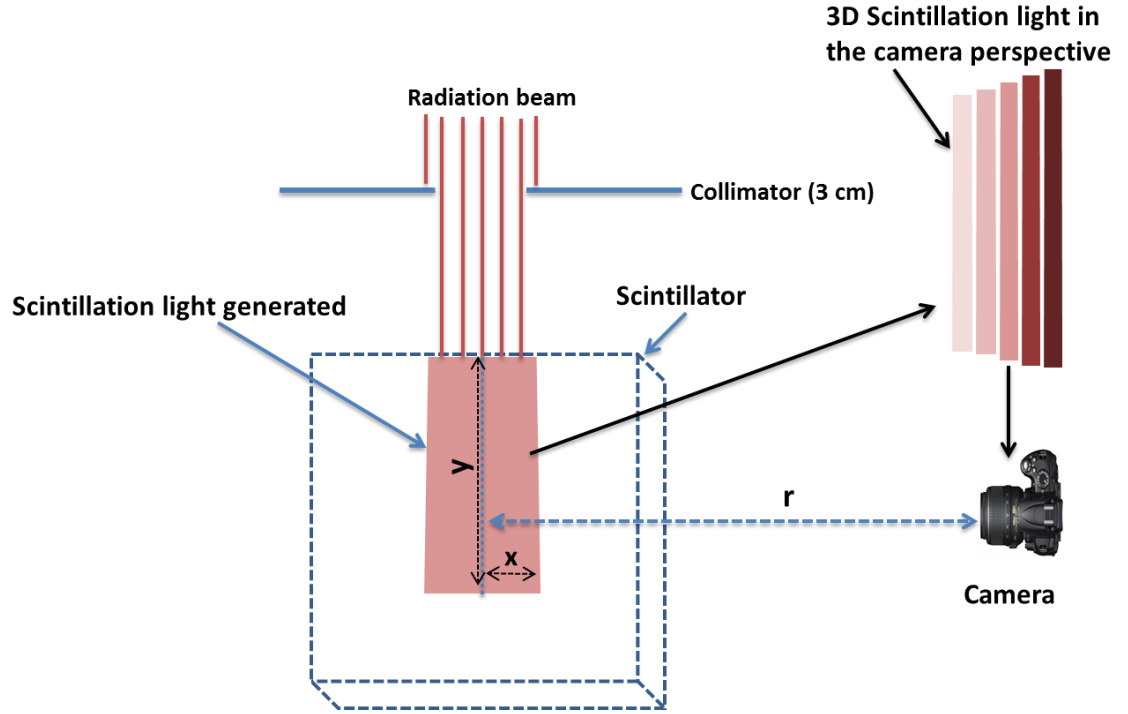


Figure 26: Demonstration of the geometrical magnification for the experiment geometry used in this work. The camera would detect the integrated scintillation light along the line of sight by which the light near the camera contributes a higher intensity and covers a wider field of view than light generated from behind the midline.

We adopted the method used by Helo et al. (2014) to correct for this. The intensity I' of the image of the given projection at distance x given the intensity of the image of the midline projection, I , estimated by the measurement can be found using equation 2.1:

$$I' = \left(\frac{r^2}{(r \pm x)^2} \right) I \quad \text{Eq 2.1}$$

Equation 2.2 can be used to predict the relative magnification effect (y') in 1D:

$$y' = \left(\frac{r \pm x}{r} \right) y \quad \text{Eq 2.2}$$

Since the distance to pixel was done at the central axis of the radiation track, the impact of the magnification of an object depends on its distance from the focal plane or midline projection. Using equation 2.1 and equation 2.2, the relative magnification can be calculated across the beam in any plane perpendicular to the camera by which the measured scintillation light distribution along the central axis can be extracted and compared to the simulated scintillation distribution.

Because we are dealing with optical light and the correction was only made to one plane within the scintillator, it could be argued that the captured image is the integrated image of the 3D light volume emitted along the line of sight. Therefore, since the light generated near the camera contributes a higher intensity and covers a wider field of view than light generated from behind the midline, it would cause distortion in the scintillation measurements. To evaluate the effects of imaging a 3D light distribution onto a 2D sensor, a MATLAB code version Matlab R2012a (The MathWorks Inc., Natick, MA) was generated. A uniform 3D cubic light source was considered (e.g. consist of 100 planes) as our region of interest. The relative intensity of each plane image can be calculated using equation 2.1. The relative geometry effect in one dimension can be calculated by using equation 2.2. Therefore, this would mimic imaging a 3D light distribution taken in consideration r and x . Summing the images of all planes for different camera-source distances (r) and different cube sizes (x) would allow to assess the effect of magnification distortion for different geometry setups. Finally, instead of using uniform cubic light source, we used measured crossbeam profiles at the central plane, and then calculate the relative intensity and the relative geometry effect of each plane image as described before.

2.4.3.6 Absorption

The scintillator selected is made to be transparent to their own light emissions, as shown in its specifications in Table 3. Absorption may decrease the light signal over distance, but it will not distort the measured light profile. The impact of the absorption was investigated using Geant4 and a 6 MeV electron beam. The impact of the absorption was measured by comparing the simulated result with and without the influence of absorption.

2.4.3.7 Refraction artefact

At the surface or boundary of the scintillator, the path of scintillation light can be changed as it passes from the scintillator to the air because of differences in the refractive index (n), as shown in Figure 27. This change of direction was described by Snell's law ($n_1 \sin\theta_1 = n_2 \sin\theta_2$), which describes the relationship between the angles of incidence θ_1 and the angle of refraction θ_2 when light passing through a boundary between two different materials [130].

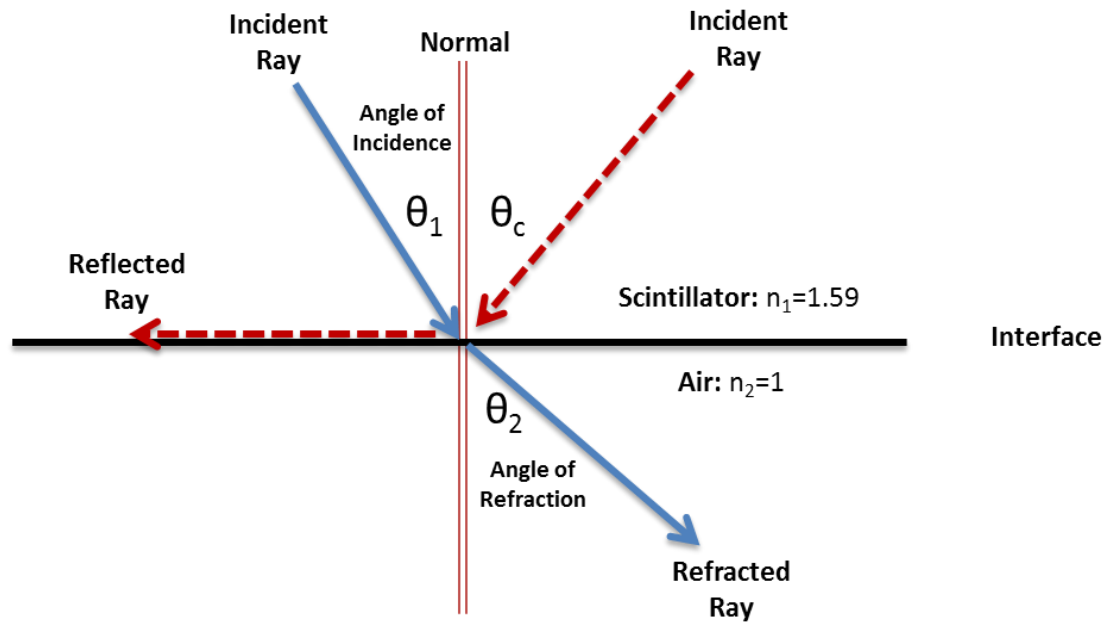


Figure 27: The refraction of light traveling from the scintillator into air bending away from the normal at the flat interface

The impact of refraction on the image resolution is similar to the magnification effect, which would appear as a shift in the expected location of individual pixels and an change in the apparent size of objects or scintillation light in the scintillator [117]. The influence of refraction on the scintillation light when it travels from the scintillator to the air was investigated experimentally by imaging a ruler fixed in the centre of a PMMA container measuring $10 \times 10 \times 10 \text{ cm}^3$, as shown in Figure 28, while it was empty (assuming there is no refraction) and filled with a liquid scintillator ($n=1.50$). The liquid scintillator was chosen over water owing to the higher refractive index and having a refractive index close to that of BC-408 scintillator. The thickness of the wall of the container was 3 mm and the dimensions of the PMMA were selected to match the thickness of the scintillator. The changes in the light profile due to

refraction can be estimated by comparing the two images of the ruler when the container was empty and filled.

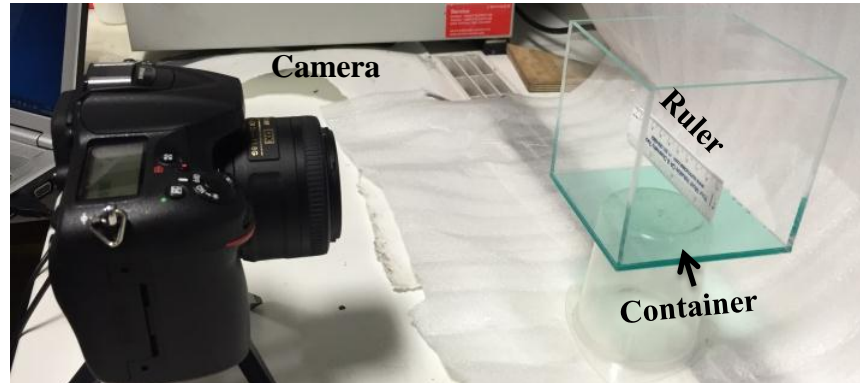


Figure 28: Demonstration of the refraction experiment setup showing the camera and the PMMA container.

2.4.3.8 Reflection artefact

Another phenomenon that can occur at the boundary is reflection, which can happen if the angle of the incident rays is larger than the critical angle (θ_c) = 39.26, as shown in Figure 27, and calculated by $\sin\theta_c = n_2/n_1$. As the light inside the scintillator is generated isotropically, the reflection on the scintillator surface would be homogenous. Each point of the scintillator surface receives an isotropic light, and the light will always be emitted within the same angle window ($\pm 39.26^\circ$). As a result, the light intensities decrease in the whole image at the same rate.

2.4.4 Results

2.4.4.1 Cerenkov light generated in the scintillator

We found that Cerenkov signals have a smaller intensity per unit length of the scintillator than the scintillation signal that would have been generated within the primary beam. Geant4 was used to examine the Cerenkov light emission and the scintillation light generated in the BC-408 scintillator using photon, electron and proton beams. Table 7 illustrates the contribution of the Cerenkov light generated by the primary radiation beam to the scintillation light.

Table 7: The magnitude of Cerenkov photons relative to the scintillation photons in the scintillator

| <i>Radiation beam</i> | <i>Number of scintillation photons per mm</i> | <i>Cerenkov generation relative to scintillation photons (%)</i> |
|------------------------|---|--|
| 6 MV photons | 10.6 | 1.9 |
| 6 MeV electrons | 1360 | 2.5 |
| 60 MeV protons | 18030 | 0.00005 |

The distal distributions of Cerenkov light emission were investigated by plotting the beam profiles of the scintillation and the Cerenkov light. For example, Figure 29 shows that the Cerenkov light generated by a 6 MeV electron beam dose not contribute to any light noise signal out of the collimated beam beyond the -50 mm and 50 mm data points.

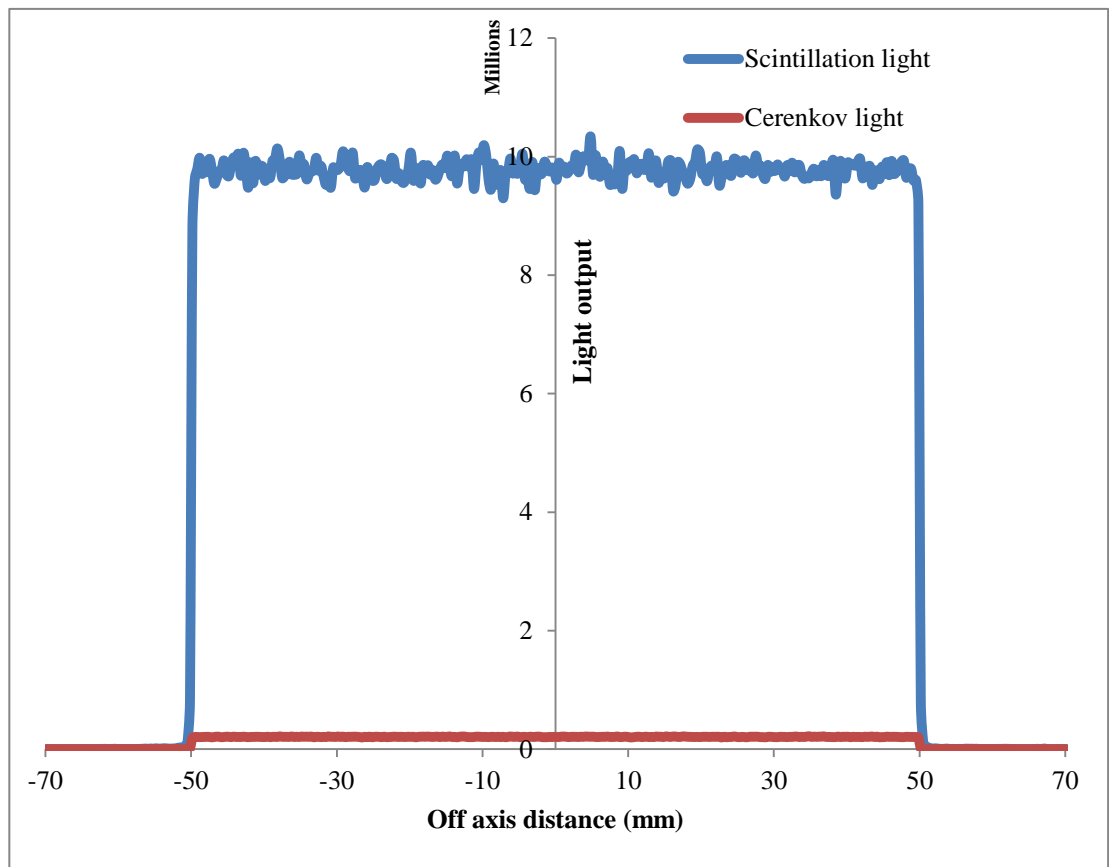


Figure 29: The scintillation compared to the Cerenkov light for $10 \times 10 \text{ cm}^2/6 \text{ MeV}$ electron beam

2.4.4.2 Impact of the magnification in the geometries used in experiments

The MATLAB code was generated to evaluate the effects of imaging a 3D light distribution onto a 2D sensor. The code starts by creating a uniform field image in one plane (i.e. $x=0$), then applies the geometry and intensity projection effects analytically on the previous plane using equation 2.1 and equation 2.2 to estimate the different images in different planes. Therefore, this would mimic the 3D light distribution taken in consideration r and x . For field size $10 \times 10 \text{ cm}^2$ and r equal to 10 cm, the resulting image which is the result of summing the images of all planes is presented in the top of Figure 30. Comparison of the cross profiles of the midline projection and the resulted image are shown in the bottom of Figure 30. The contributions of other planes in the resulting image highly and significantly distorted the resulting image profile. The resulting image's profile was expanded due to the magnification $\pm 5\text{cm}$ (representing 100% error).

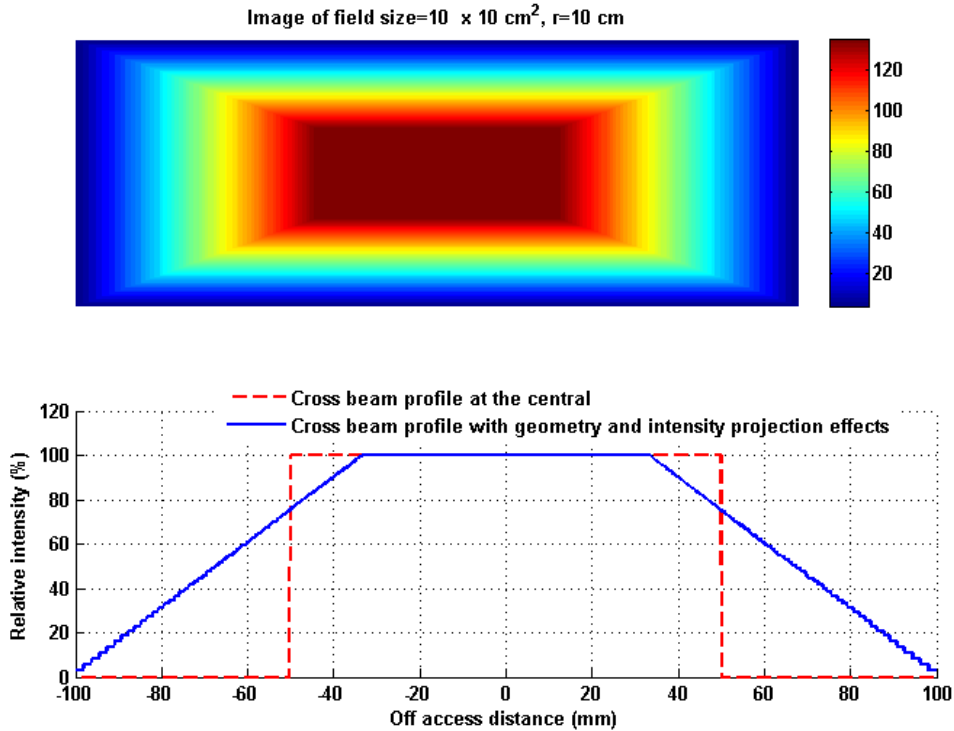


Figure 30: The resulting image of the sum of images of all planes with 100 steps across the 10 × 10 cm² field size after applying the geometry and the intensity changes assuming the distance left between the camera and the scintillator is 10 cm (top) and comparison of the profile of the central plane or axis and the profile of the sum of all plane (bottom). The results are normalised to the maximum values of each data sets.

We then evaluated the magnification effect with parameters similar to the experiments setups used. The field sizes were 10 × 10 cm² and 3 × 3 cm², while r was ~92 cm. The results are shown in Figure 31 and Figure 32 respectively. It can be noticed that as the distance between the camera and the light source become big, the magnification distortion become insignificant as shown in bottom of the Figure 31. The resulted image profile was expanded ±1mm (representing 2% error). Even more, when the filed size becomes smaller the magnification distortion becomes unnoticeable (0.42% error) as shown in bottom of Figure 32. It can be concluded that the magnitude

of the magnification artefact decreased sharply with the increasing distance r and decreasing the field size.

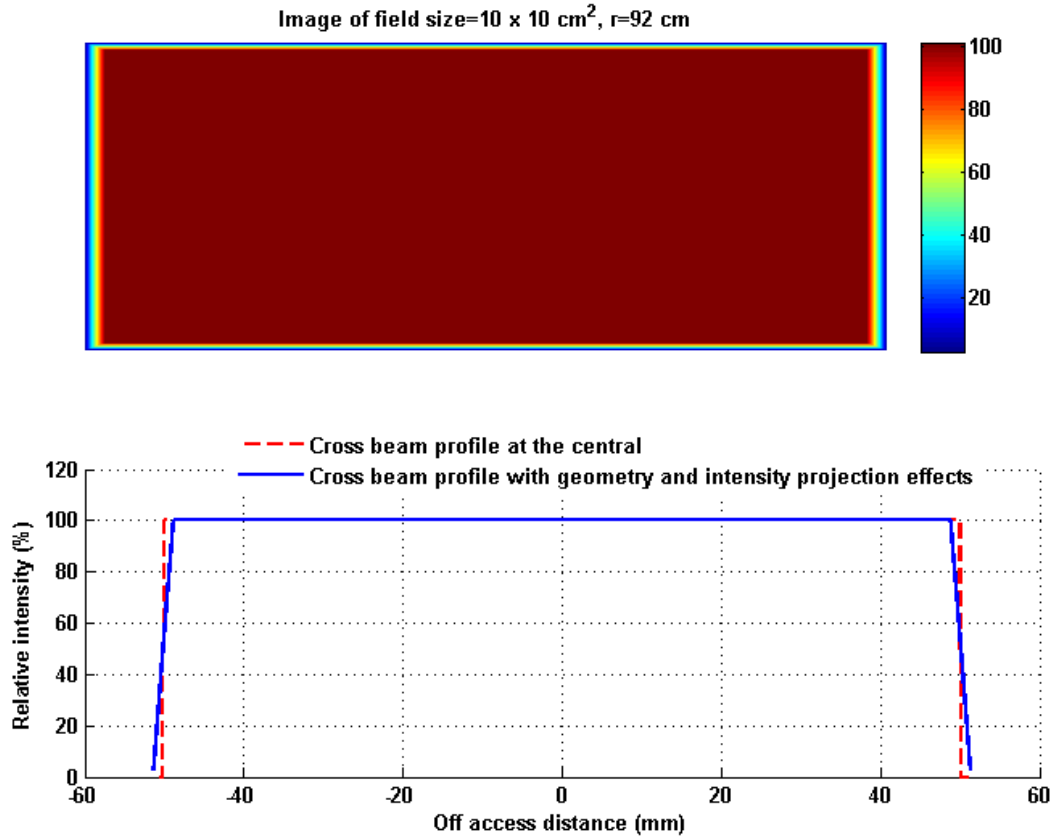


Figure 31: The resulting image of the sum of all planes with 100 steps across the 10×10 cm² field size after applying the geometry and the intensity changes assuming the distance left between the camera and the scintillator is 92 cm (top) and comparison of the profile of the central plane or axis and the profile of the sum of all plane (bottom).

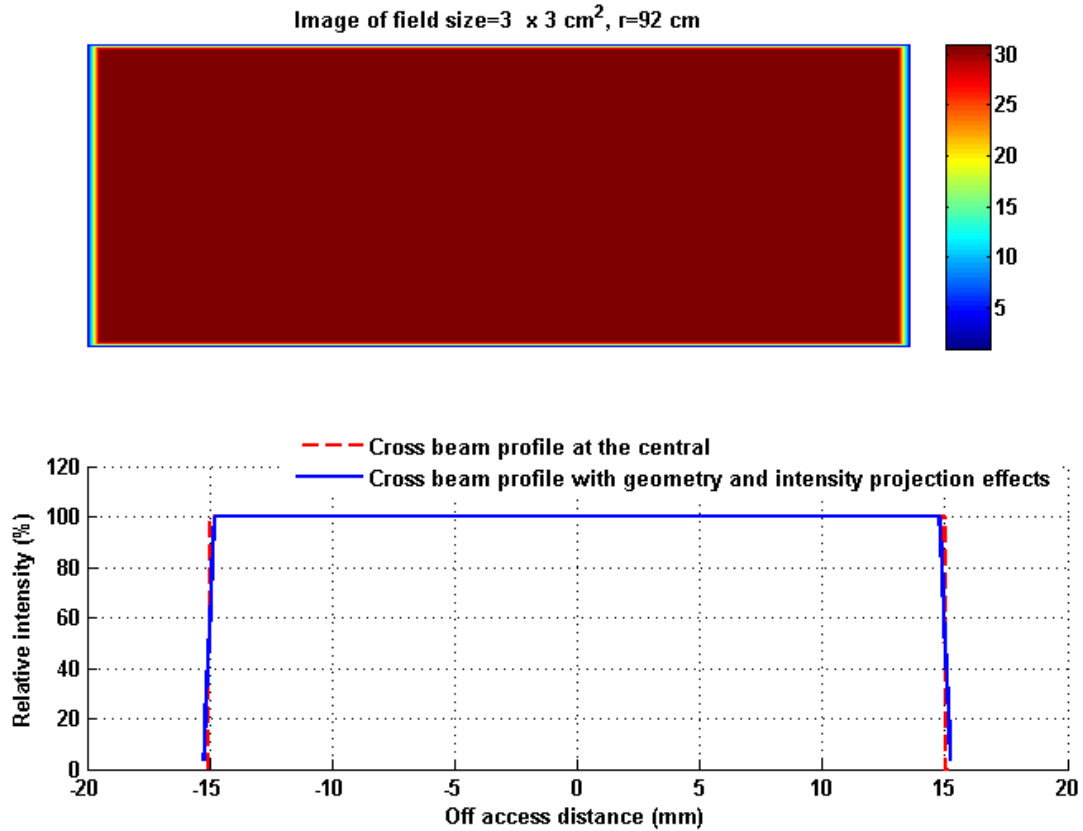


Figure 32: The resulting image of the sum of all planes with 30 steps across the $3 \times 3 \text{ cm}^2$ field size after applying the geometry and the intensity changes when the distance left between the camera and the scintillator is 92 cm (top) and comparison of the profile of the central plane or axis and the profile of the sum of all plane (bottom).

For more realistic approach of estimating the effect of magnification distortion since a sharp fall at the edge does not occur in a real measurement, we used the crossbeam profiles measured by ionisation chamber of a 6 MV photon beam and for two different field size ($10 \times 10 \text{ cm}^2$ and $3 \times 3 \text{ cm}^2$) to investigate the impact of profile distortion as a result of the geometry and intensity changes across the field size. Figure 33a and Figure 34a show the profile produced at the centre plane (y, I) , the nearest profile plane (y'_n, I'_n) and the far profile plane (y'_f, I'_f) , applying the geometry and intensity

equations (2.1 and 2.2). Figure 33b and Figure 34b show the comparison between the profile generated at the centre (y, I) and the profile resulting from the sum of the whole profiles across the field size (y'_s, I'_s). Thirteen profiles across the field size were used to generate the profile of the sum in Figure 33b and Figure 34b. For illustrative purposes, three profiles are shown in Figure 33a and Figure 34a. The results shows that very close agreement was found between (y, I) and (y'_s, I'_s) and the effect of this artefact at the edges is minimal (within ± 0.73 mm) at the biggest field size used (10×10 cm²) and ± 0.01 mm for 3×3 cm². In addition, we found this effect could add an error of ± 0.16 mm in the proton experiment setup ($r=50$ cm, field size= 2.5 cm²) and ± 0.08 mm ($r=33$ cm, field size= 1 cm²) in the x-ray experiment setup.

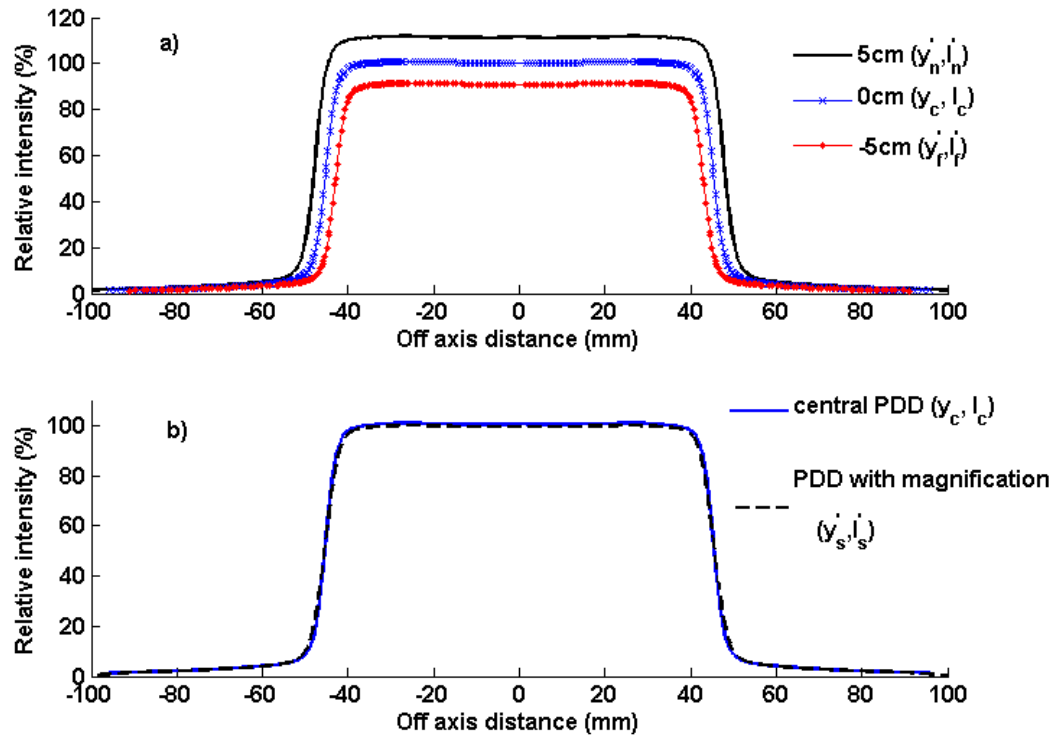


Figure 33: Magnification effects in off-axis profile of the ionisation chamber for a 10×10 cm² field size when r is 92 cm. For illustrative purposes, three profiles are shown in the top figure (a).

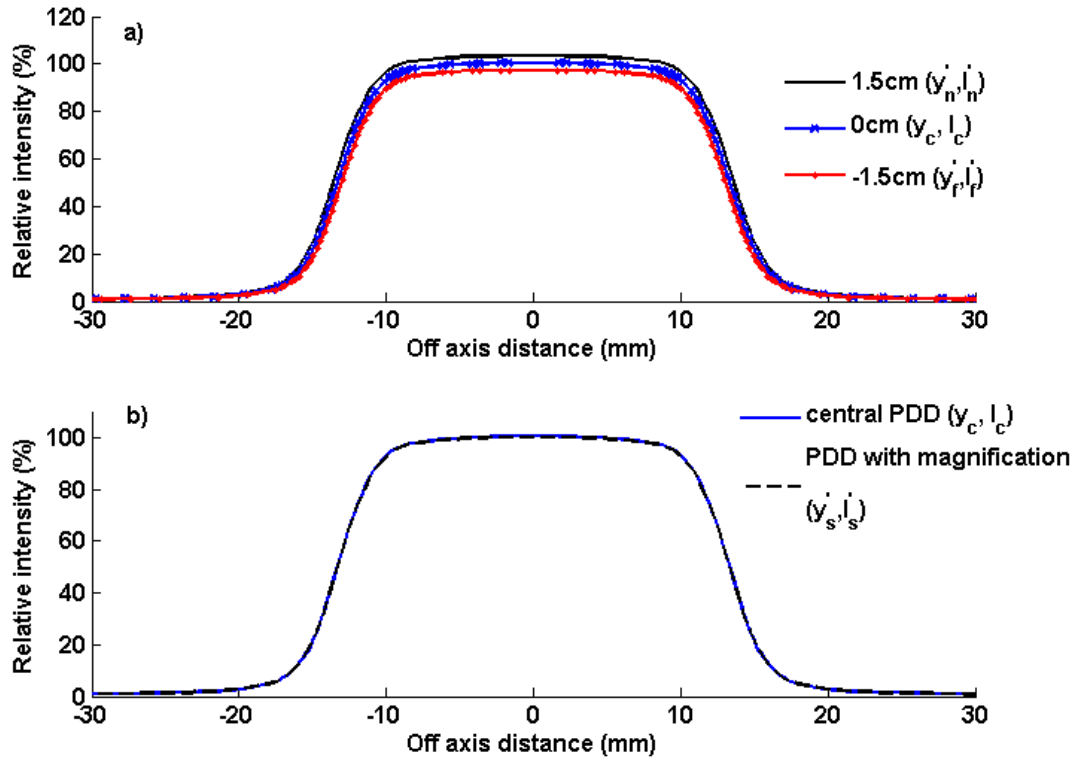


Figure 34: Magnification effects in off-axis profile of the ionisation chamber for a $3 \times 3 \text{ cm}^2$ field size when r is 92 cm.

2.4.4.3 Absorption

Figure 35 shows the off-axis profile of a 6 MeV electron beam simulated with and without optical absorption. The absorption did not show distortion in the profile shape. Rather it has an effect on the light output since the light output decreased uniformly by 2.85% as a result of absorption.

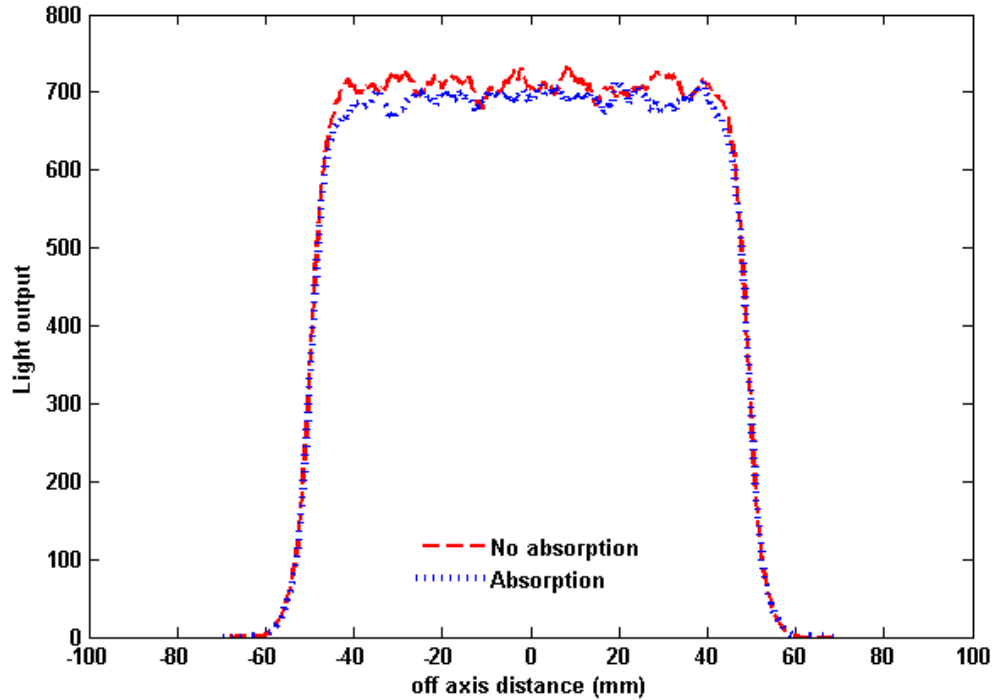


Figure 35: Demonstration of the impact of the absorption in the measured scintillation light in Geant4. The simulation used 10^7 electrons.

2.4.4.4 Impact of the refraction in the geometries used

Estimating the impact of refraction in the scintillation measurements is crucial when compared to the reference measurements. The images obtained when the container was empty and filled with the liquid scintillator were used to estimate the change of effective pixel size caused by refraction. The camera-source distance (r) is very important for estimating the refraction effect. When the distance between the container and the camera was 23 cm, two images obtained while the container was empty (no refraction) and filled (refraction effect presents due the differences of the refractive indices of scintillator liquid and air). The two images were overlaid using

MATLAB. Figure 36 demonstrates the refraction impact on the measurement at the point labelled (1) of the ruler, which translated to displacement of the point (1) by approximately 1 mm. The result shows that the refraction would impact the measurement by increasing in the apparent the length of the ruler; adding a margin of error of 3.07%, meaning that the scintillation light profile of $10 \times 10 \text{ cm}^2$ would be expanded by $3.07 \pm 0.09 \text{ mm}$ in each dimension.

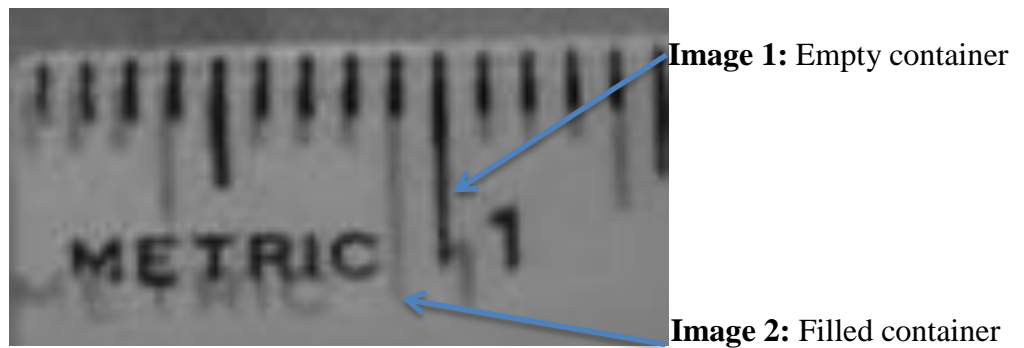


Figure 36: The resulting image of the two overlaid images of the ruler when the container was empty and filled was enlarged at the 1 cm point of the ruler. The distance between the phantom and the camera was 23 cm.

The experiment was repeated for a more realistic setup, used in the treatment rooms ($r = \sim 92 \text{ cm}$ between the camera and the scintillator), and this showed that the refraction would expand the measurement of the scintillation light profile by 0.51% (*i.e.* 0.51 mm in 10 cm). In the case of $r = 50 \text{ cm}$ used in the proton experiment, the refraction can add an error of 0.78% (*i.e.* 0.24 mm in the 60 MeV protons range of 3.09 g cm^{-2}). The impact of refraction was taken into consideration and corrected for using equation 2.2.

2.4.5 Optical artefacts discussion

We evaluated the magnification using two equations accounting for the geometry and inverse-square intensity falloff. We applied the magnification correction, assuming that the light came mainly from the nearest plane from the camera, resulting in an error in the effective pixel size. However, the profile of the scintillation light can be distorted because the light detected is the result of the accumulated light of the whole field size. The impact of geometry and the intensity of the light generated across the beam was evaluated analytically and using ionisation chamber measurements taken at the centre. This artefact is highly dependent on the field size and how far the camera is from the scintillator. With the field size used and the distance from the camera to the scintillator allowed, the impact of this artefact at the edges was minimal, being within ± 0.73 mm distance to agreement at the biggest field size used (10×10 cm²). Although this source of error could be present in the data obtained by the detector system, it remained within the 3% or 3 mm tolerance agreement widely used in radiotherapy dose evaluation. This error source has been reported in the literature [98], [100], [117] and could be resolved by using a telecentric lens that offers constant magnification at all object distances (more explanation of telecentric lenses can be found in section 7.3).

Refraction can contribute significantly to the measurement, but this is highly dependent on the distance allowed between the camera and the scintillator. We found that the refraction in our setup would add a margin of error within $\pm 0.51\%$ in the measured scintillation light profile for a 10×10 cm² radiation field, which can be corrected analytically using the magnification geometry equation.

The results demonstrate that the Cerenkov emission does not contribute significantly to the background signal generated in the low-dose region, which was discussed in the literature. In fact, the result obtained in this investigation showed that the shape of the electron profile of scintillation matches the Cerenkov profile, although the profile signals of the Cerenkov photons were insignificant compared to those generated by the scintillation photons. This is in line with experimental results when comparing the shape of the profile of the measured or simulated Cerenkov to that measured by the ionisation chamber (*i.e.* assuming the ionisation chamber measurements match the scintillation measurements) [104], [107].

2.5 Protocol of use of the detector system

2.5.1 Photodetector setup and measurements

The position and the alignment of the camera had to be considered carefully. The camera was attached to a tripod to keep it stable. Because of the difference between the refractive index of the surface of the scintillator and the air, the surface reflection artefact of the scintillator could be detected by the camera when it was centred at a depth below the surface of the scintillator [131]. The camera was placed in line with the surface of the scintillator to avoid the surface reflection in the data obtained near the scintillator surface at 90° with respect to the incident radiation beam. A reference image was taken before turning the light off to determine the edge of the scintillator to analyse the scintillation images during irradiation while it was dark. The camera was controlled remotely using Nikon camera control software (Nikon Corporation, Japan) connected

to a laptop computer via a USB cable. Black cloths and black tape were used to prevent the invasion of any ambient light.

Distance calibration was performed before placing the scintillator and covering the system with black cloth to exclude any ambient light. The relative size of an individual pixel in the final image was calibrated by imaging a metric ruler placed along the central axis of the beam in the light room conditions. Figure 37 shows an example of the distance calibration performed for a proton beam.

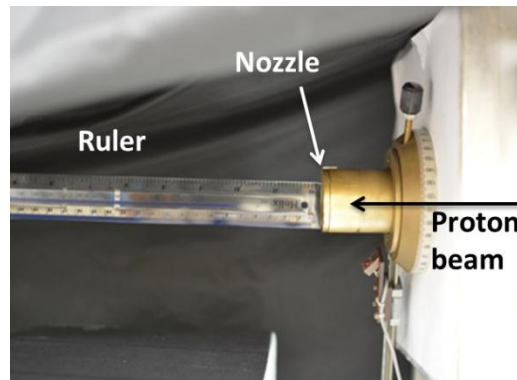


Figure 37: The distance to pixel calibration image

The distance between the scintillator and the source was adjusted, as was done for the reference measurements (*e.g.* ionisation chamber), and was kept constant for each experiment conducted in this thesis.

The camera was put in manual mode to provide precise and reproducible measurement. The settings were selected by (1) choosing the lowest ISO setting (ISO-100) to minimise noise in the image; (2) setting the aperture such that the dynamic

range of the camera was filled without reaching saturation at the highest light and the depth of field covered the field size of the radiation beam; and (3) setting the exposure time without reaching saturation.

Three repeated uncompressed raw images were acquired during each irradiation of the scintillation material to calculate the mean of the standard deviation of the results.

2.5.2 Image analysis

The data from the scintillation images was extracted in multiple steps. At the beginning, the analysis was performed using MATLAB. The raw images were converted from Nikon's proprietary .nef format to a .tiff format that could be read by MATLAB using *dcraw*, an open-source software [132]. After that, the images were subtracted from their background images and corrected for vignetting and magnification. Images were then converted to grayscale and a region of interest (ROI) at a certain region within the 2D images was determined and averaged. When applicable, the ROIs were combined to obtain a cumulative light intensity. The mean and the standard deviation of the three repeated images were calculated.

The effect of the width of the ROI on the accuracy of the measurements was tested, using two different ROIs in the scintillation image (Figure 38) and the difference between the two different ROIs was found to be less than 0.8%, as shown in Figure 39. However, the widths of the ROIs chosen to analyse the images in the following chapters, were chosen to match the reference dosimeter sensitive area. For example, the sensitive area of the parallel-plate ionisation chamber used in proton therapy was

2.5 cm².

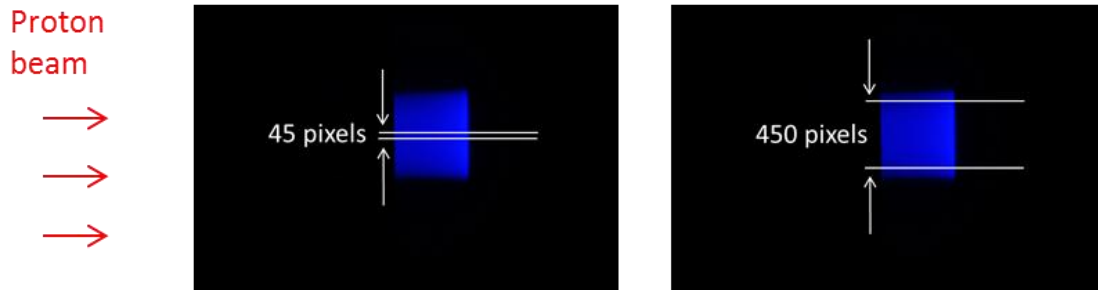


Figure 38: Demonstration of two widths of the ROIs selected for a 60 MeV proton image to extract the scintillation light depth distributions

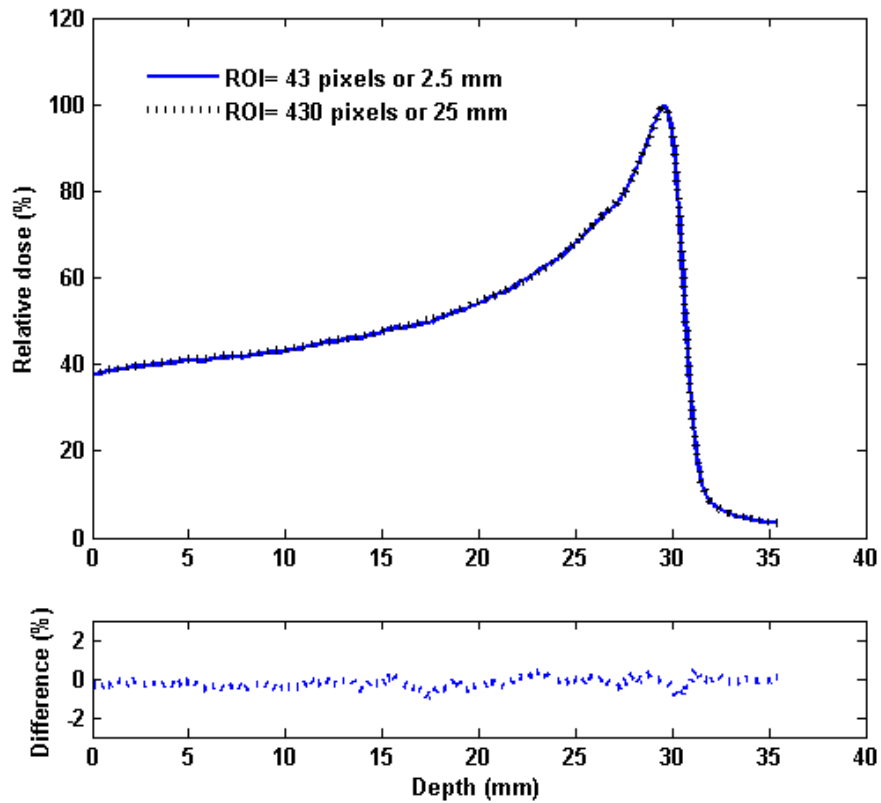


Figure 39: The scintillation light depth distributions of the two widths of the ROI and the difference between the distributions

2.6 Conclusion

The scintillator-based radiation detector system has many advantages for use in the characterisation of therapeutic radiation beams. However, many interesting optical problems were found that required evaluations and corrections. The purposes of this chapter were to optimally select a suitable scintillator for our design and to evaluate the inherent optical artefacts associated with the detector system.

The accuracy of a detector is enhanced by the careful selection of the scintillating medium. After researching several scintillators, the ideal features needed in a scintillator were; a long attenuation length, a high light output, a quick decay time, convenient for a practical detector and commercially available in a large volume. Two types of commercial scintillators were selected and tested for use in our detector system by measuring the light profiles. A liquid scintillator demonstrated some limitations that could affect the accuracy of the results, and some of these limitations have been observed in the present study. For example, the container issue of the PMMA showed an 11% error in the entrance dose due to the scintillation of the container in the proton beam. We have shown herein that a plastic scintillator is more suitable for measurements. To conclude, the evaluation and correction of optical artefacts is a vital procedure that is needed to accurately measure light distributions.

Artefacts have effects on the light measured—including vignetting, and stray radiation—that directly affect the image sensor. Because the image was produced on the centre of the image frame, the magnitude of vignetting was minor on the light distribution measured, creating a slight change in the quantitative analysis of the light distributions. The results show that Cerenkov light has little impact on the background

signal generated in the scintillator, representing 2.5% of the scintillation light photons in the case of electrons and 1.9% of the detected scintillation signal in the case of photons.

The geometry and intensity were solved analytically for a single plane. However, the effects of other planes across the field size were evaluated. The distortion of the light profile caused by the variable geometries and intensities across the beam field size impacted the accuracy of the measurement within ± 0.73 mm of the bigger field size. The setup used in this thesis at the edge of the light profile and the impact of magnification was considered minimal and could be resolved using a telecentric lens. A more practical solution when using a conventional lens to characterise and correct the issue of magnification could be to image a thin sheet of scintillator by moving it across the collimator used. The sum of all light profiles would estimate the distortion caused by magnification by comparing it to the measurement taken in the centre.

CHAPTER 3

3. SCINTILLATION DETECTOR SYSTEM FOR LOW ENERGY RADIOTHERAPY

3.1 Introduction

Two categories of photon external beam radiotherapy are commonly used including kilovoltage x-rays (produced in a x-ray tube) and megavoltage x-rays (produced in a linear accelerator) [20]. Of interest in this chapter is the kilovoltage x-rays and the spectrum is shown in Figure 40.

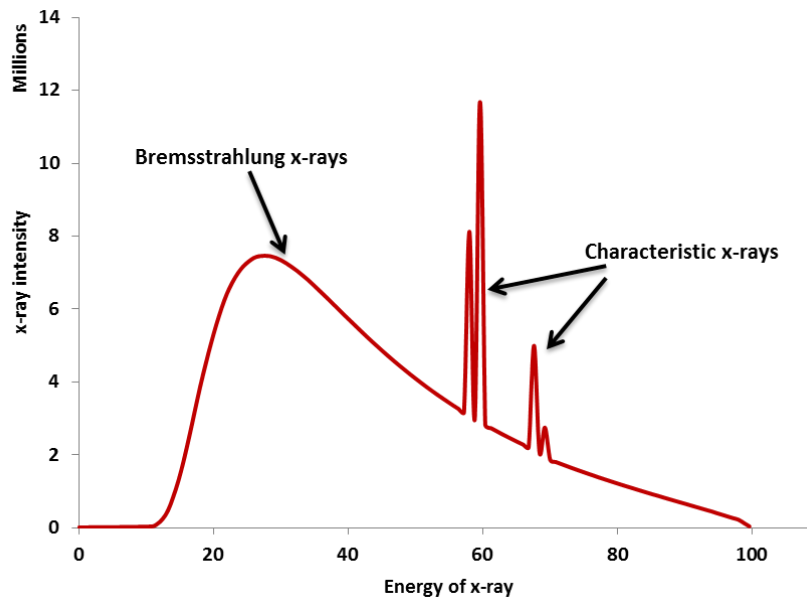


Figure 40: Approximate sketch diagram showing the spectrum of kilovoltage x-rays (100kVp) acquired using the x-rays

Many factors affect the spectrum of x-ray emissions such as tube current, applied voltage, and filtration. An increase in the tube current (mA) would result in an increase in the amplitude of the x-ray emission spectrum at all energies illustrated in Figure 41. In contrast, an increase in applied voltage (kVp) affects both the amplitude and the energy of the x-ray emission spectrum. X-ray intensity varies rapidly with changes in applied voltage. An increase in applied voltage results in an increase in the x-ray emission energy, making it more penetrating [133], [134].

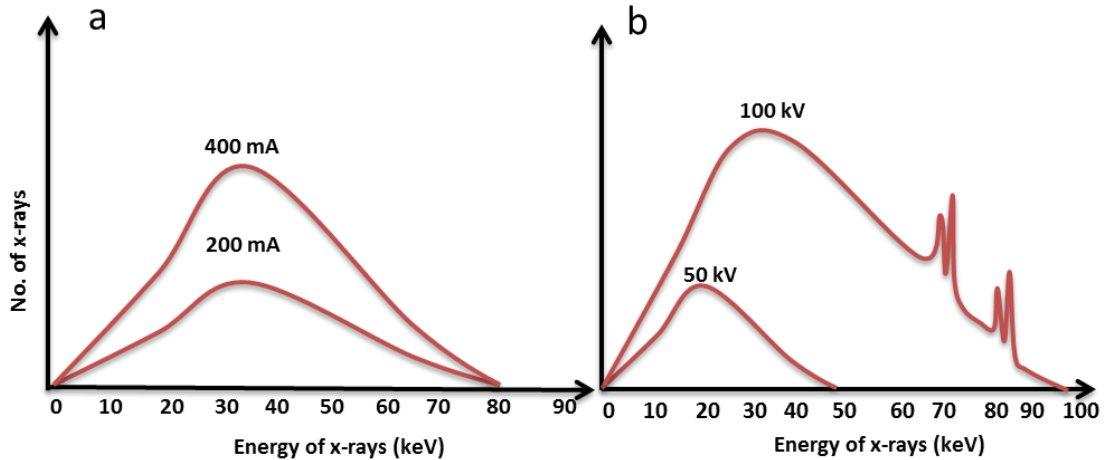


Figure 41: a) The effect of increasing the current b) The effect of increasing the applied voltage.

Most reports of scintillator-based dosimetry were in high-energy radiotherapy applications [42], [82], [83]. We extended this to a lower energy range with applied voltages of up to 300 kVp. This range is most commonly used for diagnosis, but there are also therapeutic applications, such as the treatment of skin diseases. We concentrated on the therapeutic application because the maximum dose is deposited close to the surface of the patient and the doses fall quickly with depth, owing to the attenuation and scattering of the beam [135], [136]. The therapeutic kilovoltage x-ray range used from mostly treating skin cancer can be categorised as contact therapy using 40–50 kV for treatment depths of 1–2 mm, superficial therapy using 50–150 kV for treatment depths up to 5 mm, and orthovoltage therapy with 150–300 kV for treatment depths of nearly 2 cm from the surface of the skin [36].

There is little data available in the literature about the use of a large plastic scintillator and a camera as a dosimeter for kilovoltage x-ray beams [121]. The intrinsic effectiveness of a dosimeter is its capacity to provide precise and accurate readings,

especially in clinical applications such as radiotherapy. The dosimeter has to have a well described dose response, be able to correctly resolve a PDD curve, and provide reliable results for fast changes in the dose delivery. A camera-scintillator detector system is designed as a tool for general beam QA. In kilovoltage radiotherapy dosimetry, the results of the measurement should be identical or closely similar each time the measure is conducted. Therefore, the degree to which the system allows for accurate and reproducible results shall be assessed.

For therapeutic purposes, obtaining the dose as a function of depth is essential to provide data to the treatment planning system and to confirm the accuracy of the planning system in radiotherapy. This can change with SSD, field size and beam quality (e.g. energy, half value layer (HVL)). In radiation dosimetry, the PDD is also sensitive to the detection material at this energy range as low energy photons generate short range secondary electrons unlike the megavoltage photon dosimetry [137].

We propose a detector system based on a large plastic scintillator and a commercial camera to be used for in-phantom dosimetry for kilovoltage x-rays. The system could offer a quick and easy way to measure PDD curves. According to the published dosimetry protocols (e.g. AAPM), the use of a specific solid phantom for kilovoltage x-ray beams could be feasible if the dose to the phantom can be related to the dose in water. The differences in doses between them should be within 3.5% [138]. Hence, the recommendation is that any material claimed to be water equivalent shall be quantified before it is used clinically [121]. To use a detector system for kilovoltage x-ray dosimetry, energy responses of the scintillation material compared to water are very crucial. It has been reported that the use of a scintillator (e.g. scintillating fibre) is not

feasible because that the energy response is not linear [139]. On the other hand, Lessard et al. (2012) argued that a scintillating fibre can be used as a dosimeter for low energy x-rays [140].

In this chapter, we examine the capability of the system to provide precise and reproducible results. In addition, we evaluate the system's response against current of the x-ray machine and we investigate the system's ability to measure a PDD curve. Monte Carlo simulation has become an effective method to compute dose deposition and it is used in this study to validate the measurement and to determine whether the detector system suffers from energy dependency as well as the potential usefulness in a kilovoltage energy range [141], [142].

3.2 Materials and methods

3.2.1 The detector system setup

The BC-408 plastic scintillator chosen has a high light output efficiency and response to x-ray in the kilovoltage energy range. The setup used is displayed in Figure 42 and measurements were performed in a 1 cm diameter field with an SSD of 22 cm. The camera was placed 33 cm away from the scintillator.

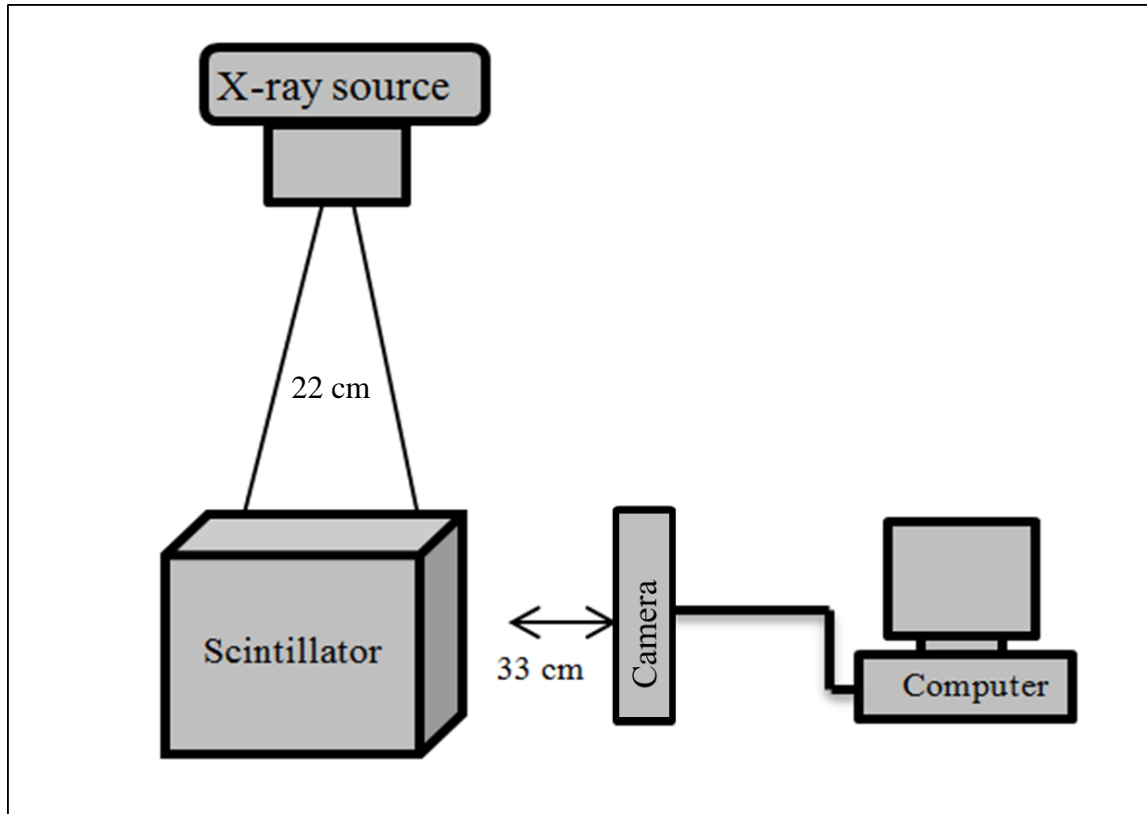


Figure 42: Schematic of the setup used in this experiment

The irradiations were performed at University College London (UCL) with x-ray source in the radiation physics laboratory. The anode of the x-ray tube was made of tungsten, had a 21° anode angle, and had an inherent filtration of 0.1 cm of beryllium (Be).

The light output could be affected by the distance between the scintillator and the camera. The camera should be controlled manually (i.e. acquisition time, and aperture size) and should have the same settings for all the measurements. Therefore, the camera settings were checked to ensure that they provide a useful and reproducible image. No saturation should be present in the images with the highest light output and with acquisition time of the 0.5 seconds.

3. Scintillation Detector System for Low Energy Radiotherapy

Table 8 lists the beam qualities used in this study provided by the National Institute of Standards and Technology (NIST) [143]. The primary incident spectrum of each applied voltage (i.e. energy) was determined with SpekCalc software from a tungsten target as well as the effective energy as shown in Figure 43 [144]. The scintillation light was imaged during irradiation from 50 up to 100 kVp because the tube available could generate x-rays up to 150 kVp but we were advised that 100 kVp is the maximum useable applied voltage. The simulated PDD curves (described below in section 3.2.4) were obtained from 50 to 300 kVp to cover all the beams energy used in therapeutic x-rays.

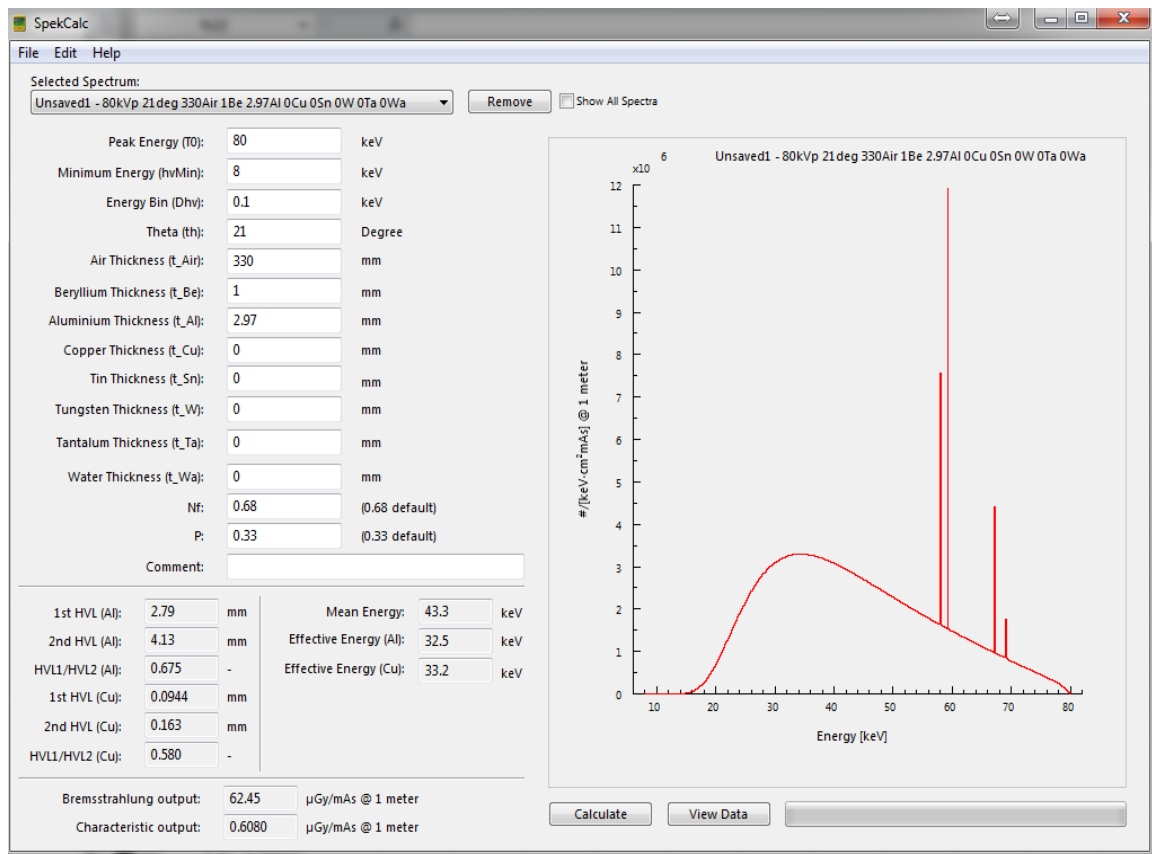


Figure 43: Main window of SpekCalc

Table 8: The characteristics of the x-ray beams

| <i>Peak tube potential (kVp)</i> | <i>Mean energy (keV)</i> | <i>HVL</i> |
|----------------------------------|--------------------------|-------------------------|
| 50 | 28.5 | 1.02 mm Al |
| 60 | 33.5 | 1.68 mm Al |
| 80 | 43.3 | 2.97 mm Al |
| 100 | 52.5 | 5.02 mm Al |
| 150 | 83.8 | 10.2 mm Al + 0.67 mm Cu |
| 200 | 112.0 | 14.9 mm Al + 1.69 mm Cu |
| 250 | 144 | 18.5 mm Al + 3.2 mm Cu |
| 300 | 173 | 22.0 mm Al + 5.3 mm Cu |

3.2.2 Background noise

Any unwanted signals will reduce the accuracy of the measurements. Therefore, different situations were characterised. First, we investigated whether noise in the image is generated by the x-ray source when there is nothing in the way of the beam. Second, a non-scintillating, scattering material (PMMA sheets) was introduced into the beam and the image noise was again measured in order to investigate whether scattered stray radiation affects the measurements. These background images can then be subtracted from images acquired during irradiation.

The results show that the mean of the background signals of three repeated images increased from 2.1% to 2.6% when the beam was turned on. In addition, the mean of the measured noise intensity was increased further to 2.8% when PMMA sheets were put in the way of the beam as a non-scintillating scattering material. This indicates that the background signal should be taken into consideration to reduce uncertainty. This is particularly important when there is a scattering material such as the plastic scintillator which contributes additional signals to our photo-detector due to scattering of the kilovoltage x-rays. In addition, the camera was placed near (33 cm) to the x-ray beam.

Figure 44 shows the scintillation depth distribution extracted from the image during x-ray irradiation. It also shows the corrected scintillation depth distribution after subtracting the background signal when there was a scatterer.

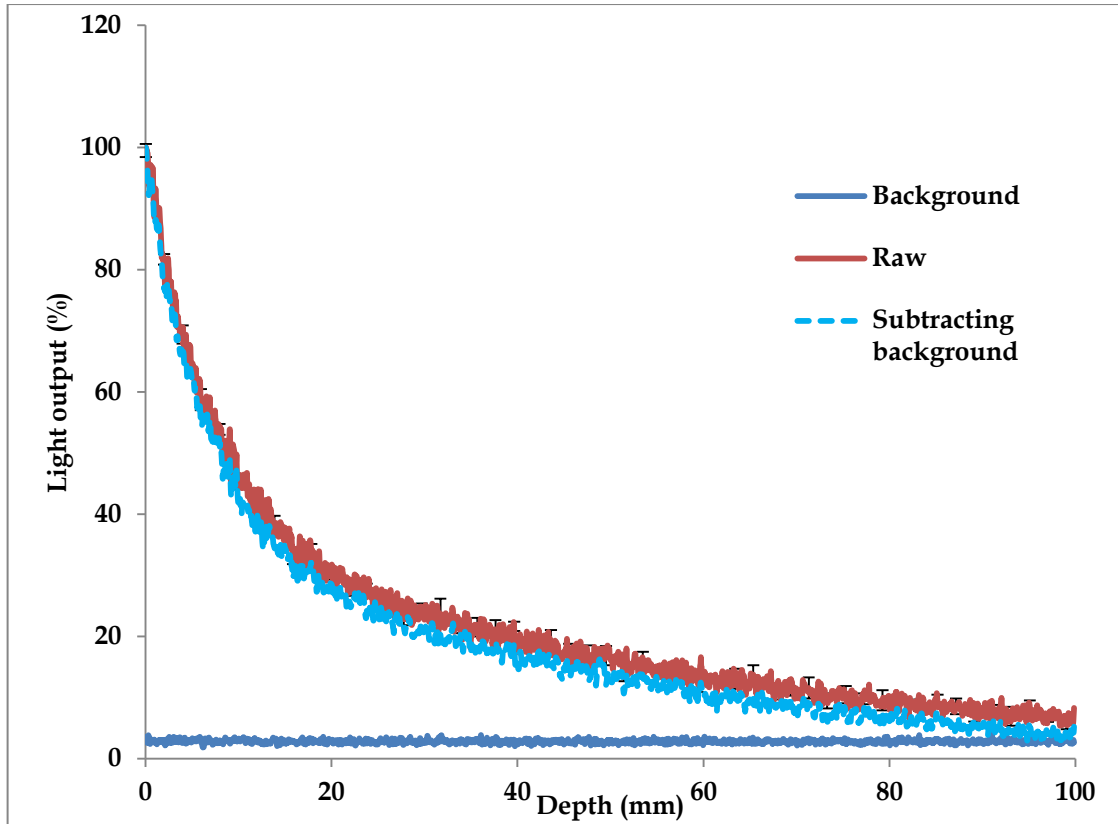


Figure 44: The impact of subtracting the background signal in the measured depth dose distribution. Error bars demonstrate the standard deviation of three repeated measurements.

3.2.3 System characterisation

3.2.3.1 Short-term reproducibility and repeatability

A QA system must be reproducible and stable. It is necessary to investigate whether the scintillator detector system can give the same result for daily use by calculating the variation in the data obtained in repeated measurements. A small standard deviation of the measurements means high precision. To test the reproducibility, the scintillator was exposed to an x-ray beam and the response imaged by the camera. The signal reproducibility of the system was tested six times for three different energies 50 kVp,

80 kVp and 100 kVp with constant 4mA.

3.2.3.2 Linearity

In order to investigate the linearity of the relation between the x-ray intensity delivered in the scintillator and the camera output, the total yield was measured for different currents, with a fixed field size of 1 cm. The measurements were performed with a constant integration time of 0.5 seconds. The response of the system to changing x-ray tube currents was tested by varying the current from 2.5 to 5.5 mA for three voltages (60, 80, 100 kV). The average light outputs were taken and plotted with the equivalent current.

3.2.3.3 Comparison of measurements with ionisation chamber

In this measurement, the scintillator was exposed to a 50 kVp beam, and the scintillation light was imaged at a constant irradiation time of 0.5 seconds to extract the PDD curve with a 1 cm diameter beam at an SSD of 22 cm.

Similar measurements were performed using an ionisation chamber connected to Keithley 35050A electrometers. The PDD obtained from the scintillation detector system was then compared to that from the ionisation chamber to investigate whether the detector system provided similar measurement. The same beam qualities of 3 mA and 50 kV were used for both measurements. The ionisation chamber measurements would ideally be obtained in a water phantom. However, a waterproof ionisation chamber

would be required along with a water phantom to do the measurements, neither of which was available in the lab. Instead, Perspex sheets were used to mimic the water phantom, as Perspex has a density almost equivalent to water. The ionisation chamber was placed behind sheets of Perspex. By doing so, the dose at any depth along the beam central axis could be measured by increasing the number of Perspex sheets. The statistical uncertainties of these measurements in both detectors were determined through repeated measurements.

3.2.4 Monte Carlo simulations

Geant4 was used to extend the experimental results which aim to investigate the energy dependency of the scintillator across the for all radiation beam qualities available in therapeutic x-rays. For radiotherapy applications, Geant4 simulations could provide a result with accuracy within 1% for low energy photon compared to a clinical beam [142].

Precise simulation of the energy loss of the primary particle and production of secondary particle is a critical requirement. Therefore, many physics packages are available in Geant4 to be used according to the radiation particle types and energy ranges used. The low energy standard physics processes (e.g. Compton scattering, Rayleigh scattering, photoelectric effect) were employed for electromagnetic interactions covering the interactions of photons and electrons in materials with atomic number between 1 and 100 [145]. In our model, the Geant4 was used to determine whether the detector system suffers from energy dependency at all the beam qualities (50 - 300 kVp) available in kilovoltage x-rays using 10^7 primary incident photons

providing statistical uncertainties smaller than 1%.

Table 9 shows the chemical elements of the materials used in the simulation, their density, and mean atomic number (\bar{Z}) which was calculated using Eq 3.1 as stated in the ICRU 35 report [26], [146], [147].

$$\bar{Z} = \sqrt[3.5]{\sum_i \omega_i Z_i^{3.5}} \quad \text{Eq 3.1}$$

where ω_i is the fraction by weight of element i which has atomic number Z_i . These materials were built in the simulation and then exposed to a photon beam placed 22 cm from the scintillator. The number of incident photons simulated was 10^7 photons.

Table 9: The fractional weight of component of the materials used in the simulation

| <i>COMPONENT</i> | <i>WATER</i> | <i>BC-408 SCINTILLATOR</i> | <i>PMMA</i> |
|------------------------------------|--------------|----------------------------|-------------|
| H | 0.1118 | 0.0850 | 0.0805 |
| C | - | 0.9150 | 0.5998 |
| O | 0.8881 | - | 0.3196 |
| Density (g cm⁻³) | 1.00 | 1.03 | 1.19 |
| \bar{Z} | 7.73 | 5.84 | 6.70 |

3.3 Results

3.3.1 Short-term reproducibility and repeatability

Results from the measurements' reproducibility test are displayed in Table 10. The results indicated that the system was stable, since the standard deviation was less than 1%. The deviation is higher when the irradiation quantity was low (i.e. less light output) and the result improves with increasing voltage.

Table 10: The reproducibility of results of six images for three set of applied voltage

| <i>The applied voltage</i> | <i>50 kVp</i> | <i>80 kVp</i> | <i>100 kVp</i> |
|---------------------------------------|---------------|---------------|----------------|
| Mean of six images | 200.16 | 249.28 | 278.86 |
| standard deviation | 1.56 | 1.23 | 0.97 |
| Relative standard deviation, % | 0.56 | 0.50 | 0.48 |

3.3.2 Linearity

The results reported here were based on the mean of three images per value of current. The influence of current is illustrated in Figure 45. The solid line in this figure represents a linear fit of the average response. The average pixel intensity is observed to increase linearly with a delivered current with a correlation coefficient (R^2) equal to 0.99. Measurement uncertainty was assessed by measuring the standard deviation relative to the mean. The uncertainties of current values may have arisen from the rotary selection switches of the values of the voltage and current which had errors of ± 0.1 mA and ± 1 kV respectively. The variation in the light output readings was highest when the voltages and currents were low.

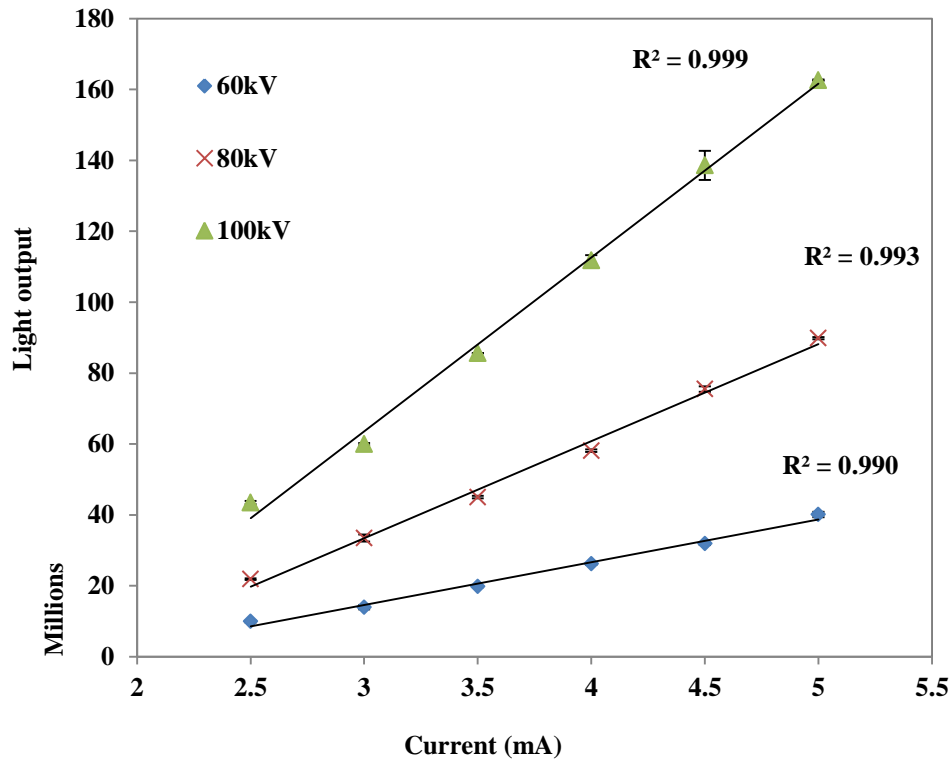


Figure 45: The scintillation light as a function of x-ray tube current for different applied voltages. Error bars demonstrate the standard deviation of three repeated measurements

3.3.3 PDD measurements

The measured PDD for the scintillator-based system and ionisation chamber at 50 kVp are displayed in Figure 46. The ionisation chamber measurement shows more rapid dose fall-off with depth. We assumed the PMMA material is equivalent to water at the energy used, but this requires investigation, which we consider in the next section. The difference between these curves demonstrates that either the PMMA or the plastic scintillator is not water equivalent or the measurements are not accurate *i.e.* backscatter is missing in the ionisation chamber measurement.

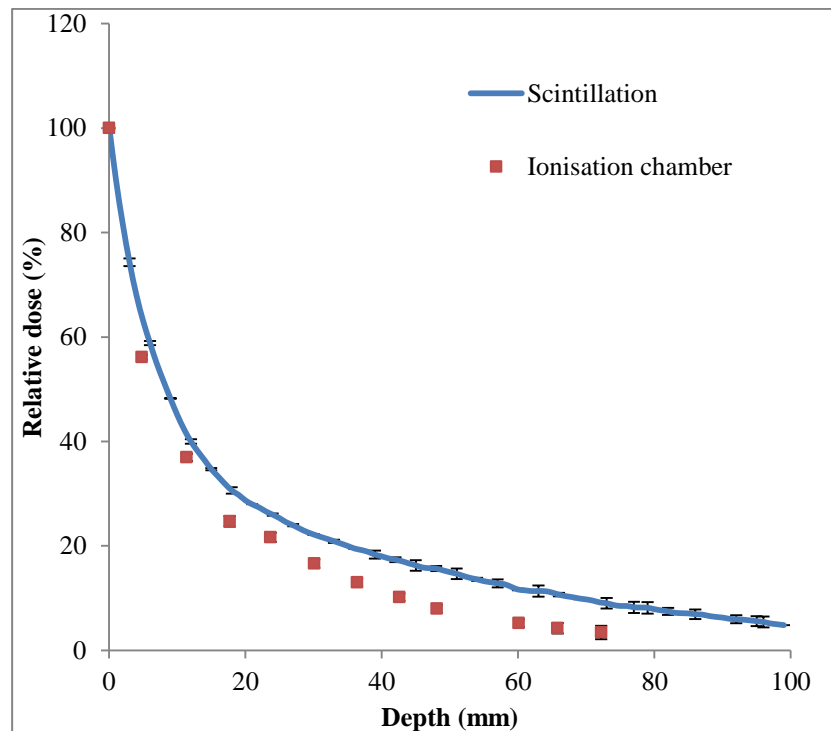


Figure 46: Comparison of measured scintillation light distribution and PDD curves by ionisation chamber for 50 kVp beam. Error bars demonstrate the standard deviation of three repeated measurements.

3.3.4 Monte Carlo validation

Percentage depth dose curves were simulated using Geant4 in three materials at 50 kVp. These are displayed in Figure 47. The PDD in PMMA was up to 7% greater than that in water, and the PDD in the plastic scintillator was up to 23% greater than that in water. Different \bar{Z} -values have an impact on the PDD. For example, the difference in the PDD of plastic scintillator ($\bar{Z}=5.84$) was larger than that in PMMA ($\bar{Z}=6.70$) compared to water ($\bar{Z}=7.73$). This could be explained due to the differences in value of Z having an impact on the PDD.

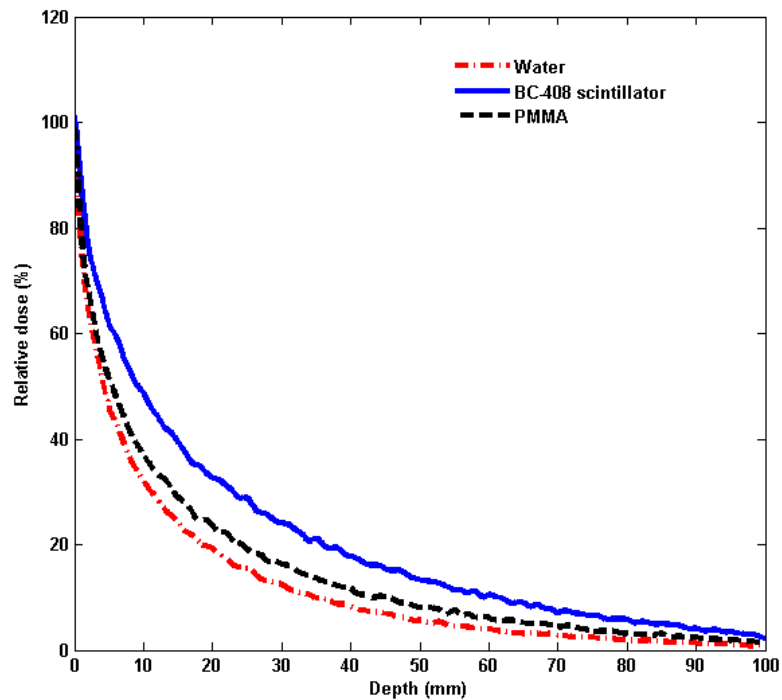


Figure 47: The simulated PDD curves for water, PMMA and BC-408 scintillator at the same irradiation parameters (50kVp)

The energy dependence of the scintillator was tested by comparing the simulated PDD curves for water and scintillator at different energies as illustrated in Figure 48.

The difference between the simulated PDD obtained in the BC-408 scintillator and that in water was found to reach 23% at low effective energy of 28 keV (50 kVp), and the difference decreases when the energy increases until 83 keV (150 kVp) is reached, where there is an acceptable difference (3%) between the two materials, as shown in Figure 49. It is observed that as the beam energy increases, the PDD differences decrease.

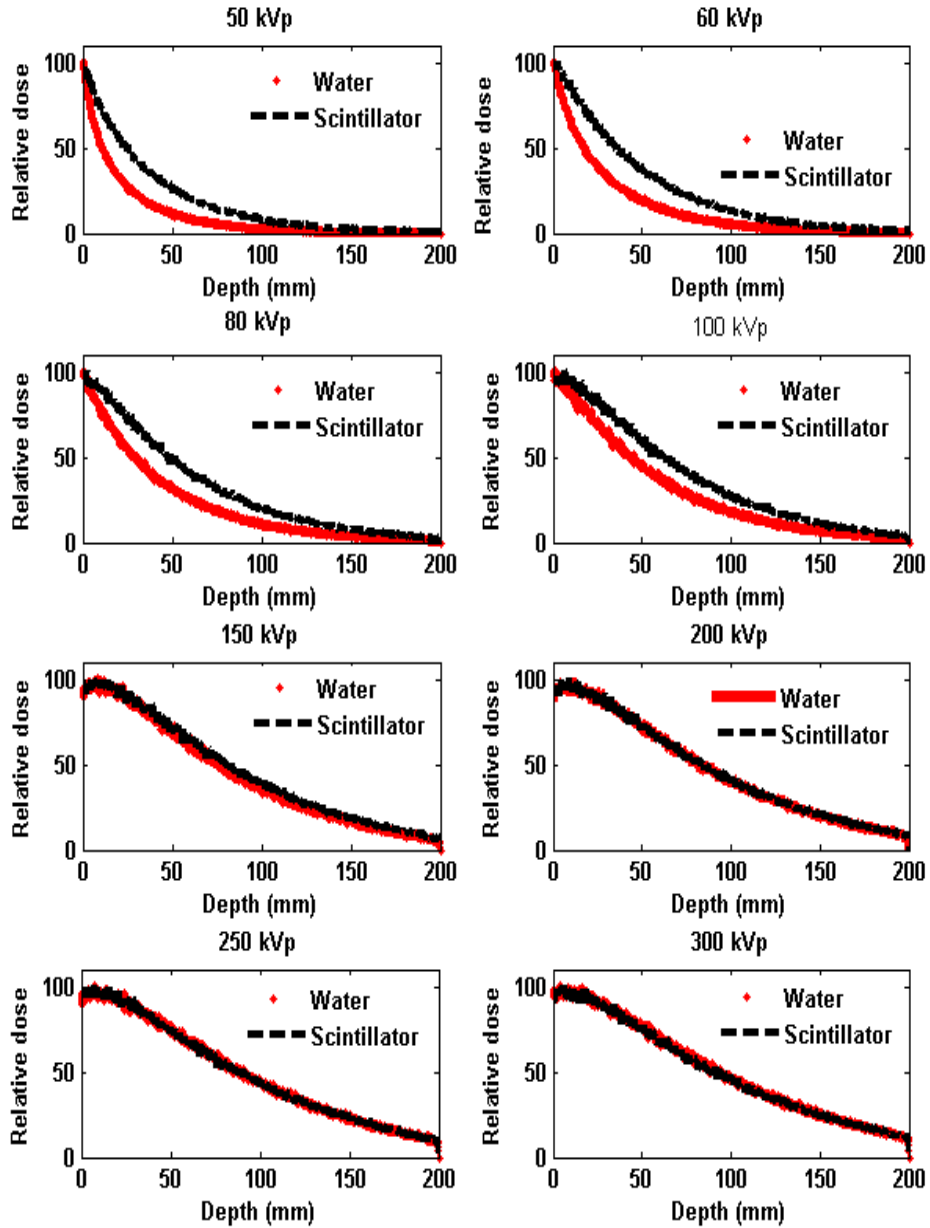


Figure 48: The simulated PDD curves for the BC-408 scintillator and liquid water for different applied voltages

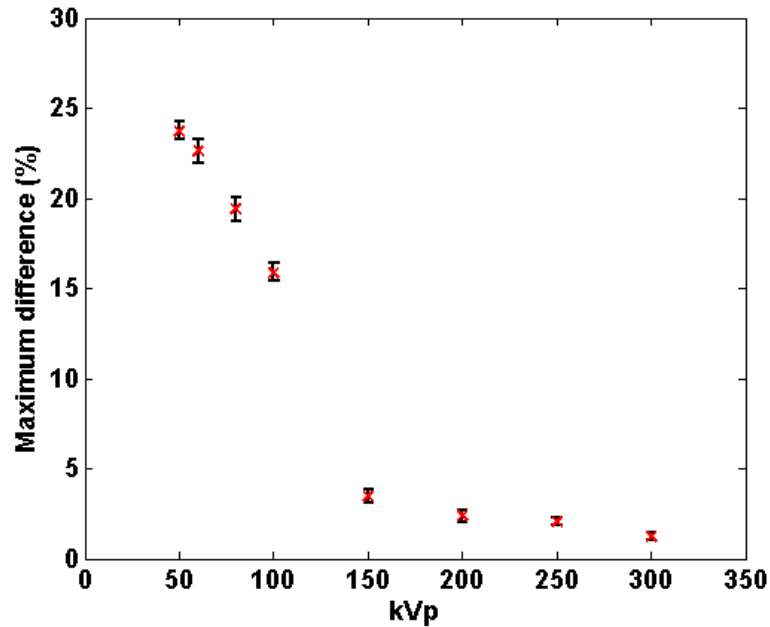


Figure 49: The percentage maximum difference between the depth-dose distributions deposited in water and scintillator for different applied voltages. Error bars demonstrate the combined statistical deviation of the simulation results.

3.4 Discussion

A prototype system has been developed using a plastic scintillator and camera offering enormous potential as a 3D volume dosimeter. System characterisation results from the prototype system used in this study showing excellent linearity with current. It has been noticed that the standard deviation is higher at lower current or applied voltage values due to the lower output at low applied voltages and currents. In addition, the detector system provided reproducible results within $\pm 0.56\%$ for low energy photon beams.

We have used measurements and Monte Carlo simulations to investigate the water equivalency of the BC-408 scintillator by comparing its depth doses and to water for

kilovoltage x-ray beams. The effective atomic number of the scintillator was found to differ from water. Unlike megavoltage x-ray beams, there are few obstacles affecting the accuracy of the current practice of the dosimetry of kilovoltage x-rays because of a more significant photoelectric interaction of incident x-ray beam [148]. The photoelectric cross section depends strongly on the atomic number of the material, so the sensitivity of a dosimeter would be reliant on the materials' composition used in its construction (i.e. \bar{Z}) [121], [149]. In the kilovoltage energy range, depth-dose distributions for the scintillator exhibit less attenuation than those for water for 50-150 kVp x-ray beams, due to the stronger relative significance of photoelectric absorption in the water [150]. It was found that the plastic scintillator cannot be considered water equivalent material at low energy photons if the applied voltage is below 150 kVp (83 keV). This indicates that the plastic scintillator should not be used below 83 keV without correction for each applied voltage used. For above than 150 kVp x-ray beam, the scintillator exhibits a very close dose reduction with depth to water with less than 3% difference.

Some properties of the ideal dosimeter discussed in this chapter are revisited here in Table 11. The scintillation responded very fast as the luminescence in the scintillation material is of the order of ns and the requirement for a dosimeter is ≤ 10 ms [127].

Table 11: The requirements of the performance of a clinical QA system

| <i>Requirement</i> | <i>Results</i> |
|--|--|
| 1) Stable | Found to be stable $\pm 1\%$ |
| 2) Response time | Provide nearly real-time measurement |
| 3) Linearity with dose | Responded linearly |
| 4) Independent of energy | Energy independent at energies greater than ~ 83 keV but not at energies less than this |
| 5) Clinic environment suitability | showed to be non-toxic |

3.5 Conclusion

The purpose of this work was to evaluate the use of the camera-scintillation detector system for the use of therapeutic kilovoltage x-rays dosimetry. In this work, we studied the measured depth dose distributions of 50 kV x-ray beam obtained by ionisation chamber and the scintillation detector system. Divergence was found between the two distributions and this required further investigation. Therefore, we used Geant4 to model the output of a kV x-ray unit (50–300 kVp). We studied the depth dose distribution obtained in water and in the BC-408 scintillator. The tolerance levels of the comparison between the depth-dose distributions obtained from scintillator detector

measurements and those obtained in water should be within $\pm 3.5\%$. By analysing the simulated depth dose distribution in both mediums, less than 3% was found in both materials for applied voltages exceeding 150 kV. We conclude that the best agreement occurred with the highest energies. The system has the advantages of providing reproducible results rapidly and directly digital. However, even though the plastic scintillator has a density equivalent to water, the elemental composition is not water-equivalent below 150 kV.

CHAPTER 4

4. SCINTILLATION DETECTOR SYSTEM FOR HIGH ENERGY RADIOTHERAPY

4.1 Introduction

Individual treatment plans are subjected to a series of well-defined checks and verifications to ensure both the prescription and the plan are identical. Therefore, pre-treatment verification of the output information of the Linac is an essential QA procedure. Because the electrons generated pass through a complicated path from production, guidance, and acceleration to the delivery of the radiation dose, the performance characteristics of the machine must be strictly monitored. Many examinations (daily, weekly, monthly, and annual) of the beam parameters are performed, such as measuring PDD and off-axis profiles at different energies and different field sizes. This is to validate the machines output and to provide data for the treatment planning system. These measurements are normally done using a standardised tank of water with an ionisation chamber [151].

Several methods have been used to extract dose information in high energy photon and electron beam such as ionisation chamber, and film. Although ionisation chambers have been shown to be robust, precise, and very well controlled, but they suffer from volume averaging because of the creation of the collected ions throughout the active chamber volume and low sensitivity in comparison to other dosimeters [152]. In addition, the ionisation chambers placed in 2D arrays do not offer sufficient spatial resolution [153]. Films possess a high spatial resolution but their responses depend on dose rate and film processing that can be affected by many parameters such as temperature. A calibration procedure is, therefore, essential when film dosimetry is used, which is a lengthy and time consuming procedure [154], [155].

During daily radiotherapy sessions, camera-scintillator combination can be used in EPIDs to monitor patient position and can also be used to verify individual leaf motion during an IMRT delivery. Recently, there has been an increase in research on characterising and evaluating organic scintillators for use as dosimeters for QA applications [33], [52]–[55]. Several authors reported the suitability of an organic scintillator for dose measurements, and many scintillators types and designs were studied. The use of scintillators is encouraging for high energy photon dosimetry because of their radiological water equivalence [57]. They exhibited many advantages in a 6 MV photon beam such as high sensitivity, reproducibility within $\pm 1\%$, linear dose response, energy independence, independence of pressure and temperature, and a fast response to ionising radiation [56], [57]. Arrays of scintillating fibres were evaluated for 2D dosimetry applications [91], [156], [157]. A thin plastic scintillating screen or sheet placed obliquely in water phantom in combination with a mirror and CCD camera were also designed for dosimetry measurements [158], [159]. An important drawback of the above designs is Cerenkov noise signals produced in optical fibres and in the whole water phantom in where the scintillating sheet was positioned. In addition, these fibres are not yet commercially available, and high accuracy is required to prepare these fibres for coupling to optical fibres as a light guide as mentioned in chapter 2. Large 3D volume liquid scintillator detectors have also been used to evaluate the dose distribution for photon beams [83]. Several attractive features of large scintillators enable them to be a good candidate for dosimetric measurements such as high resolution [83].

The use of the scintillators in electron dosimetry has not found in the literature as far as I am aware. In general, organic materials or phantoms used instead of water need to

be tested for each type of ionising radiation used in order to estimate the accuracy of the measurements obtained by a specific phantom. Materials from dosimetric point of view cannot be exactly equivalent to water because their differences in elemental compositions, production rates of secondary particles at equivalent depths, and interaction cross sections [160], [161].

Most of the previous work in radiotherapy has used liquid scintillators, which are difficult to use in the clinic, scintillating fibres connected to photodetectors, or sheets of plastic scintillator. We proposed a dosimeter in chapter 2 based on a large plastic scintillator, which has a density equivalent to water, and a camera to image the scintillator during irradiation. We found that the detector system is easy to handle compared to a scanning ionisation chamber which the setup and measurements are time consuming. In this chapter, we want to ensure that the PDD curves measured by the scintillator system match those measured in water and extend that investigation to electrons. Therefore, the performance of the whole BC-408 scintillation detector system will be compared against ionisation chambers, the most commonly used detectors in radiotherapy.

4.2 Materials and Methods

4.2.1 The detector system setup

An Elekta MLCi2 Linac (Elekta Oncology Systems, Crawley, UK) was used for this investigation which has an MLC with 40 leaf pairs as shown in Figure 50. This Linac at the National Physics Laboratory (NPL) can deliver photons and electrons. Discrete

energies in the range from 4 to 25 MeV of electron beams can be produced. The reference measurements were carried out with a PTW 31014 ionisation chamber (PTW, Freiburg, Germany) in water for photon beam. This chamber is a cylindrical air chamber and has a 2 mm diameter and is 5 mm long with a central steel electrode.

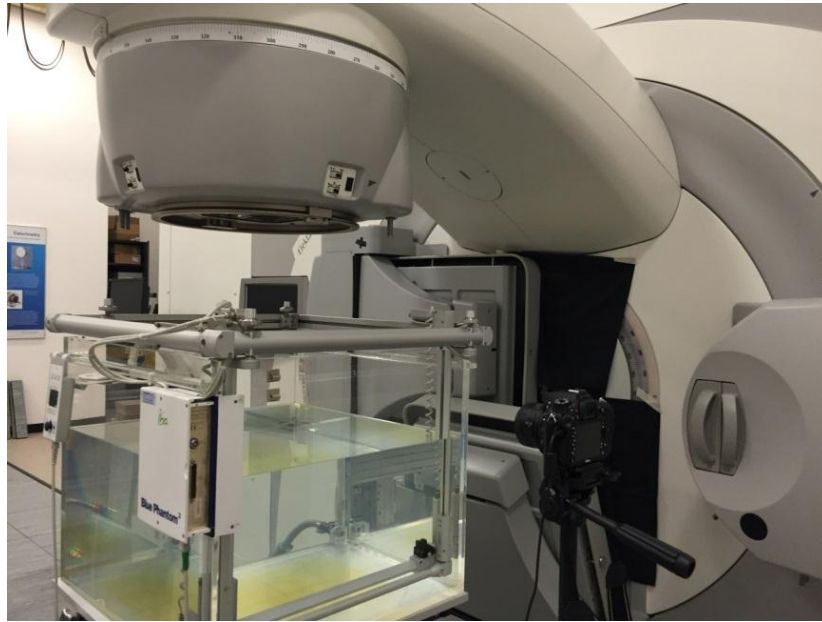


Figure 50: The Linac and the reference water tank used in this experiment

The impact of high energy radiation on the Nikon D7100 camera can either lead to the ionisation of the camera's readout circuitry, which adds noise to the signal, or damaging the readout circuitry which degrades the camera performance. To prevent high energy radiation beams from penetrating to the camera's active volume, the camera was kept a sufficient distance away from radiation beam. It is proven experimentally that the total doses drop rapidly below 0.1% of the dose at the isocentre at a distance of more than 40 cm from the central axis [54], [162], so the camera was positioned at the isocenter of the gantry at a distance of ~92 cm. The camera settings

were ISO100, f/8 and 1 s exposure time. The distance calibration was done as well the SSD adjusted to 90 cm for photons and 100 cm for electrons, as seen in Figure 52. The pixel size was 0.07 mm in the plane of the image at the beam axis

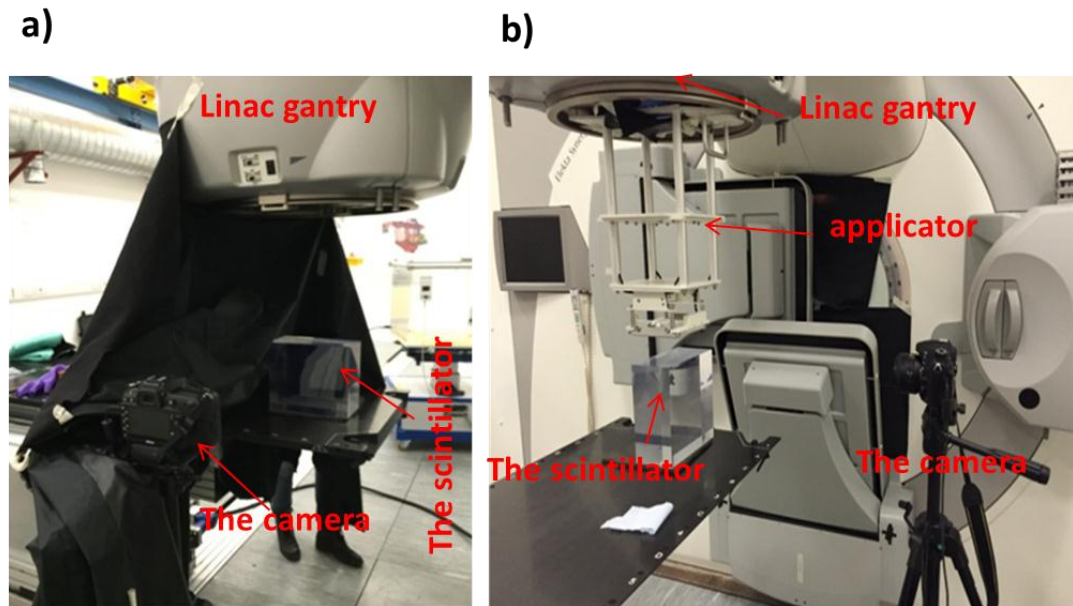


Figure 51: The scintillator setup in the case of a) photons and b) electrons

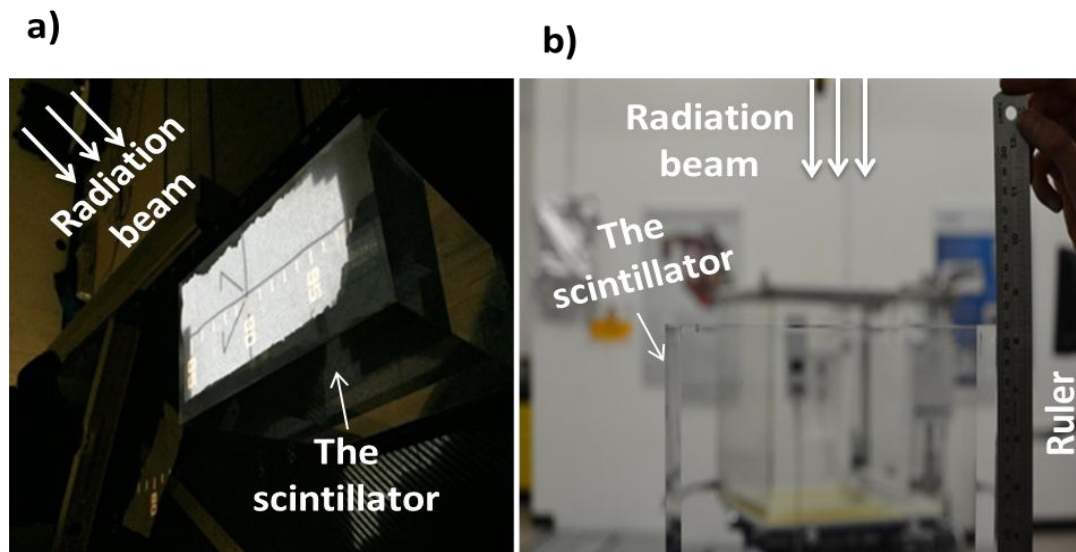


Figure 52: a) SDD adjustment b) pixel to distance calibration

4.2.2 Testing the water equivalency of BC-408 scintillator for photons and electrons

The penetration distance of photons is greater than that of charged particles since they penetrate through before interacting with the scintillator as they are electrically neutral. Photons may be scattered or absorbed. In the case of electrons, the mode of interactions with the atoms of the scintillator can be elastic or inelastic Coulomb force interactions with nuclei or the orbital electrons of the scintillator resulting in Bremsstrahlung, ionisation or excitation. Therefore, we want to find out for both photons and electrons whether the scintillator possesses similar interaction mechanisms to ideal water equivalent materials. An ideal dosimeter should have the same interaction properties as water. The Geant4 Monte Carlo simulation package was used to investigate the interaction of the passing of photon and electron beams through the water and the BC-408 plastic scintillator.

Geant4 simulations were performed in simulated homogeneous water and BC-408 scintillator to compare the PDD curves from photon and electron beams. Five million photons and electrons were utilised as a primary source entering a box phantom with dimensions of 20 cm x 20 cm x 10 cm. Electromagnetic interactions in Geant4 were simulated using a standard physics packages.

We evaluated the PDD curves for photon and electron beams using Geant4 simulation. Figure 53 shows that the build-up and d_{\max} regions in the PDD curves for 15 MV photons match for both materials with less than 0.8 % difference between the two curves.

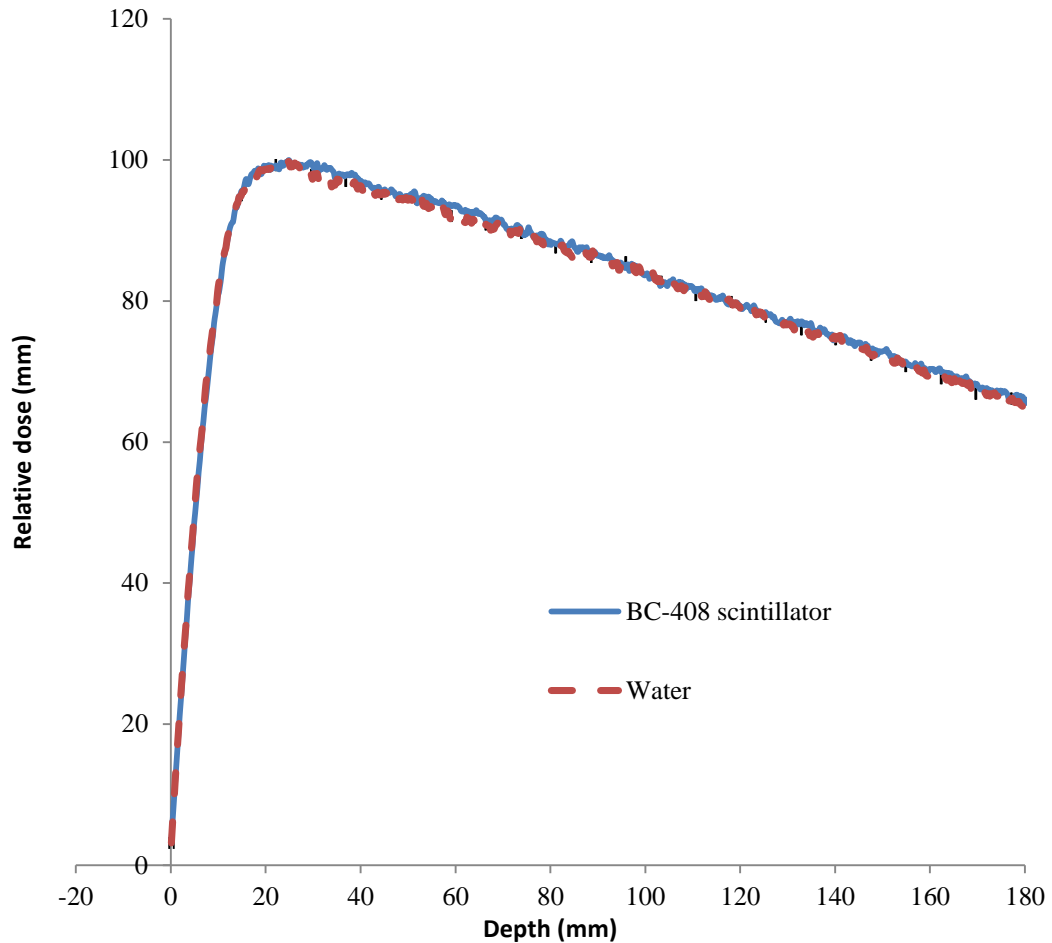


Figure 53: Comparison of simulated PDD curves obtained in water and BC-408 scintillator, for a 15 MV photon beam. Error bars demonstrate the statistical deviation of the simulation results and some of error bars appears smaller than the point size at certain points of the curve.

In addition, the comparison of the simulated PDD curves of electrons (Figure 54) obtained in the water and in the scintillator at different energies revealed that the uncertainty could be up to $\sim 7\%$ between the water and BC-408 scintillator when they were exposed to 15 MeV electron beams in Geant4. Comparisons of the PDD data of electrons have discrepancies with depth. The direct use of the detector system in electron therapy would introduce error in the measurements unless a correction is utilised.

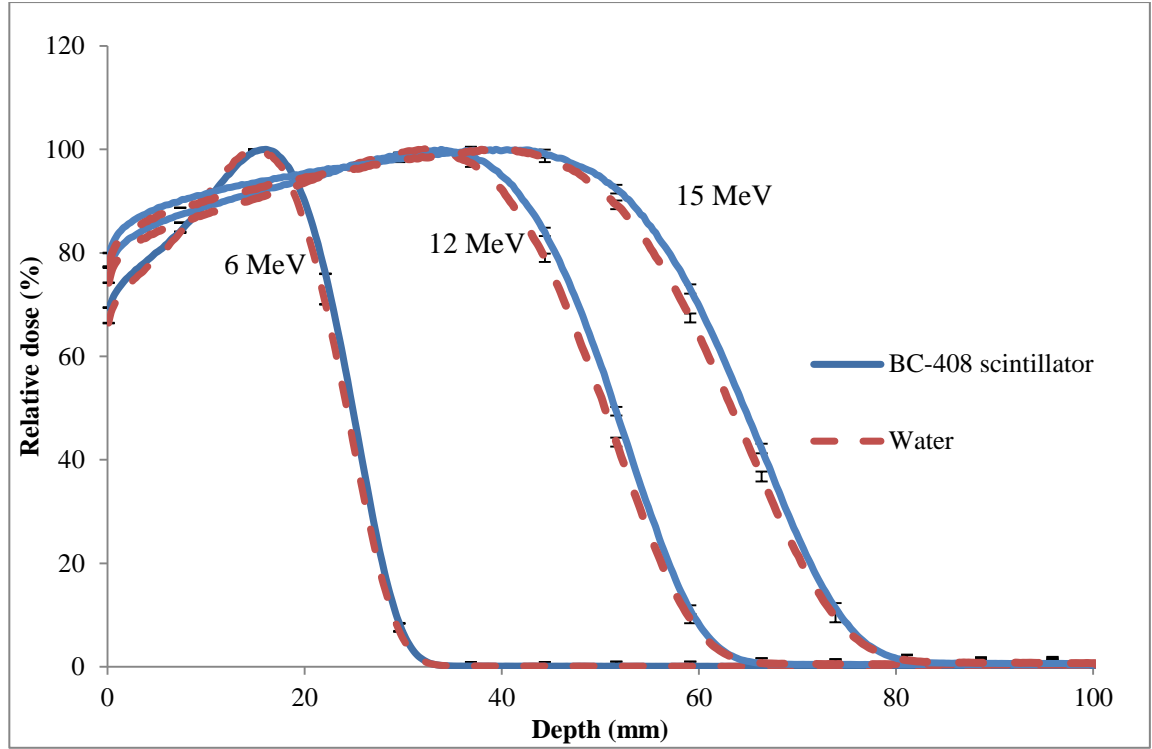


Figure 54: Comparison of PDD curves obtained in water and BC-408 scintillator for 6, 12 and 15 MeV electron beams with $10 \times 10 \text{ cm}^2$ field size. Error bars demonstrate the statistical deviation of the simulation results.

IAEA and AAPM recommended that the PDD distribution of an electron beam in a plastic phantom can be transformed to appropriate PDD distribution in water by the depth-scaling factor c_{scint} [163], [164]. For a measurement taken at a depth of x_{scint} (cm) in the scintillator, the equivalent depth in water x_w (cm) is given by

$$x_w = x_{scint} \times c_{scint} \tag{Eq 4.1}$$

where

$$c_{scint} = \frac{R_{50}^{water}}{R_{50}^{scint}} \tag{Eq 4.2}$$

c_{scint} is given by the ratio of the R_{50} (the depth of the 50% dose level) in water to that in the scintillator and it was found 0.980 ± 0.005 . The depths x_{scint} were converted to x_w and the corrected results are presented in Figure 55. As a result, we could compare our corrected measurement to the measurements obtained in water. Errors at R_{50} were reduced from 7% to 0.6%

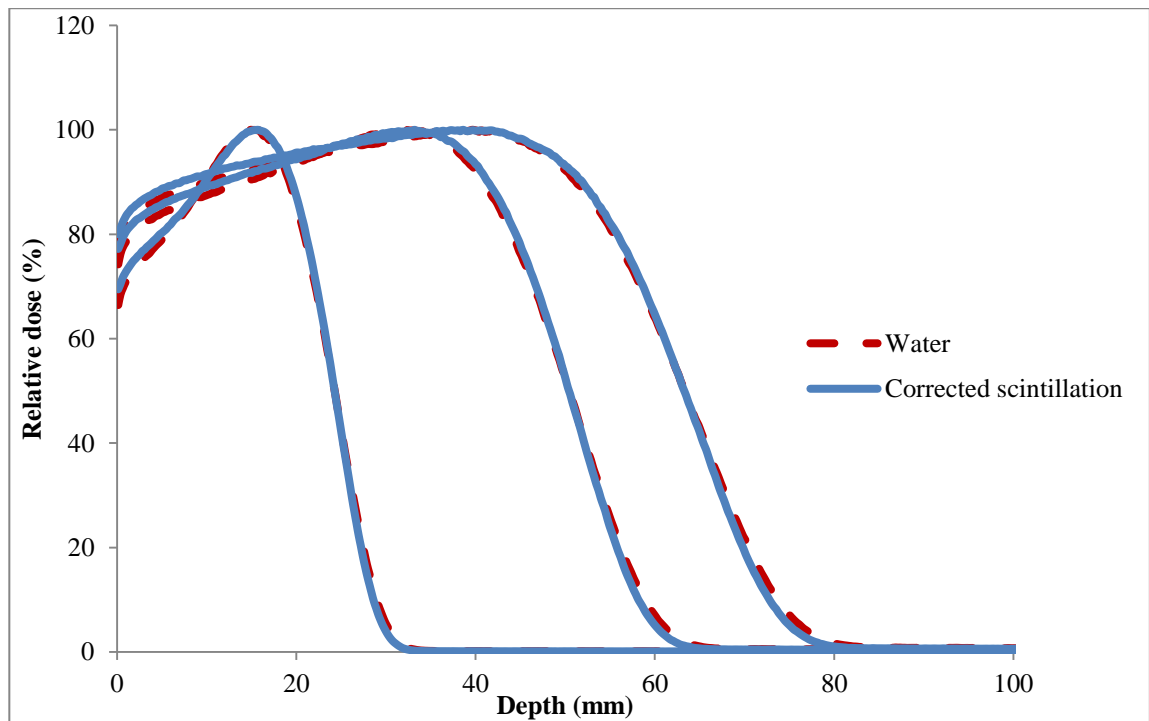


Figure 55: Comparison of PDD curves obtained in water and corrected scintillation obtained in BC-408 scintillator for 6, 12 and 15 MeV electron beam with $10 \times 10 \text{ cm}^2$ field size.

4.2.3 Measurement of short-term reproducibility and repeatability

This test was carried out to verify the short-term reproducibility of the output of the detector system by irradiating the scintillator four times using consecutive irradiations of photon beams with radiation fields $3 \times 3 \text{ cm}^2$ and $10 \times 10 \text{ cm}^2$. The irradiation energies were 6 MV and 15 MV with a dose rate equal to 620 monitor units per minute

(MU min⁻¹) at SSD equal to 100 cm. An MU is used to relate machine output with the absorbed dose.

In addition, four electron energies were used to investigate the reproducibility of the detector system for electrons with an applicator size of 10 × 10 cm² at a fixed SDD of 90±0.5 cm. The average intensity value of the generated scintillation light was obtained for four consecutive irradiations. The mean (of the average ROI pixel values) of the four consecutive readings was calculated to test for the reproducibility of the detector system results and to determine the percentage of pixel deviation from the mean value.

4.2.4 The central PDD curves for photons and electrons

Measurements were performed using the plastic scintillator-camera system to estimate the PDD with different energies and field sizes for photons and with different energies for electron beams in the scintillator and then to compare it to that in water.

We delivered a constant dose rate (620 MU/min) and an acquisition time of one second. The Linac was calibrated to deliver 1 Gy (corresponding to 100 MUs) at 95 cm SSD and at 5 cm depth in water. Two energies (6 MV and 15 MV) with different field sizes (3 × 3 cm² and 10 × 10 cm²) were used for photon beams at 95 cm SSD. Scintillation images for the field sizes used are shown in Figure 56.

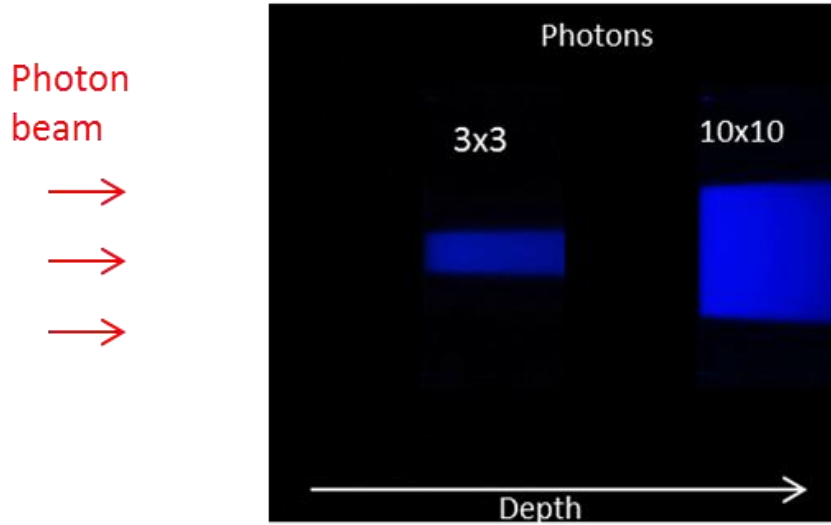


Figure 56: Demonstration of two scintillation images for 15 MV photon beam for two field sizes

According to the report of AAPM Task Group 53, different tolerances of deviations (δ) suggested for different regions in the photon PDD curve could be used to estimate the differences of normalised doses between the ionisation chamber (D_{ion}) (i.e. reference measurement) and scintillation system (D_{scint}) and can be calculated by Eq 4.3 and Eq 4.4 [165]:

$$\delta_1 = (D_{Ion} - D_{Scint}) \text{ (mm)} \quad \text{Eq 4.3}$$

$$\delta_2 = \frac{(D_{Ion} - D_{Scint})}{D_{Ion}} \times 100 \text{ (\%)} \quad \text{Eq 4.4}$$

where, δ_1 represents the deviation of the data points in the build-up region at 90% of surface dose expressed in mm as illustrated in Figure 57 and the proposed tolerance value δ_1 in homogeneous material is within 2 mm ideally. Whereas, δ_2 indicates the

local dose (D) data beyond the depth of dose maximum (d_{\max}) (e.g. at 70 mm depth). The ideal tolerance value δ_2 in homogeneous material is within 3% [166].

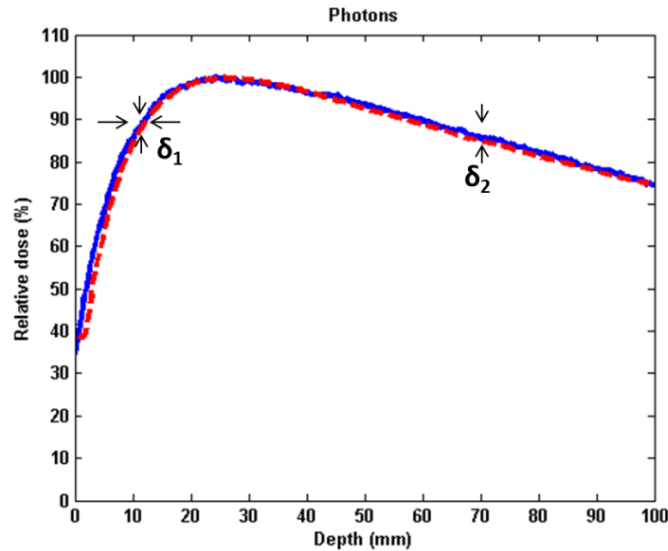


Figure 57: Regions of validity of the criteria, showing (1) the depth dose directly measured by the camera (solid blue line); and (2) the measured ionisation chamber depth dose (red dashes).

To characterise the PDD curves for electron beams obtained by the scintillator-detector system, Figure 58 shows a generic PDD with some parameters used to characterise the electron PDD curves as recommended by the ICRU (1984) [167]. These parameters should meet agreement within 3% dose or 3 mm distance [168]. These parameters are:

1. The relative surface dose (D_0) which is measured at 0.5 mm depth due to the difficulty of measuring accurate doses at an air detector interface.
2. The relative dose due to the Bremsstrahlung x-ray (D_x) which is obtained beyond the maximum range of the electrons.
3. The therapeutic range (R_t) defined as the depth which receives 90% of the dose (R_{90}).

4. The R_{50} , which is the depth of the 50% dose level.
5. The practical range (R_p) obtained by the plotting of a line tangent to R_{50} along the distal falloff of the PDD curve.

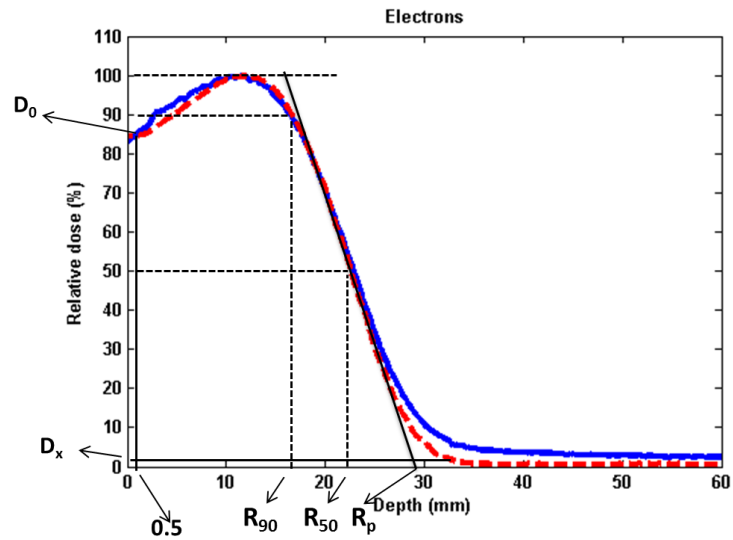


Figure 58: The characterisation of the PDD curve for an electron beam in ICRU (1984). The blue continuous line is measured from the camera-scintillator detector system and the dashed line is measured with an ionisation chamber in water.

For the above purpose, scintillation images (Figure 59) were acquired for four electron energies (6 MeV, 10 MeV, 12 MeV, and 15 MeV). The field size was $10 \times 10 \text{ cm}^2$, achieved by attaching the applicator in the Linac gantry at 100 cm SSD.

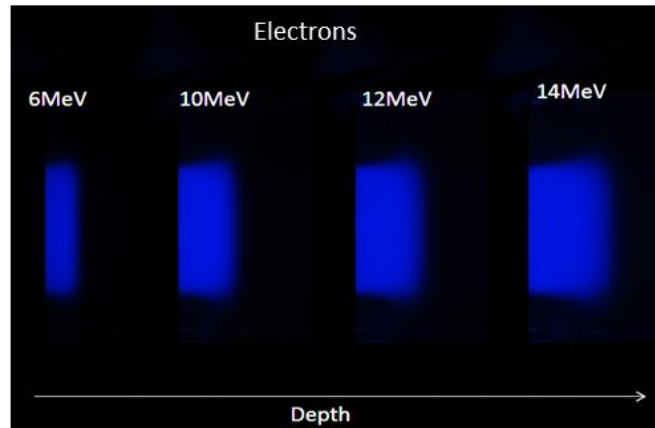


Figure 59: Scintillation images for four energies of an electron beam.

4.2.5 Off-axis dose profile

The images obtained to extract the PDD curves were also used to extract the cross profiles by extracting the dose profile perpendicular to the beam's central axis at a given depth. There will be a well-defined peak where maximum dose (d_{\max}) is deposited after which the dose decreases. The off-axis profiles could be measured at various depths such as d_{\max} and can be characterised as reported in the AAPM Task Group 53 and as shown in Figure 60.

δ_{11} : represents the difference in the data points in the build-up region and the tolerance value is ≤ 2 mm.

δ_{22} : shows the variation in the data points outside the central beam axis and the tolerance value is $\leq 3\%$.

δ_{33} : highlights the difference in the data point with low dose region (e.g. below 7%) and the tolerance value is $\leq 3\%$.

δ_{50-90} : for data point between 50% and 90% point and the tolerance value is 2 mm.

RW_{50} : the radiological width of a profile measured at 50% and the tolerance value is 2 mm.

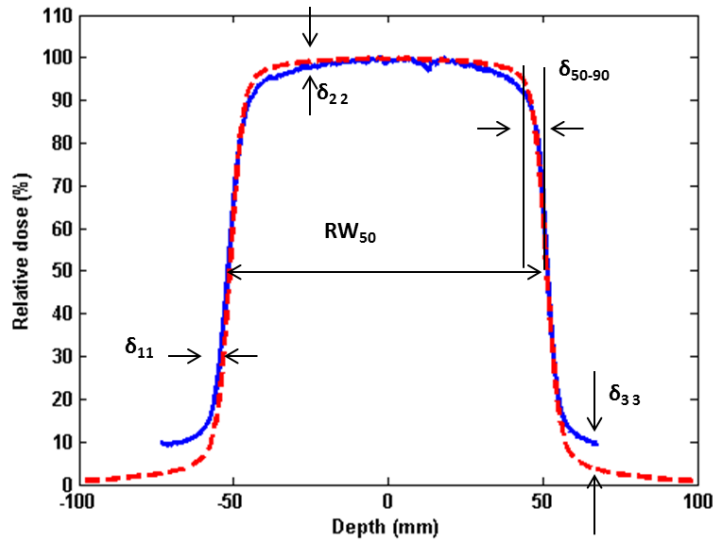


Figure 60: Profiles comparison, showing (1) the depth dose directly measured by the camera (solid blue line); and (2) the measured ionisation chamber depth dose (red dashes)

4.3 Results

4.3.1 Background signal contribution

By evaluating the background signal in Figure 61 and Figure 62, it is observed that the background signal taken when the beam was off has no obvious impact on the measurement, indicating that the camera was well shielded from ambient light. The mean background signals were 0.89 and 0.76 for photon and electron respectively. Unfortunately, stray radiation (i.e. unwanted radiation hitting the camera when the

beam is on) can be observed as spikes in Figure 61. However, the existence of spikes or active pixels in the PDD curve of the electron beam was much less than that in the photons' PDD curve and it may be due to reduced scattering and higher counts of electrons (Figure 62). The scintillation depth distributions were improved by applying a median filter and subtracting the background.

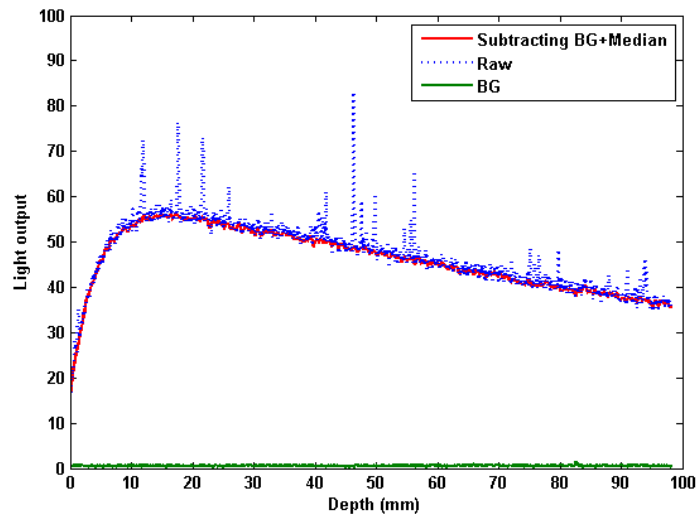


Figure 61: Comparison of the raw image and analysed image for photon beam and effect of background signal in the analysed image compared to the raw image.

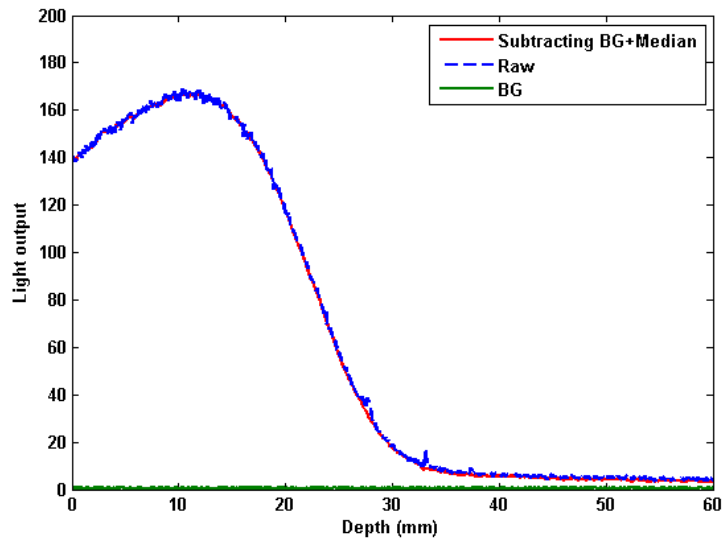


Figure 62: Comparison of the raw image and analysed image for electron beam and effect of background signal in the analysed image compared to the raw image.

4.3.2 Short-term reproducibility and repeatability

The reproducibility was calculated using the experimental average of four repeated measurements with the associated standard deviation. The reproducibility of the measurements indicates an excellent performance with a maximum standard deviation of 0.8 %.

4.3.3 The central PDD curves for photons and electrons

This test investigates the detector system's ability to provide reliable dosimetric data. The deviations (δ) suggested for different regions in the photon PDD curve were estimated for the differences of depth doses between the ionisation chamber and scintillation system and can be calculated by Eq 4.3 and Eq 4.4. Figure 63 shows a comparison between the scintillation and ionisation chamber measurements. The

detector system was used to image scintillation light from 6 MV and 15 MV photon beams. The agreement between the two detectors shown in Figure 63 and Table 12 was acceptable for all field sizes, being <1 mm in the build-up region for δ_1 and generally ~2% in the high dose gradient regions for δ_2 .

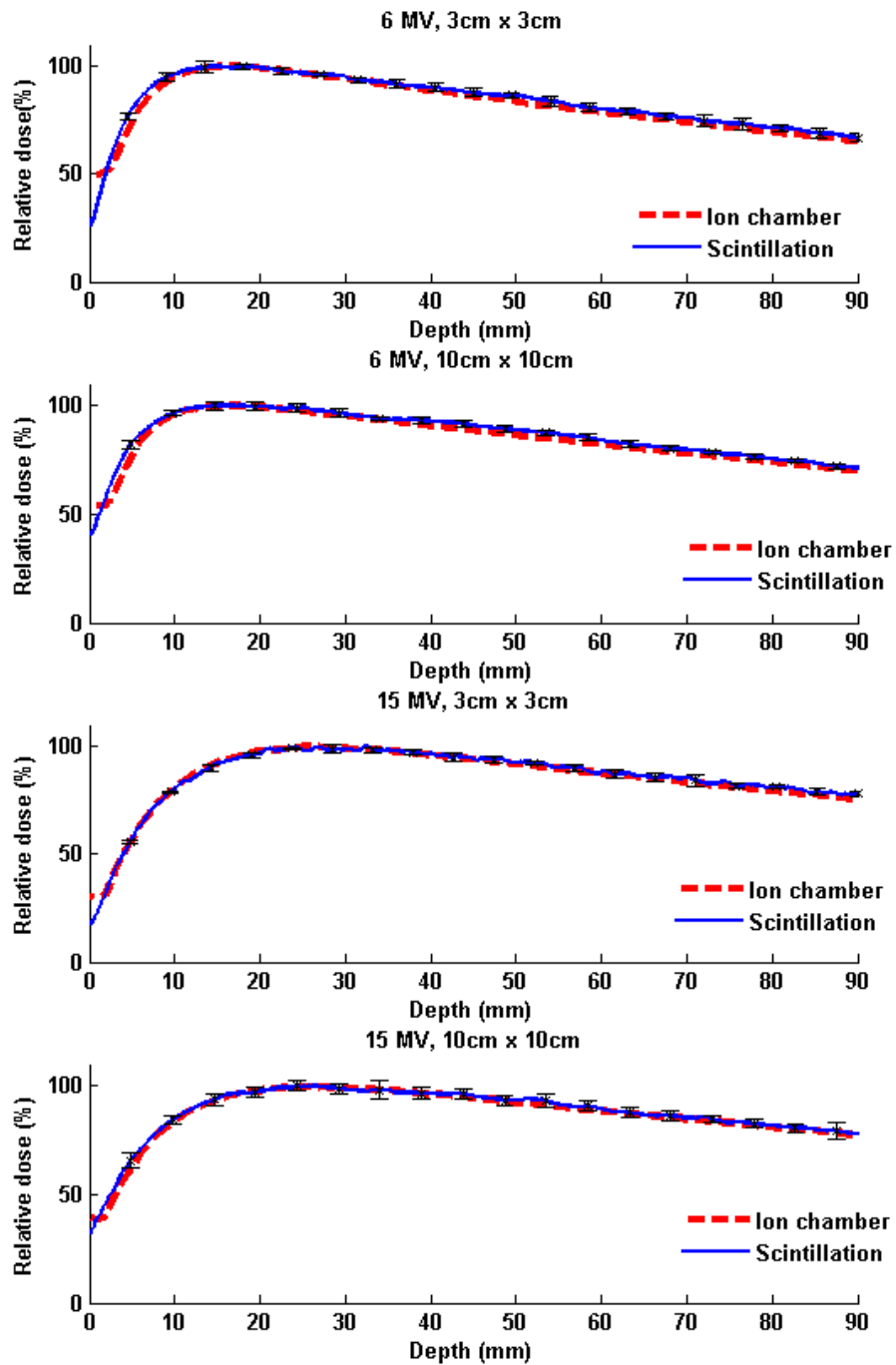


Figure 63: Comparison between the PDD values, of a 10×10 cm² field, obtained by: the scintillation detector system (continuous line) and the ionisation chamber as a function of the depth in water (dashed line) for the 6 MV and 15 MV photon beams. Error bars demonstrate the standard deviation of three repeated scintillation measurements of photon beams and some of error bars appears smaller than the point size at certain points on the curves.

Table 12: The difference values between the ionisation chamber and the scintillation detector system, obtained at 90% and at 70 mm.

| <i>Energy (MV)</i> | <i>δ_1 (mm)</i> | <i>δ_2 (%)</i> |
|------------------------|-----------------------------------|----------------------------------|
| 6 MV (3 X 3) | 0.74±0.11 | 2.01±0.07 |
| 6 MV (10 X 10) | 0.78±0.21 | 1.66±0.12 |
| 15 MV (3 X 3) | 0.65±0.13 | 1.09±0.09 |
| 15 MV (10 X 10) | 0.08±0.14 | 0.54±0.03 |

The dosimetric parameters were used to characterise the electron PDD curves as recommended by the ICRU. The PDD data of four electron beams (6, 10, 12 and 15 MeV) was extracted from the central axis of the scintillation images (Figure 64) and compared to PDDs data measured with an ionisation chamber in water. The differences in different regions of the curve between the ionisation chamber and scintillation detector system were obtained as listed in Table 13. The scintillation detector showed to provide accurate ranges for R_{90} , R_{50} and R_p within ± 0.83 mm. Due to low-intensity tail artefact, the detector system did not provide accurate results in the low dose region D_x .

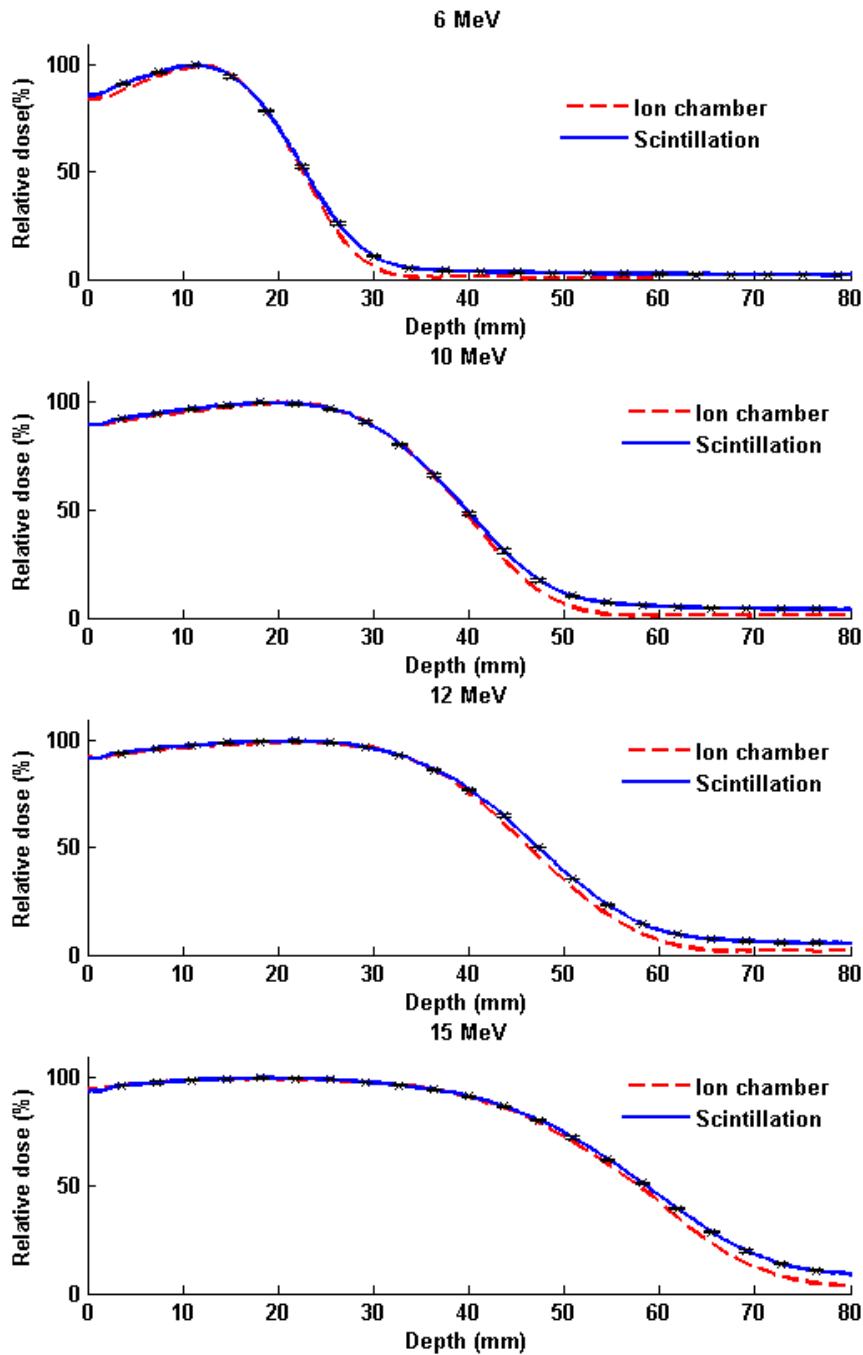


Figure 64: Comparison of depth dose profile between ionisation chamber measurement and scintillation measurements, for a 6, 10, 12 and 15 MeV electron beams. Error bars demonstrate the standard deviation of three repeated scintillation measurements of electron beams and some of error bars appears smaller than the point size at certain points along the curves.

Table 13: The electron beam characteristics for the ionisation chamber and the scintillation detector system

| <i>Energy (MeV)</i> | Variations in | | | | |
|---------------------|----------------------------|----------------------------|---------------------------|--------------------------|--------------------------|
| | <i>R₉₀ (mm)</i> | <i>R₅₀ (mm)</i> | <i>R_p (mm)</i> | <i>D₀ (%)</i> | <i>D_x (%)</i> |
| 6 | 0.09±0.01 | 0.12±0.03 | 0.30±0.05 | 0.66±0.08 | 2.94±0.14 |
| 10 | 0.51±0.02 | 0.21±0.06 | 0.70±0.08 | 0.49±0.02 | 3.88±0.08 |
| 12 | 0.35±0.03 | 0.72±0.02 | 0.80±0.07 | 0.56±0.04 | 4.33±0.10 |
| 15 | 0.15±0.02 | 0.55±0.03 | 0.83±0.18 | 1.41±0.03 | 5.45±0.07 |

4.3.4 Off-axis dose profile

To more quantitatively compare distributions, the off-axis profiles of photon beams with $3 \times 3 \text{ cm}^2$ and $10 \times 10 \text{ cm}^2$ field sizes were measured in the scintillation images and compared to the ionisation chamber measurements at d_{max} as shown in Figure 65. All data was normalised to their maximum value. The error along the off-axis of photon beams decreases with increasing field size. In addition, the profiles of 6, 10, 12, and 15 MeV electron beams at a $10 \times 10 \text{ cm}^2$ field size measured with the scintillation detector system, and in water with the ionisation chamber, are presented in Figure 66. The scintillation and ionisation chamber measurements are compared in Table 14 for photons and in Table 15 for electrons. The off-axis profiles of a $10 \times 10 \text{ cm}^2$ beam could be characterised as reported in the AAPM to find the variations in different regions of the profiles such that δ_{11} at 30%, δ_{22} at $\pm 20 \text{ mm}$, and δ_{33} at $\pm 65 \text{ mm}$.

In general, the profiles show good agreement within $\sim 1 \%$ in the δ_{22} region of the profile and up to 1.63 mm in the δ_{50-90} region of the profile. For photons, acceptable

agreement was obtained in δ_{11} region within 1.62 mm except for 15 MV, where it was noticed that the magnitude of the unwanted light signal was generated with increasing energy and field size.

For electrons, excellent agreement within 0.16 mm was observed. However, the profile measurements measured by ionisation chamber have a sharper fall off than the scintillation detector system measurements for both types of radiation used, resulting in discrepancies in δ_{33} up to 15.60% for photons and up to 4.81% for electrons in a very low-dose region (*i.e.* penumbra).

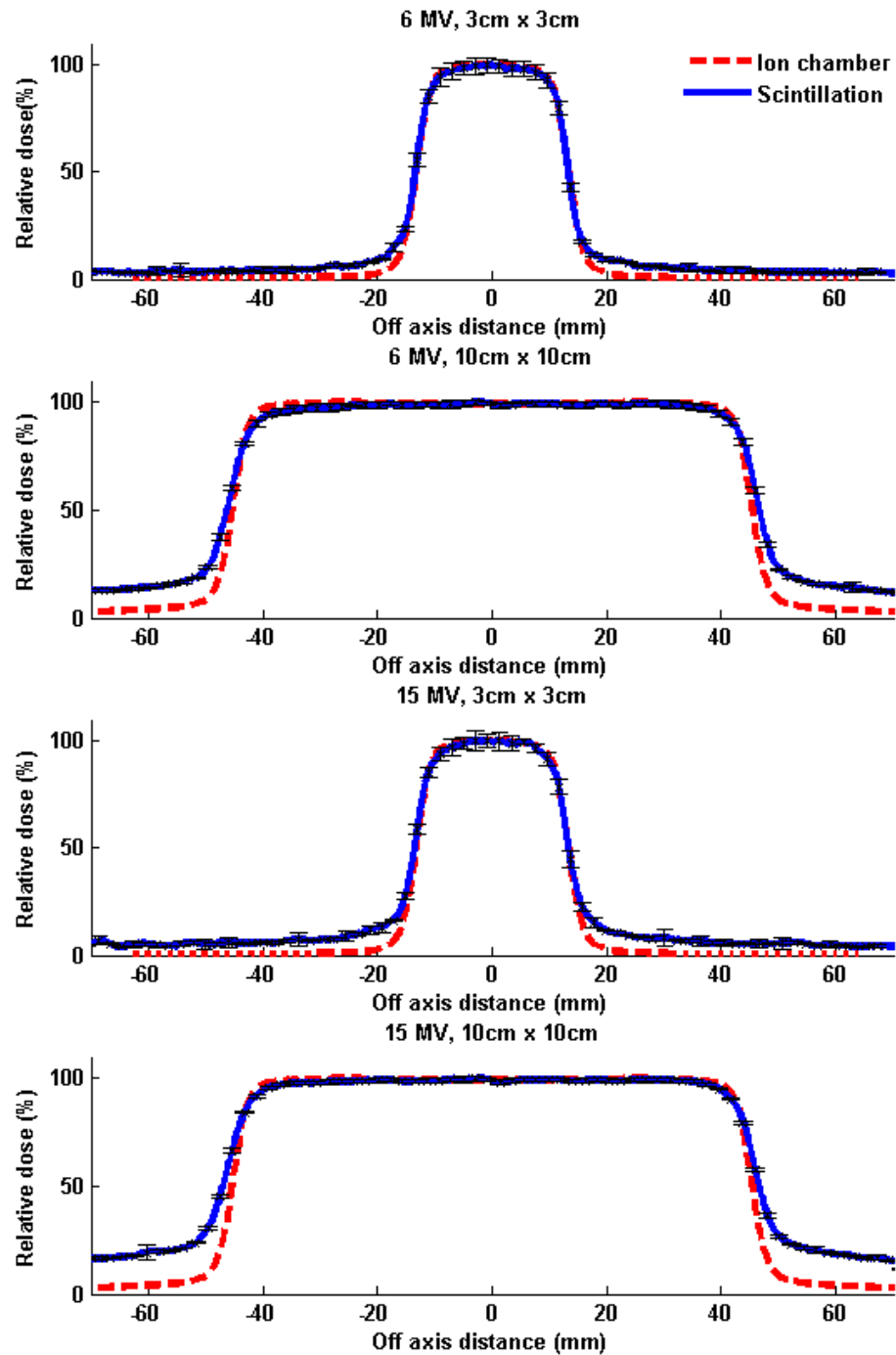


Figure 65: Comparison of normalised cross profiles obtained by the scintillator detector and the ionisation chamber for $3 \times 3 \text{ cm}^2$ and $10 \times 10 \text{ cm}^2$ and 6 MV and 15 MV photon beam at 5 cm depth. Error bars demonstrate the standard deviation of three repeated scintillation measurements of photon beams and some error bars appear smaller than the point sizes at certain points on the curves.

Table 14: The difference values between the cross beam profiles obtained by ionisation chamber and profile obtained by the scintillation detector system, for different photon beam energies and field sizes

| <i>Energy (MV)</i> | δ_{11} (mm) | δ_{22} (%) | δ_{33} (%) | RW_{50} (mm) | δ_{50-90} (mm) |
|-----------------------------------|--------------------|-------------------|-------------------|----------------|-----------------------|
| 6 (3 X 3 cm²) | 0.15±0.05 | 0.58±0.01 | 6.11±0.03 | 0.28±0.12 | 0.51±0.04 |
| 6 (10 X 10cm²) | 1.62±0.09 | 0.72±0.02 | 11.25±0.15 | 1.69±0.06 | 0.75±0.15 |
| 15 (3 X 3 cm²) | 0.50±0.04 | 0.37±0.05 | 8.86±0.08 | 0.04±0.01 | 1.05±0.07 |
| 15 (10 X 10cm²) | 2.45±0.11 | 0.45±0.07 | 15.60±0.12 | 2.06±0.05 | 1.61±0.12 |

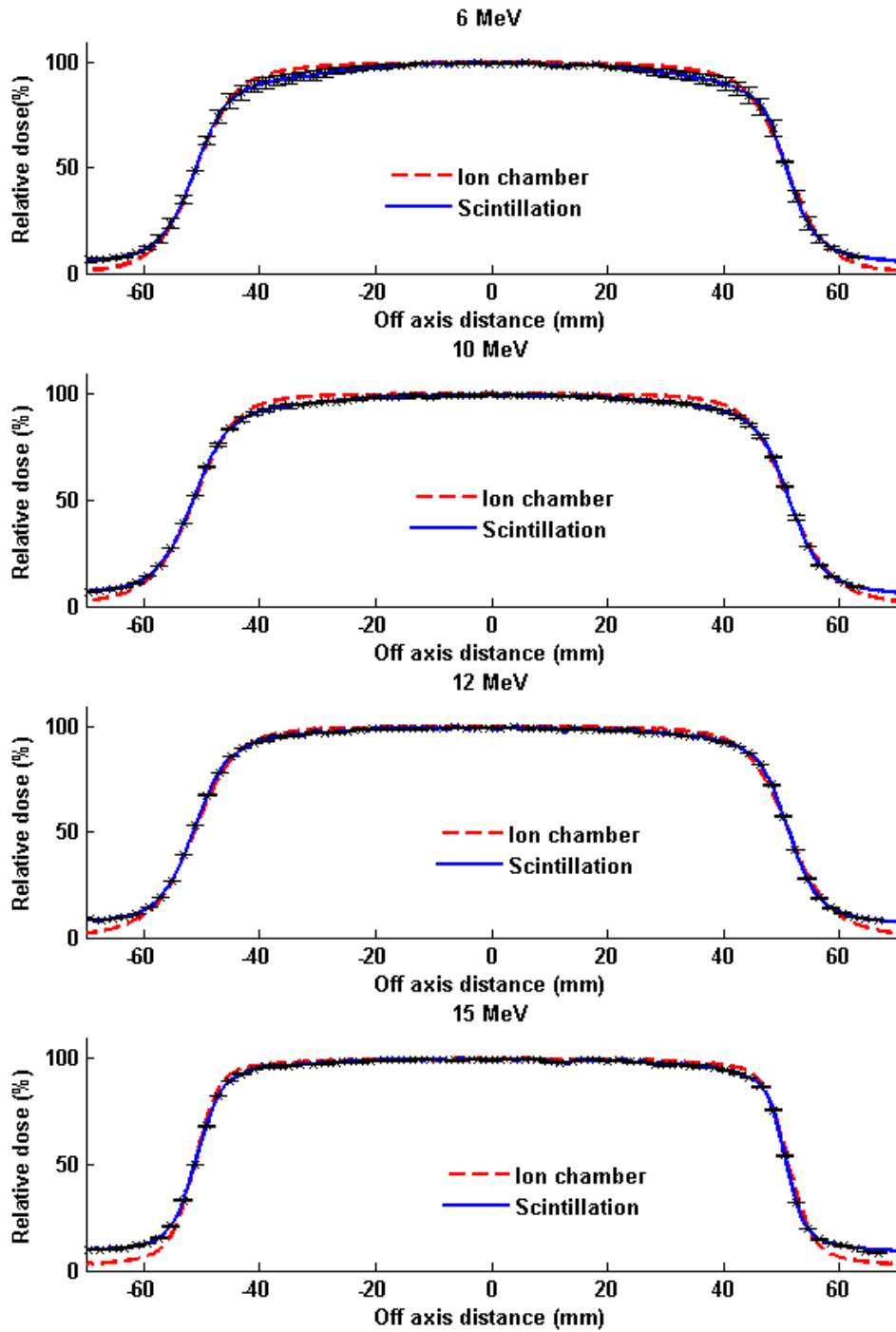


Figure 66: Comparison of normalised cross-beam profile at depth of maximum dose between ionisation chamber measurements and scintillation measurements, for a 6, 10, 12 and 15 MeV electron beams. The field size was $10 \times 10 \text{ cm}^2$. Error bars demonstrate the standard deviation of three repeated scintillation measurements of electron beams and some error bars appear smaller than the point size at certain points along the curves.

Table 15: The difference values between the cross beam profiles obtained by ionisation chamber and profiles obtained by the scintillation detector system, for different electron beam energies

| <i>Energy (MeV)</i> | δ_{11} (mm) | δ_{22} (%) | δ_{33} (%) | RW_{50} (mm) | δ_{50-90} (mm) |
|---------------------|--------------------|-------------------|-------------------|----------------|-----------------------|
| 6 | 0.13±0.03 | 1.15±0.02 | 1.33±0.11 | 0.24±0.06 | 1.63±0.03 |
| 10 | 0.11±0.02 | 1.12±0.06 | 3.08±0.03 | 0.40±0.01 | 1.17±0.02 |
| 12 | 0.01±0.01 | 0.97±0.02 | 3.79±0.02 | 0.46±0.04 | 0.39±0.02 |
| 15 | 0.16±0.02 | 0.31±0.03 | 4.81±0.04 | 0.19±0.01 | 0.55±0.04 |

4.4 Discussion

4.4.1 Measurements observation

From the results above, it could be seen that there are good agreements between the scintillation and the ionisation chamber PDD curves for both photon and electron beams. Some properties required to meet by the detector system are presented in Table 16.

Table 16: The requirements of the performance of a clinical QA system

| <i>Requirement</i> | <i>Results</i> |
|--|--|
| 1) Stable | Found to be stable $\pm 0.8\%$ below the tolerance value 2% in homogeneous radiation field [169] |
| 2) Time for setup and breakdown | Took 18 mins for the system (<i>c.f.</i> 30 min for ionisation chamber [43]) |
| 3) Ease and read out convenience | Single image to analyse the PDD and profile |
| 4) Tissue equivalent at this energy | Could be considered as tissue equivalent for photons but needs correction for electrons |
| 5) Clinic environment suitability | Revealed to be non-toxic and safe for clinical use |
| 6) Energy independent | Found to be independent of the photon and electron energy |

The agreement between the PDD curves measured with the scintillation system and an ionisation chamber are below the tolerance values suggested above. The uncertainty in the photon PDD curves is less than $\sim 2\%$ for locations deeper than 70 mm and less than ~ 1 mm in the dose build-up region.

We compared the response of the scintillator against an ionisation chamber in water for electron beams using Geant4. The simulated PDD curves revealed 7% difference between the two materials and this difference was reduced when corrected, to 0.6% using equations provided by the IAEA. Different points in the measured PDD curves of electron beams were characterised, and it was found that the scintillation data adequately matches the ionisation chamber data below the tolerance values for electrons. However, high deviations were noticed in Figure 64 at the D_x region with a maximum variation of $\sim 5.5\%$ which will be discussed in 4.4.2.

The comparison of the off-axis scintillation profiles of photons and electrons to profiles measured with an ionisation chamber in Figure 65 and Figure 66, showed good agreement in δ_{11} and δ_{22} regions between the detectors as well as an acceptable RW_{50} within 2 mm. This agreement fails at the very low-dose region δ_{33} as the scintillation results in the penumbra in the lateral direction are not reliable compared to the ionisation chamber results. The average deviation in the penumbra region (δ_{33}) is equal to 10.5% between the photon profiles, as shown in Figure 65 and is equal to 3.3% between the electron profiles, as shown in Figure 66.

4.4.2 Source of errors

The errors in the PDD curves and in the off axis profiles at the beam low-dose region of the captured images exceed recommended tolerances. This may be due to an optical blurring that leads to a low intensity tail of the measured scintillation as shown in Figure 67, analysed by ImageJ (National Institutes of Health, USA) and to a

slight reduction in the flatness of the scintillation profiles compared to the ionisation chamber profiles.

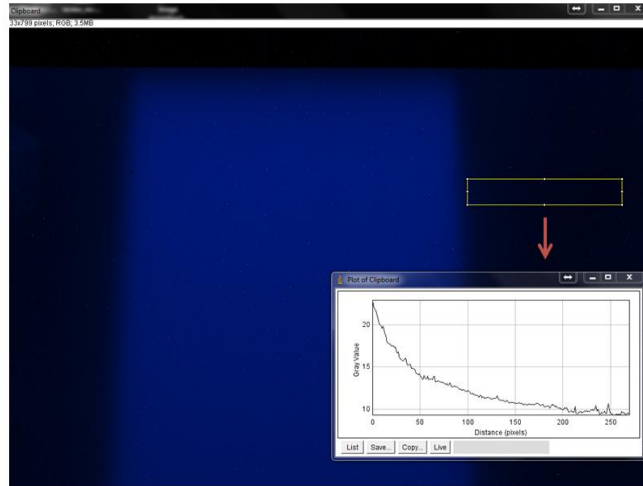


Figure 67: Scintillation image obtained in the scintillator for 6 MV photon beams and the glow in the area surrounding the edges of the radiation showing light (or dose) not being detected by the ionisation chamber Scintillation light images.

This optical artefact was attributed in the literature to various causes such as light Cerenkov emission, additional scattering because of absorption and re-emission, or propagating of generated scintillation light through the detector system [45], [81], [83]. A fitting which is not derived from any measurement was generally used to correct for this artefact as shown in Figure 68. Cerenkov emission as a source of optical blurring can be rejected due to our findings in chapter 2. We found that the noise or scattering pattern in the low-intensity tail is energy and field size dependent.

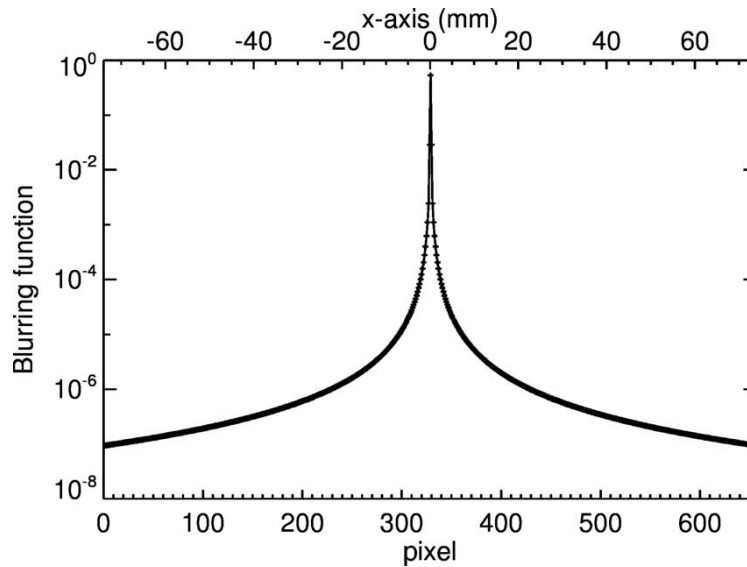


Figure 68: 1D plot of the blurring function of the CCD chip [83]

Alternatively, the accuracy of the result can be corrected by using the data acquired from another dosimeter such as a film. This was done to eliminate any optical artefacts in the scintillation detector system. The correction is derived from a calibration procedure by comparing the scintillation light distribution, acquired by the camera, and the corresponding dose distribution, obtained by a dosimetric film positioned above the scintillator [155], [159].

Overall, it has been shown that the detector system reproduced series of irradiations with high precision of less than 1% error. The source of this blurring is still unclear. Therefore, the accuracy of the results could be enhanced if the blurring artefact within the scintillator is tackled.

4.5 Conclusion

The use of the detector systems in radiotherapy is generally restricted matching measurements obtained by the system to those in water on the central beam axis PDD and off-axis profile. In this study, we examined a scintillation detector system for dosimetric measurement in modern radiotherapy. We evaluated the scintillation detector system for regular radiation fields with various incident energies using photon and electron beams. We analysed the PDD distributions for photon and electron beams which were extracted from images and were then compared to those measured by an ionisation chamber along with the off-axis dose profiles. The AAPM suggested a method with a set of tolerances to characterise the beam output on the PDD extracted from beam axis alongside the profile extracted from the off-axis measurements for high-energy photon beams. In addition, ICRU recommended a method to extract the beam parameters from the PDD curve of an electron beam which the comparison between the measured and the anticipated outcomes should meet agreement within 3% dose or 3 mm distance. The detector system has been demonstrated to be a potential method for measuring the PDD of the beam within clinically accepted tolerances which could be used as a QA tool, for instance, in daily and periodically tests of PDD curves in radiotherapy. The overall results of off-axis profile measurements which were performed in many data points showed satisfactory agreement. However, a single region in the off-axis profile exceeded the tolerances values in which a difference was noticed with average equal to 10.5% in photon beams and within 3.3% in electron beams between the measured scintillation and the ionisation chamber measurements

because of scattering adding background light noise at low dose region. Therefore, it may be needed to combine data from other dosimeters or a correction factor derived from measurements to correct for the background light noise in low dose regions. To conclude, the system was fast because a single image could be used to manipulate the data for PDD curves and profile measurements not taken in low dose regions.

CHAPTER 5

5. SCINTILLATION DETECTOR SYSTEM FOR PROTON THERAPY

5.1 Introduction

Proton beam therapy has become widely available and studied in recent years due to its high precision dose localisation performance achieved by the Bragg peak effect, in which protons deposit most of their energy at the end of their paths. With the high demand of proton therapy worldwide, most of the detectors available are currently being re-evaluated for use in proton beam dosimetry. Extensive research is ongoing in the proton therapy field which may lead to more complex delivery techniques requiring accurate dosimeters. For spot scanning beam proton therapy, a pristine Bragg peak (PBP) has initially a narrow beam, but the beam may be spread over a larger area to effectively treat a large tumours if the delivery technique is passive scattering beams [14]. With the proton radiotherapy field rapidly growing, there is a need for fast and accurate dosimetry tools. Scintillators' properties appear to make them viable for use in proton quality assurance. However, no internationally accepted standards are available for dosimetry of proton beams. Many dosimeters have been reported for the use of clinical proton dosimetry such as ionisation chambers. However, the 2D array of ionisation chambers is not widely used although they provide fast measurements because a high spatial resolution is required to measure the sharp fall of depth dose and range, the protons spot's shape, profile of an narrow proton beam. Alternatively, films could be used to measure off-axis profiles [16], [17]. Recently, large 3D volume liquid scintillator detectors were used to verify the protons' range and position for scanned proton beams and showed to provide precise results within 0.7% and accurate proton range to within 0.3 mm on average [42], [81]. Several attractive features of large

scintillators enable them to be good candidates for dosimetric measurements of proton beam such as high resolution [83].

We proposed a camera and large plastic scintillator detector system for dose distribution verification to measure passive scattering proton beams. Prior to any attempts to measure doses from a proton beam, several basic features of the scintillation-detector system were evaluated by studying the relation of the light output response of a plastic scintillator during proton beam irradiation with different dosimetry parameters such as the dose rate, and the thickness of Perspex in the beam which is equivalent to changing the energy. In this chapter, we investigate the system's response to changes in energy and dose rate, and compare the depth-dose measured with the scintillation detector to that measured with an ionisation chamber.

5.2 Materials and methods

5.2.1 Proton therapy cyclotron

This work has been carried out on the only clinical beam available in the UK - an ocular treatment beam which has been in service since 1989. Proton irradiations were performed using the Douglas cyclotron at the Clatterbridge Cancer Centre. The proton facility uses passive scattering beams to provide single Bragg Peak and SOBPs. The cyclotron produces a 62 MeV proton beam delivered by a fixed horizontal gantry. However, the proton energy is 60.0 MeV at the treatment isocentre 7 cm from the collimator nozzle. A range modulator consisting of stepped thicknesses of PMMA (in 0.84 mm steps) is usually placed in the beam to provide a SOBPs when treating patients

with eye tumours [9].

5.2.2 Detector system set up

A schematic overview of the prototype scintillator detector system used previously is shown in figure 69. The scintillator was exposed to the proton beam, and the camera was used to image the emitted light. The front surface of the scintillator was positioned 7 cm away from the proton nozzle. Images were taken with a 25 mm collimator, at a constant dose rate of 20 MU/min unless stated otherwise. The camera exposure settings were selected by setting the aperture ($f/22$) such that the dynamic range of the camera was filled without reaching saturation at the highest light and the depth of field covered the field size of the proton beam; and setting the exposure time so that the shutter was closed once a particular dose had been delivered.

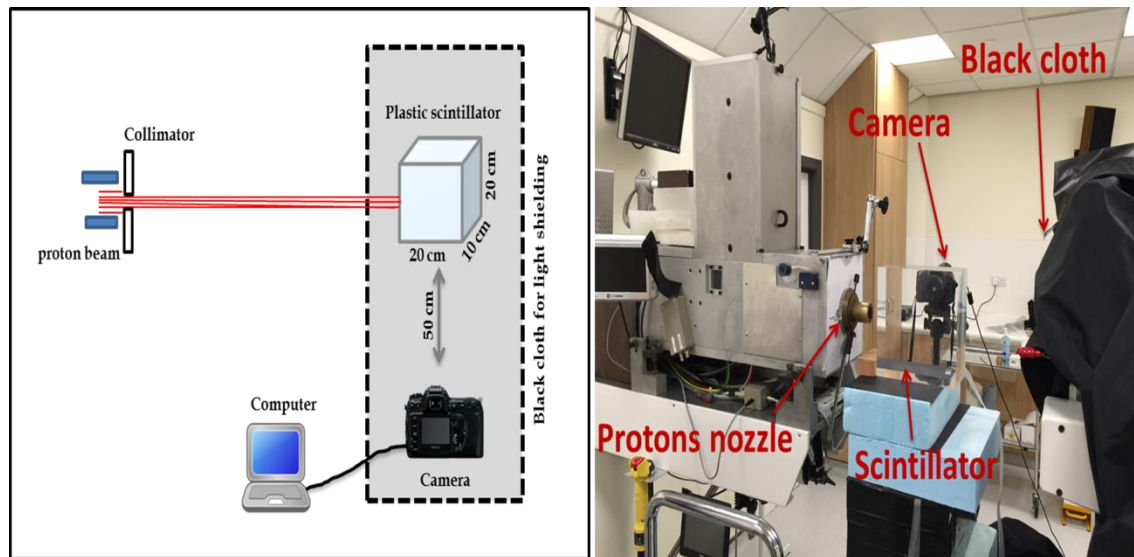


Figure 69: The experimental setup. The camera was positioned at 50 ± 0.5 cm perpendicular to the proton beam.

5.2.3 Dark image measurements

Unwanted signals can reduce the accuracy of the measurements and so should be removed from the raw data where possible. First the level of the dark signal due to electronic interference from the cyclotron and delivery system was determined by acquiring a photograph with the beam on, but in the absence of the scintillator. Secondly, a scattering material (paraffin wax of a similar size to the scintillator, wrapped in black cloth to exclude direct optical light) was placed in the beam to determine the effect of scattered emissions on the detected signal. Background images were then subtracted where appropriate.

5.2.4 Detector system characterisation

5.2.4.1 Bragg peak measurement

The scintillation light output distributions were measured using the Nikon D7100 camera. Two modes were used to acquire the images: the scintillator was irradiated with a PBP beam and with the SOPB beams achieved by placing a modulator (Figure 70) in the beamline. 5 MU was delivered at a nominal dose rate of 20 MU/min. The shutter of the camera was opened manually and closed once 5 MU had been delivered.

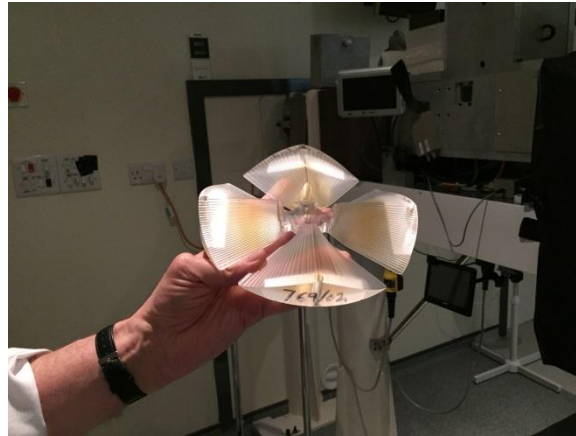


Figure 70: The SOBP modulator wheel

5.2.4.2 Short-term reproducibility and stability

The reproducibility of the system was tested by irradiating the scintillator seven times under identical irradiation parameters (4.5 Gy at 18 Gy/min).

5.2.4.3 Dose linearity

To assess the linearity of the dose response, the scintillation light output distributions were imaged at a range of doses between 0.45 and 10.5 Gy during irradiation of PBP and SOBP.

5.2.4.4 Dose rate proportionality

The output should be independent of dose rate in a clinical detector system. The dose rate proportionality of the detector was therefore investigated at different dose rate settings. In order to test this, images were acquired using five dose rates to deliver 4.5 Gy at dose rates from 4.5 to 36 Gy/min.

5.2.4.5 Energy dependency

In order to study the scintillator response to proton beam energy, different thicknesses of PMMA, which reduces energy of a proton beam, were placed in the path of the 60 MeV proton beam, and the generated scintillation light imaged. Ionisation energy loss software was used to calculate the energy loss in the PMMA for each thickness to estimate the proton energy [170]. The scintillation light depth profile was measured as a function of the proton energy. The pixel intensities were summed and then plotted against beam energy. At beam energies greater than the 4 MeV used in this study, the relation is expected to be linear. Below this energy, the relationship is non-linear due to the quenching effect, as described in 1.5.3 [3].

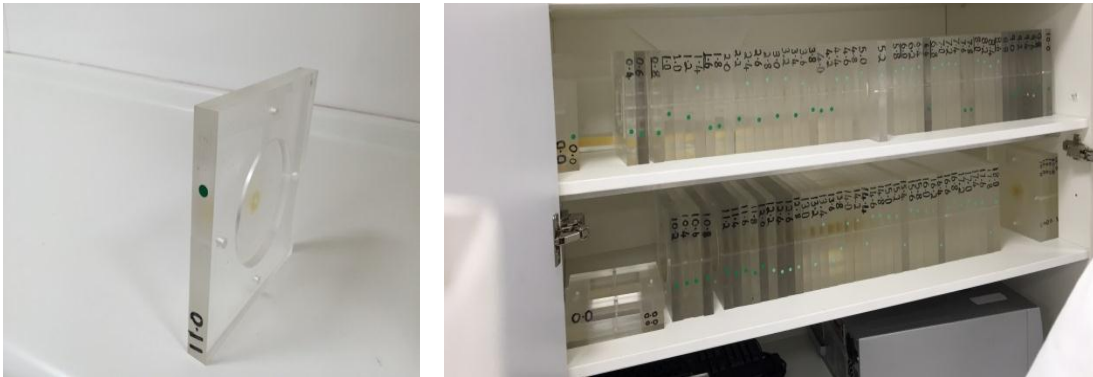


Figure 71: The PMMA sheets placed in the way of the proton beam to obtain different energies

5.2.5 **Validation**

The scintillation light imaged using the camera was compared to measurements taken with an ionisation chamber calibrated for use with this beam. The depth-dose curve was measured along the central axis in the plastic scintillator with a 2.5 cm

diameter beam at an SSD of 7 cm, and compared to a depth-dose curve measured with a parallel-plate ionisation chamber (PTW, Freiburg, Germany) using the same proton beam at 60 MeV. Two modes were used to acquire the images: the first was a 60 MeV PBB; the second was a SOPB achieved by placing a modulator in the beamline. For the PBB mode, 1 MU corresponds to 0.9 Gy at the Bragg peak whereas 1 MU corresponds to 0.7 Gy for the SOPB mode.

5.3 Results

5.3.1 Background images

The mean image intensity (Figure 72) with the beam on but without a scatterer present was 2.3 times that with the beam off. When the wrapped scatterer was present, the background was 2.7 times that with the beam off. However, the total background count was still small compared to the signal, and Figure 73 shows there is no substantial background impact on the measured signal, nevertheless, we still correct for background in our data.

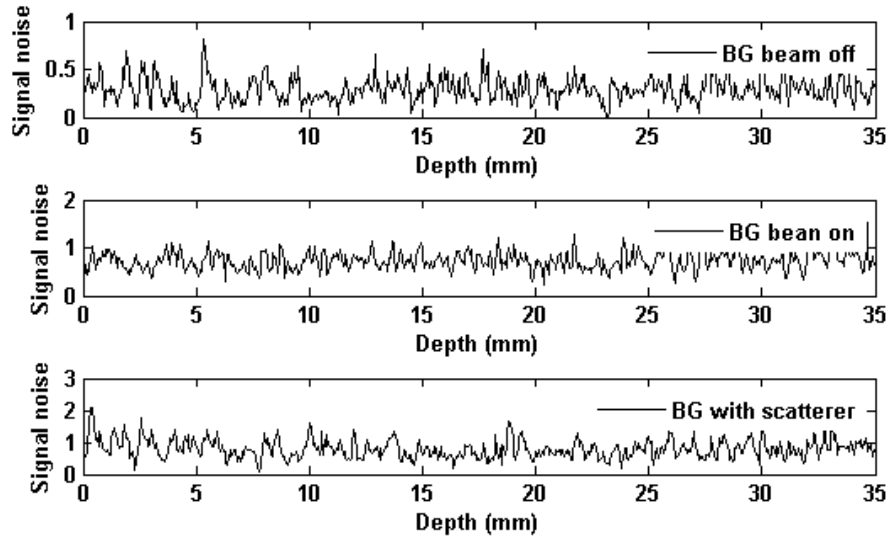


Figure 72: Background signals in three different situations

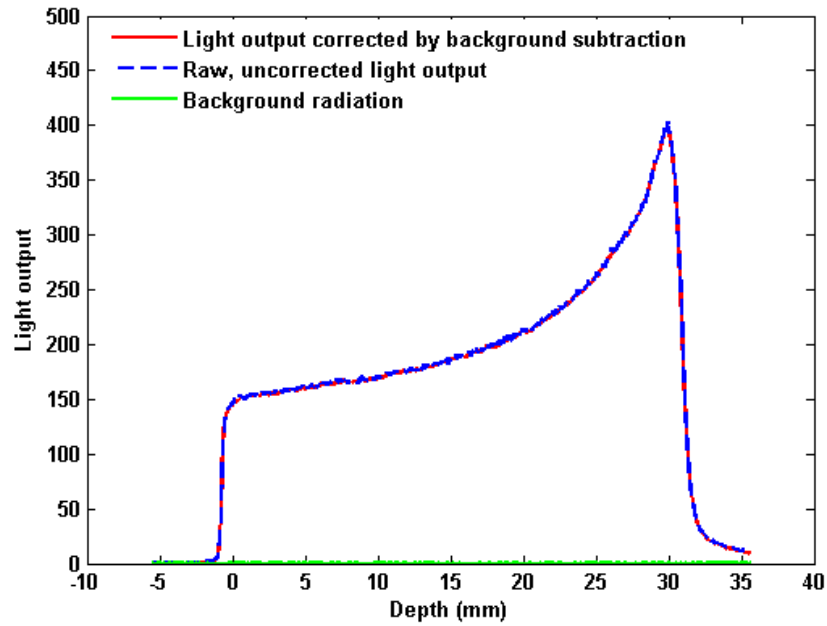


Figure 73: Comparison between the raw and corrected image

5.3.2 Bragg peak measurements

Photographs showing the PBP and SOBP are shown in Figure 74. In addition, it shows the measured scintillation light depth distributions, showing the PBP and SOBP measured from the photograph.

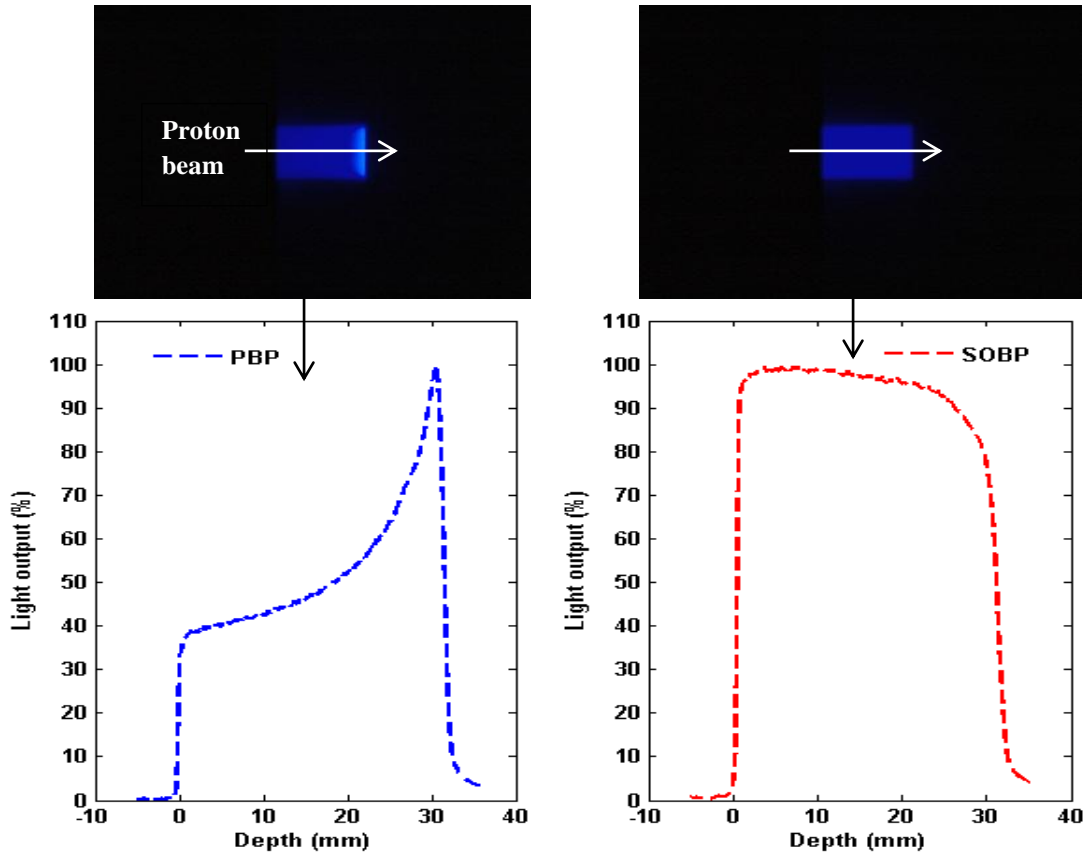


Figure 74: Measurements of dose distributions produced by a 60 MeV proton beam.

5.3.3 Short-term reproducibility

Reproducibility was calculated to observe any trend in short-term fluctuations of the measurements of the detector system. The reproducibility of the normalised light signal in the scintillator is shown in Figure 75. The results indicate that the system was stable

as the variation of seven repeated subsequent results was found to be less than 0.80%.

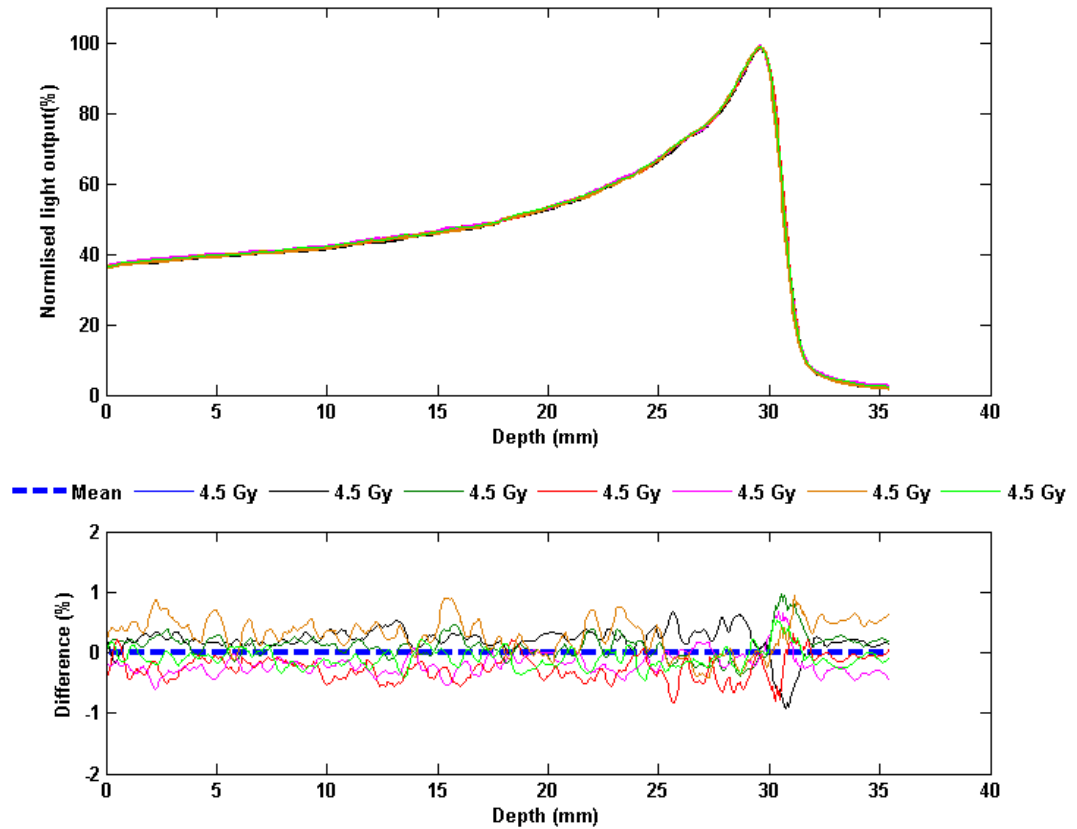


Figure 75: Scintillation light depth distributions of seven repeated measurements to deliver 4.5 Gy in top graph and the difference between the measurements to the mean in the bottom graph.

5.3.4 Dose linearity

The dose-response relation of the detector was checked by delivering different doses to the scintillator and imaging the emitted light. Figure 76 shows the scintillation light depth distributions for PBP and SOBP. In addition, the figure shows a solid line in both two right figures representing a linear fit of the average response of the system to dose

delivered for both PBP and SOBP beams. The curve has a correlation coefficient R^2 greater than 0.99.

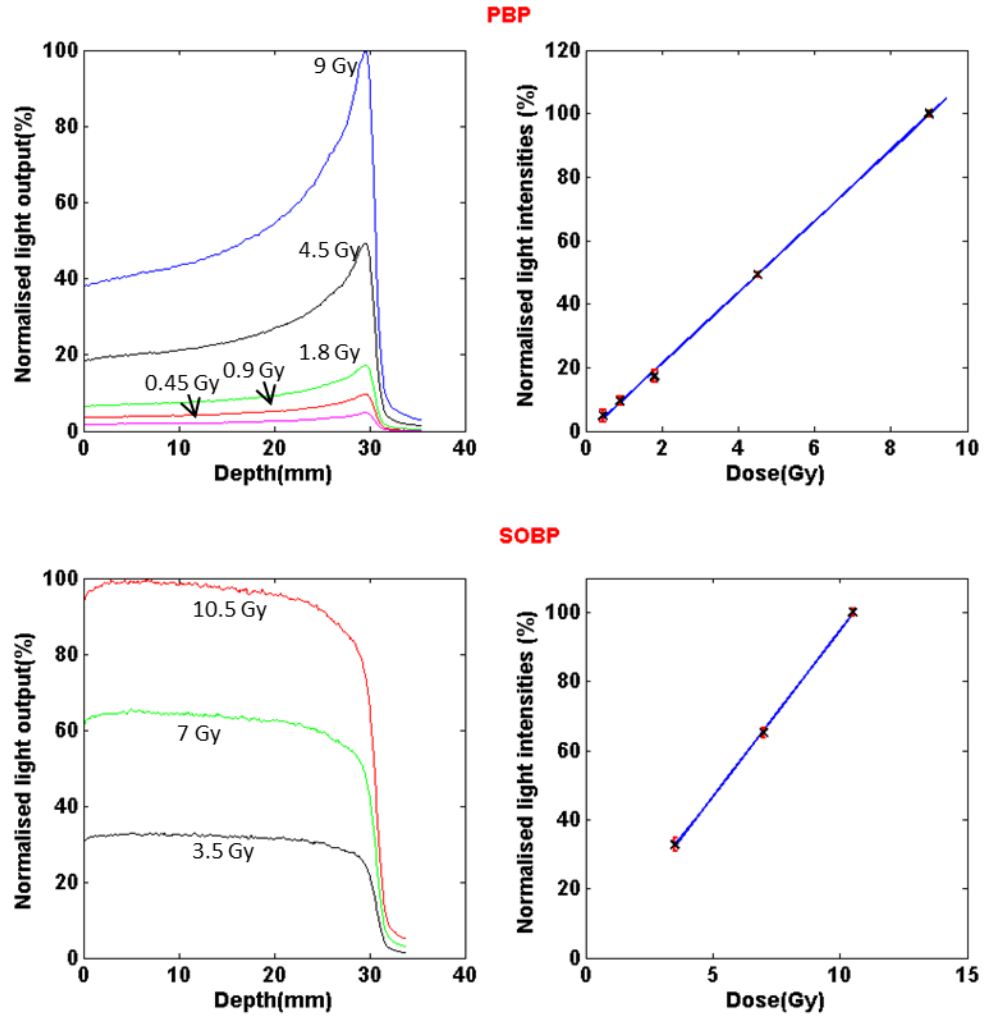


Figure 76: The impact of the radiation dose on the scintillation light on PBP and SOBP irradiations. Error bars demonstrate the standard deviation of three repeated scintillation measurements and some error bars appear smaller than the point size at certain points.

5.3.5 Scintillation light with different dose rate

Results from the dose rate dependency test are displayed in figure 77. The measurement uncertainties, assessed by measuring the deviation relative to the mean at different dose rates, were less than 1.1%.

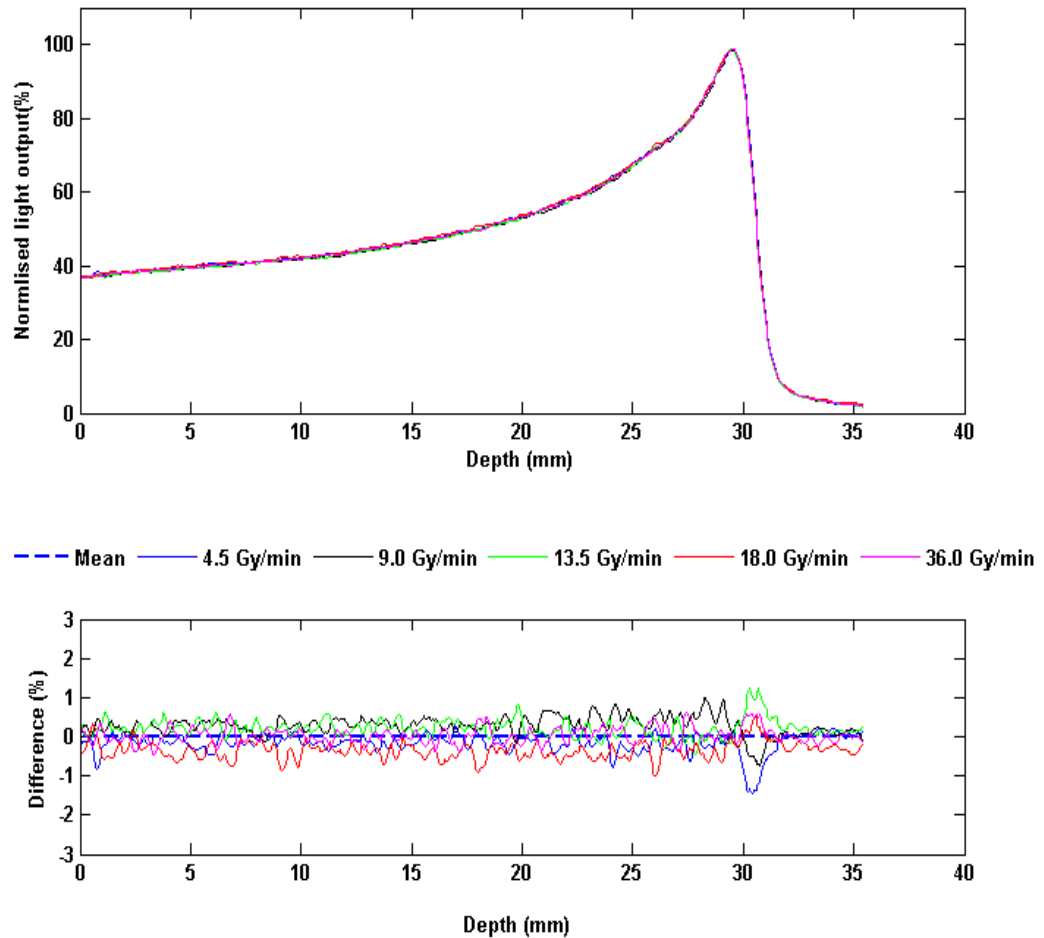


Figure 77: The scintillation light after delivering 5MU at different dose-rates

5.3.6 Scintillation light with different energy

Figure 78 illustrates the scintillation light images and depth distributions produced by the different energy delivered.

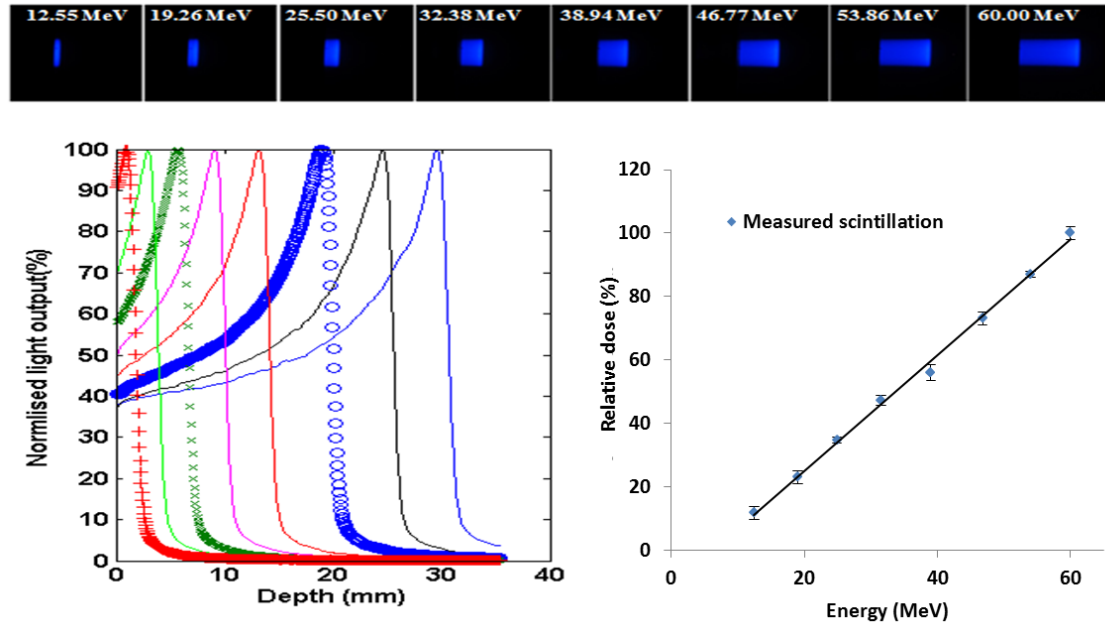


Figure 78: The impact of the beam energy on the scintillation light. The images represent each curve in the figure and protons came from the left.

5.3.7 Measurement validation

Two modes were used to acquire the images: the first was a pristine 60 MeV Bragg peak; the second was a fully SOBP achieved by placing a modulator in the beamline. Relative depth-dose curves of a PBP and SOBP measured with both an ionisation chamber and the scintillator-based detector system using a 60 MeV proton beam are shown in Figure 79. There is an obvious reduction in the Bragg peak as measured by the scintillator, reflecting the quenching effect. The Bragg peak at the PBP mode is reduced to 2.8 times the plateau height in the scintillator measurements compared to 5.1 times the plateau when measured by the ionisation chamber.

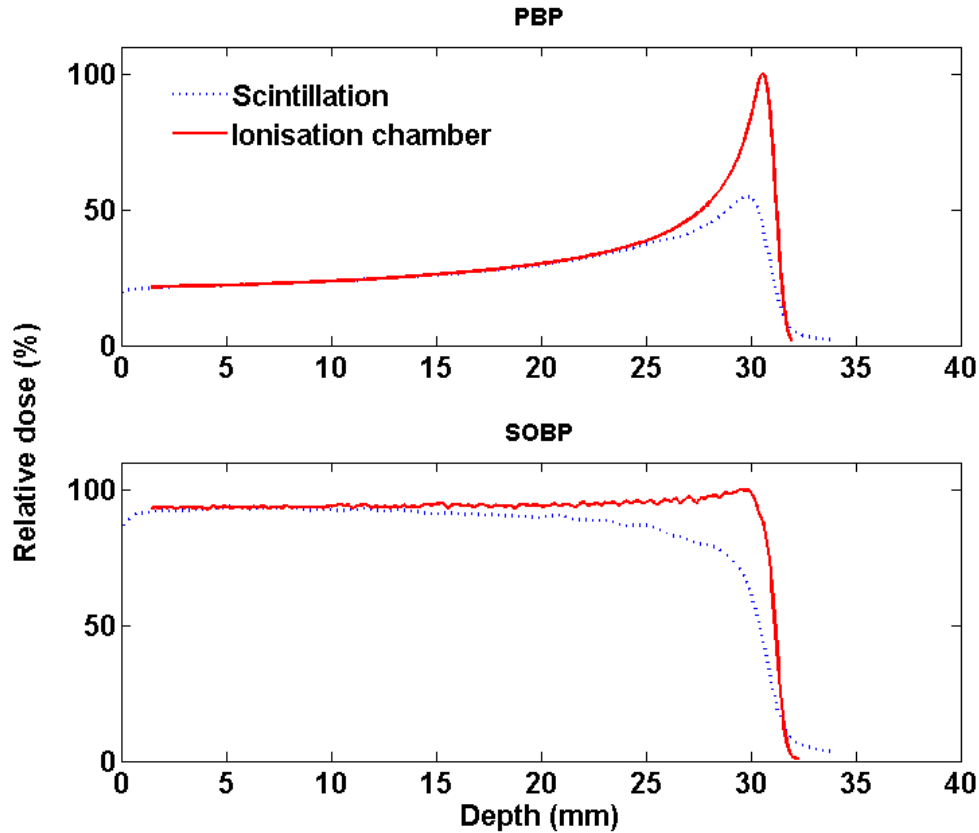


Figure 79: Scintillation light profile measured with the camera-scintillation detector system along the depth of the beam and compared to ion chamber depth dose curve measurements.

5.4 Discussion

A prototype system for proton therapy QA has been designed using a plastic scintillator and a commercial camera. The characterisation results for this prototype system show excellent linearity. In addition, the system shows reproducibility of results of around 0.55 %. The results are also independent of the applied dose-rate to within 1%. These errors may arise from either the instability of the cyclotron or the time integrated by the camera. Table 17 show the dosimetric requirements that the detector system needs to satisfy.

Table 17: The requirements of the performance of a clinical QA system

| <i>Requirement</i> | <i>Result</i> |
|--|--|
| 1) Stable | Showed excellent reproducibility $\pm 0.8\%$ |
| 2) Time for setup and breakdown | Took 22 mins for the system |
| 3) Dose linearity | Responded linearly for PBP and SOBP |
| 4) Dose rate independent | Found to be independent of dose rate |
| 5) Ease and read out convenience | Single image to analyse PDD instead of scanning diode or ionization chamber across the beam |
| 6) Tissue equivalent at this energy | Found to have the same range as measured by ionisation chamber |
| 7) Clinic environment suitability | Revealed to be non-toxic and safe for the clinical use |
| 8) Energy independent | Found to be independent over the range of the proton energy used when it was tested for energy indecency in section 5.3.6. However, at very low energy, some energy dependent happened due to LET varying of charged particle observed in the Bragg peak observed in section 5.3.7 |

Background signals, especially from scattered radiation, have a slight impact on the accuracy of the camera measurements. However, the contribution of these signals to the measurements is much smaller than the measured scintillation signal, but depends on the geometry of the experimental set-up, the distance between the camera and the beam line and energy. A possible solution could be to shield the camera which we will attempt for future work. The results showed that there were variations in the light distribution in the scintillator and the dose distribution in the ionisation chamber due to the quenching effect as a result of the changing LET of the incoming particle beam versus depth.

5.5 Conclusion

The measurements of scintillation light responses to a proton beam in plastic scintillator are presented in this chapter. We have investigated the use of a camera-scintillator detector system in high energy proton beams. This system is fast and independent of the applied dose-rate, shows excellent linearity to dose, provides reproducible results and could provide real-time measurement. Our results demonstrated that the scintillation light depth distribution indicated an imperfect match compared to the ionisation chamber measurement. A degradation of the signal was noticed when the images of the PBP and SOBPs of the proton beam were analysed as shown in Figure 79. The most notable disagreement between the scintillation and ionisation chamber measurements was in high dose region (i.e. in the Bragg peak region), which differed by approximately 50% at the PBP mode. This is the result of the quenching effect and prevents the direct use of this detector system. This detector

system could be an excellent dosimeter for proton beam if the quenching effect is corrected for. This dependency can be well investigated in a Monte Carlo study.

CHAPTER 6

6. ANALYSIS AND CORRECTION OF QUENCHING IN A PROTON BEAM

6.1 Introduction

In the previous chapter, the response of the plastic scintillator was shown to be independent of dose rate, and linear with dose. However, the results suffered from the quenching effect when irradiated with protons with high LET resulting in an under estimation of the dose. Quenching is highly influenced by the ionisation energy loss of the incoming radiation beam and hence the kind of particle. Because the LET for the proton beam is a function of the energy distribution and varies with depth, the result of quenching would be clearer in the Bragg peak because the LET is the highest [71].

The explanation of the physical mechanism underlying quenching is not fully understood although years of research have been carried out on the subject of scintillation response [171]. Most of the models describing the ionisation quenching were based on assumption about the physical processes involved. The earliest description of quenching was due to the saturation of the scintillator atoms which means that the yield of scintillation light would not increase if all scintillating atoms are fully excited leading to quenching of high LET particle. This hypothesis was proven to be not accurate because increasing the scintillator atoms in a compound would result in decreasing the magnitude of quenching but this is not shown experimentally [172]. Further description of ionisation quenching verified empirically was due to damage of the scintillation process through the excitation and ionisation due to the high LET incoming charged particle. Therefore, the region with high LET protons would be less efficient in their transmission of electronic excitation energy to the excited state in scintillator allowing the scintillation light production [72], [171]. As protons slow down,

they become more ionising and deposit more total energy and more LET. A greater proportion of energy is lost to interactions in the scintillator which do not emit light. This effect was explained quantitatively by Birks, as discussed in 1.5.3 [72].

Several studies have used Birks' equation to estimate Birks' constant in order to calculate the quenching of the measured scintillation [84], [85], [116]. Recently, a study was conducted in proton therapy to correct for quenching [55]. The quenching factor value k_B was estimated and used to analytically correct the measured scintillation results. The height of the Bragg peak for the corrected measured scintillation agreed to within $\pm 10\%$ of the depth-dose profiles. In this study, we extend previous work in proton therapy by using a large solid plastic scintillator, and a completely numeric technique for quenching correction.

In this chapter, we propose and characterise a method for simulating and correcting the quenching effect using a Geant4 simulation package which can track all photons generated inside the scintillator [129], [173], [174]. Although different simulation packages are available, the only available package that has the capability to handle both radiation and optical light transportation simultaneously is Geant4 [128]. We simulated the expected quenched scintillation and ideal scintillation light in a plastic scintillator for 38.94 to 60 MeV proton beams using Geant4 Monte Carlo simulation [129]. This makes the system more applicable, precise and easy to provide a quenching correction at any given beam energy.

6.2 Quenching correction

6.2.1 Methods

6.2.1.1 Measurement results and determination of Birks constant

As protons penetrate a scintillator, the LET of the incoming proton beam increases nonlinearly, leading to a reduction in the expected light output due to the quenching effect. If k_B is 0, no quenching effect would be shown and dL/dx is directly proportional to the LET. However, for high LET particles, $k_B > 0$ and dL/dx is non-linear with light output.

$$\frac{dL}{dx} = L_0 \frac{\frac{dE}{dx}}{1 + k_B \cdot \frac{dE}{dx}}$$

Eq 6.1

In order to obtain k_B in equation 6.1 for implementation into the simulation, LET was modelled in Geant4 by averaging the collision energy deposited over a finite trajectory length as described by a recent study [175], along with the depth dose curve and measured scintillated light output. The current model neglects any ionisation that comes from secondary particles. The depth scintillation light distribution was obtained experimentally, and these two parameters were then used to fit the measured data points with Birks' equation to derive k_B , which in turn was used in the Geant4 simulation which allowed quenching to be corrected. The Geant4 LET of a 60 MeV proton beam in the BC-408 scintillator, along with the depth-dose curve and measured

scintillated light distribution are shown in Figure 80.

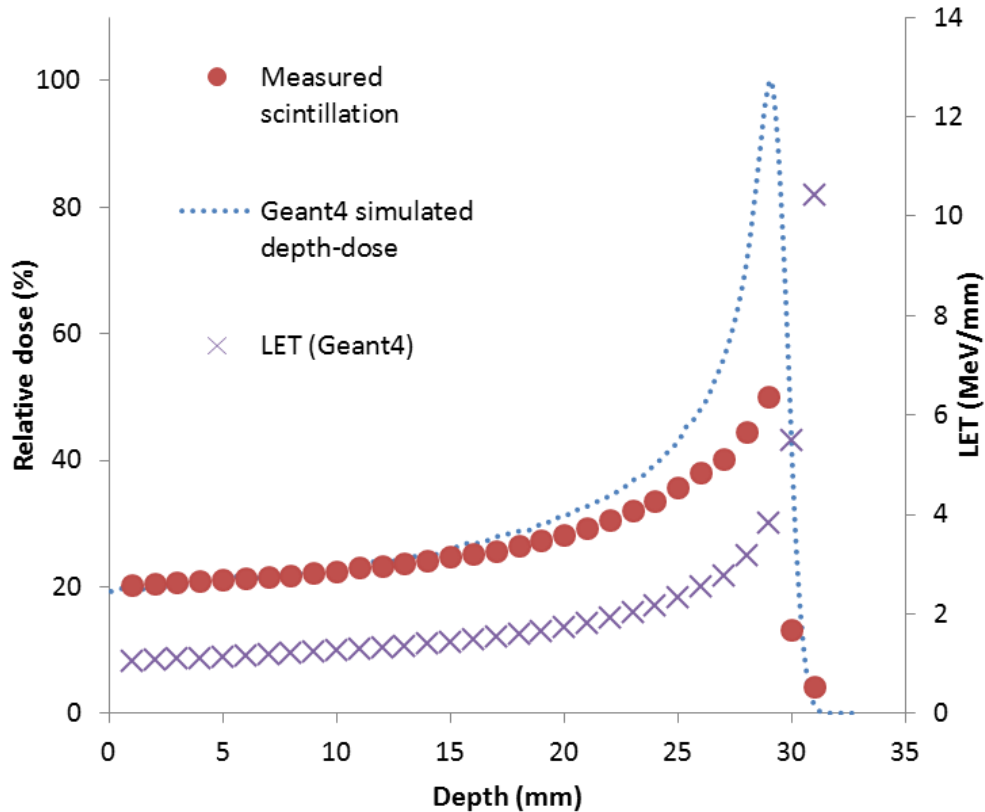


Figure 80: LET values simulated by Geant4, depth dose profile simulated in Geant4, and the measured scintillation light distribution as a function of depth for a 60 MeV proton beam in a BC-408 scintillator

6.2.1.2 Monte Carlo simulation

To account for LET-dependent quenching, Monte Carlo simulations were carried out to simulate the dose and scintillation production depth profiles using Geant4. The response of the scintillator to the proton beam was investigated by modelling the scintillation detector system virtually in Geant4. The simulated scintillator was a 20 cm × 20 cm × 10 cm block of the BC-408 plastic scintillator as used previously in section (2.4.3). The scintillation process is implemented in Geant4 by adding the

inherent scintillator optical properties as provided in the manufacturer's data sheet. The refractive index and the absorption path length were 1.58 and 380 cm respectively. The spectral light yield of the scintillator was included at a wavelength resolution of 25 nm.

The simulated primary beam consisted of 10^6 incident protons, with energies taken from a Gaussian distribution of mean 60 MeV and standard deviation of 0.36 MeV, matching previous studies done in the Clatterbridge Cancer Centre which used Geant4 [103]. A circular collimator of diameter 2.5 cm was used. Prior to entering the scintillator, the protons passed through 7 cm of air. The physics list class used contains primarily the QGSP_BIC_EMY, which is the reference physics list recommended for the simulation of hadron therapy applications [176], with additional list to model optical processes such as boundary interactions (i.e. G4OpBoundaryProcess) and scintillation (i.e. G4Scintillation) including Birks law (i.e. G4EmSaturation).

By knowing the range modulator wheel that was used at the Clatterbridge, we can simulate the steps of the range modulator wheel used to deliver the SOBPs, which consists of a sum of pristine Bragg peaks at different energies. The quenching effect can be calculated for each beam individually before weighted summing to form the SOBP. A simulated SOBP was composed of 24 PBP from 60 MeV to 16 MeV in 2 MeV intervals.

In order to translate the depth-dose in scintillator into depth in water, we simulated depth dose in the scintillator material and water, and we found the difference between them in a range of error of approximately 0.25 mm (Figure 81). This could explain the inconstancy observed in the next section 6.2.1.3 when comparing the simulated depth-

dose distributions in the scintillator and the measured depth-dose distributions measured by an ionisation chamber in water.

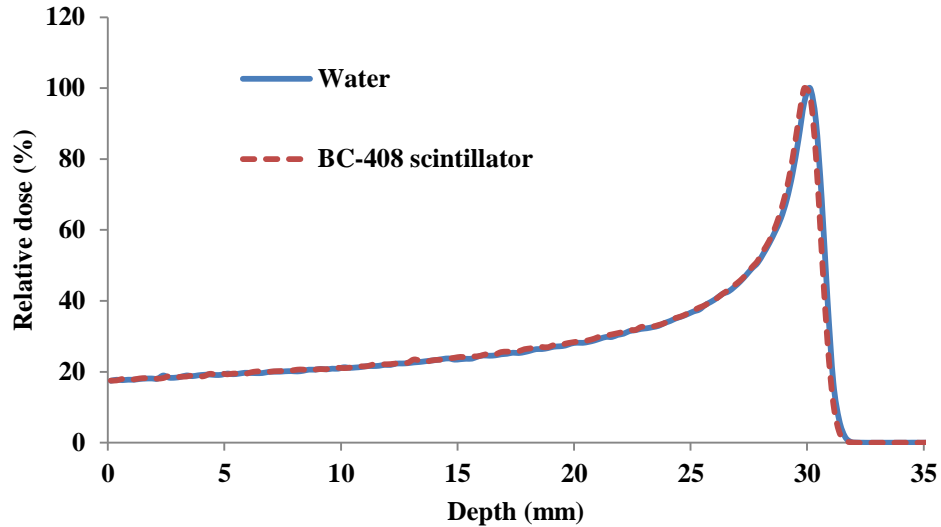


Figure 81: The depth- dose simulated in water and BC-408 scintillator.

6.2.1.3 Monte Carlo code validation

To validate the model, the depth dose curves of the PBP at 55.4 MeV and 60 MeV were simulated using a 2.5 cm² diameter proton beam, neglecting quenching effects and compared them to ionisation chamber measurements taken in water (figure 82). The measured and simulated positions of the Bragg peak agreed to within 0.24 mm, suggesting that the model does adequately represent the measured data. In Figure 83, the transverse profile of the proton beam was measured using a GAFCHROMIC EBT3 film (Ashland, USA) and compared to the simulation using a scoring volume of a square film of 5 x 5 cm² with resolution equal to 0.005 mm). The results show an adequate agreement between the measured and simulated profile.

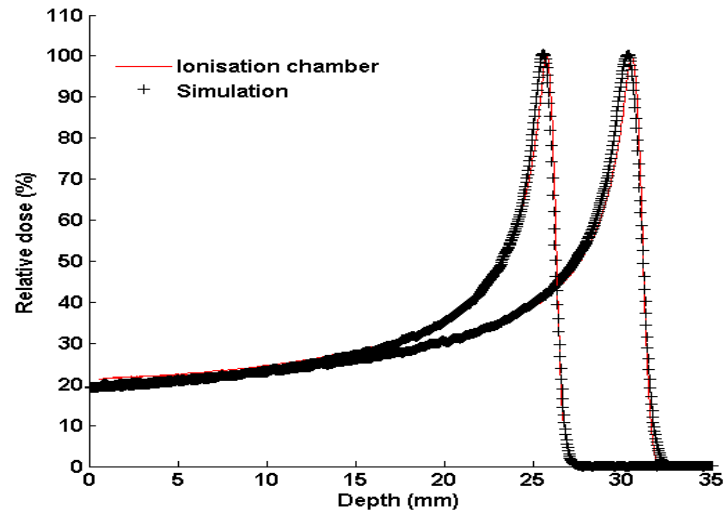


Figure 82: Validation of the simulated scintillation light with ionisation chamber measurements.

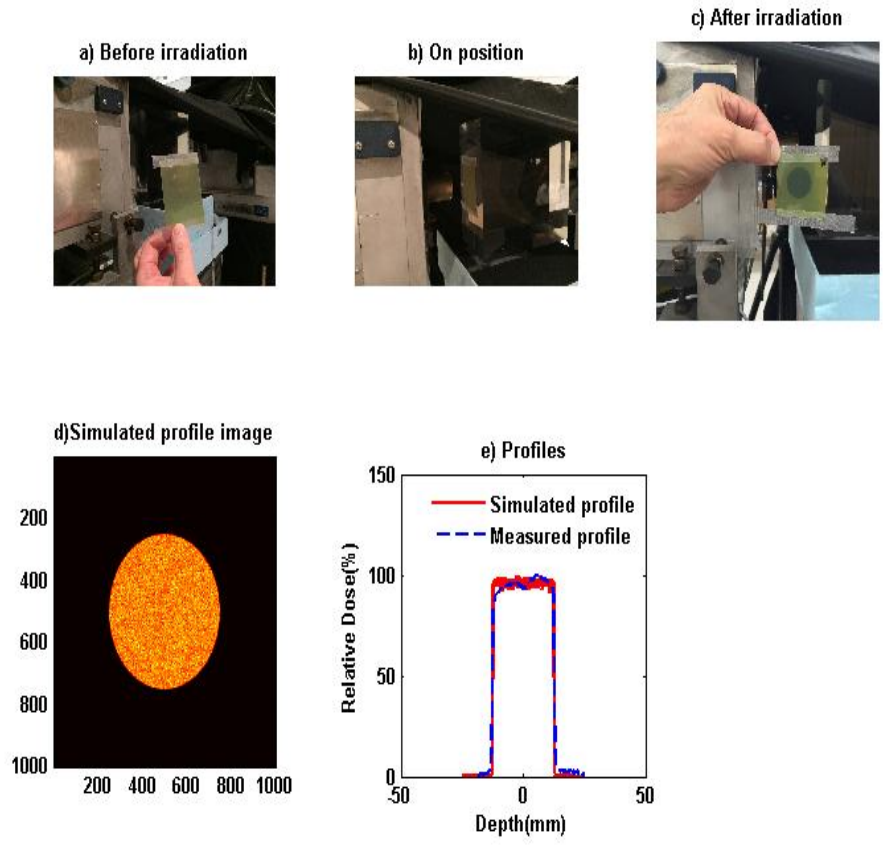


Figure 83: simulation and measurements validation of the transverse profile of 2.5 cm² proton beam.

6.2.1.4 Quenching correction procedure

The average energy deposited in the scintillator was scored alongside the scintillation light generated. Knowledge of the kB factor allows the light distribution to be scored both with and without the influence of quenching. Ideal and quenched scintillation depth distributions were simulated and used to generate a correction which was applied to the measured distribution to produce the corrected scintillation output. The correction procedure is summarised in Figure 84.

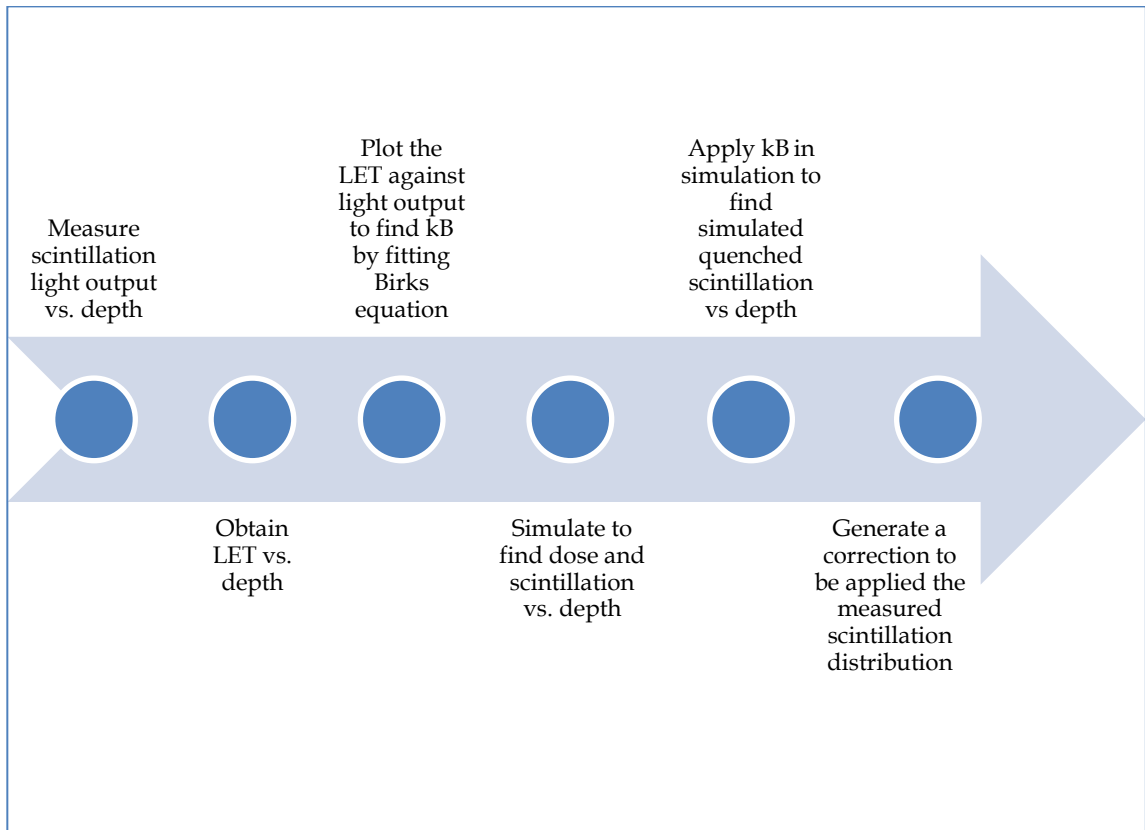


Figure 84: The summary of the quenching correction procedure

6.2.2 Results

6.2.2.1 Determination of Birks constant

Figure 85 shows the measured scintillated light output plotted against LET, and demonstrates a non-linearity due to quenching. Equation 6.1 was fitted to the data in Figure 85 (using the 'NonlinearLeastSquares' option in the 'fit' routine in MATLAB, and k_B was found to be $0.154 \text{ mm MeV}^{-1}$ (95% confidence level at 0.137 to $0.170 \text{ mm MeV}^{-1}$). To our knowledge, this is the first report of k_B for the BC-408 plastic scintillator and it lies within the range of published values of k_B for a closely related BC-400 plastic scintillator which vary from $0.124 \text{ mm MeV}^{-1}$ to $0.207 \text{ mm MeV}^{-1}$ [84], [116]. To validate this, LET was also calculated in "Stopping and Range of Ions in Matter" (SRIM), an online software package [177], and found to be $0.147 \text{ mm MeV}^{-1}$ (95% confidence 0.133 to $0.160 \text{ mm MeV}^{-1}$), which is in good agreement with the Geant4 results beyond the Bragg peak, where we have noticed that SRIM can slightly underestimate the LET value due to the mono-energetic input of the primary beam.

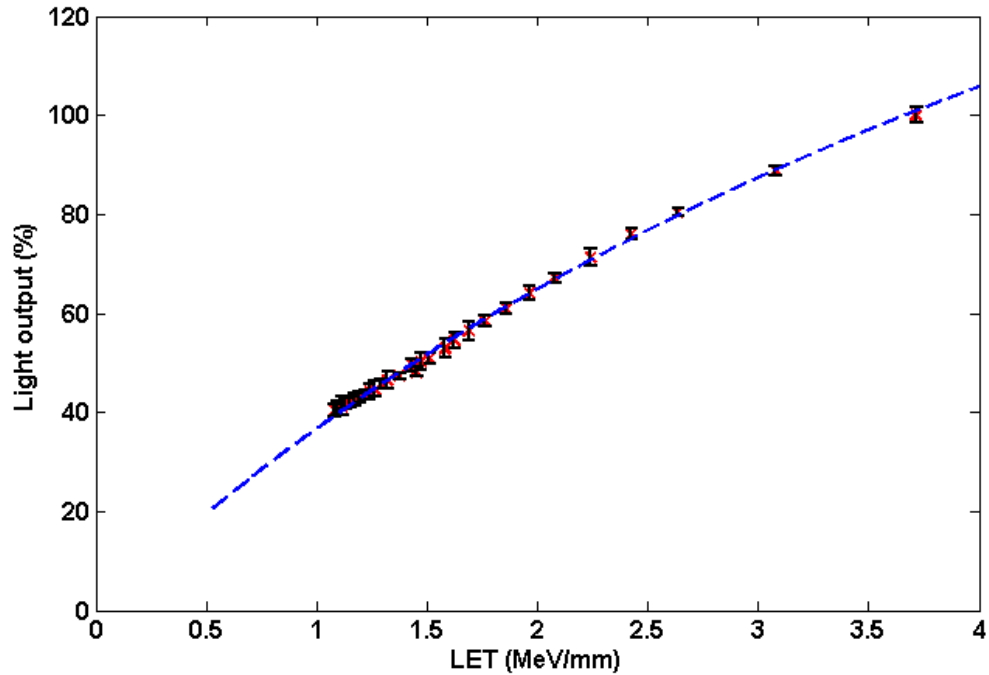


Figure 85: The measured scintillation light vs simulated LET for the 60 MeV proton beam.

6.2.2.2 Quenching correction

Figure 86 shows percentage depth dose curves for beams with energies of 38.94, 46.77, 53.86 and 60.00 MeV, and ionisation chamber measurements for the 60 MeV beam. For each energy, four plots are shown: (1) the simulated depth dose (blue crosses); (2) the depth dose directly measured by the camera (solid black line); (3) the simulated quenched light output (blue bars); and (4) the measured light output after correction for quenching (red dashes). As expected, the measured light output after correction for quenching agrees with the simulated depth dose.

For the 60 MeV proton beam, the simulated Bragg peak range and the range taken

from the corrected measured scintillation both agree with the range measured from the ionisation chamber (black crosses), with 0.2 mm accuracy and 3% accuracy for the peak/plateau ratio.

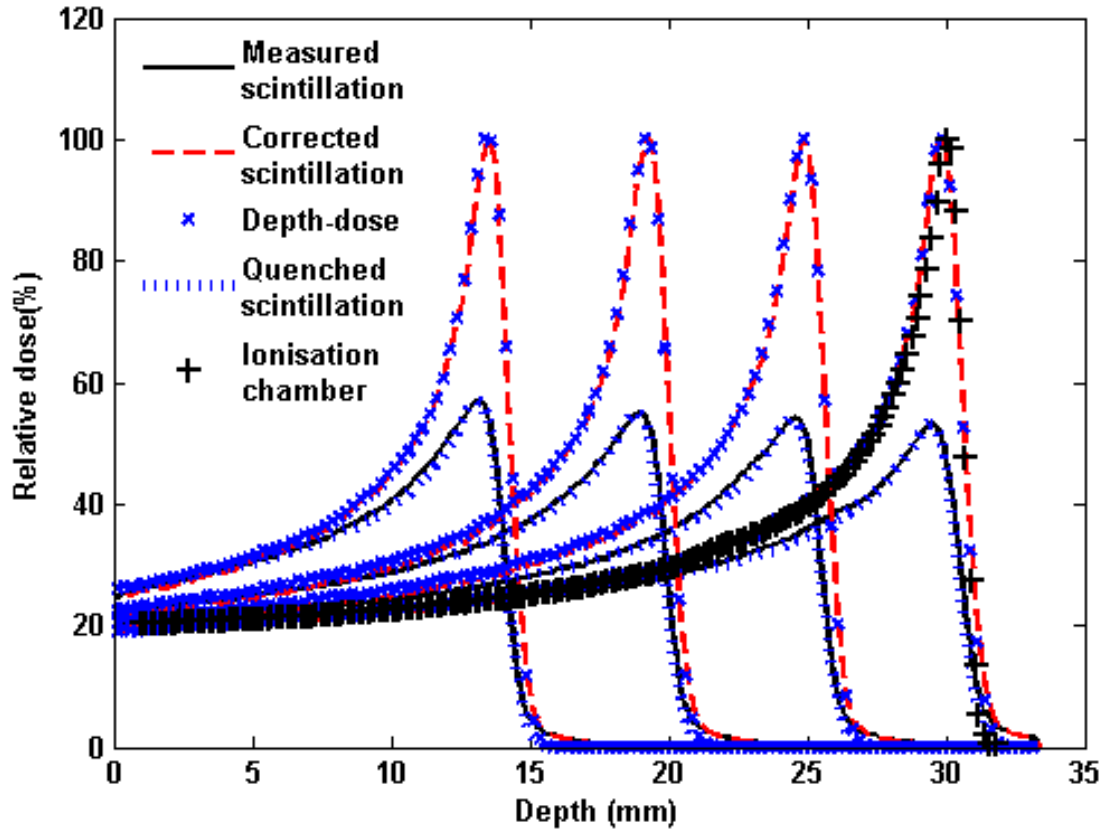


Figure 86: Percentage depth dose curves at 38.94, 46.77, 53.86 and 60.00 MeV, showing (1) the simulated depth dose (blue crosses); (2) the depth dose directly measured by the camera (solid black line); (3) the simulated quenched light output (blue bars); and (4) the measured light output after correction for quenching (red dashes).

We have performed the simulations to investigate quenching effect. The detector system can also be used to correct SOBPs for the quenching effect. This is done by knowing the information for the modulated beam. Figure 87a shows a good agreement between the simulated scintillation distribution and measured ionisation chamber using SOBPs. A satisfactory agreement within 2.3% between simulated quenched

and measured scintillation was shown in Figure 87b. The corrected scintillation distribution for the SOBP used is presented in Figure 87c.

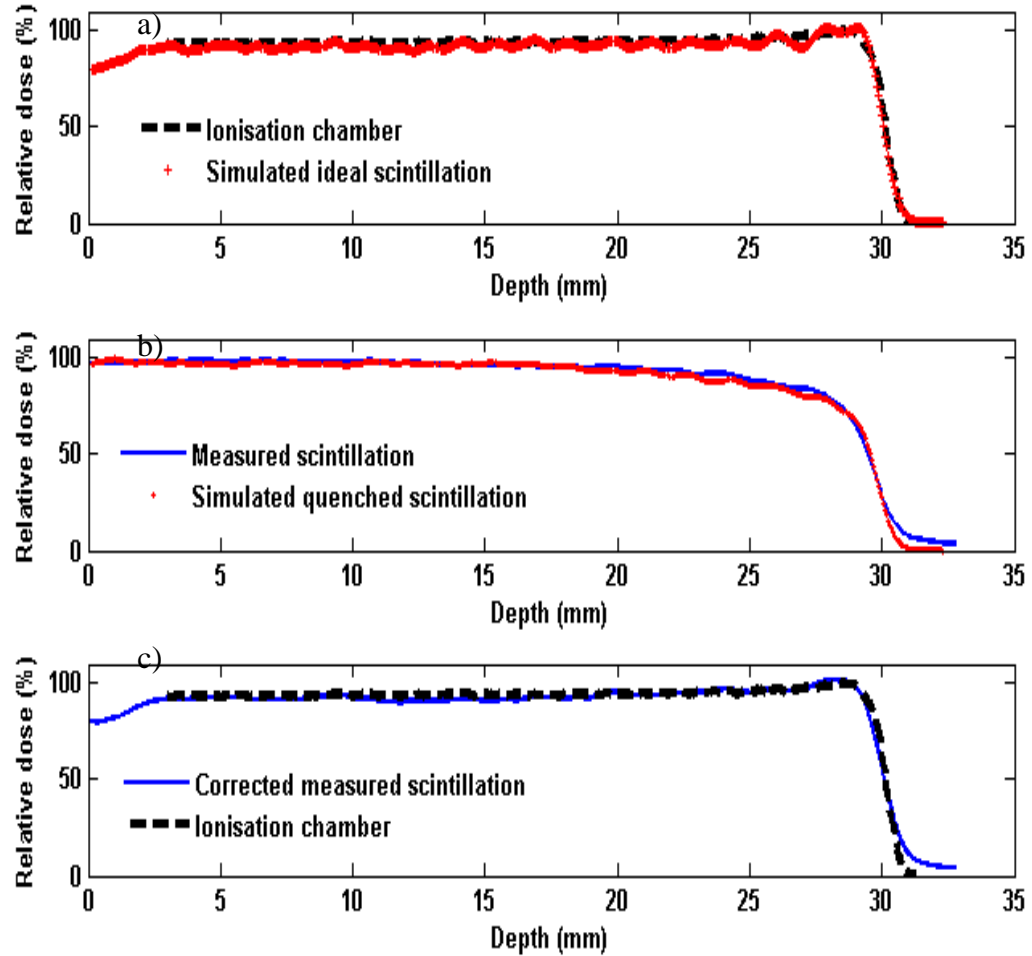


Figure 87: The simulated ideal and quenched scintillation depth distribution using Geant4, the measured scintillation depth distribution, the ionisation chamber depth-dose and the corrected scintillation depth distribution of the SOBP beams used at the Clatterbridge Cancer Centre.

6.3 System validation

6.3.1 Method

A method was developed, based on Monte Carlo simulations and measured scintillation output, to correct for the observed quenching. Depth-dose distributions were extracted from the photographs of three repeated scintillation measurements and corrected for the quenching effect. The dose linearity and dose rate and energy dependency were re-evaluated after correcting for quenching effect. All results below refer to measured distribution after the quenching correction was applied.

6.3.2 Results

6.3.2.1 Corrected detector responses

The dose-response relation of the detector was checked by delivering different doses to the scintillator and imaging the emitted light. Figure 88 demonstrates the system is linear with dose.

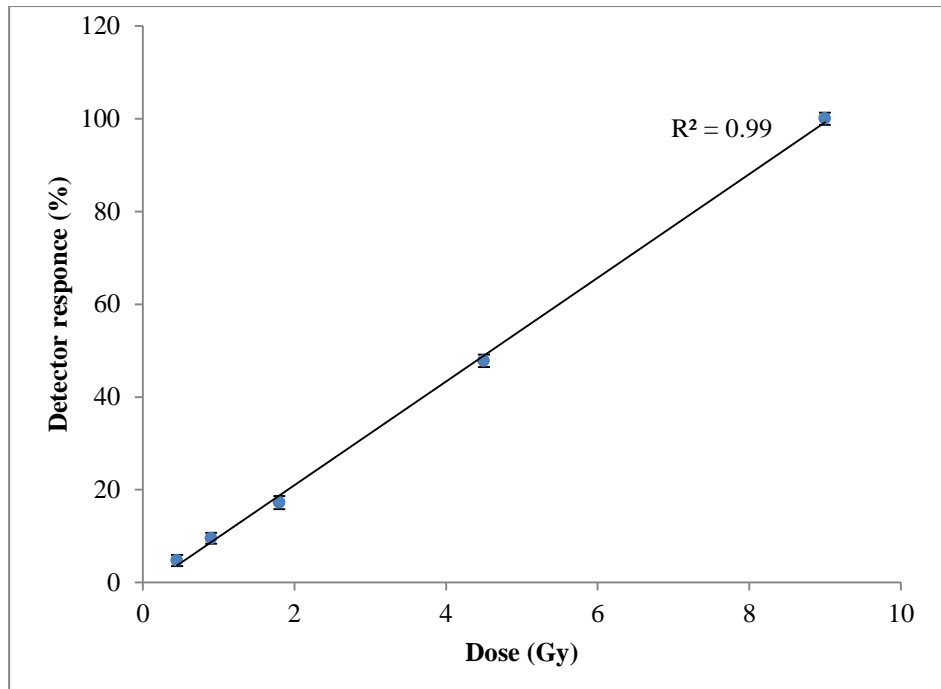


Figure 88: Linearity of the scintillation detector system as a function of dose for a 60 MeV proton beam.

Results from the dose rate dependency test are displayed in Figure 89. The measurement uncertainties, assessed by measuring the standard deviation relative to the mean at different dose rates, were ~1%.

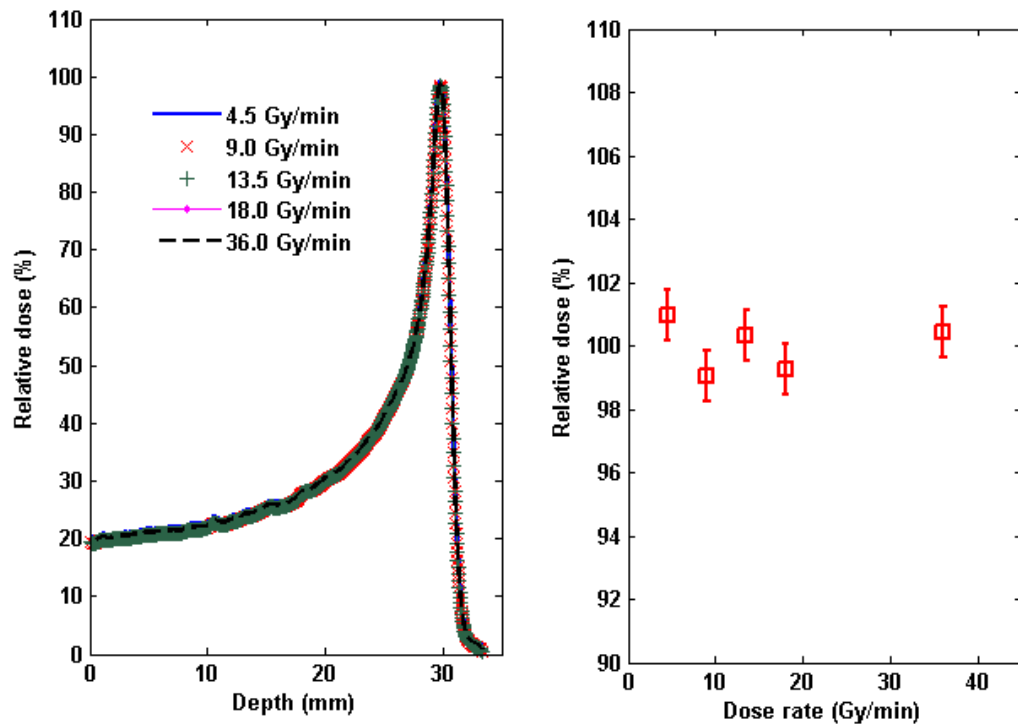


Figure 89: The response of the scintillation detector system after delivering 4.5 Gy at different dose-rates for a 60 MeV proton beam. Vertical bars on the right hand graph give the measurements error of three repeated scintillation measurements.

Figure 90 shows the measured range in the scintillator for 8 different proton beam energies achieved by placing varying thicknesses of PMMA in the beam. In addition, the fit shows that the system responds linearly. The measured protons ranges in plastic scintillator were compared to the range data from ICRU 49 as seen in Figure 91 [31]. The agreement was very good with maximum difference of 0.16 mm.

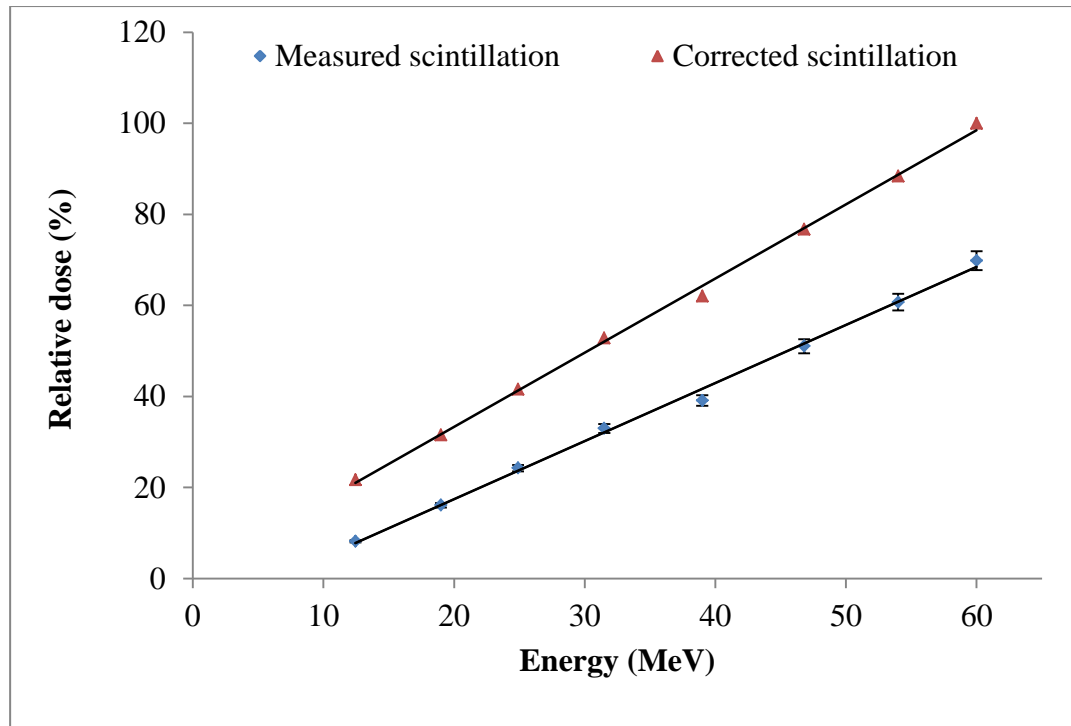


Figure 90: The response of the scintillation detector system with the proton energies used in this study.

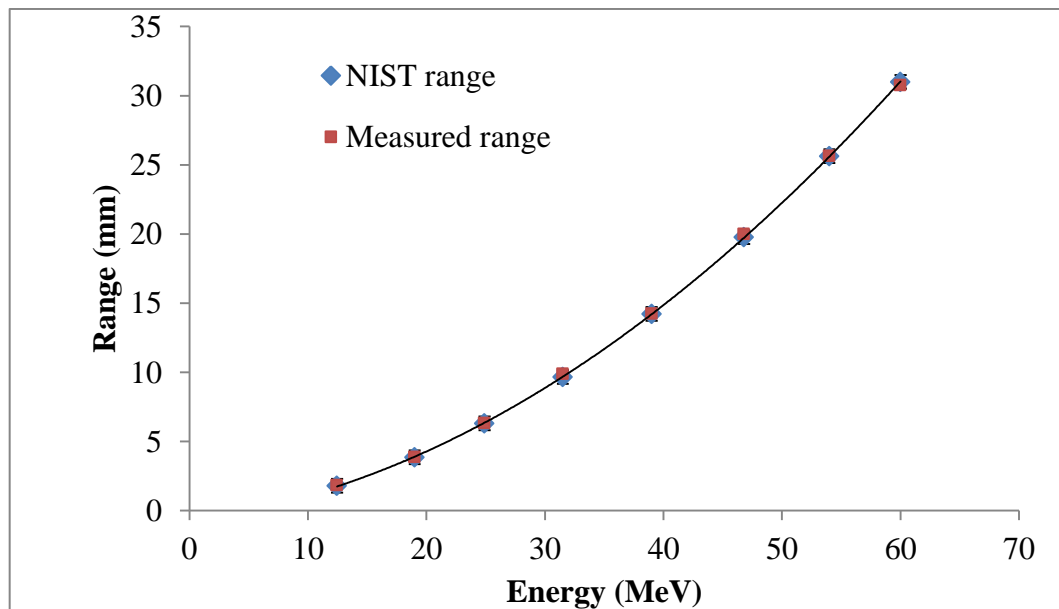


Figure 91: Comparison between the range measured by the scintillation detector system and the tabulated range by ICRU in plastic scintillator of different proton beams.

6.4 Discussion

Our results are promising and indicate that the quenching problem can be solved effectively by Geant4 simulation, allowing the system to be used for relative dosimetry in proton therapy. Quenching correction means errors were reduced from ~50% to 3%. Nevertheless, optical artefacts require further consideration in order to enhance the peak/plateau ratios and the appearance of the Bragg peak tail.

To progress the system to stage for translation into daily use in a clinical setting, there are some further points that will need to be addressed such as how we translate this system to a larger field size, wider energy range and SOBP.

For a bigger field size with a passive scattering system, the magnification effect will increase. We expect that the analytical method we have used in this work to correct for the magnification effect could be applied for clinically relevant field sizes. In more complex cases, such as use of multileaf collimators, very large field sizes, or if non-linear optical propagation such as attenuation become significant, an equivalent correction factor could be obtained numerically. The system can also be used to measure transverse profiles.

The current system can be used for energies up to 175 MeV (~ 20 cm range in water). For higher energies a bigger scintillator could be used, or the scintillator currently used could be immersed in water to ensure the Bragg peak remains within the scintillator.

The detector system can be used to correct SOBP beams for the quenching effect. By knowing the modulator wheel that has been used, we can simulate the SOBP, which

consists of a sum of pristine Bragg peaks at different energies. The quenching effect can be calculated for each beam individually before weighted summing to form the SOBP.

Dose linearity and dose rate dependency show that the system is capable to determine the dose within 1% error, which is within required tolerances for much of radiotherapy QA [165]. We have demonstrated the system is reproducible over short periods of up to a day, with an accumulated dose of 140 Gy. Over longer periods, the reproducibility will be limited by radiation damage to the scintillator and the camera.

These features lead to a versatile system that can be used to do a quick QA measurement for the dose and the energy simultaneously. For example, we propose that images of energy and dose can be compared every morning to test the stability of the treatment machine. This could be quicker than scanning a diode, with the advantage that the beam is visualized with a photograph.

6.5 Conclusion

Despite the common use of scintillators, there is little data available for the correlation between dose and scintillation output, especially in proton therapy when using a camera for imaging. Here, we developed in this chapter a correction method based on a semi-empirical Birks model using equation 6.1 of the scintillator response by measuring the relationship between the LET of the incident 60 MeV proton beam and the measured scintillation light produced in the scintillator. The correction for the LET-dependence of the scintillator response is possible to with an accuracy of $\pm 3\%$. We then re-evaluated the dosimetric characteristics for the corrected responses of a camera-scintillation detector system for dosimetry of proton beams.

The system has the advantages of providing a 2D view of dose distribution for individual radiation fields, while being fast, directly digital and tissue equivalent [45]. Our results were found the measured depth-dose distributions using this system were lower than those measured with an ionisation chamber due to quenching effect occurring in the scintillator. We have proposed a method for correcting for quenching which shows promising results. This low-cost, convenient, clinically achievable system builds upon previous work by using a large plastic scintillator, a commercial camera and a completely numeric technique for quenching correction. It can be concluded that the detector system has the potential to be translated for use in quality assurance of clinical proton beams. Future challenges include 3D time-varying data acquisition.

CHAPTER 7

7. OVERALL CONCLUSIONS

While technical advances have been shown in radiation therapy treatment machines and techniques, their QA procedures are challenging. We proposed a dosimeter which has several advantages (e.g. water density equivalence, linear dose response) and is also capable of taking measurements in 3D volume which could potentially be extended for 3D dosimetry measurements. The purpose of this work was to evaluate the potential use of the scintillator detector system to measure the dose deposited by both low and high energy photon beam, electron and proton beam, and to correct for scintillation light quenching in proton therapy.

7.1 Accomplished work

Scintillator selection and optical artefacts evaluation: The first step of the project was to select the scintillator suitable for the design that should be suitable and easy enough to use in a clinical environment. Different scintillators were irradiated and the findings are presented in Chapter 2. An analysis of the dosimetry output revealed that a large plastic scintillator could show some advantages during comparisons. Although this detector system design has the potential to reduce the time required for QA tests, the accuracy of the measurements of the scintillation light distribution is affected by several optical artefacts which require evaluation and correction. Therefore, potential correction methods to remove or mitigate these artefacts were developed to obtain meaningful dosimetric measurements.

Scintillator detector as a QA tool in low energy radiotherapy: Results presented in Chapter 3 investigated the usability of the detector system for low energy x-rays. Basic characteristics of the dosimeter indicate excellent dose response linearity and reproducibility. The reproducibility of the result was ~1% and could be improved if higher beam parameters (voltage and current) were used. The measured scintillation light was directly correlated to the dose distribution across the scintillator. The detector system was found to be suffering from energy dependence due to the interaction mechanism at low energy up to 150 kVp when the simulated depth dose distributions in the scintillator were compared to that produced in water.

Scintillator detector as a QA tool in photons and electrons radiotherapy: We extended the investigation to study the feasibility of the detector system for high energy radiotherapy. Dosimetric results displayed in Chapter 4 showed good agreements with ionisation chamber measurement with photon beams and fulfilled the 3% dose variation criteria in radiotherapy. Discrepancies between off-axis dose profiles obtained by the scintillation detector system and the ionisation are mainly the result of the optical photon blurring. It was essential to investigate the water equivalence of the scintillator prior use in charge particle beam, such as electron to insure the electron interactions in the scintillator are similar to that in water. We compared the simulated depth dose in water and in the scintillator, and variations were found up to 7% due to 0.03 g cm^{-3} difference in the physical density between the water and scintillator. This affected the energy loss procedure in the medium or the LET. These inadequacies can be corrected by applying the IAEA recommended scaling procedure allowing the detector system to be used in QA of electron beams for routine constancy checks.

However, optical photon blurring was an issue that resulted in inaccurate estimation of the dose in very low dose region.

Scintillator detector as a QA tool in proton therapy: Chapter 5 dealt with characterising and testing the detector system in proton therapy. The dose and dose rate responses of the system were assessed using 60 MeV protons. The relationship was found to be linear with dose and independent of dose rate. The reproducibility of the result was promising with 0.80%. In addition, this detector has been found to have the ability to show the theoretical interaction of protons (i.e. Bragg peak) in the scintillator by imaging the light distribution produced. The system was also useful to define the range of proton beams. However, the quenching was presented when the dose distribution was compared to the ionisation chamber measurement and this affected the linearity of light output against low proton energy (i.e. high LET proton).

Correction for quenching (Chapter 6) could be done to calibrate the energy versus the light output. The comparison between the corrected light distribution and the ionisation chamber measurement agreed well, with 0.25 mm uncertainty. Overall, this approach seems to be easy, fast in response and simple to measure the range and Bragg peak of a proton beam using the detector system.

7.2 Potential QA applications of the scintillator detector system

The current QA procedures that a scintillation detector system could provide are that:

- The delivery of proton treatment requires different beam energies to cover a useful range of treatment depths. As a part of the QA procedure, the measurements of dose depth dose distribution and the off-axis profile should be performed periodically at each of these beam energies [178]. In practice, this is a challenge to do because the procedure is time consuming with the current available detectors. The current verification procedure is that several beam energies are selected to be verified during commissioning and the rest of energies are simulated instead of measurements using a Monte Carlo beam model [179], [180]. Such system could offer fast and easy measurements and can be used as a daily QA measurement to show the range of protons in proton therapy. It is usually done using an ionisation chamber placed in a water phantom.
- It could be a potential system for the use of performance QA, such as characterising the machine data (e.g. output).
- The detector system showed to be less time consuming and can be used as a relative dosimeter for QA routine constancy checks and for the range characterisations for electron beams.
- In addition, it could be used in periodic QA to ensure continued planning and delivery data as at commissioning.

- Fast daily check of the depth-dose curves to work out energy for photons, and easy and quick measurement of the off-axis beam profile.
- A potential advantage which could be counted for the 3D volume of the scintillator detector system is the possibility of acquiring the 3D dose distribution. In addition, the shape of the delivered dose can be identified by the tomography method which allows for MLCs QA.

7.3 Future direction

The possibility of using the scintillation detector system has been investigated for QA of photon, electron and proton beams. This thesis aimed to develop a scintillator detector system, to investigate the feasibility of the detector system in radiation therapy and to enhance the performance of the detector system by correcting some of the inherent artefacts of the system such as noise, vignetting and magnification, as well as correcting for quenching effect in proton beam. While the study appears promising, much more work is required before it is possible to assess fully the potential of the tissue equivalent scintillator system as a means of verifying the dose in radiation therapy. Such system is still in demand clinically as the 3D dose distribution might be obtained. However, more work would be needed to develop a clinically acceptable system especially the optical artefacts of the detector system. Future developments should look into:

Optical artefacts: The most important area of future work for detector system is a thorough investigation into the optical artefacts impacting the accuracy of an image such as the blurring and magnification. The issue of magnification was solved analytically and showed very good agreement with measurement. A future study will aim to solve this empirically by moving a thin scintillating sheet along the beam axis. This will be imaged many times and the individual profiles summed for comparison with the profile of the beam in the large scintillator. In addition, a telecentric lens could be an effective solution for the magnification artefact.

The telecentric lens shown in Figure 92 has the entrance pupil at infinity, achieved simply by using an external aperture with regard to the conventional lens [181], [182]. Consequently, the principal ray that passes through the centre of aperture would be parallel to the optical axis between the object and lens. Therefore, there would not be magnification on the image with varied object distance because the image is generated by the parallel projection[183].

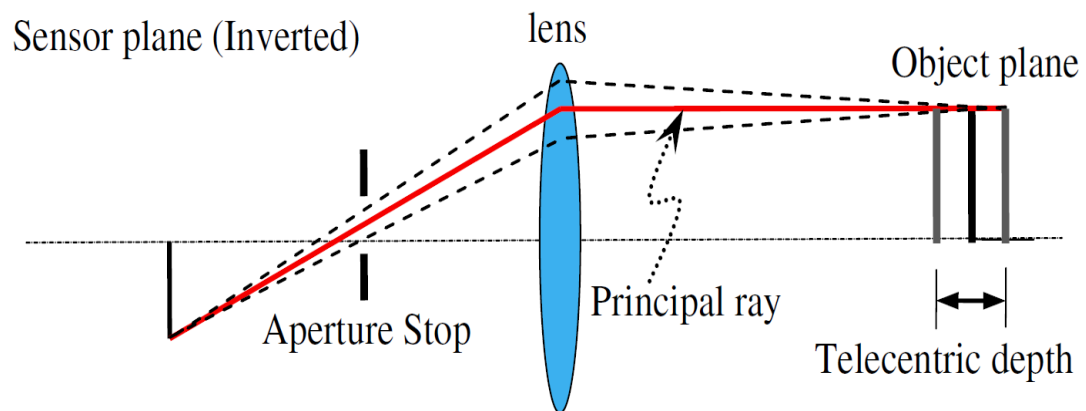


Figure 92: Telecentric lens arrangement [184]

Long-term reproducibility: More work could also be looked at the long term reproducibility of the whole system including the camera and the scintillator. It is very important to investigate whether the system provides stable results during a period of time in high energy radiation.

Simulation of scintillation depth distribution: It is useful to add a virtual pinhole camera in the Geant4 simulation to allow comparison with the experimental scintillation image. It is simple and there is no need to simulate the complex lens system, and no vignetting effect. However, the resolution of the image is highly dependent on the dimension of the hole or aperture, meaning that the smaller aperture results in lower light collection efficiency and hence lower collected intensity.

Measurement of both the depth dose and transverse profile in a single irradiation: We have developed a large plastic scintillator detector system for the purpose of 2D of photon, electron and proton beams. Due to their advantages (e.g. fast, high resolution and immediate readout), using two orthogonal cameras in the system design (Figure 93) could offer QA measurements of the range, width of the transverse profile in a single measurement simultaneously. In addition, it could be useful if multiple scanned proton pencil beams are used to determine lateral position of scanned proton beams. However, further dosimetric investigations are required to examine the accuracy and precision.

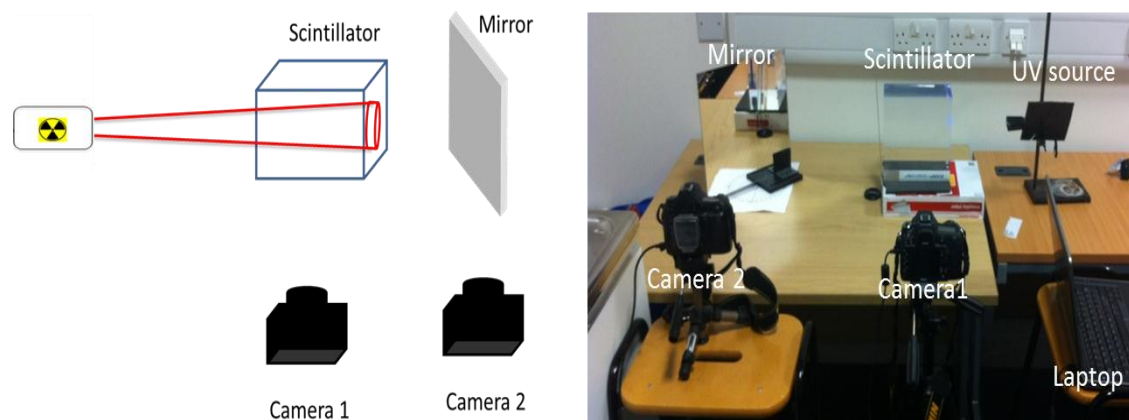
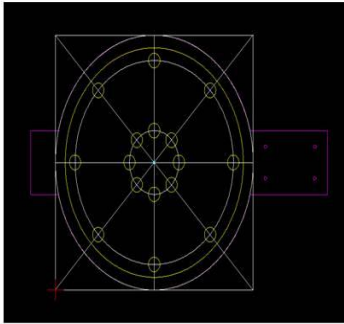


Figure 93: The dual-camera detector system design

3D image acquisition using the scintillator detector system: Using an image reconstruction algorithm is a possible way to obtain the 3D dose distribution. By rotating the camera around the scintillator, tomography can be achieved by using filtered back projection (FBP) method. The setup of the experiment is shown in Figure 94. The scintillator and the camera were placed in a motorised rotating stage. The movement of the camera was relative to the movement of the scintillator. Therefore, the camera captured optical light emerging from the flat surface scintillator. This method seems to be applicable in this work and developments still need to be carried out; this will be the trend of the future work on this project.

Phase 1: The design



Phase 2: The base



Phase 3: The motor



Phase 4: The motorised rotating stage



Phase 5: The 3D acquiring system (2 different views)

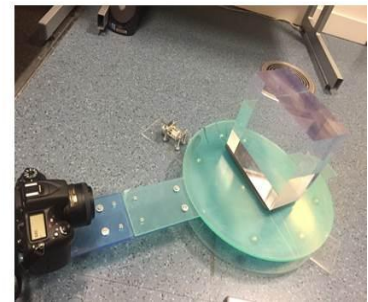


Figure 94: Experimental setup of the proposed optical dosimetry system

Appendices

Appendix A: Camera Control Pro software

This software permits remote control of the settings including exposure mode, shutter speed and aperture, from a computer on most Nikon digital SLRs[185]. Connection between the computer and camera can be via USB cable.

Advanced camera features are supported including LiveView to provide a real-time preview, the Picture Control system allowing image parameters to be selected and adjusted such image storage control including sizes and formats on a computer and the Viewer, which collectively enable the preview and selection of images prior to transfer to a computer.

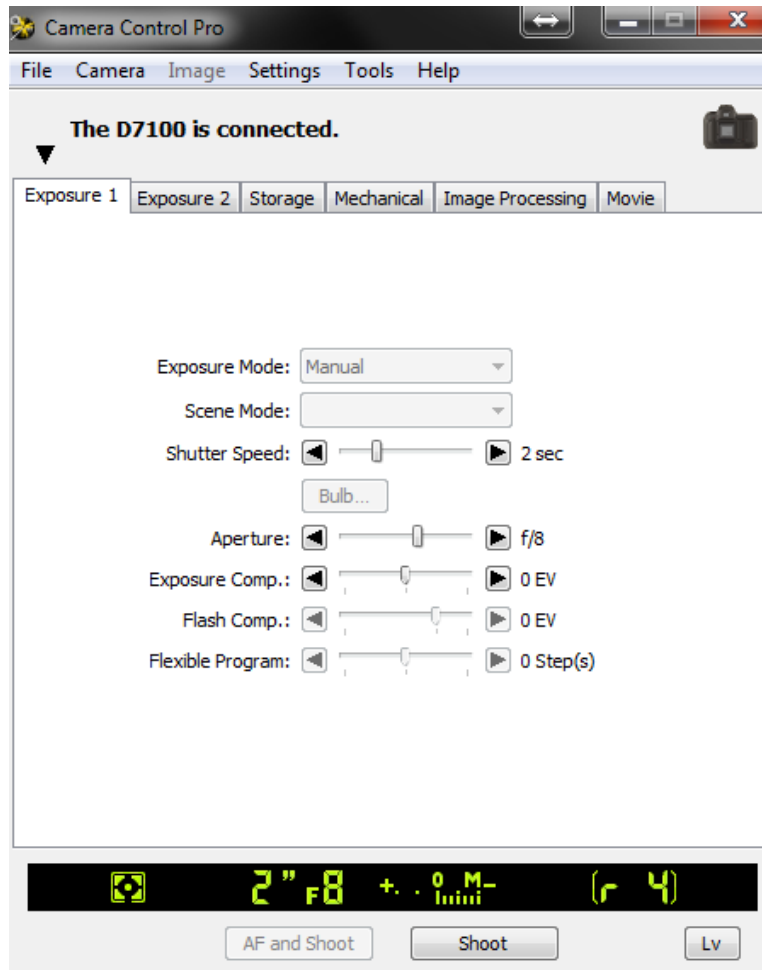


Figure 95: Camera Control Pro2 software

Appendix B: Radiation impact on the camera

In the radiation treatment room, many cameras are used to observe patients during the delivery of the treatment. An investigation into the impact of radiation to the camera in the treatment room was made [186]. The sensors in CMOS cameras are usually made of silicon as the base material and silicon dioxide as the coating [187]. It was concluded that the radiation damage of the camera can be temporary if the silicon atom (camera chip) is ionised by the scattered radiation and then the excited electron will recoil to its place, and can be permanent by either the excited electrons are trapped by the silicon oxide insulator result in increase in dark current signal of the camera or Bulk damage caused by neutrons. It can happen when neutrons perturb the structure of silicon atoms generating a large local electric field that results in hot pixels seen as bright dots in the images [186].

In order to investigate the impact of secondary ionising radiation on the camera, the mean pixel intensity was found for images acquired prior to the day's experiment, immediately after the experiment (during which approximately 94 Gy had been delivered to the Bragg peak) and then a further 120 minutes after exposure. Prior to exposure, the mean intensity was 0.313; after exposure, the intensity increased to 2.702, and then reduced to 0.499 after 120 minutes, indicating that that the performance of the camera degrades due to scattered radiation, but was largely temporary.

After 120 min, the number of pixels, which found higher than 20 grey values (i.e. the threshold value), was 8 pixels and found to be lower than that in the study [186]. The result indicated that no Bulk damage would impact the performance of the used camera.

Appendix C: Correction for the magnification and refraction artefacts in the 60 MeV proton beam

It was necessary to correct the scintillation light depth distribution for magnification and refraction and validate the result to the simulated quenched distribution. Since the distance to pixel was done at the central axis of the radiation track, the change of the geometry and intensities can be calculated across the beam using equation 2.1 and 2.2. The measured scintillation depth distribution along the central axis can be calculated and then be compared to the simulated quenched distribution using Geant4, as shown in Figure 96

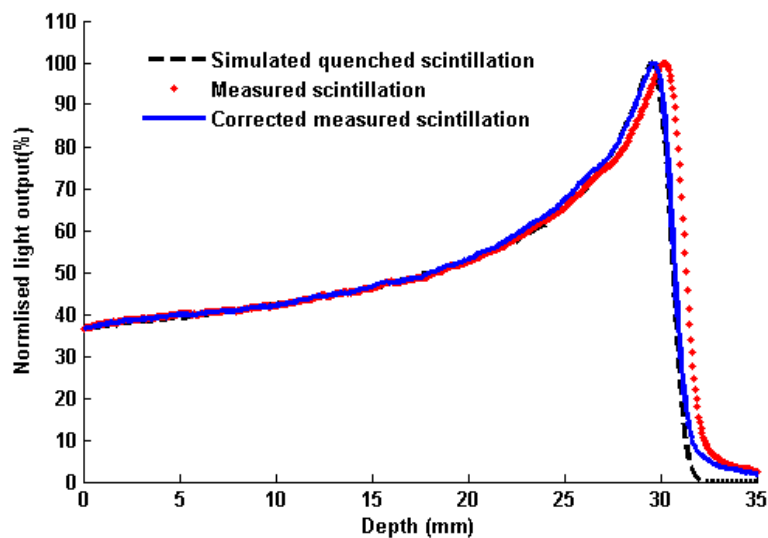


Figure 96: Measured scintillation data after correction for magnification was applied, compared with simulated scintillation distribution and actual measurement.

Appendix D: Definition of the BC-408 scintillator in Geant4

```
// --- BC-408 Scintillator Material as defined in Detector construction class -----

G4double a, z, density;
G4int nelements;

// BC-408 Scintillator compositions
G4Element* H = new G4Element("Hydrogen", "H", z=1 , a=1.01*g/mole);
G4Element* C = new G4Element("Carbon", "C", z=6 , a=12.00*g/mole);

G4Material* scintillator = new G4Material("scintillator", density= 1.032*g/cm3,
nelements=2);
scintillator->AddElement(H, 30);
scintillator->AddElement(C, 27);

// ----- Generate & Add Material Properties ---

// ----- Emission spectrum from BC-408-----

const G4int nEntries = 12;

G4double PhotonEnergy[nEntries] =
{ 2.08*eV, 2.38*eV, 2.58*eV,
  2.7*eV, 2.76*eV, 2.82*eV,
  2.92*eV, 2.95*eV, 3.02*eV,
  3.1*eV, 3.26*eV, 3.44*eV

};

G4double Scintillation1[nEntries] =
{ 0.00, 0.03, 0.17,
  0.40, 0.55, 0.83,
  1.00, 0.84, 0.49,
  0.20, 0.07, 0.04
};
```

```
//----- optical Properties of the BC-408 Scintillator-----

G4double RefractiveIndex1[nEntries] =
{ 1.58, 1.58, 1.58,
  1.58, 1.58, 1.58,
  1.58, 1.58, 1.58,
  1.58, 1.58, 1.58 };

G4double Absorption1[nEntries] =

{ 380*cm, 380*cm, 380*cm,
  380*cm, 380*cm, 380*cm,
  380*cm, 380*cm, 380*cm,
  380*cm, 380*cm, 380*cm };

G4MaterialPropertiesTable* myMPT1 = new G4MaterialPropertiesTable();
myMPT1->AddProperty("RINDEX", PhotonEnergy,
RefractiveIndex1,nEntries);
myMPT1->AddProperty("ABSLENGTH", PhotonEnergy, Absorption1,
nEntries);
myMPT1->AddProperty("FASTCOMPONENT", PhotonEnergy,
Scintillation1, nEntries);

myMPT1->AddConstProperty("SCINTILLATIONYIELD",100./MeV);
myMPT1->AddConstProperty("RESOLUTIONSCALE",1.0);
myMPT1->AddConstProperty("FASTTIMECONSTANT", 0.9*ns);
myMPT1->AddConstProperty("SLOWTIMECONSTANT",2.1*ns);
myMPT1->AddConstProperty("YIELDRATIO",1.);

scintillator->SetMaterialPropertiesTable(myMPT1);

// Set the Birks Constant for the BC-408 scintillator

scintillator->GetIonisation()->SetBirksConstant(0.154*mm/MeV);
```

BIBLIOGRAPHY

- [1] Cancer Research UK, "Lifetime risk of cancer," 2012. [Online]. Available: <http://www.cancerresearchuk.org/cancer-info/cancerstats/incidence/risk/>.
- [2] T. Kron, "Radiation therapy requirements: what do we expect from gel dosimetry," in *DOSGEL*, 2001, pp. 2-9.
- [3] G. F. Knoll, *Radiation Detection and Measurement, Fourth Edition*. John Wiley & Sons, 2010.
- [4] M. Lecchi, P. Fossati, F. Elisei, R. Orecchia, and G. Lucignani, "Current concepts on imaging in radiotherapy," *Eur. J. Nucl. Med. Mol. Imaging*, vol. 35, no. 4, pp. 821-837, Apr. 2008.
- [5] K. Newbold, M. Partridge, G. Cook, S. a Sohaib, E. Charles-Edwards, P. Rhys-Evans, K. Harrington, and C. Nutting, "Advanced imaging applied to radiotherapy planning in head and neck cancer: a clinical review," *Br. J. Radiol.*, vol. 79, no. 943, pp. 554-561, Jul. 2006.
- [6] M. N. Graves, A. V Thompson, M. K. Martel, D. L. McShan, and B. a Fraass, "Calibration and quality assurance for rounded leaf-end MLC systems," *Med. Phys.*, vol. 28, no. 11, p. 2227, 2001.
- [7] J. L. Bedford, Y. K. Lee, P. Wai, C. P. South, and A. P. Warrington, "Evaluation of the Delta 4 phantom for IMRT and VMAT verification," *Phys. Med. Biol.*, vol. 54, no. 9, pp. N167-N176, May 2009.
- [8] Varian Medical Systems, "Multileaf Collimators," 2012. [Online]. Available: <http://newsroom.varian.com>.
- [9] A. Kacperek, "Protontherapy of eye tumours in the UK: A review of treatment at Clatterbridge," *Appl. Radiat. Isot.*, vol. 67, no. 3, pp. 378-386, Mar. 2009.
- [10] M. Alber, S. Broggi, C. De Wagter, I. Eichwurz, P. Engström, C. Fiorino, D. Georg, G. Hartmann, T. Knöös, A. Leal, H. Marijnissen, B. Mijnheer, M. Paiusco, F. Sánchez-Doblado, R. Schmidt, M. Tomsej, and H. Welleweerd, *GUIDELINES FOR THE VERIFICATION OF IMRT*. Belgium: ESTRO, 2008.

-
- [11] T. Elsässer, W. K. Weyrather, T. Friedrich, M. Durante, G. Iancu, M. Krämer, G. Kragl, S. Brons, M. Winter, K.-J. Weber, and M. Scholz, "Quantification of the Relative Biological Effectiveness for Ion Beam Radiotherapy: Direct Experimental Comparison of Proton and Carbon Ion Beams and a Novel Approach for Treatment Planning," *Int. J. Radiat. Oncol.*, vol. 78, no. 4, pp. 1177–1183, Nov. 2010.
- [12] M. Scholz and T. Elsässer, "Biophysical models in ion beam radiotherapy," *Adv. Sp. Res.*, vol. 40, no. 9, pp. 1381–1391, Jan. 2007.
- [13] W. P. Levin, H. Kooy, J. S. Loeffler, and R. Reznick, "Proton beam therapy," *Br. J. Cancer*, vol. 93, no. 8, pp. 849–854, Oct. 2005.
- [14] H. Paganetti, "Range uncertainties in proton therapy and the role of Monte Carlo simulations," *Phys. Med. Biol.*, vol. 57, no. 11, pp. R99–117, Jun. 2012.
- [15] A. Lomax, "Intensity modulation methods for proton radiotherapy," *Phys. Med. Biol.*, vol. 44, pp. 185–205, 1999.
- [16] P. Andreo, M. S. Huq, M. Westermarck, H. Song, A. Tilikidis, L. DeWerd, and K. Shortt, "Protocols for the dosimetry of high-energy photon and electron beams: a comparison of the IAEA TRS-398 and previous international codes of practice. International Atomic Energy Agency," *Phys. Med. Biol.*, vol. 47, pp. 3033–3053, 2002.
- [17] S. Vatnitsky, M. Moyers, D. Miller, G. Abell, J. M. Slater, E. Pedroni, A. Coray, A. Mazal, W. Newhauser, O. Jaekel, J. Heese, A. Fukumura, Y. Futami, L. Verhey, I. Daftari, E. Grusell, A. Molokanov, and C. Bloch, "Proton dosimetry intercomparison based on the ICRU report 59 protocol," *Radiother. Oncol.*, vol. 51, no. 3, pp. 273–279, 1999.
- [18] M. Goitein, *Radiation Oncology: A Physicist's-Eye View (Biological and Medical Physics, Biomedical Engineering)*. Springer, 2007.
- [19] H. Johns and J. Cunningham, *The physics of radiology*, Fourth Edi. Springfield: Thomas, 1983.
- [20] E. B. Podgorsak, *Review of radiation oncology physics: a handbook for teachers and students*. VIENNA: IAEA, 2005.
- [21] R. Sigrú, *Introduction to Experimental Nuclear Physics*. Wiley Eastern, 1972.
- [22] O. Gilmore, *Practical Gamma-Ray Spectroscopy, Second edition*. John Wiley & Sons, 2008.
- [23] C. Leroy and P.-G. Rancoita, *Principles of Radiation Interaction in Matter and Detection*,

Second edition. World Scientific, 2009.

- [24] J. A. Pope, *Medical Physics: Imaging*. Heinemann, 1999.
- [25] J. H. Hubbell, "Photon mass attenuation and energy-absorption coefficients," *Int. J. Appl. Radiat. Isot.*, vol. 33, no. 11, pp. 1269–1290, 1982.
- [26] P. Andreo, "CALIBRATION OF PHOTON AND ELECTRON BEAMS," in *Review of radiation oncology physics: a handbook for teachers and students*, E. B. Podgorsak, Ed. VIENNA: IAEA, 2005, pp. 301–354.
- [27] F. Khan, *The Physics of Radiation Therapy*. Lippincott Williams & Wilkins, 2010.
- [28] M. K. Sundareshan, *Handbook of Particle Physics*. Florida: CRC Press, 2001.
- [29] A.-C. Knopf and A. Lomax, "In vivo proton range verification: a review.," *Phys. Med. Biol.*, vol. 58, no. 15, pp. 131–160, 2013.
- [30] D. E. Groom and S. R. Klein, "Passage of particles through matter," *Eur. Phys. J. C*, vol. 15, no. 1, pp. 163–173, Mar. 2000.
- [31] ICRU, "Stopping Power and Ranges for Protons and Alpha, ICRU Report No. 49," Bethesda MD, 1993.
- [32] Y.-S. Park, J.-H. Kim, G.-B. Kim, B.-H. Hong, I.-S. Jung, and T.-K. Yang, "Proton Beam Energy Determination Using a Device for Range Measurement of an Accelerated High Energy Ion Beam," *J. Korean Phys. Soc.*, vol. 59, no. 22, pp. 679–685, Aug. 2011.
- [33] M. Guillot, L. Beaulieu, L. Archambault, S. Beddar, and L. Gingras, "A new water-equivalent 2D plastic scintillation detectors array for the dosimetry of megavoltage energy photon beams in radiation therapy.," *Med. Phys.*, vol. 38, no. 12, pp. 6763–74, Dec. 2011.
- [34] S. Vynckier, D. E. Bonnett, and D. T. L. Jones, "Code of practice for clinical proton dosimetry," *Radiother. Oncol.*, vol. 20, no. 1, pp. 53–63, Jan. 1991.
- [35] Z. Chen, F. D'Errico, and R. Nath, "Principles and requirements of external beam dosimetry," *Radiat. Meas.*, vol. 41, no. SUPPL. 1, pp. 2–21, Dec. 2007.
- [36] V. Wolstenholme and J. P. Glees, "The Role of Kilovoltage X-rays in the Treatment of Skin Cancers," *Eur. Oncol. Haematol.*, vol. 1, no. 1, p. 32, 2006.
- [37] A. POLLACK, A. L. HANLON, E. M. HORWITZ, S. J. FEIGENBERG, R. G. UZZO, and

- G. E. HANKS, "Prostate Cancer Radiotherapy Dose Response: An Update of the Fox Chase Experience," *J. Urol.*, vol. 171, no. 3, pp. 1132–1136, 2004.
- [38] F. Roeder, C. Timke, M. Uhl, G. Habl, F. W. Hensley, M. W. Buechler, R. Krempien, P. E. Huber, J. Debus, and J. Werner, "Aggressive local treatment containing intraoperative radiation therapy (IORT) for patients with isolated local recurrences of pancreatic cancer: a retrospective analysis," *BMC Cancer*, vol. 12, p. 295, 2012.
- [39] D. I. Thwaites, B. J. Mijnheer, and J. A. Mills, "Quality Assurance of External Beam Radiotherapy," in *Review of Radiation Oncology Physics: A Handbook for Teachers and Students*, no. i, E. Podgorsak, Ed. IAEA, 2005, pp. 335–370.
- [40] V. La Rosa, A. Kacperek, G. Royle, and A. Gibson, "Range verification for eye proton therapy based on proton-induced x-ray emissions from implanted metal markers," *Phys. Med. Biol.*, vol. 59, no. 11, pp. 2623–2638, 2014.
- [41] M. Aznar, "Real-time in vivo luminescence dosimetry in radiotherapy and mammography using Al₂O₃:C," Denmark, 2005.
- [42] L. Archambault, F. Poenisch, N. Sahoo, D. Robertson, A. Lee, M. T. Gillin, R. Mohan, and S. Beddar, "Verification of proton range, position, and intensity in IMPT with a 3D liquid scintillator detector system," *Med. Phys.*, vol. 39, no. 3, p. 1239, Mar. 2012.
- [43] T. A. Simon, J. Kozelka, W. E. Simon, D. Kahler, J. Li, and C. Liu, "Characterization of a multi-axis ion chamber array," *Med. Phys.*, vol. 37, no. 11, p. 6101, 2010.
- [44] E. Spezi, a L. Angelini, F. Romani, and A. Ferri, "Characterization of a 2D ion chamber array for the verification of radiotherapy treatments," *Phys. Med. Biol.*, vol. 50, no. 14, pp. 3361–3373, Jul. 2005.
- [45] M. P. Petric, J. L. Robar, and B. G. Clark, "Development and characterization of a tissue equivalent plastic scintillator based dosimetry system," *Med. Phys.*, vol. 33, no. 1, p. 96, 2006.
- [46] M. Williams, P. Metcalfe, A. Rosenfeld, T. Kron, F. D'Errico, and M. Moscovitch, "Radiochromic Film Dosimetry and its Applications in Radiotherapy," 2011, vol. 75, no. 1, pp. 75–99.
- [47] Y. Fukushima, M. Hamada, T. Nishio, and K. Maruyama, "Development of an easy-to-handle range measurement tool using a plastic scintillator for proton beam therapy," *Phys. Med. Biol.*, vol. 51, no. 22, pp. 5927–36, Nov. 2006.

-
- [48] S. Steciw, B. Warkentin, S. Rathee, and B. G. Fallone, "Three-dimensional IMRT verification with a flat-panel EPID," *Med. Phys.*, vol. 32, no. 2, p. 600, 2005.
- [49] A. Van Esch, T. Depuydt, and D. P. Huyskens, "The use of an aSi-based EPID for routine absolute dosimetric pre-treatment verification of dynamic IMRT fields," *Radiother. Oncol.*, vol. 71, no. 2, pp. 223–234, May 2004.
- [50] B. Warkentin, S. Steciw, S. Rathee, and B. G. Fallone, "Dosimetric IMRT verification with a flat-panel EPID," *Med. Phys.*, vol. 30, no. 12, p. 3143, 2003.
- [51] L. J. Schreiner, "Where does gel dosimetry fit in the clinic?," *J. Phys. Conf. Ser.*, vol. 164, p. 12001, May 2009.
- [52] M. Guillot, L. Gingras, L. Archambault, S. Beddar, and L. Beaulieu, "Toward 3D dosimetry of intensity modulated radiation therapy treatments with plastic scintillation detectors," *J. Phys. Conf. Ser.*, vol. 250, p. 12006, Nov. 2010.
- [53] F. Lacroix, a. S. Beddar, M. Guillot, L. Beaulieu, and L. Gingras, "A design methodology using signal-to-noise ratio for plastic scintillation detectors design and performance optimization," *Med. Phys.*, vol. 36, no. 11, p. 5214, 2009.
- [54] F. Lacroix, L. Archambault, L. Gingras, M. Guillot, a. S. Beddar, and L. Beaulieu, "Clinical prototype of a plastic water-equivalent scintillating fiber dosimeter array for QA applications," *Med. Phys.*, vol. 35, no. 8, p. 3682, 2008.
- [55] D. Robertson, D. Mirkovic, N. Sahoo, and S. Beddar, "Quenching correction for volumetric scintillation dosimetry of proton beams," *Phys. Med. Biol.*, vol. 58, no. 2, pp. 261–273, 2013.
- [56] A. S. Beddar, T. R. Mackie, and F. H. Attix, "Water-equivalent plastic scintillation detectors for high-energy beam dosimetry: I. Physical characteristics and theoretical considerations," *Phys. Med. Biol.*, vol. 37, no. 10, pp. 1883–1900, Oct. 1992.
- [57] A. S. Beddar, T. R. Mackie, and F. H. Attix, "Water-equivalent plastic scintillation detectors for high-energy beam dosimetry: II. Properties and measurements," *Phys. Med. Biol.*, vol. 37, no. 10, pp. 1901–1913, Oct. 1992.
- [58] P. Liu, N. Suchowerska, J. Lambert, P. Abolfathi, and D. McKenzie, "Plastic scintillation dosimetry: comparison of three solutions for the Cerenkov challenge.," *Phys. Med. Biol.*, vol. 56, no. 18, pp. 5805–21, Sep. 2011.
- [59] L. Archambault, a. S. Beddar, L. Gingras, R. Roy, and L. Beaulieu, "Measurement

- accuracy and Cerenkov removal for high performance, high spatial resolution scintillation dosimetry," *Med. Phys.*, vol. 33, no. 1, p. 128, 2006.
- [60] B. Arjomandy, R. Taylor, A. Anand, N. Sahoo, M. T. Gillin, K. Prado, and M. Vicic, "Energy dependence and dose response of Gafchromic EBT2 film over a wide range of photon, electron, and proton beam energies," *Med. Phys.*, vol. 37, no. 5, pp. 1942–1947, 2010.
- [61] H. Bouchard and J. Seuntjens, "Ionization chamber-based reference dosimetry of intensity modulated radiation beams," *Med. Phys.*, vol. 31, no. 9, pp. 2454–2465, 2004.
- [62] H. Seliger, "Wilhelm Conrad Röntgen and the glimmer of light," *Phys. Today*, vol. 48, no. 11, pp. 25–31, 1995.
- [63] C. Dujardin, D. Amans, A. Belsky, F. Chaput, G. Ledoux, and A. Pillonnet, "Luminescence and Scintillation Properties at the Nanoscale," *IEEE Trans. Nucl. Sci.*, vol. 57, no. 3, pp. 1348–1354, Jun. 2010.
- [64] S. E. Derenzo, M. J. Weber, E. Bourret-Courchesne, and M. K. Klintenberg, "The quest for the ideal inorganic scintillator," *Nucl. Instruments Methods Phys. Res. Sect. A Accel. Spectrometers, Detect. Assoc. Equip.*, vol. 505, no. 1–2, pp. 111–117, Jun. 2003.
- [65] P. R. Bell, "The Use of Anthracene as a Scintillation Counter," *Phys. Rev.*, vol. 73, no. 11, pp. 1405–1406, Jun. 1948.
- [66] H. Kallmann, "Scintillation Counting with Solutions," *Phys. Rev.*, vol. 78, no. 5, pp. 621–622, Jun. 1950.
- [67] M. Ageno, M. Chiozzotto, and R. Querzoli, "Scintillations in Liquids and Solutions," *Phys. Rev.*, vol. 79, no. 4, p. 720, Aug. 1950.
- [68] L. E. Antonuk, "Electronic portal imaging devices: a review and historical perspective of contemporary technologies and research," *Phys. Med. Biol.*, vol. 47, no. 6, pp. 31–65, Mar. 2002.
- [69] B. Flynn, "Molecular Expressions Microscopy Primer: Fluorescence," Florida, 2006.
- [70] a. Jouini, J. C. Gâcon, M. Ferid, and M. Trabelsi-Ayadi, "Luminescence and scintillation properties of praseodymium poly and diphosphates," *Opt. Mater. (Amst.)*, vol. 24, no. 3, pp. 175–180, 2003.
- [71] F. Lacroix, L. Beaulieu, L. Archambault, and A. S. Beddar, "Simulation of the precision

- limits of plastic scintillation detectors using optimal component selection," *Med. Phys.*, vol. 37, no. 2, p. 412, 2010.
- [72] J. B. Birks, *The Theory and Practice of Scintillation Counting*. Pergamon, 1964.
- [73] P. Instrument, "The Effect of Quench on Quantitating Alpha Radionuclides by Liquid Scintillation Counting," Meriden, 2007.
- [74] K. Dong Wook, L. YoungKyung, S. Jungwook, A. Sungwhan, Y. Myongguen, L. SeByeong, P. Sung-Yong, K. DaeYong, K. Jungwon, and K. Jinsung, "A Dose Verification Method for Proton Therapy by Using a Plastic Scintillation Plate," *J. Korean Phys. Soc.*, vol. 55, no. 2, p. 702, Aug. 2009.
- [75] Saint-Gobain Crystals, "Premium Plastic Scintillators," 2005. [Online]. Available: <http://www.crystals.saint-gobain.com/>.
- [76] Saint-Gobain Crystals, "Organic Scintillation Materials," 2011. [Online]. Available: <http://www.crystals.saint-gobain.com/>.
- [77] A. S. Beddar, K. J. Kinsella, A. Ikhlef, and C. H. Sibata, "A miniature 'scintillator-fiberoptic-PMT' detector system for the dosimetry of small fields in stereotactic radiosurgery," *IEEE Trans. Nucl. Sci.*, vol. 48, no. 3, pp. 924–928, Jun. 2001.
- [78] J. M. Fontbonne, G. Iltis, G. Ban, A. Battala, J. C. Vernhes, J. Tillier, N. Bellaize, C. Le Brun, B. Tamain, K. Mercier, and J. C. Motin, "Scintillating fiber dosimeter for radiation therapy accelerator," *IEEE Trans. Nucl. Sci.*, vol. 49, no. 5, pp. 2223–2227, Oct. 2002.
- [79] J. S. Li, C. Ozhasoglu, J. Deng, A. L. Boyer, and C.-M. Ma, "Verification of IMRT dose distributions using a water beam imaging system," in *Proceedings of the 22nd Annual International Conference of the IEEE Engineering in Medicine and Biology Society (Cat. No.00CH37143)*, 2000, vol. 2, pp. 1158–1161.
- [80] M. Petric, "Verification of intensity modulated radiation therapy beams using tissue equivalent plastic scintillator dosimetry system," The University of British Columbia, 2006.
- [81] S. Beddar, L. Archambault, N. Sahoo, F. Poenisch, G. T. Chen, M. T. Gillin, and R. Mohan, "Exploration of the potential of liquid scintillators for real-time 3D dosimetry of intensity modulated proton beams," *Med. Phys.*, vol. 36, no. 5, pp. 1736–1743, 2009.
- [82] S. Beddar, "A Liquid Scintillator System for Dosimetry of Photon and Proton Beams," *J. Phys. Conf. Ser.*, vol. 250, p. 12038, Nov. 2010.

- [83] F. Pönisch, L. Archambault, T. M. Briere, N. Sahoo, R. Mohan, S. Beddar, and M. T. Gillin, "Liquid scintillator for 2D dosimetry for high-energy photon beams," *Med. Phys.*, vol. 36, no. 5, p. 1478, 2009.
- [84] G. D. Badhwar, C. L. Deney, B. R. Dennis, and M. F. Kaplon, "The non-linear response of the plastic scintillator NE102," *Nuclear Instruments and Methods*, vol. 57, no. 7. pp. 116–120, 1967.
- [85] L. L. W. Wang, L. a Perles, L. Archambault, N. Sahoo, D. Mirkovic, and S. Beddar, "Determination of the quenching correction factors for plastic scintillation detectors in therapeutic high-energy proton beams.," *Phys. Med. Biol.*, vol. 57, no. 23, pp. 7767–81, 2012.
- [86] L. Torrisi, A. Desiderio, and G. Foti, "High energy proton induced luminescence in F-doped polyvinyltoluene," *Nucl. Instruments Methods Phys. Res. Sect. B Beam Interact. with Mater. Atoms*, vol. 166, pp. 664–668, 2000.
- [87] G. a Ezzell, J. W. Burmeister, N. Dogan, T. J. LoSasso, J. G. Mechalakos, D. Mihailidis, A. Molineu, J. R. Palta, C. R. Ramsey, B. J. Salter, J. Shi, P. Xia, N. J. Yue, and Y. Xiao, "IMRT commissioning: multiple institution planning and dosimetry comparisons, a report from AAPM Task Group 119.," *Med. Phys.*, vol. 36, no. 11, pp. 5359–5373, 2009.
- [88] D. A. Low, W. B. Harms, S. Mutic, and J. a Purdy, "A technique for the quantitative evaluation of dose distributions.," *Med. Phys.*, vol. 25, no. 5, pp. 656–61, 1998.
- [89] X. R. Zhu, F. Poenisch, X. Song, J. L. Johnson, G. Ciangaru, M. B. Taylor, M. Lii, C. Martin, B. Arjomandy, A. K. Lee, S. Choi, Q. N. Nguyen, M. T. Gillin, and N. Sahoo, "Patient-specific quality assurance for prostate cancer patients receiving spot scanning proton therapy using single-field uniform dose," *Int. J. Radiat. Oncol. Biol. Phys.*, vol. 81, no. 2, pp. 552–559, 2011.
- [90] B. Arjomandy, N. Sahoo, G. Ciangaru, R. Zhu, X. Song, and M. Gillin, "Verification of patient-specific dose distributions in proton therapy using a commercial two-dimensional ion chamber array.," *Med. Phys.*, vol. 37, no. 11, pp. 5831–5837, 2010.
- [91] L. Archambault, a. S. Beddar, L. Gingras, F. Lacroix, R. Roy, and L. Beaulieu, "Water-equivalent dosimeter array for small-field external beam radiotherapy," *Med. Phys.*, vol. 34, no. 5, p. 1583, 2007.
- [92] a. S. Beddar, "Plastic scintillation dosimetry and its application to radiotherapy," *Radiat.*

- Meas.*, vol. 41, pp. S124–S133, Dec. 2006.
- [93] R. A. Winyard, J. E. Lutkin, and G. W. McBeth, "Pulse Shape Discrimination in Inorganic and Organic Scintillators. I," *Nucl. Instruments Methods Phys. Res. Sect. A*, vol. 95, no. 1, pp. 141–153, 1971.
- [94] W. van Elmpt, L. McDermott, S. Nijsten, M. Wendling, P. Lambin, and B. Mijnheer, "A literature review of electronic portal imaging for radiotherapy dosimetry," *Radiother. Oncol.*, vol. 88, no. 3, pp. 289–309, 2008.
- [95] S. S. Samant and A. Gopal, "Study of a prototype high quantum efficiency thick scintillation crystal video-electronic portal imaging device.," *Med. Phys.*, vol. 33, no. 2006, pp. 2783–2791, 2006.
- [96] A.-M. Frelin, J.-M. Fontbonne, G. Ban, A. Batalla, J. Colin, A. Isambert, M. Labalme, T. Leroux, and A. Vela, "A new scintillating fiber dosimeter using a single optical fiber and a CCD camera," *IEEE Trans. Nucl. Sci.*, vol. 53, no. 3, pp. 1113–1117, Jun. 2006.
- [97] J. Lambert, Y. Yin, D. R. McKenzie, S. Law, and N. Suchowerska, "Cerenkov-free scintillation dosimetry in external beam radiotherapy with an air core light guide," *Phys. Med. Biol.*, vol. 53, no. 11, pp. 3071–3080, Jun. 2008.
- [98] R. Zhang, C. J. Fox, A. K. Glaser, D. J. Gladstone, and B. W. Pogue, "Superficial dosimetry imaging of Čerenkov emission in electron beam radiotherapy of phantoms.," *Phys. Med. Biol.*, vol. 58, no. 16, pp. 5477–93, 2013.
- [99] B. Marczewska, P. Bilski, L. Czopyk, P. Olko, M. P. R. Waligórski, and S. Zapotoczny, "Two-dimensional thermoluminescence dosimetry using planar detectors and a TL reader with CCD camera readout," *Radiat. Prot. Dosimetry*, vol. 120, no. 1–4, pp. 129–132, 2006.
- [100] A. K. Glaser, S. C. Davis, D. M. McClatchy, R. Zhang, B. W. Pogue, and D. J. Gladstone, "Projection imaging of photon beams by the Čerenkov effect," *Med. Phys.*, vol. 40, no. 1, p. 12101, Feb. 2013.
- [101] J. M. Andreozzi, R. Zhang, A. K. Glaser, L. A. Jarvis, B. W. Pogue, and D. J. Gladstone, "Camera selection for real-time in vivo radiation treatment verification systems using Cherenkov imaging," *Med. Phys.*, vol. 42, no. 2, pp. 994–1004, Feb. 2015.
- [102] J. E. Garcia, P. A. Wilksch, G. Spring, P. Philp, and A. Dyer, "Characterization of Digital Cameras for Reflected Ultraviolet Photography; Implications for Qualitative and

- Quantitative Image Analysis During Forensic Examination," *J. Forensic Sci.*, vol. 59, no. 1, pp. 117-122, 2014.
- [103] Y. Helo, A. Kacperek, I. Rosenberg, G. Royle, and A. P. Gibson, "The physics of Cerenkov light production during proton therapy," *Phys. Med. Biol.*, vol. 59, no. 23, pp. 7107-7123, 2014.
- [104] Y. Helo, I. Rosenberg, D. D'Souza, L. Macdonald, R. Speller, G. Royle, and A. Gibson, "Imaging Cerenkov emission as a quality assurance tool in electron radiotherapy," *Phys. Med. Biol.*, vol. 59, no. 8, pp. 1963-78, Apr. 2014.
- [105] J. Axelsson, A. K. Glaser, D. J. Gladstone, and B. W. Pogue, "Quantitative Cherenkov emission spectroscopy for tissue oxygenation assessment," *Opt. Express*, vol. 20, no. 5, pp. 5133-5142, 2012.
- [106] C. H. Jenkins, D. J. Naczynski, S.-J. S. Yu, and L. Xing, "Monitoring external beam radiotherapy using real-time beam visualization," *Med. Phys.*, vol. 42, no. 1, pp. 5-13, Jan. 2014.
- [107] A. K. Glaser, S. C. Davis, W. H. a Voigt, R. Zhang, B. W. Pogue, and D. J. Gladstone, "Projection imaging of photon beams using Čerenkov-excited fluorescence.," *Phys. Med. Biol.*, vol. 58, no. 3, pp. 601-19, 2013.
- [108] "Nikon Electronic Format," 2016. [Online]. Available: <http://www.nikonusa.com>.
- [109] DxOMark, "Nikon D7100: Measurements," 2016. [Online]. Available: <https://www.dxomark.com>.
- [110] G. Ayotte, L. Archambault, L. Gingras, F. Lacroix, a. S. Beddar, and L. Beaulieu, "Surface preparation and coupling in plastic scintillator dosimetry," *Med. Phys.*, vol. 33, no. 9, p. 3519, 2006.
- [111] L. Archambault, J. Arsenault, L. Gingras, A. Sam Beddar, R. Roy, and L. Beaulieu, "Plastic scintillation dosimetry: Optimal selection of scintillating fibers and scintillators," *Med. Phys.*, vol. 32, no. 7, p. 2271, 2005.
- [112] K. W. Jang, W. J. Yoo, S. H. Shin, D. Shin, and B. Lee, "Fiber-optic Cerenkov radiation sensor for proton therapy dosimetry.," *Opt. Express*, vol. 20, no. 13, pp. 13907-14, 2012.
- [113] T. BATSCH and M. MOSZYNSKI, "TIMING PROPERTIES OF THIN SCINTILLATOR FOILS," *Nucl. INSTRUMENTS METHODS*, vol. 23, pp. 341-352, 1974.

- [114] kuraray, "Plastic Scintillating Fibers," 2015. [Online]. Available: <http://kuraraypsf.jp>.
- [115] Eljen Technology, "Plastic and liquid scintillators," 2011. [Online]. Available: <http://www.eljentechnology.com/index.php/products>.
- [116] L. Torrasi, "Plastic scintillator investigations for relative dosimetry in proton therapy," *Nucl. Instruments Methods Phys. Res.*, vol. 170, pp. 523-530, 2000.
- [117] D. Robertson, C. Hui, L. Archambault, R. Mohan, and S. Beddar, "Optical artefact characterization and correction in volumetric scintillation dosimetry," *Phys. Med. Biol.*, vol. 59, no. 1, pp. 23-42, Jan. 2013.
- [118] M. Miyajima, S. Sasaki, and H. Tawara, "Numbers of scintillation photons produced in NaI(Tl) and plastic scintillator by gamma-rays," *IEEE Trans. Nucl. Sci.*, vol. 40, no. 4 pt 1, pp. 417-423, 1993.
- [119] Saint-Gobain Crystals, "Physical Properties of Common Inorganic Scintillators," 2009. .
- [120] K. S. Shah, J. Glodo, M. Klugerman, W. W. Moses, S. E. Derenzo, and M. J. Weber, "LaBr₃:Ce Scintillators for Gamma-Ray Spectroscopy," *IEEE Trans. Nucl. Sci.*, vol. 50, no. 6 II, pp. 2410-2413, 2003.
- [121] R. Hill, B. Healy, L. Holloway, Z. Kuncic, D. Thwaites, and C. Baldock, "Advances in kilovoltage x-ray beam dosimetry.," *Phys. Med. Biol.*, vol. 59, no. 6, pp. R183-231, Mar. 2014.
- [122] J. Deasy, "ICRU Report 49, Stopping Powers and Ranges for Protons and Alph Particles," *Med. Phys.*, vol. 21, no. 5, p. 709, 1999.
- [123] R. Zhang and W. D. Newhauser, "Calculation of water equivalent thickness of materials of arbitrary density, elemental composition and thickness in proton beam irradiation," *Phys. Med. Biol.*, vol. 54, no. 6, pp. 1383-1395, Mar. 2009.
- [124] M. Berger, J. Coursey, M. Zucker, and J. Chang, "NIST Stopping-Power and Range Tables: Electrons, Protons, Helium Ions," 2009.
- [125] S. Rowan, A. Apollonio, B. Auchmann, A. Lechner, O. Picha, W. Riegler, H. Schindler, R. Schmidt, and F. Zimmermann, "INTERACTIONS BETWEEN MACROPARTICLES AND HIGH-ENERGY PROTON BEAMS," in *6th International Particle Accelerator Conference (IPAC 2015)*, 2015, no. 2, pp. 1-4.
- [126] D. CLARK, "THE INTRINSIC SCINTILLATION EFFICIENCY OF PLASTIC

- SCINTILLATORS FOR Co GAMMA EXCITATION," *Nucl. INSTRUMENTS METHODS*, vol. 7, no. 117, pp. 295–303, 1974.
- [127] I. J. Das, C.-W. Cheng, R. J. Watts, A. Ahnesjö, J. Gibbons, X. A. Li, J. Lowenstein, R. K. Mitra, W. E. Simon, and T. C. Zhu, "Accelerator beam data commissioning equipment and procedures: Report of the TG-106 of the Therapy Physics Committee of the AAPM," *Med. Phys.*, vol. 35, no. 9, pp. 4186–4215, Sep. 2008.
- [128] A. K. Glaser, S. C. Kanick, R. Zhang, P. Arce, and B. W. Pogue, "A GAMOS plug-in for GEANT4 based Monte Carlo simulation of radiation-induced light transport in biological media.," *Biomed. Opt. Express*, vol. 4, no. 5, pp. 741–759, May 2013.
- [129] S. Agostinelli, J. Allison, K. Amako, J. Apostolakis, H. Araujo, P. Arce, M. Asai, D. Axen, S. Banerjee, G. Barrand, F. Behner, L. Bellagamba, J. Boudreau, L. Broglia, a. Brunengo, H. Burkhardt, S. Chauvie, J. Chuma, R. Chytracsek, G. Cooperman, G. Cosmo, P. Degtyarenko, a. Dell'Acqua, G. Depaola, D. Dietrich, R. Enami, a. Feliciello, C. Ferguson, H. Fesefeldt, G. Folger, F. Foppiano, a. Forti, S. Garelli, S. Giani, R. Giannitrapani, D. Gibin, J. J. Gomez Cadenas, I. Gonzalez, G. Gracia Abril, G. Greeniaus, W. Greiner, V. Grichine, a. Grossheim, S. Guatelli, P. Gumplinger, R. Hamatsu, K. Hashimoto, H. Hasui, a. Heikkinen, a. Howard, V. Ivanchenko, a. Johnson, F. W. Jones, J. Kallenbach, N. Kanaya, M. Kawabata, Y. Kawabata, M. Kawaguti, S. Kelner, P. Kent, a. Kimura, T. Kodama, R. Kokoulin, M. Kossov, H. Kurashige, E. Lamanna, T. Lampen, V. Lara, V. Lefebure, F. Lei, M. Liendl, W. Lockman, F. Longo, S. Magni, M. Maire, E. Medernach, K. Minamimoto, P. Mora de Freitas, Y. Morita, K. Murakami, M. Nagamatu, R. Nartallo, P. Nieminen, T. Nishimura, K. Ohtsubo, M. Okamura, S. O'Neale, Y. Oohata, K. Paech, J. Perl, a. Pfeiffer, M. G. Pia, F. Ranjard, a. Rybin, S. Sadilov, E. di Salvo, G. Santin, T. Sasaki, N. Savvas, Y. Sawada, S. Scherer, S. Sei, V. Sirotenko, D. Smith, N. Starkov, H. Stoecker, J. Sulkimo, M. Takahata, S. Tanaka, E. Tcherniaev, E. Safai Tehrani, M. Tropeano, P. Truscott, H. Uno, L. Urban, P. Urban, M. Verderi, a. Walkden, W. Wander, H. Weber, J. P. Wellisch, T. Wenaus, D. C. Williams, D. Wright, T. Yamada, H. Yoshida, and D. Zschiesche, "GEANT4 - A simulation toolkit," *Nucl. Instruments Methods Phys. Res. Sect. A Accel. Spectrometers, Detect. Assoc. Equip.*, vol. 506, no. 3, pp. 250–303, 2003.
- [130] E. Hecht, *Optics, Fourth Edition*. Essex: Addison Wesley, 2001.
- [131] A. K. Glaser, S. C. Davis, W. H. a Voigt, R. Zhang, B. W. Pogue, and D. J. Gladstone, "Projection imaging of photon beams using Čerenkov-excited fluorescence.," *Phys. Med.*

- Biol.*, vol. 58, no. 3, pp. 601–19, 2013.
- [132] D. Coffin, “Decoding raw digital photos,” 2000. [Online]. Available: <https://www.cybercom.net/~dcoffin/dcraw/>.
- [133] P. Allisy-Roberts and J. Williams, *Farr’s Physics for Medical Imaging*, 2nd edtion. Saunders Ltd., 2007.
- [134] J. T. Bushberg, J. A. Seibert, E. M. Leidholdt, J. M. Boone, and M. Mahesh, *The Essential Physics of Medical Imaging, Third Edition.*, vol. 40, no. 7. 2011.
- [135] R. Hill, Z. Kuncic, and C. Baldock, “The water equivalence of solid phantoms for low energy photon beams,” *Med. Phys.*, vol. 37, no. 8, p. 4355, 2010.
- [136] R. Hill, L. Holloway, and C. Baldock, “A dosimetric evaluation of water equivalent phantoms for kilovoltage x-ray beams,” *Phys. Med. Biol.*, vol. 50, no. 21, pp. N331–N344, Nov. 2005.
- [137] G. Hajdok, J. Yao, J. J. Battista, and I. A. Cunningham, “Signal and noise transfer properties of photoelectric interactions in diagnostic x-ray imaging detectors,” *Med. Phys.*, vol. 33, no. 10, pp. 3601–3620, 2006.
- [138] C.-M. Chair, C. W. Coffey, L. a DeWerd, C. Liu, R. Nath, S. M. Seltzer, and J. P. Seuntjens, “AAPM protocol for 40–300 kV x-ray beam dosimetry in radiotherapy and radiobiology,” *Med. Phys.*, vol. 28, no. 6, pp. 868–893, Jun. 2001.
- [139] L. Peralta and F. Rêgo, “Response of plastic scintillators to low-energy photons,” *Phys. Med. Biol.*, vol. 59, no. 16, pp. 4621–4633, 2014.
- [140] F. Lessard, L. Archambault, M. Plamondon, P. Despres, F. Therriault-Proulx, S. Beddar, and L. Beaulieu, “Validating plastic scintillation detectors for photon dosimetry in the radiologic energy range,” *Med. Phys.*, vol. 39, no. 9, pp. 5308–16, Sep. 2012.
- [141] S. Chauvie, S. Guatelli, V. Ivanchenko, F. Longo, a. Mantero, B. Mascialino, P. Nieminen, L. Pandola, S. Parlati, L. Peralta, M. G. Pia, M. Piergentili, P. Rodrigues, S. Saliceti, and a. Tnnade, “Geant4 low energy electromagnetic physics,” *IEEE Symp. Conf. Rec. Nucl. Sci. 2004.*, vol. 3, no. C, pp. 1881–1885, 2004.
- [142] E. Poon and F. Verhaegen, “Accuracy of the photon and electron physics in GEANT4 for radiotherapy applications,” *Med. Phys.*, vol. 32, no. 6, pp. 1696–1711, 2005.
- [143] P. J. Lamperti and M. O’Brien, “NIST Measurement Services: Calibration of X-Ray and

- Gamma-Ray Measuring Instruments," *Nist Special publication-250-58*. 2001.
- [144] G. Poludniowski, G. Landry, F. DeBlois, P. M. Evans, and F. Verhaegen, "SpekCalc: a program to calculate photon spectra from tungsten anode x-ray tubes.," *Phys. Med. Biol.*, vol. 54, no. 19, pp. N433-8, Oct. 2009.
- [145] W. S. Jae, H. Seung-Woo, L. Chung-Il, and S. Tae-Suk, "Application of a GEANT4 Simulation to a 60Co Therapy Unit," *J. Korean Phys. Soc.*, vol. 59, no. 1, p. 12, 2011.
- [146] International Commission on Radiation Units and Measurements, "Electron beams with energies between 1 and 50 MeV," ICRU Report No. 35, 1984.
- [147] T. Tabata and P. Andreo, "A method to convert absolute depth - dose curves of electrons between different phantom materials," *Japanese J. Med. Phys.*, vol. 160, pp. 1-12, 1997.
- [148] J. C. L. Chow and R. Jiang, "Bone and mucosal dosimetry in skin radiation therapy: a Monte Carlo study using kilovoltage photon and megavoltage electron beams.," *Phys. Med. Biol.*, vol. 57, no. 12, pp. 3885-99, Jun. 2012.
- [149] C. M. Ma and a E. Nahum, "Bragg-Gray theory and ion chamber dosimetry for photon beams.," *Phys. Med. Biol.*, vol. 36, no. 4, pp. 413-28, Apr. 1991.
- [150] T. Gorjiara, R. Hill, Z. Kuncic, S. Bosi, J. B. Davies, and C. Baldock, "Radiological characterization and water equivalency of genipin gel for x-ray and electron beam dosimetry," *Phys. Med. Biol.*, vol. 56, no. 15, pp. 4685-4699, Aug. 2011.
- [151] SSRFM, "Quality Control of Medical Electron Accelerators Recommendations," 2014.
- [152] D. a Low, J. M. Moran, J. F. Dempsey, L. Dong, and M. Oldham, "Dosimetry tools and techniques for IMRT.," *Med. Phys.*, vol. 38, no. 3, pp. 1313-1338, 2011.
- [153] S. Amerio, a Boriano, F. Bourhaleb, R. Cirio, M. Donetti, a Fidanzio, E. Garelli, S. Giordanengo, E. Madon, F. Marchetto, U. Nastasi, C. Peroni, a Piermattei, C. J. Sanz Freire, a Sardo, and E. Trevisiol, "Dosimetric characterization of a large area pixel-segmented ionization chamber.," *Med. Phys.*, vol. 31, no. 2, pp. 414-420, 2004.
- [154] C. Shi, N. Papanikolaou, Y. Yan, X. Weng, and H. Jiang, "Analysis of the sources of uncertainty for EDR2 film-based IMRT quality assurance," *J. Appl. Clin. Med. Phys.*, vol. 7, no. 2, pp. 1-8, 2006.
- [155] A. M. Frelin, J. M. Fontbonne, G. Ban, J. Colin, M. Labalme, A. Batalla, A. Vela, P. Boher, M. Braud, and T. Leroux, "The DosiMap, a new 2D scintillating dosimeter for IMRT

- quality assurance: characterization of two Cerenkov discrimination methods," *Med Phys*, vol. 35, no. 5, pp. 1651–1662, 2008.
- [156] S. Safai, S. Lin, and E. Pedroni, "Development of an inorganic scintillating mixture for proton beam verification dosimetry," *Phys. Med. Biol.*, vol. 49, no. 19, pp. 4637–4655, Oct. 2004.
- [157] M. Guillot, L. Gingras, L. Archambault, S. Beddar, and L. Beaulieu, "Spectral method for the correction of the Cerenkov light effect in plastic scintillation detectors: A comparison study of calibration procedures and validation in Cerenkov light-dominated situations," *Med. Phys.*, vol. 38, no. 4, p. 2140, 2011.
- [158] S. N. Boon, "Dosimetry and quality control of scanning proton beams," Journal Article, University Library Groningen, 1998.
- [159] V. Collomb-Patton, P. Boher, T. Leroux, J. M. Fontbonne, A. Vela, and A. Batalla, "The DOSIMAP, a high spatial resolution tissue equivalent 2D dosimeter for LINAC QA and IMRT verification," *Med. Phys.*, vol. 36, no. 2, pp. 317–328, 2009.
- [160] L. Al-Sulaiti, D. Shipley, R. Thomas, P. Owen, A. Kacperek, P. H. Regan, and H. Palmans, "Water equivalence of some plastic-water phantom materials for clinical proton beam dosimetry," *Appl. Radiat. Isot.*, vol. 70, no. 7, pp. 1052–7, Jul. 2012.
- [161] R. Zhang, P. J. Taddei, M. M. Fitzek, and W. D. Newhauser, "Water equivalent thickness values of materials used in beams of protons, helium, carbon and iron ions," *Phys. Med. Biol.*, vol. 55, no. 9, pp. 2481–2493, May 2010.
- [162] K. R. Kase, X. S. Mao, W. R. Nelson, J. C. Liu, J. H. Kleck, and M. Elsalim, "NEUTRON FLUENCE AND ENERGY SPECTRA AROUND THE VARIAN CLINAC 2100C / 2300C MEDICAL ACCELERATOR," *Health Phys.*, vol. 74, no. 1, pp. 38–47, 1998.
- [163] P. Andreo, D. Burns, K. Hohlfeld, M. S. Huq, T. Kanai, F. Laitano, V. Smyth, and S. Vynckier, "Absorbed Dose Determination in External Beam Radiotherapy: An International Code of Practice for Dosimetry based on Standards of Absorbed Dose to Water," Austria, 2006.
- [164] F. M. Khan, K. P. Doppke, K. R. Hogstrom, G. J. Kutcher, R. Nath, S. C. Prasad, J. A. Purdy, M. Rozenfeld, and B. L. Werner, "Clinical electron-beam dosimetry: Report of AAPM Radiation Therapy Committee Task Group No. 25," New York, 1990.
- [165] J. Venselaar, H. Welleweerd, and B. Mijnheer, "Tolerances for the accuracy of photon

- beam dose calculations of treatment planning systems," *Radiother. Oncol.*, vol. 60, no. 2, pp. 191–201, Aug. 2001.
- [166] D. Thwaites, "Accuracy required and achievable in radiotherapy dosimetry: have modern technology and techniques changed our views?," *J. Phys. Conf. Ser.*, vol. 444, p. 12006, Jun. 2013.
- [167] ICRU, "Electron Beams with Energies between 1 and 50 MeV," 1984.
- [168] B. J. Gerbi, J. a Antolak, F. C. Deibel, D. S. Followill, M. G. Herman, P. D. Higgins, M. S. Huq, D. N. Mihailidis, E. D. Yorke, K. R. Hogstrom, and F. M. Khan, "Recommendations for clinical electron beam dosimetry: Supplement to the recommendations of Task Group 25," *Med. Phys.*, vol. 38, no. 1, pp. 548–548, Jan. 2011.
- [169] E. E. Klein, J. Hanley, J. Bayouth, F. F. Yin, W. Simon, S. Dresser, C. Serago, F. Aguirre, L. Ma, B. Arjomandy, C. Liu, C. Sandin, T. Holmes, and A. A. of P. in M. Task Group, "Task Group 142 report: quality assurance of medical accelerators," *Med Phys*, vol. 36, no. 9, pp. 4197–4212, 2009.
- [170] S. Meroli, "Energy Loss Calculator Program," 2012. [Online]. Available: <http://meroli.web.cern.ch/meroli/EnergyLossCalculation.html>.
- [171] S. Beddar and L. Beaulieu, *Scintillation dosimetry*. New York: CRC Press, 2016.
- [172] J. W. Blue and D. C. Liu, "Scintillation Response of Aikali Iodides to Alpeha Particles and Protons," *IRE Trans. Nucl. Sci.*, vol. 9, no. 3, pp. 48–51, Jun. 1962.
- [173] F. Ciocia, A. Braem, E. Chesi, R. De Leo, C. Joram, L. Lagamba, E. Nappi, J. Séguinot, I. Vilardi, and P. Weilhammer, "GEANT4 studies on the propagation and detection of scintillation light in long thin YAP crystals," *Nucl. Instruments Methods Phys. Res. Sect. A Accel. Spectrometers, Detect. Assoc. Equip.*, vol. 600, no. 2, pp. 506–512, 2009.
- [174] S. Riggi, P. La Rocca, E. Leonora, D. Lo Presti, G. S. Pappalardo, F. Riggi, and G. V. Russo, "Geant4 simulation of plastic scintillator strips with embedded optical fibers for a prototype of tomographic system," *Nucl. Instruments Methods Phys. Res. Sect. A Accel. Spectrometers, Detect. Assoc. Equip.*, vol. 624, no. 3, pp. 583–590, 2010.
- [175] F. Guan, C. Peeler, L. Bronk, C. Geng, R. Taleei, S. Randeniya, S. Ge, D. Mirkovic, D. Grosshans, R. Mohan, and U. Titt, "Analysis of the track- and dose-averaged LET and LET spectra in proton therapy using the geant4 Monte Carlo code," *Med. Phys.*, vol. 42, no. 11, pp. 6234–6247, Nov. 2015.

- [176] G. Cirrone and G. Cuttone, "Hadrontherapy: a Geant4-based tool for proton/ion-therapy studies," *Prog. Nucl. Sci.*, vol. 2, pp. 207–212, 2011.
- [177] J. Ziegler, J. Biersack, M. Ziegler, D. Marwick, G. Cuomo, W. Porter, and S. Harrison, "SRIM 2013 Code 1984–2013," 2013. [Online]. Available: <http://www.srim.org/>.
- [178] ICRU, "Prescribing, Recording, and Reporting Proton-Beam Therapy," 2007.
- [179] M. T. Gillin, N. Sahoo, M. Bues, G. Ciangaru, G. Sawakuchi, F. Poenisch, B. Arjomandy, C. Martin, U. Titt, K. Suzuki, A. R. Smith, and X. R. Zhu, "Commissioning of the discrete spot scanning proton beam delivery system at the University of Texas M.D. Anderson Cancer Center, Proton Therapy Center, Houston," *Med. Phys.*, vol. 37, no. 1, p. 154, 2010.
- [180] X. R. Zhu, F. Poenisch, M. Lii, G. O. Sawakuchi, U. Titt, M. Bues, X. Song, X. Zhang, Y. Li, G. Ciangaru, H. Li, M. B. Taylor, K. Suzuki, R. Mohan, M. T. Gillin, and N. Sahoo, "Commissioning dose computation models for spot scanning proton beams in water for a commercially available treatment planning system," *Med. Phys.*, vol. 40, no. 4, p. 41723, 2013.
- [181] M. Watanabe and S. Nayar, "Telecentric optics for computational vision," in *Proc. of European Conference on Computer Vision*, 1995, pp. 439–451.
- [182] J. Kitzhofer and C. Brücker, "Tomographic particle tracking velocimetry using telecentric imaging," *Exp. Fluids*, vol. 49, no. 6, pp. 1307–1324, Dec. 2010.
- [183] D. Li and J. Tian, "An accurate calibration method for a camera with telecentric lenses," *Opt. Lasers Eng.*, vol. 51, no. 5, pp. 538–541, May 2013.
- [184] B. Pan, L. Yu, and D. Wu, "High-Accuracy 2D Digital Image Correlation Measurements with Bilateral Telecentric Lenses: Error Analysis and Experimental Verification," *Exp. Mech.*, vol. 53, no. 9, pp. 1719–1733, Nov. 2013.
- [185] Nikon Corporation, "Camera Control Pro 2," 2014. [Online]. Available: http://imaging.nikon.com/lineup/software/control_pro2/.
- [186] J. Kok, "Low cost CCD camera protection against neutron radiation damage," *J. Med. Eng. Technol.*, vol. 29, no. 1, pp. 27–32, 2005.
- [187] M. Facchini, A. Tsoulou, and S. Hutchins, "Radiation tests on solid state cameras for instrumentation," in *Proceedings of DIPAC*, 2005, pp. 315–317.